Demixing phenomena in 2D bose gases

Edouard Le Cerf

Thèse de doctorat de
Sorbonne Université

présentée par

Édouard Le Cerf

pour obtenir le grade de Docteur de Sorbonne Université
sur le sujet :

DEMIXING PHENOMENA IN 2D BOSE GASES

préparé au Laboratoire Kastler-Brossel
sous la direction de **Jérôme Beugnon** et **Jean Dalibard**

Laboratoire Kastler Brossel
Physique quantique et applications

CONTENTS

A beginning is the time for taking the most delicate care that the balances are correct. This every sister of the Bene Gesserit knows.

— Princess Irulan, *Manual of Muad'Dib*

I CAN DO MAGIC! FEAR ME, LAWS OF PHYSICS, I'M COMING TO VIOLATE YOU!

— A certain version of Harry James Potter-Evans-Verres

Introduction

INTRODUCTION

Cold atom physicists telling their relatives that they cool atoms with high power lasers are often met with bewildered, or even suspicious looks. Instinctively, we tend to think that light heats, and not cools, matter. This can however be better understood in a quantum mechanical framework, where an atom absorbing a photon transitions to an excited state and recoils towards the direction opposite to the light's propagation. Upon spontaneous emission, the atom will recoil again, in a random direction this time, so that in average, this second event averages to zero. With the help of additional magnetic fields, one can then use three pairs of lasers to confine an atomic cloud and reduce its temperature. The development of such methods 'to cool and trap atoms with laser light' by Steven Chu, Claude Cohen-Tannoudji, and William D. Phillips, was rewarded by the 1997 Nobel Prize.

At very low temperature, quantum phenomena are brought into play. Atoms behave differently depending on their bosonic or fermionic nature. This gives rise to the famous Bose-Einstein condensation phenomenon, first predicted by Einstein in 1925, and observed in 1938 for liquid Helium by Pyotr Kapitsa, John Allen and Don Misener ([1, 2], Nobel Prize 1978), and in 1995 for dilute gases by Eric Cornell, Wolfgang Ketterle, and Carl Wieman ([3–5], Nobel Prize 2001). In a Bose-Einstein condensate, the lowest quantum state is macroscopically populated, and the system can be described by a single wave function, leading to unintuitive properties like superfluidity.

The advent of techniques leading to condensation triggered a few years of intense exploration of this new phase of matter ([6]). For instance, coherence properties were studied, and it was shown that two Bose-Einstein condensates interfered as waves do ([7]), while long range coherence was observed below the condensation point ([8]). Moreover, the superfluid behaviour of such a system was demonstrated by the formation of vortices ([9]) and their organisation into lattices ([10]).

Quickly, new tools enlarging the range of possibilities enabled the growing number of teams working in this field to go from this weakly interacting regime, to a more complex one. Thanks to the ability to tune the s-wave interaction strength with Feshbach resonances ([11, 12]), the strong coupling regime could eventually be reached ([13]), with the ability to tune interactions to both attractive and repulsive. However, with large interactions came large atomic losses, thus limiting the sample's lifetime. Another development, instead of tuning the interaction strength, was thus to change the potential felt by the atoms. Techniques involving optical lattices allowed researchers to reduce the dimensionality of their system, leading to the observation of a Kosterlitz-Thouless phase transition in 2D ([14]), or to the study of a Tonks-Girardeau Bose gas in 1D ([15, 16]). Finally, interactions are not necessarily limited to short range, and Bose-Einstein condensates with large magnetic moment atoms, such as Chromium or Dysprosium, have also been produced ([17, 18]). Using Feshbach resonances, the interplay between dipolar and contact interactions could also be tuned to change the interaction's nature and range ([19]).

Not only are ultracold atoms an interesting tool for fundamental physics advances, they also have interesting applications in metrology or quantum simulations ([20]). Due to their high degree of controllability, MW atomic clock have long been the standard for defining time; however, the advent of more precise optical transitions based experiments have increased sensitivity a great deal: today, the most precise atomic clock in operation reaches the 10^{-19} level for one hour of averaging time ([21]), while a range of new proposals taking advantage of these progresses are proposed each year, like for instance the detection of gravitational waves from space using optical lattice atomic clock ([22]). These breakthroughs have also been applied to other metrological problems, like the search for possible time variation of fundamental constants ([23]), or the construction of very precise gravimeters ([24]). As these systems provide

experimentalists with easily controllable, clean, and defect-free ensembles, these advances have also been used in the realm of quantum simulations ([6, 25]), in particular in the study of the Bose-Hubbard ([26]) or Fermi-Hubbard model ([27]).

The 2D Bose gas

As we have mentioned, low dimensional systems are no longer out of reach, and interesting experiments have been conducted in order to explore their particular features. The case of 2D differs from the 3D case on several points. For an ideal 3D gas, what gives rise to the condensation phenomenon is that below a certain critical temperature, the total population of the excited states is limited, leading to an accumulation of bosons in the ground state. In 2D, however, there is no saturation of the excited states' population, and hence no condensation in the thermodynamical limit ([28]). In terms of coherence, this translates into a vanishing first order correlation function at long distances. However, the decay of this observable is far slower below a certain critical point, which can be understood in the framework of the Berezinskii–Kosterlitz–Thouless transition. As a matter of fact, a signature of this topological transition is the proliferation of vortices above the critical temperature T_{BKT} ([29, 30]), which in turn causes the first order correlation function to decay exponentially fast, while this decay is only algebraic below the transition point, where existing vortices of opposite circulations are closely paired. In a realistic, finite-size system, this slow decrease permits to restore a semblance of long range order, and the physics is essentially similar to what happens in the case of regular 3D condensation.

This transition was experimentally observed in [14], where authors trapped two atomic planes in a vertical lattice before letting them interfere. At low temperatures, straight fringes were observed, whereas conducting the same experiment at a higher T lead to the apparition of dislocations among the fringes, which the authors attributed to the presence of vortices. Moreover, the algebraic behaviour of the first order correlation function below T_{BKT} was measured both for polaritons ([31–33]), dipolar excitons ([34]) and for cold atoms in a harmonic potential ([35–37]); however each of these experiments suffer from different limitations, and the measured power-law exponent did not agree with theoretical predictions.

Moreover, the interest of the bidimensional system also resides in its scale invariance: for a weakly interacting 2D Bose gas, the equation of state does not depend on the temperature T and the chemical potential μ independently, but rather on the single parameter μ/k_BT. This equation of state has been studied experimentally for a 2D Bose gas in our group ([38, 39]); in addition, the behaviour of the 2D Bose gas was predicted ([40]) and observed ([41]) to be universal in the critical region. Other consequences on the system's dynamical properties have also been connected to hidden symmetries of the 2D Bose gas ([42]), and explored in our group during my thesis ([43]).

Historically, most of the 2D experiments have been conducted in harmonic traps, which forced the authors to use the so-called local density approximation to extrapolate their observations for homogeneous systems. As a drawback, results obtained for these systems can be hard to interpret: for instance, the measurement of the first order correlation function g_1 performed with cold atoms was ultimately limited by the harmonic confinement, which changed the behaviour of g_1 compared to the uniform case. Fortunately, new techniques to produce box potentials have recently been implemented ([44, 45]), which paves the way for the production of degenerate 2D gases trapped in uniform horizontal planes. Finally, spatial light modulators, which can be used to taylor the flat box's walls, allow one to change the in plane confinement geometry at will ([45, 46]).

Our system, merging these two techniques, is thus able to cool a 2D Bose gas down to degeneracy and trap the cloud in a uniform box with an arbitrary shape, which makes it an ideal setup for precise and controlled 2D physics experiments. While this path had not really been pursued before I joined the team, we are also able to perform two-component experiments, which opens the way to new and exciting possibilities. In particular, we can study the dynamics

that emerge when a mixture of two immiscible species is produced and let to evolve. This is the subject of this thesis.

Demixing phenomena

When two immiscible species are mixed together, they phase separate. Demixing dynamics are present in many physical systems, classical hydrodynamics being the first example that usually comes to mind. However, the fact that cold atom ensembles abide by hydrodynamical-like equations shows that these phenomena are also relevant for such systems.

The versatility and tunability of cold atom experiments make them ideal to study demixing phenomena. The first experiments to involve a two-component Bose-Einstein condensate was performed by [47] and involved two hyperfine states of ^{87}Rb. Swiftly, other experiments followed, first with spinor condensates ([48, 49]), with mixtures of bosons and fermions ([50, 51]), and later with mixtures of different atomic species ([52]).

In these systems, the miscibility parameter Δ is usually determined by the values of the intra and inter s-wave scattering lengths. As a consequence, this parameter has been tuned with the help of Feshbach resonances ([52, 53]), where authors observed a clear spatial separation of the two components on one side of the resonance, while the two condensates remained overlapped on the other side of the resonance. Other ways of tuning this parameter exist, for instance by adding a MW dressing field coupling the two components ([54–56]), which can also be used to study a system close to a quantum critical point ([57]).

Spontaneous formation of spin domains have been observed when a miscible system is tuned to immiscibility, for instance when part of a single component gas was transferred to another state, immiscible with the first one ([58, 59]), or when a Feshbach resonance was used to tune Δ from miscible to immiscible ([60]). The formation of these patterns is well explained by the concept of hydrodynamical instability: in the immiscible regime, small population fluctuations can be exponentially amplified, leading to the formation of well polarised spin domains. A mode analysis of the spatial population fluctuations between the two components shows that only a certain range of wave vectors k can actually grow, while in this naive picture, the emerging patterns are set by the fastest growing mode ([61]). It can thus be interesting to study the growth of these domains and see how this simple picture is modified in real systems.

Interestingly, once they have appeared, these spin domains can act as spin barriers and prevent motion when a force is applied, effectively pinning the system down ([62]). Other non equilibrium dynamics have also been explored, either by letting the system demix before destabilising it ([63, 64]), or by looking at superfluid currents ([65]) or counterflow dynamics ([66]); in addition, it has been shown that spin droplets can also be stabilised by mean-field effects ([67, 68]). Finally, numerical studies investigating various dynamical instabilities in these systems have also been performed ([69–71]).

Then, what is left to do? Many of these experiments were carried out in harmonically trapped clouds, which, as we have seen, can have non negligible differences with uniform systems. For instance, in the first case, the instability leading to phase separation is triggered by the non-homogeneity of the gas. Then, in a box potential, where does the modulation start? Moreover, our total control over the geometry of the box's walls enables us to vary the cloud's in plane confinement from a 2D square shape to a 1D ring very easily, which might also have an interesting influence of the observed dynamics. This is thus a good motivation to try implementing these experiments in our 'ideal'-like, 2D uniform system, and study comprehensively the instabilities that appear when immiscible fluids are mixed.

Detailed outline of this thesis

This manuscript is organised into two independent parts: the first one deals with the necessary tools, both theoretical and experimental, important to understand and produce a 2D degenerate Bose gas; it also details an implementation of a correction method that can be used to taylor the profile of a light beam and can be used to improve certain homogeneity defects that appear on

the experiment, or help imprinting complex shapes on the atomic density. The second part is devoted to demixing phenomena in 2D Bose gases, including a numerical study of this system, and experimental data analysis. Here is a brief summary of each chapter's content:

I. The 2D Bose gas: theory and experimental implementation

Chapter 1 is a theoretical presentation of the 2D Bose gas: it contains a description of the BKT phase transition along with details about the symmetries of this system. Moreover, an introduction to the behaviours of the first and second order correlation function is also presented.

Chapter 2 provides a general description of the experimental setup, from the production of 2D uniform gases, to the tools used to reach quantum degeneracy. The methods for measuring the system's parameters such as the phase space density or the atom number are also presented.

Chapter 3 introduces an iterative method using a grey-levelled spatial light modulator that can be employed to taylor a laser profile. It can be used to control the 2D atomic density, for instance by improving the homogeneity defects that inevitably appear in our system, or by trapping atoms in complex potentials, or by imprinting complex shapes on the atomic density.

II: Demixing phenomena in 2D uniform boxes

Chapter 4 gives a general description of demixing phenomena, from classical hydrodynamics to cold atom systems. It details the theoretical tools that will be used in the rest of the thesis, and introduces the specific parameters that are relevant to our system.

Chapter 5 studies numerically a two-component Bose gas, and in particular details the influence of the box's geometry on the appearing dynamics. It deals with the two types of demixing that are studied experimentally in the final chapters: natural demixing (the two species are initially uniformly overlapped), and seeded demixing (a certain modulation is imprinted on the initial system).

Chapter 6 presents experimental data taken in a system with periodic boundary conditions, namely a 1D ring of atoms. The two previously mentioned cases, natural and seeded demixing, are both studied.

Chapter 7 details the same kind of experiences, but performed in square 2D boxes, thus adding edges to the system. The role of the temperature in the demixing dynamics is also briefly discussed.

Publications

Here is a list of the articles in link with this thesis. Several more articles are in the process of being written. All articles are reproduced at the end of this thesis.

J. L. Ville, R. Saint-Jalm, É. Le Cerf, M. Aidelsburger, S. Nascimbène, J. Dalibard, and J. Beugnon
Sound Propagation in a Uniform Superfluid Two-Dimensional Bose Gas
Phys. Rev. Lett. **121**, 145301(2018)

R. Saint-Jalm, P. C. M. Castilho, É. Le Cerf, B. Bakkali-Hassani, J.-L. Ville, S. Nascimbène, J. Beugnon, and J. Dalibard
Dynamical Symmetry and Breathers in a Two-Dimensional Bose Gas
Phys. Rev. X **9**, 021035 (2019)

Y. Zou, B. Bakkali-Hassani, C. Maury, É. Le Cerf, S. Nascimbène, J. Dalibard, and J. Beugnon
Tan's two-body contact across the superfluid transition of a planar Bose gas
Submitted, arXiv:2007.12385

Y. Zou, B. Bakkali-Hassani, C. Maury, É. Le Cerf, S. Nascimbène, J. Dalibard, and J. Beugnon
Magnetic dipolar interaction between hyperfine clock states in a planar alkali Bose gas
Submitted, arXiv:2007.12389

I

The 2D Bose gas: theory and experimental implementation

> The disc, being flat, has no real horizon. Any adventurous sailor who got funny ideas from staring at eggs and oranges for too long and set out for the antipodes soon learned that the reason why distant ships sometimes looked as though they were disappearing over the edge of the world was that they were disappearing over the edge of the world.
>
> —Terry Pratchett, *The Light Fantastic*

1

THEORETICAL CONSIDERATIONS

The effects of dimensionality on physical systems are well known. In particular, some ordered phases of matter, like crystals for instance, are forbidden in dimensions 1 and 2. The same result goes for Bose-Einstein condensation (BEC): for finite temperatures, long range order cannot exist in 2D. However, we will show that a semblance of order can be restored at low temperature. We will first see what phenomena take place in 2D for Bose gases instead of regular condensation. Then, in order to better characterise the physics of this phase transition, we will examine the behaviour of the first and second order correlation functions across the transition.

1.1 THE UNIFORM 2D BOSE GAS

1.1.1 *Does Bose-Einstein condensation occur?*

1.1.1.1 *Condensation of the 3D Bose gas*

Historically, BECs have long stayed a *Gedankenexperiment* in quantum physics. While the idea of bosonic condensation was first proposed by Einstein in 1925 following a paper by Bose, the necessary technology to observe this state of matter simply did not exist for another 70 years. Although the superfluidity of Helium 4 does correspond to a Bose-Einstein condensation, and was indeed identified as such by London in the 40s, the large density of this system leads to high repulsive interactions between particles, and only ~ 10 % of atoms end up in the condensate state. This situation is quite different from the ideal Bose gas textbook example, which we are going to address now.

We remind here the basics of BEC physics in 3D. We take a box of volume $V = L^3$ with periodic boundary conditions in which N bosons of mass m evolve. The eigenfunctions of the hamiltonian $H = \frac{p^2}{2m}$ are well known:

$$\phi_{\mathbf{p}}(\mathbf{r}) = \frac{1}{\sqrt{V}} e^{i\mathbf{p}\cdot\mathbf{r}/\hbar}. \tag{1.1}$$

Each wave function corresponds to a momentum $\mathbf{p} = \hbar\mathbf{k} = 2\pi\mathbf{n}\hbar/L$ where $\mathbf{n} \in \mathbb{Z}^3$, and is an eigenfunction of H for the eigenvalue $\varepsilon_{\mathbf{p}} = \mathbf{p}^2/2m$. We know that for bosons, the mean occupation of a state $\phi_{\mathbf{p}}$ is given in the grand canonical ensemble by the Bose-Einstein distribution:

$$N_{\mathbf{p}} = \frac{1}{e^{\beta(\varepsilon_{\mathbf{p}}-\mu)} - 1} \text{ with } \beta = (k_B T)^{-1}. \tag{1.2}$$

For simplicity, we fix $\varepsilon_0 = 0$, which means $\mu < 0$. It is then tempting to write, for a large occupation of the lowest state ($N_0 \gg 1$):

$$N_0 = \frac{1}{e^{-\beta\mu} - 1} \Rightarrow \mu = -\frac{1}{\beta} \ln\left(1 + \frac{1}{N_0}\right) \simeq -\frac{1}{\beta N_0}. \tag{1.3}$$

We immediately understand that as $\mu \to 0$, the population of the lowest state might diverge, and that we should treat this state separately from the others. Let us consider the population $N_e = N - N_0$ of atoms in excited states. Introducing the fugacity $z = e^{\beta\mu}$ and the de Broglie wavelength $\lambda_T = h/\sqrt{2\pi m k_B T}$, we have:

$$\begin{aligned} N_e &= \sum_{\mathbf{k}\neq 0} \frac{1}{e^{\beta(\hbar^2\mathbf{k}^2/2m-\mu)}-1} \\ &= \frac{V}{(2\pi)^3}\int_0^\infty \frac{1}{z^{-1}e^{\beta\frac{\hbar^2k^2}{2m}}-1} 4\pi k^2\,\mathrm{d}k \\ &= \frac{V}{\lambda_T^3}\mathrm{Li}_{3/2}(z) \;\text{ where }\; \mathrm{Li}_p(z) = \sum_{l=1}^{\infty}\frac{z^l}{l^p}. \end{aligned} \tag{1.4}$$

One should note that the replacement of the sum by an integral in eq. 1.4 is only valid if the spacing between the eigenvalues of H is negligible compared to thermal energy: $\beta h^2/2mV^{2/3} \ll 1$. Moreover, the fact that for $z \in [0,1]$, the polylog function $\mathrm{Li}_{3/2}(z)$ saturates at $z = 1$ (corresponding to $\mathrm{Li}_{3/2}(1) = 2.612$), yields the famous saturation of excited states: N_e possesses an upper bound, which gives rise to an accumulation of atoms in the lowest energy state when one adds atoms to the system. This of course, is the Bose-Einstein phase transition.

Considering now the phase space density of excited states $\mathscr{D}_e = \frac{N_e}{V}\lambda_T^3 = \mathrm{Li}_{3/2}(z)$, we have:

$$\mathscr{D}_e^{\max} = \mathrm{Li}_{3/2}(1) \simeq 2.612 \;\Rightarrow\; T_c = \frac{2\pi\hbar^2}{mk_B}\left(\frac{n}{\mathrm{Li}_{3/2}(1)}\right)^{2/3}. \tag{1.5}$$

Below this temperature, the lowest level is macroscopically populated, and by setting $\mu = 0$ in Eq. 1.4, we have:

$$N_0(T) = N\left[1-\left(\frac{T}{T_c}\right)^{3/2}\right]. \tag{1.6}$$

1.1.1.2 *Absence of condensation in 2D*

It is important to note that in 2D, the derivation done in Eq. 1.4 no longer stands as the 3D integration now has to be performed in 2D. In this case, one has:

$$\mathscr{D}_e = \frac{L^2}{(2\pi)^2}\int_0^\infty \frac{z}{e^{\beta\frac{\hbar^2k^2}{2m}}-z} 2\pi k\,\mathrm{d}k = -\ln(1-z). \tag{1.7}$$

We thus see that $\mathscr{D}_e$ is no longer bounded when $z \to 1$: there is no saturation of excited states in 2D, and no proper Bose-Einstein condensation.

This is actually a particular case of the Mermin-Wagner theorem stating that in dimensions lower or equal to 2 with short-range interactions, there can be no spontaneous breaking of a continuous symmetry at finite temperature. This general result was proven independently by Mermin and Wagner ([72]), taking the example of (anti-)ferromagnetism in 1D and 2D, and by Hohenberg ([73]), who studied the properties of Bose liquids and Cooper pairs for superconductors.

The destruction of order in 2D was already noted by Peierls in 1934 ([74, 75]): considering a 2D crystal in which the positions of atoms were affected by thermal fluctuations, he realised that the knowledge about the position of atom n was transmitted to atom 0 via a chain comprising more atoms in 3D than in 2D, and that it would take larger fluctuations (which decreased the likelihood of such an event) to destroy the crystalline order in higher than in lower dimensions. Quantitatively, he found that there was a 'stacking' of defects when increasing the distance between two sites in 2D:

$$\left\langle \left(x_n - x_n^0\right)^2 \right\rangle \propto T\ln(n), \tag{1.8}$$

where x_n is the position of an atom at site n and x_n^0 is its equilibrium position if no thermal fluctuations are present. This stacking is absent in 3D.

In other words, in 2D, one can always find a distance at which the uncertainty in x_n is arbitrarily large, which means that thermal fluctuations kill the order at long distance. However,

we will see later that for cold enough samples, order is only destroyed at very large distances: for a small enough sample, a semblance of order can be restored.

1.1.2 *The Berezinskii-Kosterlitz-Thouless phase transition*

1.1.2.1 *Suppression of density fluctuations*

A common way of describing a cold atomic gas in its ground state is the Gross-Pitaevskii equation. The idea is to start from the Schrödinger equation, and to use a mean field treatment to add interactions. Moreover, at low temperature, most of the atoms are in the condensate phase, and we will replace the operator $\hat{\varphi}$ by a classical field φ. In the general case, the operator $\hat{\varphi}$ describing a quantum system with two-body interactions fulfils the equation:

$$i\hbar\frac{\partial\hat{\varphi}(\mathbf{r},t)}{\partial t} = \left[-\frac{\hbar^2\nabla^2}{2m} + V_{\text{ext}}(\mathbf{r},t) + \int \hat{\varphi}^\dagger(\mathbf{r}',t)V_{\text{int}}(\mathbf{r}'-\mathbf{r})\hat{\varphi}(\mathbf{r}',t)\,\mathrm{d}\mathbf{r}'\right]\hat{\varphi}(\mathbf{r},t). \tag{1.9}$$

Furthermore, in the case of a short range interaction potential (where the typical scale on which φ varies is very large compared to the scattering length), one can replace the interaction potential by a Dirac distribution: $V_{\text{int}}(\mathbf{r}'-\mathbf{r}) = g\delta(\mathbf{r}'-\mathbf{r})$. The coupling constant g is chosen so that the pseudo-potential $g\delta$ gives the same low energy scattering properties as the real potential V_{int}. Thus, the Gross-Pitaevskii equation reads:

$$i\hbar\frac{\partial\varphi}{\partial t} = \left(-\frac{\hbar^2}{2m}\nabla^2 + V + g|\varphi|^2\right)\varphi. \tag{1.10}$$

For temperatures low enough so that only s-wave scattering processes are relevant for interatomic interactions, V_{int} is entirely determined by the s-wave scattering length a, and a 3D computation yields $g = 4\pi a\hbar^2/m$. In 2D however, the movement is frozen along one axis, that we denote z, and we can factorise the wave function: $\phi(x,y,z) = \psi(x,y)\chi_0(z)$. For a deep vertical confinement, we will approximate the shape of the trap by a harmonic potential of pulsation ω_z. An integration along z yields:

$$i\hbar\frac{\partial\psi}{\partial t} = \left(-\frac{\hbar^2}{2m}\nabla^2 + V + \frac{\hbar^2}{m}\tilde{g}|\psi|^2\right)\psi, \tag{1.11}$$

where we have defined the dimensionless interaction strength:

$$\tilde{g} = 4\pi a\int|\chi_0(z)|^4\,\mathrm{d}z = \sqrt{8\pi}\frac{a}{\sqrt{\hbar/m\omega_z}}. \tag{1.12}$$

This 2D Gross-Pitaevskii equation characterises well the gas in the condensed regime, and will be a major tool to characterise our low temperature gases. From this equation, we can express the kinetic and interactions energies:

$$E_k = \frac{\hbar^2}{2m}\int|\nabla\psi|^2\,\mathrm{d}^2r \text{ and } E_i = \frac{\hbar^2\tilde{g}}{2m}\int n^2(r)\,\mathrm{d}r = \frac{\hbar^2\tilde{g}}{2m}L^2\langle n^2(\mathbf{r})\rangle, \tag{1.13}$$

where we have normalised ψ to $\int\psi(\mathbf{r})\,\mathrm{d}^2r = N$. Moreover, we see that if we keep the average $n_0 = \langle n(\mathbf{r})\rangle$ and $\tilde{g}$ fixed, the only way to minimise the interaction energy is to minimise:

$$(\Delta n)^2 = \langle n^2(\mathbf{r})\rangle - n_0^2. \tag{1.14}$$

Additionally, we can see that the interaction energy per particle e_i always dominate the thermal energy k_BT at low enough temperature:

$$\frac{e_i}{k_BT} \simeq \frac{\frac{\hbar^2\tilde{g}}{2m}n_0}{k_BT} = \frac{\tilde{g}\mathcal{D}}{4\pi}. \tag{1.15}$$

This means that at high enough degeneracy ($\tilde{g}\mathcal{D} \gg 4\pi$), any significant deviation of $n(\mathbf{r})$ with respect to its mean value will cost a lot of interaction energy compared to k_BT: density fluctuations are effectively suppressed. This is often referred to as the 'quasi-condensate' regime.

1.1.2.2 *Superfluidity*

This suppression of density fluctuations has an interesting consequence: when $\mathcal{D}$ is high enough, the wave function can be approximated by a complex field of constant modulus and varying phase:

$$\psi \simeq \sqrt{n_0} e^{i\theta(\mathbf{r})} \quad \Rightarrow \quad E_k \simeq \frac{\hbar^2}{2m} n_0 \int (\nabla\theta)^2 \, \mathrm{d}^2 r. \tag{1.16}$$

This state with a frozen density and a fluctuating phase is usually called a 'quasi-condensate' state. The discrete version of this hamiltonian $H \propto \int (\nabla\theta)^2$ is the hamiltonian of the XY model, which explains why this model is often used on the 2D Bose gas.

In this degenerate regime, most of the atoms are in the condensed fraction, and one can use a Bogoliubov approach, where quantum operators are replaced by classical fields. The idea is to use the order parameter $\psi = \sqrt{n} e^{i\theta}$ to describe the $T = 0$ system and find the excitation spectrum. This method might seem questionable as we know order to be destroyed in 2D; however, this approach is justified by the fact that when $\mathcal{D}$ is high enough, only at very large distances does the order vanish, while a local order parameter can still be defined. It should be noted that this treatment is purely phononic and that as the computation develops θ into a Fourier series, it does not take other excitations, like vortices, into account. A lengthy calculation done in [28] shows that the dispersion relation of the system's excitations follows the famous Bogoliubov spectrum:

$$\omega_k = \sqrt{\frac{\hbar k^2}{2m} \left(\frac{\hbar k^2}{2m} + \frac{2 g n_0}{\hbar} \right)}. \tag{1.17}$$

This relation has two interesting limits, with a crossover around $k = \sqrt{\tilde{g} n_0}$:

- the small k limit where $\omega \simeq c_0 k$ with $c_0 = \sqrt{g n_0 / m}$, which corresponds to the propagation of phonons,
- the high k regime, where $\hbar\omega_k = \frac{\hbar^2 k^2}{2m} + g n_0$, where we find the free particle spectrum shifted by the interaction energy.

We see immediately that according to the Landau criterion, the system should be superfluid for $v < c_0$. Thus, even if there is no proper condensation in 2D, we recover a state with superfluid behaviour at high enough $\mathcal{D}$, as in 3D. At $T = 0$, neglecting the quantum depletion due to (our weak) interactions, we have $n_s = n_0$ where n_s is the superfluid density, and the whole system is in the superfluid phase. We will see in the next section that as T is increased to the critical temperature of the Berezinksii-Kosterlitz-Thouless phase transition T_c, the superfluid fraction continuously decreases, and then jumps to 0 at the transition.

Interestingly, we have studied the speed of such excitations for 2D Bose gases during my thesis (more details in [76, 77]). A thorough analysis shows that at $T < T_c$, as two fractions (superfluid and non superfluid) exist, there are two modes of sound propagation, usually referred to as first and second sounds. The second sound mode is the one we expect to see when creating a density perturbation at $T < T_c$: its speed is directly related to the superfluid density, and should thus jump to 0 (no second sound) above the transition. In [77], we created a perturbation that propagated in our uniform atomic box. By integrating the density along one direction and measuring the displacement of the perturbation with time, we were able to measure the speed of sound in our gas. An image of our protocol is given in Fig. 1.1. At low temperature, we found $c = c_0$, in good agreement with the expected Bogoliubov spectrum. For a higher temperature, however, our observations departed from the theoretical predictions; in particular, we did not see a jump of c at the transition. An explanation for this is the fact that above the transition, the physics is more complex as the simple two-fluid model breaks down. In the normal phase, the gas may not follow the hydrodynamical predictions, which could explain our observations. Our paper is reproduced at the end of this thesis.

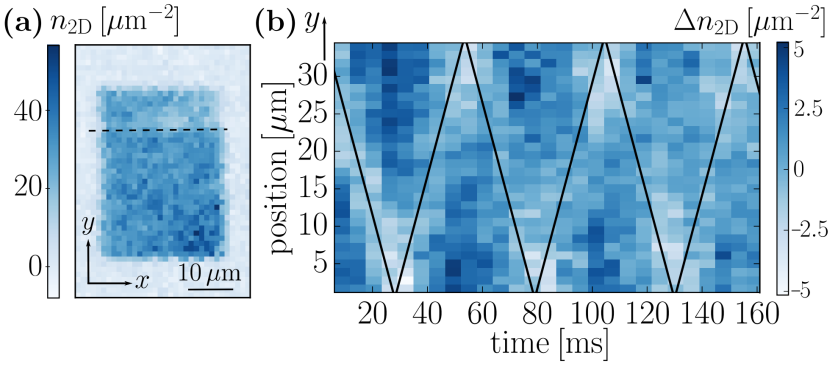

Figure 1.1: Excitation of sound waves. An extra potential step is added on our uniform gas, creating a perturbation that is free to propagate in the atomic box (a). By integrating the atomic density along x for different times (b), one can monitor the displacement of the wave front, and measure the speed of sound. Figure taken from [77].

1.1.2.3 *Vortex proliferation*

We have seen that the relevant Hamiltonian for our system is related to the one of the XY model. In 2D, this model possesses a phase transition called the Berezinksii-Kosterlitz-Thouless, or BKT phase transition, for which a proliferation of isolated vortices destroy phase coherence above a certain critical temperature T_c ([29, 30]). However, the model used in the previous section is purely phononic, and does not take the existence of vortices into account. We attempt here to include these phenomena.

A vortex is defined as a zero of the wave function ψ; as ψ must be single valued, the phase winding around such a point has to be a multiple of 2π:

$$\oint \nabla\theta(\mathbf{r}) \cdot \mathrm{d}\mathbf{l} = 2\pi m, \quad m \in \mathbb{Z}. \tag{1.18}$$

The number m is called the charge of the vortex. It is a topological invariant: a vortex with $m \neq 0$ cannot be spontaneously created or destroyed within the sample. Two mechanisms are possible for the emergence of such vortices: a vortex can be created on the edge of the gas, where ψ goes to zero, or a pair of vortices with opposite charges can be created on a zero of ψ where no phase winding initially exists.

We intuitively understand that the apparition of such vortices is detrimental to the long range order. A way to understand this is to note that for a single charged vortex, the phase of the field between two points A and B goes from ϕ to $\phi + \pi$ when a vortex is created between A and B. If the vortices are randomly distributed in the gas, the length on which the cloud is phase coherent can only be smaller than the mean distance between two vortices.

As the field of velocities created by a vortex is orthoradial, we will here place ourselves in a cylindrical geometry. We consider a disk of radius R uniformly filled with N atoms, and having one single vortex in its centre. We can take a simplified model for the vortex density, and write both density and velocity fields as:

$$n(\mathbf{r}) = n_0(1 - \chi_{[0,\xi]}(r)) \text{ and } \mathbf{v}(\mathbf{r}) = \frac{\hbar}{mr}\mathbf{e}_\phi, \tag{1.19}$$

where we have introduced the healing length $\xi = 1/\sqrt{2\tilde{g}n_0}$, the indicator function $\chi_{[0,\xi]}(r)$ of $[0, \xi]$ (being 1 in this interval and 0 elsewhere), and $\mathbf{e}_\phi = \mathbf{e}_z \times \mathbf{r}/r$. We can then compute the kinetic energy of a fluid having one vortex:

$$E_k = \frac{1}{2}m \int n(\mathbf{r})v(\mathbf{r})^2 \,\mathrm{d}^2r \simeq \frac{1}{2}mn_0\frac{\hbar^2}{m^2}\int_\xi^R \frac{1}{r^2}2\pi r \,\mathrm{d}r = \pi\frac{\hbar^2 n_0}{m}\ln(R/\xi). \tag{1.20}$$

Moreover, since n_0 is increased from $N/\pi R^2$ to $N/\pi(R^2-\xi^2)$, there must be a corresponding increase of E_i by:

$$\varepsilon_0 = \frac{\hbar^2\tilde{g}}{2m}\left[\left(\frac{N}{\pi(R^2-\xi^2)}\right)^2\pi(R^2-\xi^2) - \left(\frac{N}{\pi R^2}\right)^2\pi R^2\right] \simeq \frac{\pi}{4}\frac{\hbar^2 n_0}{m}. \tag{1.21}$$

At this point, we should note two things. The first one is that the kinetic energy of such a gas diverges when its size goes to infinity, even though the single change that we have made is the apparition of a microscopic defect. This divergence is independent of the exact shape that we have taken for n: a smoother cancellation of ψ, for instance, will simply add a constant. The second one is that the increase of interaction energy ε_0, on the other hand, is constant when the disk's size goes to infinity. We can thus neglect this contribution for an isolated vortex; it will however not be the case for a vortex-antivortex pair, a situation in which the contribution of E_k is greatly diminished.

Let us now use a thermodynamical approach: now that we know the energetic contribution of a vortex, can we have an idea of when such a defect is created? We can write the free energy of the system:

$$F = E - TS, \tag{1.22}$$

and we can approximate the energy $E \simeq E_k$. As this energy is linked to the phase stiffness of the gas, we will replace n_0 by the superfluid density n_s. Here, S is the entropy associated to the vortex configuration. As the state of the gas is essentially determined by the position of the vortex, which has a size $\pi\xi^2$, we have $W = \pi R^2/\pi\xi^2$ different possibilities for our gas. Writing that $S = k_B\ln(W)$, we have:

$$F = \left(\pi\frac{\hbar^2 n_s}{m} - 2k_BT\right)\ln(R/\xi) \Rightarrow \frac{F}{k_BT} = \frac{1}{2}(\mathcal{D}_s - 4)\ln(R/\xi), \tag{1.23}$$

where we have introduced the superfluid phase space density $\mathcal{D}_s = n_s\lambda_T^2$. We immediately see that for $\mathcal{D}_s < 4$, it is energetically favourable to have a vortex, while this is not the case for $\mathcal{D}_s > 4$. Actually, starting from a case where $\mathcal{D}_s < 4$, *i.e.* where F is large and negative, the creation of a vortex will reduce n_s, which will in turn decrease F and make the appearance of a second vortex even easier. There will thus be an avalanche of vortices that will bring n_s to 0. This proliferation of vortices is one of the signatures of the BKT phase transition. One can actually show that when $\mathcal{D}_s > 4$, vortices appear in closely bound pairs, while when $\mathcal{D}_s$ is decreased, these pairs tend to be less and less bound, until the two elements of the pair dissociate and form isolated vortices, which destroy the long range order. As the location of these vortices becomes random, two points of the gas will see their phase become less and less correlated, until phase coherence is entirely lost. The value $\mathcal{D}_s^c = 4$ appears thus as the critical phase space density for the BKT transition.

Interestingly, the previous argument shows that $\mathcal{D}_s$ can either be equal to 0 (no superfluidity), or bigger than 4 (and the system exhibit some superfluidity, even if $\mathcal{D}_s < \mathcal{D}$ at finite temperature). Values of $\mathcal{D}_s$ between 0 and 4, however, are forbidden: this is the famous jump of the superfluid fraction at the BKT phase transition. Experimentally, this jump has been measured with torsion pendula placed in liquid Helium ([78]). When the transition is crossed, the moment of inertia of the the system pendulum + Helium is dramatically reduced (see Fig. 1.2).

It should be noted that if the relation $n_s^c(\lambda_T^c)^2 = 4$ is universal (it does not depend on $\tilde{g}$), it does not give any information on the link between n and T at the critical point. In other words, it is an equation that involves n_s^c and T_c, but not n_c and T_c. Monte-Carlo simulations performed in [79] actually show that one can write:

$$\mathcal{D}_c = \ln\left(\frac{\xi_{\mathcal{D}}}{\tilde{g}}\right) \text{ and } \left(\frac{\mu}{k_BT}\right)_c = \ln\left(\frac{\xi_\mu}{\tilde{g}}\right) \text{ where } \xi_{\mathcal{D}} = 380 \pm 3 \text{ and } \xi_\mu = 13.2 \pm 0.4. \tag{1.24}$$

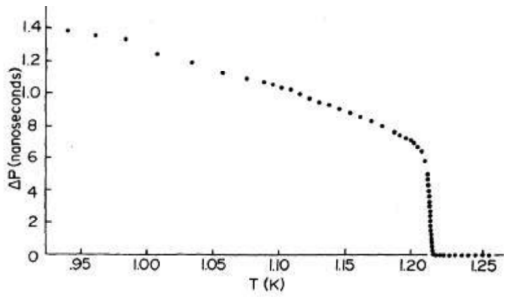

Figure 1.2: Measurement of the superfluid jump. When the temperature is decreased below the critical temperature, some superfluid fraction appears, which reduces the moment of inertia of the system torsion pendulum + Helium. Figure taken from [78].

Interestingly, we see that the critical point is determined by the ratio μ/k_BT alone, and does not depend on μ and k_BT independently. This is a consequence of scale invariance, as we will see in the next section.

1.1.3 *Symmetries of the 2D Bose gas and consequences*

1.1.3.1 *Scale invariance*

Scale invariance is a powerful concept used in many different fields of physics. The basic idea is that when there is no characteristic scale in a system, the laws governing this system do not change if certain variables such as length, time, or energy, are multiplied by a common factor. In our case, we will see that the adimensionality of $\tilde{g}$ in the 2D case, and the lack of a length scale associated with E_i thereof, makes the equation of state only depend on μ/k_BT and not on μ and T independently, as in the 3D or 1D case. The scale invariant nature of the 2D Bose gas has been previously studied in our group ([38, 39]).

In our case, we can show ([80]) that the transformations where ℓ is replaced by $\lambda\ell$ and t is replaced by $\lambda^2 t$, that we note:

$$\ell \leftarrow \lambda\ell \text{ and } t \leftarrow \lambda^2 t, \tag{1.25}$$

imply that the energy scales are transformed as:

$$E \leftarrow \frac{1}{\lambda^2} E. \tag{1.26}$$

In addition, let us note that this transformation also implies that $p \leftarrow p/\lambda$.

First, let us assume that we have such a system. In this case, one can compute the equilibrium average density $\bar{n}(T,\mu)$ in the thermodynamic picture: we have N bosons with positions $\{\mathbf{r_i}\}$ and impulsions $\{\mathbf{p_i}\}$; we can thus write:

$$\bar{n}(T,\mu) = \sum_N \int \mathscr{P}(N,\{\mathbf{r_i}\},\{\mathbf{p_i}\})\, n(N,\{\mathbf{r_i}\},\{\mathbf{p_i}\}) \prod_{i=1}^{N} \mathrm{d}\mathbf{r_i}\, \mathrm{d}\mathbf{p_i}, \tag{1.27}$$

where $\mathscr{P}$ represents the Boltzmann weight of a given configuration: $\mathscr{P} = e^{-\frac{E-\mu N}{k_BT}}$. We then perform the transformation:

$$T \leftarrow T/\lambda^2 = T', \quad \mu \leftarrow \mu/\lambda^2 = \mu'. \tag{1.28}$$

In order to compute $\bar{n}(T',\mu')$, one can operate the change of variables $r_i' = r_i/\lambda$ and $p_i' = \lambda p_i$. Eq. 1.26 implies that $\mathscr{P}$ remains unchanged, while n, being the inverse square of a length, is transformed into n/λ^2. Writing the definition of $\mathscr{D}$ and using the scaling on n, this yields:

$$\bar{\mathcal{D}}(T/\lambda^2, \mu/\lambda^2) = \frac{h^2}{2\pi m k_B} \frac{\bar{n}(T/\lambda^2, \mu/\lambda^2)}{T/\lambda^2} = \frac{h^2}{2\pi m k_B} \frac{\bar{n}(T,\mu)}{T} = \bar{\mathcal{D}}(T,\mu). \tag{1.29}$$

Then, taking $\lambda^2 = T$ immediately gives $\mathcal{D}(\mu, T) = \mathcal{D}(1, \mu/T)$, which proves that $\mathcal{D}$ does indeed only depend on the ratio μ/T. This is a particular case of a wider result: for a scale invariant system, if a quantity $\mathcal{F}$ possesses a scaling $\mathcal{F} \leftarrow \mathcal{F}/\lambda^{2\nu}$, then it can be written:

$$\mathcal{F}(T,\mu) = (k_B T)^\nu f\left(\frac{\mu}{k_B T}\right). \tag{1.30}$$

In our previous example, we have applied this result to $\mathcal{F} = n(\mathbf{r})$ with $\nu = 1$.

Now, let us prove that we have such a scaling. In our case, the hamiltonian of the system can be written as:

$$\hat{H} = \frac{\hbar^2}{2m} \int \nabla\hat{\Psi}^\dagger(\mathbf{r}) \cdot \nabla\hat{\Psi}(\mathbf{r}) \,\mathrm{d}^2 r + \frac{1}{2} \iint V(\mathbf{r}-\mathbf{r}') \hat{\Psi}^\dagger(\mathbf{r}) \hat{\Psi}^\dagger(\mathbf{r}') \hat{\Psi}(\mathbf{r}') \hat{\Psi}(\mathbf{r}) \,\mathrm{d}^2 r \,\mathrm{d}^2 r', \tag{1.31}$$

where $V(\mathbf{r}-\mathbf{r}') = \frac{\hbar^2}{m}\tilde{g}\delta^2(\mathbf{r}-\mathbf{r}')$, and where $\hat{\Psi}$ annihilates a particle in $\mathbf{r}$:

$$\hat{\Psi}(\mathbf{r}) = \sum_\alpha \psi_\alpha(\mathbf{r}) \hat{a}_\alpha, \tag{1.32}$$

with $\{\psi_\alpha\}$ being an orthonormal basis, and $\hat{a}_\alpha$ being the annihilation operator of a particle in ψ_α. Moreover, we note that as length scales are rescaled, we also have to rescale the wave functions ψ_α in order to keep them normalised:

$$\psi_\alpha(\mathbf{r}) \leftarrow \frac{1}{\lambda}\psi_\alpha\left(\frac{\mathbf{r}}{\lambda}\right). \tag{1.33}$$

We then immediately see that this expression abides by a $\hat{H} \leftarrow \frac{1}{\lambda^2}\hat{H}$ scaling, implying that we do also have $E \leftarrow \frac{1}{\lambda^2}E$.

1.1.3.2 $SO(2,1)$ *symmetry*

We summarise here the main results of [43]. The whole article is reproduced at the end of this thesis. The results that we are discussing here are reproduced in Fig. 1.3.

Let us consider two systems:

- N weakly interacting free bosons confined in 2D,
- the same system with the addition of an in-plane harmonic trap.

It has been shown ([42]) that the Lie groups of both systems' symmetries have the structure of $\mathrm{SO}(2,1)$. This means that when determining the transformations that leave the action of these systems invariant, and determining the generators L_1, L_2, L_3 of these transformations, one has:

$$\begin{aligned} [L_1, L_2] &= iL_3, \\ [L_2, L_3] &= -iL_1, \\ [L_3, L_1] &= -iL_2. \end{aligned} \tag{1.34}$$

In other words, these generators have commutation relations characteristic of the Lie algebra of the group $SO(2,1)$. A first consequence of this fact is the periodicity of the system's poten-

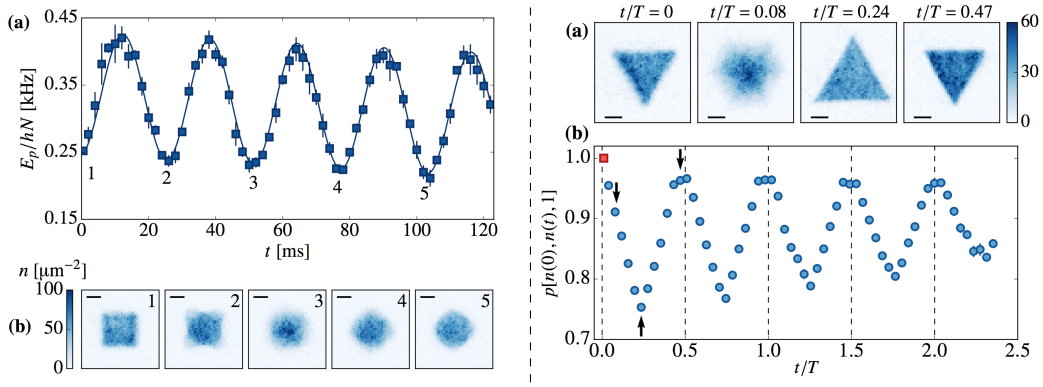

Figure 1.3: Left: periodic evolution of the potential energy of our system (a), with a fit performed by a cosine function and an additional linear slope to account for atomic losses. Note that ψ is not periodic at all (b). The black line represents 10 μm. Right: example of a breather. A uniformly filled equilateral rectangle reforms itself with periodicity $T/2$ (a). The scalar product between the density at time t and the initial one (red square) is shown in (b). The dashed lines correspond to times $t = pT/2$, $p \in \mathbb{N}$. Figures taken from [81].

tial energy for harmonically trapped bosons. Indeed, noting ω the pulsation of the trap, the generators L_i can be written under the form:

$$\begin{aligned} L_1 &= \frac{i}{2}\cos(2\omega t)(1 + \mathbf{r}\cdot\nabla) - \frac{1}{2\omega}\sin(2\omega t)\left(\frac{m\omega^2\mathbf{r}^2}{\hbar} - i\frac{\partial}{\partial t}\right), \\ L_2 &= -\frac{1}{2\omega}\cos(2\omega t)\left(\frac{m\omega^2\mathbf{r}^2}{\hbar} - i\frac{\partial}{\partial t}\right) - \frac{i}{2}\sin(2\omega t)(1 + \mathbf{r}\cdot\nabla), \\ L_3 &= -\frac{i}{2\omega}\frac{\partial}{\partial t}. \end{aligned} \tag{1.35}$$

Using these generators, one can write the operator $m\omega^2\mathbf{r}^2/2$ associated with the potential energy per particle:

$$\frac{1}{2}m\omega^2\mathbf{r}^2 = -\hbar\omega(L_3 + \cos(2\omega t)L_2 + \sin(2\omega t)L_1). \tag{1.36}$$

Moreover, one can write:

$$\frac{\partial}{\partial t}\left\langle\frac{1}{2}m\omega^2\mathbf{r}^2\right\rangle = \left\langle\left[\frac{\partial}{\partial t}, \frac{1}{2}m\omega^2\mathbf{r}^2\right]\right\rangle = -2\hbar\omega^2 i\langle[L_3, L_3 + \cos(2\omega t)L_2 + \sin(2\omega t)L_1]\rangle. \tag{1.37}$$

Iterating this process, one eventually finds:

$$\frac{\partial^2}{\partial t^2}\left\langle\frac{1}{2}m\omega^2\mathbf{r}^2\right\rangle = -4\omega^2\left\langle\frac{1}{2}m\omega^2\mathbf{r}^2\right\rangle, \tag{1.38}$$

whose solution is, when the gas is initially prepared in a steady state of the trapping potential so that $\dot{E}_p(0) = 0$:

$$E_p(t) = \frac{1}{2}E_{\text{tot}} + \frac{1}{2}\Delta E\cos(\omega t), \tag{1.39}$$

where E_{tot} is the total energy of the system and $\Delta E = 2E_p(0) - E_{\text{tot}}$.

As these two systems (free and harmonically trapped) are linked by a shared algebra, one can actually compute a mapping of solutions from one system to another. More generally, in the hydrodynamic regime where the healing length is small compared to the size L of the gas, a solution $\psi(\mathbf{r}, t)$ of a Gross-Pitaevskii equation characterised by the triplet $(\omega, \tilde{g}N, L)$

can be mapped onto another solution $\psi'(\mathbf{r}', t')$ of an equation with $(\omega', \tilde{g}'N', L')$[1]. In the non hydrodynamic case, only the mapping for different ω, but same $\tilde{g}N$ and L, would hold. This very powerful tool is used in order to calibrate the gas' atom number, which will be treated in the next chapter.

Of course, the fact that E_p is periodic does not imply that ψ is. In fact, the Gross-Pitaevskii equation governing the system being non linear, it is not expected for ψ to be periodic. However, we found two counterexamples to this statement. When let to evolve in a harmonic trap, we observed that a uniformly filled equilateral triangle had a periodic behaviour, and that the initial shape would reform with a fixed periodicity of $T/2$, with T the period of the harmonic trap. This was also true for a uniformly filled disk, with a periodicity $2T$. We did not find an analytical proof that these 'breathers' should exist in a harmonic potential, but we could convincingly reproduce their behaviour with Gross-Pitaevskii numerical simulations.

1.1.3.3 *Equation of state in 2D*

As stated above, scale invariance has a very strong consequence on the equation of state: while in 1D and 3D, the phase space density (PSD) depends on both μ and T, it only depends on the ratio μ/k_BT in 2D. If there is no general expression for $\mathcal{D}(\beta\mu) = \mathcal{D}\left(\mu/k_BT\right)$, there is, however, two interesting limits in which an analytical form exists.

- The Hartree-Fock regime describes a gas far away from degeneracy. For an ideal gas, one has:
$$\mathcal{D} = \frac{N\lambda_T^2}{L^2} = \frac{\lambda_T^2}{L^2}\int \rho(\varepsilon) f_{\mathrm{BE}}(\varepsilon)\,\mathrm{d}\varepsilon = -\ln\left(1 - e^{\beta\mu}\right), \tag{1.40}$$
where we have introduced the Bose-Einstein function $f_{\mathrm{BE}}(\varepsilon) = \frac{1}{e^{\beta(\varepsilon-\mu)}-1}$ and the 2D density of states $\rho(\varepsilon) = \frac{mL^2}{2\pi\hbar^2}$. An approximation for weakly interacting gases consists in replacing the chemical potential μ by its mean field equivalent $\mu - 2gn$. This amounts to taking $g_2(0) = 2$, g_2 being the normalised second order correlation function. This yields:
$$\beta\mu = \frac{\tilde{g}\mathcal{D}}{\pi} - \ln\left(1 - e^{-\mathcal{D}}\right) \tag{1.41}$$

- The Thomas-Fermi regime describes the gas in a very degenerate case. In this regime, the kinetic energy of the gas is small compared to its chemical potential, and one can write $\mu = gn$. Inputing this in $\mathcal{D} = n\lambda_T^2$, one finds:
$$\beta\mu = \frac{\tilde{g}\mathcal{D}}{2\pi}. \tag{1.42}$$
In this regime, the gas obeys hydrodynamic-like equations that support Bogoliubov excitations. A derivation done in [82] shows that when one considers that these excitations are thermally occupied, one gets for the next term:
$$\beta\mu = \frac{\tilde{g}\mathcal{D}}{2\pi} - \frac{\tilde{g}}{2\pi}\ln\left(\frac{\tilde{g}\mathcal{D}}{\pi}\right). \tag{1.43}$$

Monte Carlo simulations performed in [40] have also determined the total equation of state for a 2D weakly interacting Bose gas. Their result is in agreement with the two aforementioned limits, as shown in Fig. 1.4. We will use the results of these simulations to determine an interpolating function in order to measure the PSD $\mathcal{D}$ of our gas. This point is detailed in the next chapter.

1 Throughout this section, we restrict ourselves to two solutions having the same geometry: with this method, a square can be mapped on an another square, but non on a circle, for instance.

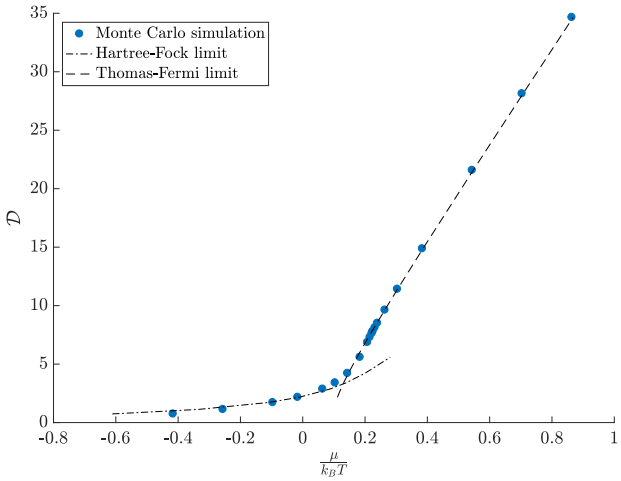

Figure 1.4: Equation of state of the 2D weakly interacting Bose gas, with $\tilde{g} = 0.16$. The blue points are the results of Monte Carlo simulation performed in [40], and agree well with both Hartree-Fock and Thomas-Fermi limits.

1.2 CORRELATION FUNCTIONS

We aim here at gaining a fuller understanding of the BKT transition, in particular through the coherence behaviour of the 2D Bose gas across the transition. To do so, we will calculate the two first correlation functions of our system. We will also explain how to measure them, and briefly summarise the attempts that have been made in this matter. Unless otherwise specified, we suppose the gas to be uniform.

1.2.1 *Theoretical basis*

1.2.1.1 *Introduction*

In optics, correlation functions are of great use in order to characterise a source. In most cases, only first and second order correlation functions are studied. For a classical, stationary electric field $E(t)$, one can define:

$$g_1(\tau) = \frac{\langle E^*(t)E(t+\tau)\rangle}{\langle |E(t)|^2\rangle} \text{ and } g_2(\tau) = \frac{\langle I(t)I(t+\tau)\rangle}{\langle I(t)\rangle^2}, \text{ with } I(t) = |E(t)|^2. \tag{1.44}$$

Here, the two correlation functions have been normalised. The first order correlation function measures whether E can interfere with itself at a later time; as such, it is a measure of the field's coherence. The second order correlation function characterises the temporal coherence, not in amplitude, but in intensity.

In order to study the spatial coherence instead of the temporal one, these two functions can also be defined with variables of space and not of time: in this case, g_1 typically represents the contrast of the interference created by two different areas of the source, while g_2 can be used to characterise the spatial fluctuations in intensity, the speckle for instance.

In the context of ultracold atoms, the same two functions can be used to study a quantum field. In 3D, a Bose-Einstein condensation phenomenon can be observed below a certain temperature, which implies a total phase coherence over the whole sample. Nevertheless, we have seen in the previous section that there can be no long range order in 2D at finite temperature as thermal fluctuations always end up destroying order at large enough distances. However, a local order can be restored when $\mathcal{D}$ is high enough: the idea is that if the phase coherence tends to 0 at

large distances when $T \neq 0$, this decay might be slow. A good observable to quantify these different behaviours is the first order correlation function.

The second order correlation function, however, does not deal with the coherence of the field, but rather with density correlations. As such, it can be used to measure (anti-)bunching effects created by quantum statistics, like in the Hanbury Brown and Twiss experiment. As bosons (resp. fermions) have a tendency to cluster together (resp. to avoid each other), the probability to detect a particle in the vicinity of another particle is increased (resp. decreased) compared to the classical case. This corresponds to an increase (resp. decrease) of $g_2(0)$.

1.2.1.2 *Definitions in first quantisation*

We use here the first quantisation approach in order to define the first and second order correlation functions. As the system has a translational symmetry, both functions $G_1(\mathbf{r}, \mathbf{r}')$, and $G_2(\mathbf{r}, \mathbf{r}')$ only depend on $\mathbf{r} - \mathbf{r}'$ and we will usually simplify: $G_i(\mathbf{r}, 0) = G_i(\mathbf{r})$.

The first order correlation function can be defined as follows:

$$G_1(\mathbf{r}, \mathbf{r}') = \langle \mathbf{r}|\hat{\rho}_1|\mathbf{r}'\rangle, \tag{1.45}$$

where $\hat{\rho}_1$ is the one body density operator. Taking advantage of the translation symmetry of our system, we can write, in dimension d:

$$N(\mathbf{p}) = \langle \mathbf{p}|\hat{\rho}_1|\mathbf{p}\rangle = \int \langle \mathbf{p}|\mathbf{r}\rangle G_1(\mathbf{r}, \mathbf{r}') \langle \mathbf{r}'|\mathbf{p}\rangle \, \mathrm{d}^d r \, \mathrm{d}^d r' = \int e^{-i\mathbf{r}\cdot\mathbf{p}/\hbar} G_1(\mathbf{r}) \, \mathrm{d}^d r. \tag{1.46}$$

It thus appears that the functions $N(\mathbf{p})$ and $G_1(\mathbf{r})$ are reciprocally Fourier transforms. This general result holds in any dimension, whether the gas is ideal or not. We will use this property later.

The second order correlation function can be defined as follows:

$$G_2(\mathbf{r}, \mathbf{r}') = \langle \mathbf{r}, \mathbf{r}'|\hat{\rho}_2|\mathbf{r}, \mathbf{r}'\rangle, \tag{1.47}$$

where we have introduced the two-body density operator ρ_2. It can be seen as the first order correlation function in density.

The normalised corresponding correlation functions, which have the advantage of being independent of N, can also be defined:

$$g_1(\mathbf{r}, \mathbf{r}') = \frac{G_1(\mathbf{r}, \mathbf{r}')}{\sqrt{G_1(\mathbf{r}, \mathbf{r})}\sqrt{G_1(\mathbf{r}', \mathbf{r}')}} \text{ and } g_2(\mathbf{r}, \mathbf{r}') = \frac{G_2(\mathbf{r}, \mathbf{r}')}{G_1(\mathbf{r}, \mathbf{r}) G_1(\mathbf{r}', \mathbf{r}')}. \tag{1.48}$$

1.2.1.3 *Definitions in second quantisation*

Depending on the case, it might be useful to either use first or second quantisation for computing G_1 or G_2. Let us here introduce the quantum field operators that we use for this approach:

$$\hat{\psi}(\mathbf{r}) = \sum_i \phi_i(\mathbf{r}) \hat{a}_i \text{ and } \hat{\psi}^\dagger(\mathbf{r}) = \sum_i \phi_i^*(\mathbf{r}) \hat{a}_i^\dagger, \tag{1.49}$$

where $\hat{a}_i$ and $\hat{a}_i^\dagger$ respect the usual commutation relations: $[\hat{a}_i, \hat{a}_j^\dagger] = \delta_{ij}$, and δ_{ij} is the Kronecker symbol. We will here use the system's translational invariance. In the case where the $\{\phi_i(\mathbf{r})\}$ are plane waves, one has $\langle \hat{a}_i^\dagger \hat{a}_j \rangle = \delta_{ij} \langle \hat{a}_i^\dagger \hat{a}_i \rangle$. One can then show that in the language of second quantisation, eq. 1.45 is equivalent to:

$$G_1(\mathbf{r},\mathbf{r}') = \langle\hat{\psi}^\dagger(\mathbf{r})\hat{\psi}(\mathbf{r}')\rangle = \sum_i \phi_i^*(\mathbf{r})\phi_i(\mathbf{r}')\langle\hat{a}_i^\dagger\hat{a}_i\rangle. \tag{1.50}$$

Let us give here an interpretation of G_1 in terms of phase coherence. If we take a uniform system where only the phase fluctuates (for instance a 2D Bose gas in the very degenerate regime), we have: $\psi(\mathbf{r},t) \simeq \sqrt{n_0}e^{i\theta(\mathbf{r},t)}$, which yields, for a random gaussian variable:

$$G_1(\mathbf{r}) \simeq n_0\langle e^{i(\theta(\mathbf{r})-\theta(0))}\rangle \simeq n_0 e^{-\langle(\theta(\mathbf{r})-\theta(0))^2\rangle/2}. \tag{1.51}$$

It is thus easy to understand that G_1 represents the phase coherence of the sample: if there is no fluctuation of phase, $G_1 = n_0$, while any loss of coherence will decrease G_1.

For G_2, adapting eq. 1.47 to second quantisation gives the following expression for the second order correlation function:

$$G_2(\mathbf{r},\mathbf{r}') = \langle\hat{\psi}^\dagger(\mathbf{r})\hat{\psi}^\dagger(\mathbf{r}')\hat{\psi}(\mathbf{r}')\hat{\psi}(\mathbf{r})\rangle = \sum_{ijkl} \phi_i^*(\mathbf{r})\phi_j^*(\mathbf{r}')\phi_k(\mathbf{r}')\phi_l(\mathbf{r})\langle\hat{a}_i^\dagger\hat{a}_j^\dagger\hat{a}_k\hat{a}_l\rangle. \tag{1.52}$$

1.2.2 *First order correlation function G_1*

1.2.2.1 *The 3D ideal gas*

We have seen with eq. 1.46 that $G_1(\mathbf{r})$ and $N(\mathbf{p})$ are Fourier transforms from one another. Thus, we can obtain G_1 by taking the inverse Fourier transform of $N(\mathbf{p})$. By developing $N(\mathbf{p})$ into an infinite series, we obtain:

$$N(\mathbf{p}) = \sum_{l=1}^{\infty} z^l e^{-\frac{\beta l\mathbf{p}^2}{2m}} \quad\Rightarrow\quad G_1(\mathbf{r}) = \frac{1}{h^3}\int e^{i\mathbf{p}\cdot\mathbf{r}/\hbar}N(\mathbf{p})\,\mathrm{d}^3p = \frac{N_0}{L^3} + \frac{1}{\lambda_T^3}\sum_{n=1}^{\infty}\frac{z^n}{n^{3/2}}e^{-\pi r^2/n\lambda_T^2}, \tag{1.53}$$

where we have separated the $\mathbf{p}=0$ term from the $\mathbf{p}\neq 0$ contribution in the integral as it can be macroscopically populated and would otherwise be omitted.

For a very non-degenerate gas, we have $n\lambda_T^3 \ll 1$, hence, no condensate fraction, and we can neglect the term in N_0 in the previous equation. Moreover, in this Boltzmann regime, as $z \ll 1$, we only keep the first term of the sum. This yields:

$$G_1(\mathbf{r}) \simeq \frac{N}{L^3}e^{-\frac{\pi r^2}{\lambda_T^2}}. \tag{1.54}$$

We see that G_1 goes to zero on a typical length scale $\lambda_T/\sqrt{\pi}$: there is no phase coherence for large distances above the transition.

For a gas that has reached condensation, we have $z = 1$, and we have to separate the condensed and non condensed contributions:

$$G_1(\mathbf{r}) = \frac{N_0}{L_3} + G_1^c(\mathbf{r}) \text{ where } G_1^c(\mathbf{r}) = \frac{1}{\lambda_T^3}\sum_{n=1}^{\infty}\frac{1}{n^{3/2}}e^{-\pi r^2/n\lambda_T^2}. \tag{1.55}$$

When the density keeps increasing, $G_1^c(\mathbf{r})$, which corresponds to the excited states, does not change. What changes is the value of the offset N_0/L^3, and G_1 does no longer vanish at infinity. This means that for a condensed gas, the coherence length is infinite.

The behaviour of these two cases is summarised in Fig. 1.5.

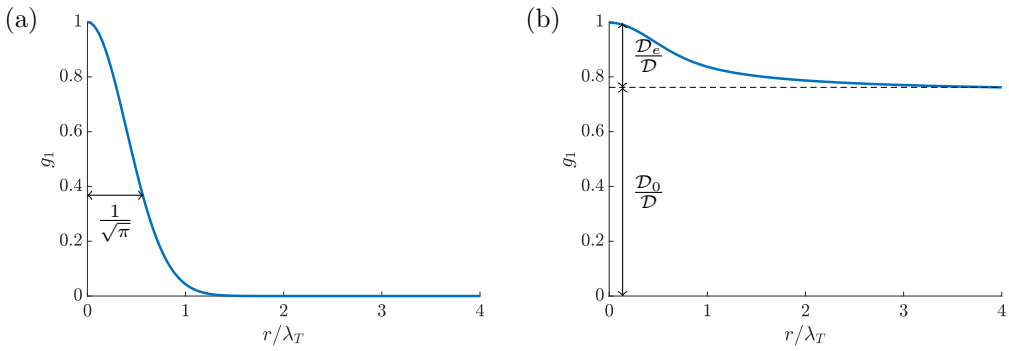

Figure 1.5: First order correlation function for the 3D ideal case. Non condensed gas (left), and gas that has reached condensation (right). In the first case, g_1 goes to zero on a typical distance given by the de Broglie wavelength and there is no global phase coherence. For a condensed gas, however, the condensed fraction gives a global offset to g_1 and the function saturates at $\mathcal{D}_0/\mathcal{D}$ at high distance: a global phase coherence emerges. Figure inspired from [83].

1.2.2.2 *The 2D ideal gas*

As stated before, the Fourier link between G_1 and $N(\mathbf{p})$ is a general result and holds is any dimension. We can thus still use it here:

$$G_1(\mathbf{r}) = \frac{1}{h^2}\int e^{i\mathbf{p}\cdot\mathbf{r}/\hbar}N(\mathbf{p})\,\mathrm{d}^2p = \frac{1}{\lambda_T^2}\sum_{n=1}^{\infty}\frac{z^n}{n}e^{-\pi r^2/n\lambda_T^2}. \tag{1.56}$$

In the low degenerate case, the gaussian shape of $N(\mathbf{p})$ implies that G_1 is also gaussian:

$$N(\mathbf{p}) = \frac{1}{e^{\beta(\varepsilon_\mathbf{p}-\mu)}-1} \simeq ze^{-p^2/2mk_BT} \;\Rightarrow\; G_1(\mathbf{r}) \simeq ne^{-\pi r^2/\lambda_T^2}. \tag{1.57}$$

In this case, the spatial extent of coherence is also given by the de Broglie wavelength.

In the very degenerate case ($z \simeq 1$), we have two contributions in N:

- for low momenta $\frac{p^2}{2m} < k_BT$, we can linearise the denominator of the Bose-Einstein distribution:

$$N(\mathbf{p}) \simeq \frac{k_BT}{\frac{p^2}{2m}+|\mu|} = \frac{4\pi\hbar^2}{\lambda_T^2}\frac{1}{p^2+p_c^2} \text{ with } p_c = \sqrt{2m|\mu|} \ll \sqrt{2mk_BT}. \tag{1.58}$$

- for higher momenta $\frac{p^2}{2m} > k_BT$, we can neglect the bosonic amplification term. We then find a Boltzmann distribution:

$$N(\mathbf{p}) \simeq e^{-p^2/2mk_BT}. \tag{1.59}$$

One can actually compute the contribution of both terms and find that the gaussian term is negligible. As the Fourier transform of a 2D lorentzian is proportional to the modified Bessel function K_0 whose asymptotic behaviour is:

$$K_0(x) \underset{r\to\infty}{\sim} \sqrt{\frac{\pi}{2x}}e^{-x}, \tag{1.60}$$

we will have the following asymptotic behaviour:

$$G_1(r) \underset{r\to\infty}{\sim} \frac{1}{\sqrt{r}}e^{-r/\ell} \text{ where } \ell = \frac{\hbar}{p_c} \simeq \frac{\lambda_T}{\sqrt{4\pi}}e^{\mathcal{D}/2}. \tag{1.61}$$

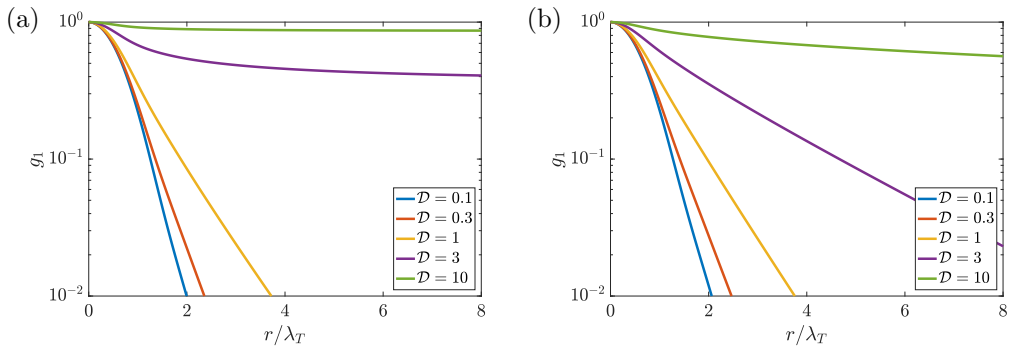

Figure 1.6: First order correlation function for ideal Bose gases in the 3D case (a) and in the 2D case (b), calculated with the sums up to $n = 10^4$ in eq. 1.53 and 1.56. We see that above $\mathcal{D}_c \simeq 2.612$, g_1 saturates in 3D; the level of its offset is dictated by the population of the condensed fraction. In 2D, however, and even if g_1 decreases more slowly when $\mathcal{D}$ increases, the function tends to 0 for large distances.

We see that in both cases, G_1 goes to 0 when r goes to infinity, which satisfies the Mermin-Wagner theorem. However, for a very degenerate gas, phase coherence is only lost on a scale of ℓ. This means that finite size effects can still play a significant role. In effect, when $\ell \gtrsim L$, *i.e.* when $\mathcal{D} \gtrsim \ln(4\pi L^2/\lambda_T^2)$, we can neglect the decay of the phase coherence. For cold atoms experiments, one typically has $\lambda_T \simeq 1$ μm, which, for $\mathcal{D}$ around 30, gives $\ell \sim 1$ m. In this case, the variations of the phase over the whole sample can be neglected, and the physics is essentially the same as for a true Bose-Einstein condensate. A comparison between the 2D and 3D case is shown in Fig. 1.6.

Finally, it should be noted that this discussion corresponds to an ideal gas, which is not the case for our experiment. The presence of interactions will change the behaviour of G_1, as we will see in the next section.

1.2.2.3 *The 2D weakly interacting case*

We will now review the weakly interacting case. The main difference between this section and the previous one is the suppression of density fluctuations in the quasi-condensate regime.

For a gas above the BKT transition, we have seen that vortices proliferate, which destroys the phase coherence. This means that one cannot have phase coherence between two points of the gas if the probability to find a vortex in between these two points is non negligible. As a consequence, G_1 cannot be long range, and one can show that it decays exponentially in this region:

$$G_1(\mathbf{r}) \propto e^{-r/\ell}. \tag{1.62}$$

Moreover, when approaching the transition from the $T > T_c$ side, this correlation length ℓ diverges:

$$\ell \propto \lambda_T \exp\left(\sqrt{\frac{\zeta T_{\mathrm{BKT}}}{T - T_{\mathrm{BKT}}}}\right), \tag{1.63}$$

where ζ is a model dependant constant.

For a gas that has crossed the BKT transition, one can write the wave function as a sole function of θ: $\psi = \sqrt{n_0} e^{i\theta(\mathbf{r})}$. A lengthy calculation done in [80] gives:

$$\langle \theta(\mathbf{r}) - \theta(0) \rangle \simeq \frac{2}{n_s \lambda_T^2} \ln(r/\lambda_T). \tag{1.64}$$

Finally, we can compute the first order correlation function:

$$\begin{aligned} G_1(\mathbf{r}) &= \langle \psi(\mathbf{r})\psi^*(0)\rangle \simeq n_s \langle e^{i(\theta(\mathbf{r})-\theta(0))}\rangle \simeq n_s e^{-\langle(\theta(\mathbf{r})-\theta(0))^2\rangle/2} \\ &\simeq n_s \left(\frac{\lambda_T}{r}\right)^{\alpha} \quad \text{where} \quad \alpha = \frac{1}{n_s \lambda_T^2}. \end{aligned} \tag{1.65}$$

We thus see an important difference between the ideal gas and the weakly interacting case below the BKT critical temperature. For the first one, G_1 was decaying exponentially, while adding weak interactions renders the decay algebraic. This corresponds to a much slower decay, even if G_1 still vanishes at infinity, as this would otherwise violate Mermin-Wagner's theorem. We have also seen that in the superfluid region, we always have $\mathcal{D}_s > 4$, which means that the decay should always be slower than $r^{-1/4}$. At the transition, $\mathcal{D}_s^c = 4$ and we thus expect the critical exponent to be equal to 0.25.

It can be useful to have a comparison between the cases with and without interactions. To keep things simple, we will take $n = n_s = 50\ \mu\text{m}^{-2}$ and $T = 100$ nK, which are values that we typically have on our experiment. This gives $D \simeq 18$ (very degenerate gas), $\lambda_T \simeq 0.6\ \mu$m and $\ell \simeq 1$ mm. In a box of side $L = 50\ \mu$m, $g_1(L)$ is typically equal to 0.04 for the ideal gas and 0.71 for the interacting one. We see that in this system, the phase coherence is totally destroyed for the first case; for the second one, however, the two sides of the gas are still highly phase correlated.

Moreover, it is important to note that as ℓ diverges at the transition, there is a temperature T_f above T_c where $\ell > L$ and a significant condensed fraction appears. An estimate of $T_f/T_c - 1$ is typically in the 5-20 % range ([28]).

1.2.2.4 *Measurement of G_1 for a weakly interacting gas*

Properly measuring the decay of G_1 is a complicated task. There have been several attempts, some with polaritons ([31–33]), some other with ultracold atoms in an in-plane harmonic confinement ([35–37]). A recent study with dipolar excitons also showed interesting results ([34]).

Although the experiments with polaritons see a decay of G_1 compatible with a power law, the decay exponents do not agree with the theoretical predictions. Moreover, as polaritons typically have similar thermalisation and life times, these systems have to be continuously driven: these non equilibrium systems can therefore have very different properties from closed systems at equilibrium.

Ultracold atoms, on the other hand, have thermalisation times of typically a few ms, but life times in the second range, and are thus more faithful to the picture of a system in thermal equilibrium. The aforementioned experiments with ultracold atoms also measured an algebraic decay below a certain critical temperature; however, the harmonic trapping changes the behaviour of G_1 compared to the uniform case, and the measured decay exponents were significantly bigger than the predicted one (the experiments typically measured an exponent above 0.5 while we expect 0.25 at T_c).

Finally, while $s-$wave collisions are in many cases the only relevant two-body interactions for ultracold atomic gases, interesting collective phenomena arise when one considers gases with dipolar interactions. Moreover, excitons systems have stronger dipolar interactions, and can be realised in layers of semiconductors. A recent publication performed in such a system ([34]) observed an algebraic decay of G_1 below the transition point in the 2D case. The authors obtained an exponent for this decay compatible with the theoretical value of 0.25, although the precise measured value was limited by the inhomogeneity of the experimental system.

This pushed us to try to measure the decay of G_1 in our system. During my PhD, we actually did two attempts at measuring G_1: both these attempts are described in more details in [81].

We have seen that G_1 and the distribution in momentum $N(\mathbf{p})$ are linked via Fourier transformations. Our first attempt tried to use this result. We prepared the cloud at various degeneracies, and let it evolve for a quarter of a period in an in-plane harmonic confinement created by a quadrupole field. This operation transforms the spatial distribution at time $T/4$ into the initial momentum distribution:

$$\psi\left(\mathbf{r}, t = \frac{\pi}{2\omega}\right) = \psi_{\mathbf{p}}(\mathbf{p} = m\omega\mathbf{r}, t = 0), \tag{1.66}$$

where $\omega = 2\pi/T$ is the in-plane trapping frequency. As this result holds only for non-interacting clouds, we removed the vertical confinement in order to let the atoms expand in this direction (and thus lower the interactions). We then let the cloud evolve in the harmonic trap. Only a thin slice of these atoms were repumped and imaged in order to keep the signal in focus with our imaging system.

However, due to experimental limitations coming in part from the residual interactions between atoms which tended to influence the measured size of the cloud, we could not properly conclude. Notably, we could not properly assign the shape of G_1 to be either exponential or algebraic, as both expressions fitted equally well our data. We however measured two things.

- If we assume an algebraic decay for G_1, then the corresponding exponent is below 0.3 for $T < T_c$, which is in agreement with the BKT theory. This exponent dramatically increases when T is increased above T_c, which reflects the loss of coherence when the transition is crossed.

- If we assume an exponential decay for G_1, then the characteristic length of this exponential is bigger than the size of our sample for $T < T_c$ (we have a fully coherent sample), and decreases when leaving the superfluid regime. This is also in agreement with the BKT theory according to which this length scale diverges at the transition.

We then turned to another method. The idea was to use an interferometric measurement by letting two parts of the cloud interfere with one another. We used Raman beams to select two lines of our initial cloud, while the other atoms were expelled from the trap. After a 2D time of flight, the two lines were made to interfere with each other, and by repeating the same experiment several times, we could extract the average contrast of the interference pattern, which at the centre of the cloud, is proportional to $G_1(d)$, d being the initial distance between the two lines. An example of our protocol is given in Fig. 1.7. It is important to note that even for a thermal cloud, two lines will always yield a non-zero contrast; however, without phase coherence, the phase of the appearing pattern will be random and the contrast will be washed out when an average is performed. By varying the distance between the two lines, we could measure $G_1(r)$ at a certain phase space density. Repeating the experiment with different phase-space densities gave us information on the phase coherence across the transition.

At the time when this thesis was written, the analysis of this set of data was still being carried out, and definitive results were not available. We give here preliminary results. Our method has limitations: the inherent size of our sample ($L = 40$ μm) limits the range of distances on which we can measure G_1; this in turn restricts us in our determination of its exact shape, and we are still not able to discriminate between an exponential and an algebraic behaviour. However, below T_c, assuming an algebraic decay, we get decay exponents very close to what the theory predicts; in particular, we are around $1/4$ at the transition, which is in agreement with the BKT prediction of $\mathcal{D}_s^c = 4$. Above the transition, G_1 decreases dramatically faster than at $T < T_c$. Assuming an exponential behaviour, we find that the characteristic length scale associated with this decay increases when T is brought closer to T_c. In conclusion, these results are compatible to the ones yielded by the first method, and give a more accurate measurement of the decay exponent that is brought into play during the BKT phase transition.

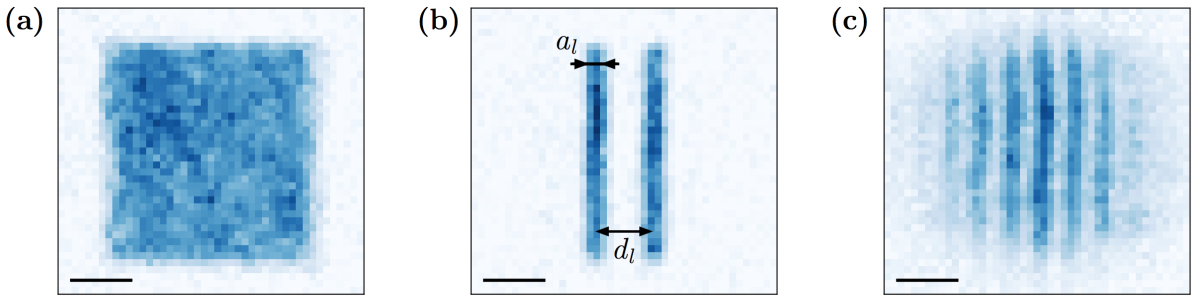

Figure 1.7: Measurement of g_1 with an interferometric method. Two lines (b) are selected from the initial cloud (a) and interfere (c). Averaging (c) over different iterations and extracting the central interference contrast enables us to measure $G_1(d_l)$. The black line represents 10 μm. Figure taken from [81].

1.2.3 *Second order correlation function G_2*

Contrarily to G_1, the second order correlation function is not connected to phase coherence, but rather to the density distribution of the gas. As density fluctuations are largely suppressed for 2D highly degenerate bosons, G_2 can be an important parameter to describe the state of the gas at various temperatures. A natural question would then be to investigate wether G_2, like G_1, also has specificities in 2D, and to know in particular how G_2 evolves across the BKT transition. Nevertheless, predicting or measuring the exact variation of this function across the critical point is hard, and literature on the topic is scarce. This is a good motivation for measuring g_2 at various T/T_c, as we are currently doing at the time when this thesis is written. We will first present the general characteristics of G_2 that can be found in literature, then give a small review of some measurement that have been done on that topic.

1.2.3.1 *Ideal gas*

We start by looking at the ideal case, and use eq. 1.52 in order to compute G_2. We follow here computations done for 3D in [84].

For temperatures above T_c, there is no condensed fraction, and we can use Wick's theorem[2]:

$$\langle \hat{a}_i^\dagger \hat{a}_j^\dagger \hat{a}_k \hat{a}_l \rangle = \langle \hat{a}_i^\dagger \hat{a}_k \rangle \langle \hat{a}_j^\dagger \hat{a}_l \rangle + \langle \hat{a}_i^\dagger \hat{a}_l \rangle \langle \hat{a}_j^\dagger \hat{a}_k \rangle. \tag{1.67}$$

Using the system's translational invariance, we also have $\langle \hat{a}_i^\dagger \hat{a}_j \rangle = \delta_{ij} \langle \hat{a}_i^\dagger \hat{a}_j \rangle$. This yields:

$$\begin{aligned} G_2(\mathbf{r}) &= \langle \hat{\psi}^\dagger(\mathbf{r}) \hat{\psi}(\mathbf{r}) \rangle \langle \hat{\psi}^\dagger(0) \hat{\psi}(0) \rangle + |\langle \hat{\psi}^\dagger(0) \hat{\psi}(\mathbf{r}) \rangle|^2 \\ &\quad + \sum_m |\phi_m(\mathbf{r})|^2 |\phi_m(0)|^2 \left(\langle \hat{a}_m^\dagger \hat{a}_m^\dagger \hat{a}_m \hat{a}_m \rangle - 2 \langle \hat{a}_m^\dagger \hat{a}_m \rangle \langle \hat{a}_m^\dagger \hat{a}_m \rangle \right) \\ &= G_1(0)^2 + |G_1(\mathbf{r})|^2 \text{ and hence,} \\ g_2(\mathbf{r}) &= 1 + |g_1(\mathbf{r})|^2. \end{aligned} \tag{1.68}$$

We immediately see two things:

- as $\lim_{r \to \infty} g_1(\mathbf{r}) = 0$, we have $\lim_{r \to \infty} g_2(\mathbf{r}) = 1$;
- as $g_1(0) = 1$, we also have $g_2(0) = 2$. This is the famous bunching effect that appears for bosons.

The behaviour of g_2 in this case is plotted in Fig. 1.8.

2 Wick's theorem is only applicable in the grand canonical ensemble, which can lead to non physical results for an ideal condensed system, for instance the computation of atom number fluctuations.

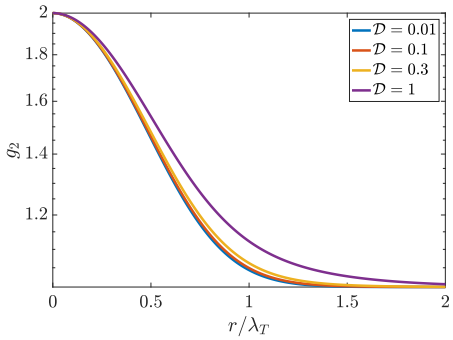

Figure 1.8: Behaviour of $g_2(r)$ for an ideal gas above the condensation threshold: the value of the function is 2 in 0, and decays to 1 in a scale set by λ_T.

For temperatures below T_c, one has to separate the condensed and the non condensed parts. For condensed bosons, the grand canonical ensemble predicts huge condensate fluctuations; in this case, one has to resort to treating the condensate part with the canonical ensemble. In this case, Wick's theorem can no longer be applied. For a very degenerate gas, however, the thermal part can be treated in the grand canonical ensemble, the condensate playing the role of a never-empty reservoir ([84]).

We can then approximate $\psi(\mathbf{r}) = \sqrt{\langle \hat{a}_0^\dagger \hat{a}_0 \rangle}\phi_0(\mathbf{r})$, which yields:

$$G_2(\mathbf{r}) = G_1(0)^2 + |G_1(\mathbf{r})|^2 - |\psi(\mathbf{r})|^2|\psi(0)|^2, \tag{1.69}$$

or, equivalently,

$$g_2(\mathbf{r}) = 1 + |g_1(\mathbf{r})|^2 - \frac{|\psi(\mathbf{r})|^2|\psi(0)|^2}{G_1(0)^2}. \tag{1.70}$$

We can again examine the two following limits:

- in the limit $r \to \infty$, the value of $g_2(\mathbf{r})$ remains 1,
- in 0, we have:

$$g_2(0) = 2 - \left(\frac{|\psi(0)|^2}{G_1(0)}\right)^2. \tag{1.71}$$

For a very degenerate gas, we have $G_1(0) \simeq n(0) = |\psi(0)|^2$, which means that we will have $g_2(0) = 1$.

Let us stress this important result: for a thermal gas, we have $g_2(0) = 2$, and we observe the bunching effect caused by the Bose statistics. For a very degenerate gas, $g_2(0)$ goes to 1, and the density fluctuations decrease. This is compatible with the image of a gas whose density fluctuations are frozen ((quasi-)condensate regime). Moreover, while g_2 can be expressed as a sole function of g_1 for a non degenerate gas, this does not correspond to a general case, and the expression below the transition involves the modulus of the wave function.

1.2.3.2 *Interacting gas*

For interacting gases, the story is a bit different. In particular, the quantity $g_2(0)$ is ill-defined and diverges when $r \to 0$ in 2D and 3D. It is then safer to examine Tan's contact instead, which is a parameter that can be used to describe the short range interactions of an ultracold gas :

$$C = \frac{8\pi m a^2}{\hbar^2}\frac{\partial E}{\partial a}, \tag{1.72}$$

E denoting the gas' internal energy. Thanks to the Hellmann–Feynman theorem, one can write:

$$\frac{\partial E}{\partial a} = \left\langle \frac{\partial \hat{H}_{\text{int}}}{\partial a} \right\rangle = \frac{2\pi\hbar^2}{m}\left\langle \iint \hat{\psi}^\dagger(\mathbf{r})\hat{\psi}^\dagger(\mathbf{r}')\hat{\delta}(\mathbf{r}-\mathbf{r}')\hat{\psi}(\mathbf{r}')\hat{\psi}(\mathbf{r})\,\mathrm{d}\mathbf{r}\,\mathrm{d}\mathbf{r}' \right\rangle. \tag{1.73}$$

In the case where the contact potential does not need to be regularised, one finds:

$$C = C_0 \text{“}g_2(0)\text{”} \quad \text{with} \quad C_0 = 16\pi^2 a^2 \bar{n} N. \tag{1.74}$$

In this case, we find that C is proportional to $g_2(0)$. For an ideal gas, we have seen in the previous section that $g_2(0)$ goes from 1 in the very degenerate regime to 2 when $\mathcal{D} \ll \mathcal{D}_c$, and we thus also expect here a variation of C by a factor of 2.

Oppositely, when the contact interaction needs to be regularised, it is safer to work with C only, which remains regular. One can show that for an interacting system, the zero-temperature part of $g_2(0)$ diverges ([85]), but one can still relate the contact to the thermal contribution of g_2:

$$\frac{C}{C_0} = 1 + g_2^{T\neq 0}(0). \tag{1.75}$$

A project that was conducted towards the end of my thesis consisted in measuring the variation of the contact with degeneracy using Ramsey spectroscopy ([85]). Moreover, this project also provided us with a measurement of our system's $s-$wave scattering lengths a_{ij} ([86]). This is discussed in more details in the Outlook section.

1.2.3.3 *Examples of noise correlation measurements*

Historically, the first experiment to measure a bunching effect in bosons was the Hanbury Brown and Twiss experiment ([87]). The goal was initially to measure the angular diameter of a star using an interferometric method, but first, a test on a mercury lamp was carried out. A measure of the temporal coherence of the source was performed by separating the beam coming from the source on two different paths and counting the number of photons arriving on two detectors placed on each path. Hanbury Brown and Twiss found that while there was no correlation when the two paths had very different lengths, it was not the case when the lengths were equal. They observed that there was a 'bunching' of photons for equal paths, meaning that the photons had a tendency to be found in pairs.

The same kind of experiment was then reproduced for massive particles, first for an atomic beam ([88]), then for atoms trapped in an optical lattice ([89, 90]). In [88], the authors realised a continuous atomic beam falling under the effect of gravity on a detector. The temporal correlations of the arrival of atoms on the detector were then recorded. In order to enhance the coherence of this source, the authors used an electric lens to select one class of velocities. When no selection was made, there was no bunching effect. When the lens was added, however, an increase of the correlations at 0 delay time was observed. Their result is presented in Fig. 1.9. Similar experiments measuring the absence of bunching for condensed bosons ([91]), or comparing the correlations between bosons and fermions ([92]) have also been performed.

In [89], the authors prepared an ultracold Bose gas in a 3D optical lattice in the Mott insulator phase, and then released the cloud and imaged it. The density fluctuations were then analysed and the density-density correlator:

$$C(\mathbf{d}) = \frac{\int \langle n(\mathbf{x}+\mathbf{d}/2)n(\mathbf{x}-\mathbf{d}/2)\rangle\,\mathrm{d}^2\mathbf{x}}{\int \langle n(\mathbf{x}+\mathbf{d}/2)\rangle\langle n(\mathbf{x}-\mathbf{d}/2)\rangle\,\mathrm{d}^2\mathbf{x}}, \tag{1.76}$$

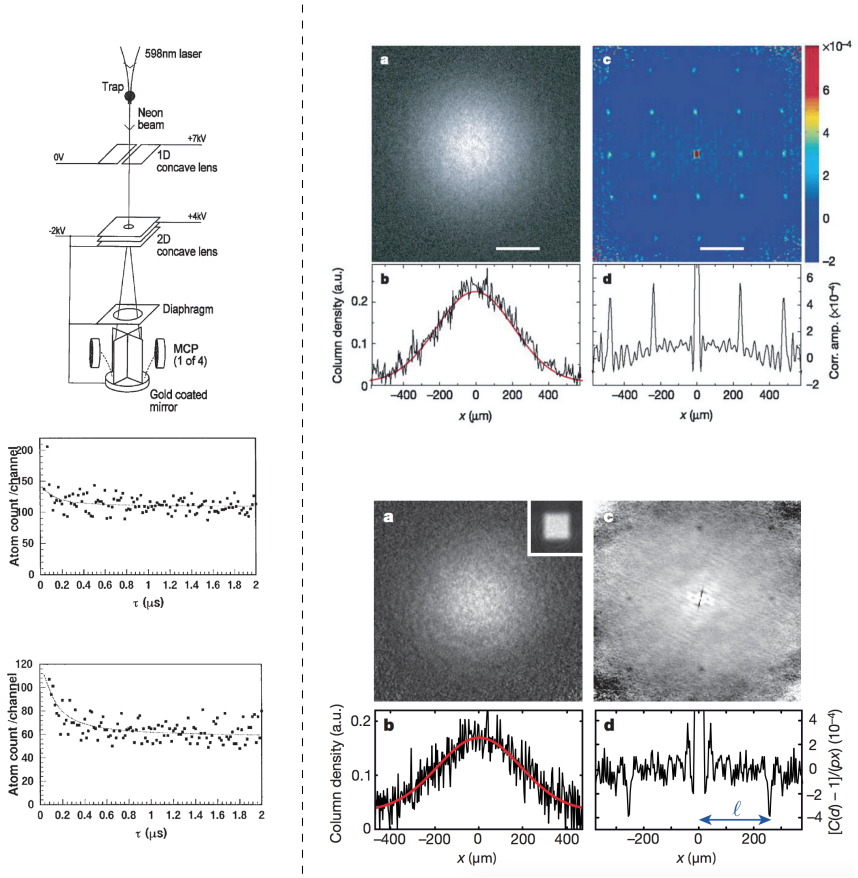

Figure 1.9: Left: measurement of temporal correlations in falling Neon atoms. The top figure is a scheme of their apparatus. The authors measured no correlation in the arrival time (middle), but a bunching effect (bottom) appeared when a velocity selection was made, increasing the coherence of the source. Figures taken from [88]. Right: experiment in a 3D optical lattice performed for bosons (top) and fermions (bottom). Figures (a) show an absorption image taken after a TOF, while (c) show the corresponding calculated density-density correlator. Figures (b) and (d) are cuts of (a) and (c), respectively. We see clear peaks for bosons, and dips for fermions, corresponding to respectively bunching and anti-bunching phenomena. Figures taken from [89] and [90].

was computed. Here, n is a column density obtained from an absorption image, and the notation $\langle\cdot\rangle$ refers to ensemble averages over different images. They observed peaks with $C(0) > 1$ as expected for bosons. The same experience was also performed for fermions ([90]), and authors measured $C(0) < 1$, confirming the impact of the particle's nature on the density correlations. Their result is also presented in Fig. 1.9.

While these experiments clearly show a bunching effect for bosons, they do not treat the dependance of this effect with the interaction strength. A measurement of the nature of these fluctuations was performed in [93] and [94] for 1D gases, by looking at in situ images. Instead of computing a correlator, the authors looked at the fluctuations of the mean atom number $\langle\delta N^2\rangle$ in a pixel, and binned the values of $\langle\delta N^2\rangle$ corresponding to the same values of $\langle N\rangle$. This quantity is related to the density *fluctuations* correlation function:

$$\nu(\mathbf{r}) = \langle\delta n(\mathbf{r})\delta n(0)\rangle = \bar{n}\delta(\mathbf{r}) + \bar{n}^2(g_2(\mathbf{r}) - 1). \tag{1.77}$$

In 1D, $g_2(0)$ remains a pertinent quantity and does not diverge. For an ideal non-degenerate gas, we know that $g_2(0) = 2$, giving rise to super-Poissonian fluctuations. Increasing the density increases the degeneracy and thus decreases $g_2(0)$ to 1, translating into a decrease of $\langle\delta N^2\rangle$. For interacting gases, the story is similar, and one can even have $g_2(0) \ll 1$ in the strongly interacting regime, thus yielding sub-Poissonnian fluctuations.

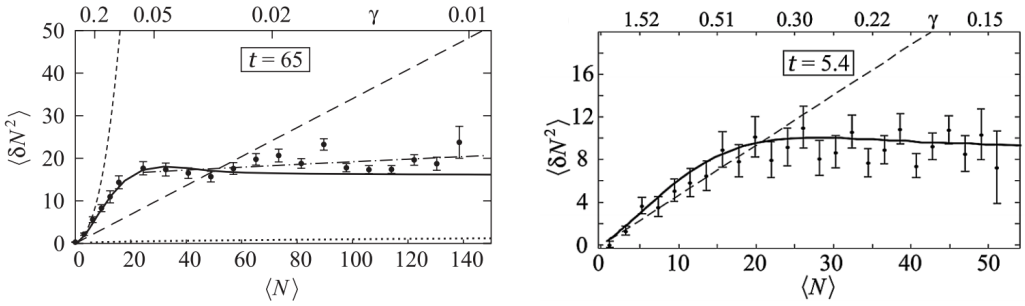

Figure 1.10: Variance of atom number fluctuations for different mean atom number in a weakly interacting gas (left) and close to the strongly interacting regime (right). The parameters t and γ correspond to an adimensioned temperature: $t = 2\hbar^2 k_B T/mg^2$ and an adimensioned interaction strength: $\gamma = mg/\hbar^2 n$. In the weakly interacting case, the fluctuations go from super to sub-Poissonian when the density is increased and the quasi-condensate regime is reached. In the strongly interacting case, the super-Poissonian fluctuations are suppressed even at small densities. The Yang-Yang prediction is shown as a solid line, the ideal Bose gas prediction as a short dashed one, and the quasi-condensate prediction as dashed-dotted one. The long dashed line corresponds to Poissonian fluctuations. Figure taken from [94].

The authors observed three different regimes. For an ideal gas, they indeed find $\langle \delta N^2 \rangle$ bigger than shot noise fluctuations. When increasing the atom number, they eventually reach the quasi condensate regime, in which $\langle \delta N^2 \rangle$ is lower than the ideal gas case. Finally, preparing the gas in the strongly interacting regime ($g_2(0) \ll 1$), the authors observe sub-Poissonian fluctuations, with super-Poissonian fluctuations suppressed even at low densities. Their results are presented in Fig. 1.10.

In higher dimensions, one has to resort to dropping the variable $g_2(0)$, and using Tan's contact C instead. A way of measuring C can then be the use of a spectroscopic method ([95]). The exact value of the transition's frequency between two hyperfine levels is influenced by mean field effects and depends explicitly on C. By measuring the frequency of a clock transition for various degeneracies, we can hope to see the value of C being divided by 2 between high and low temperatures. Such a method will be developed in the Outlook section.

CONCLUSION

In conclusion, we have explored what happens for a 2D Bose gas across the BKT phase transition. At the critical point of this transition, unpaired vortices proliferate, giving rise to an exponential decay of G_1 for weakly interacting gases, while this decay is algebraic below T_c. This slow decrease coupled with finite size effects are sufficient to create a situation where the physics is essentially similar to what happens in the case of regular 3D condensation. Moreover, the value of $g_2(0)$ is an interesting signature of the appearance of a condensed fraction: for an ideal gas, it goes from 2 in the thermal regime to 1 in the condensed one. For interacting gases, this quantity is ill-defined in 2D; however, on can instead measure Tan's contact across the superfluid transition, which will be the subject of a future publication.

2

THE RB EXPERIMENT

When my PhD started, the experiment was already built and working on a daily basis. Thanks to the expertise of the builders and the quality of the set-up, we seldom (a few times a year) need to realign optics and fix problems. However, there was still room for improvement, and we will detail in the next chapter one of the tools that I have implemented during my PhD. Even if details of the experimental set-up have been covered extensively by my predecessors ([96], [97], [76], [81]), we will give a quick overview of the steps that routinely allow us to create 2D degenerate Bose gases.

2.1 PRODUCTION OF 2D UNIFORM GASES

2.1.1 *Electronic structure of ^{87}Rb*

Rubidium is an alkali atom, and as such only has one electron on the outermost shell. Its transitions are easy to access with commercial lasers; it is one of the most used atoms in the community. The low-energy electronic structure of ^{87}Rb is summarised in Fig. 2.1. In brief, the ground state of ^{87}Rb is $^2S_{1/2}$ and its first excited state has two fine levels: $^2P_{1/2}$ (corresponding to the so called D1 line), and $^2P_{3/2}$ (corresponding to the D2 line). Each of these states has in turn a hyperfine structure due to the coupling between the nucleus' spin and the electron's total angular momentum. The transition that we use for the cooling procedure and the imaging scheme is the $^2S_{1/2} \rightarrow {}^2P_{3/2}$ one. During the sequence, the atoms are usually prepared in the $|F = 1, m_F = 0\rangle$ state, and evolve in the $|F = 1, 2\rangle$ ground-state manifolds. These levels are also subdivided into different Zeeman states, whose exact energies depend on the ambient magnetic field. A magnetic field of about 1 G is kept at all times in order to lift the degeneracy between different Zeeman states. In the following, if not stated otherwise, we always note $|n, m\rangle$ the state $|F = n, m_F = m\rangle$.

2.1.2 *Reaching 3D condensation*

We need about 25 s to obtain a 3D BEC, and since we absorption image it (and hence destroy it), we need to run the following sequence and recreate a BEC for each point we take. To obtain one, we follow a standard procedure.

The sequence starts with a commercial 2D MOT with which we cool atoms loaded from an oven in two directions. A push beam, resonant with the D2 line and orthogonal to the cooling directions then pushes the atoms to the main science cell, about 30 cm away.

About 1×10^9 atoms are loaded from the 2D MOT to a 3D MOT at about 250 μK. The compression of the 3D MOT, followed by a molasses stage, leaves us with 6×10^8 atoms at around 15 μK. At this stage, our atoms have been optically pumped into the $F = 1$ state.

The atoms are then loaded into a quadrupole trap and evaporatively cooled by an RF ramp down to 2.5 MHz. As only atoms in $|1, -1\rangle$ are trapped in the quadrupole, we lose two thirds of the atoms during the loading stage. At the end of the evaporation, we have approximately 2.5×10^7 atoms at 20 μK.

Finally, the atoms are transferred into a far-red detuned (attractive) optical dipole trap located 50 μm below the zero of the quadrupole. This trap is produced by two lasers at 1064 nm. The power in each arm at the level of the atoms is of about 3 W, with waists of 30 and 90 μm along the vertical and horizontal direction. This anisotropy will help us load the atoms into 2D during the next section. While the power is ramped down, we further evaporate the cloud. At this

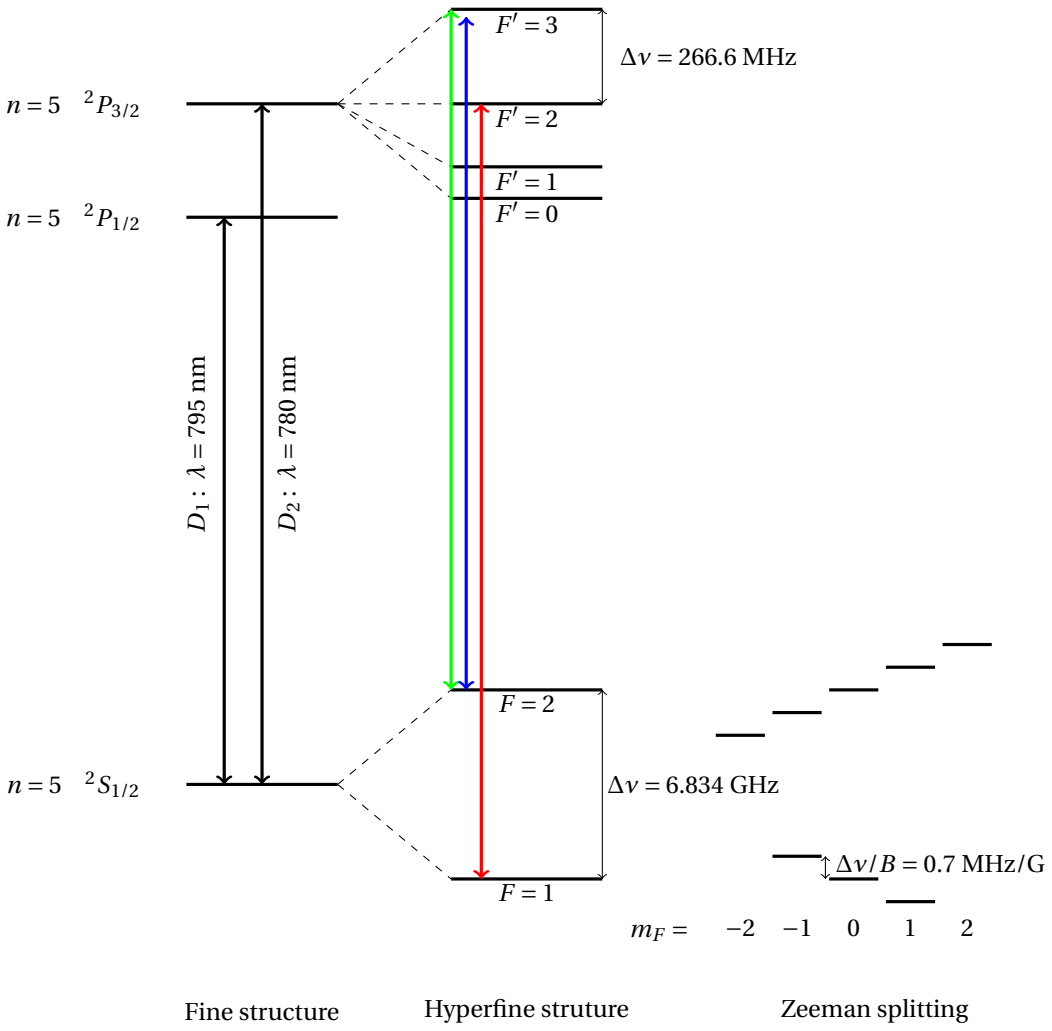

Figure 2.1: Electrical level of ^{87}Rb. We work with the D2 line. The cooling transition is indicated in blue and the imaging one in green. We also have a repumper beam depicted in red.

point, we have obtained an almost pure 3D BEC of typically 3×10^5 atoms at about 200 nK. A magnetic field of 1 G maintains the $|1, -1\rangle$ polarisation.

2.1.3 *Going to 2D*

In order to reach a 2D regime, we need to compress the gas to a point where transverse degrees of freedom are frozen out. This is realised by adding an optical trap in order to create a strong vertical confinement. It can be done, for instance, by using a Hermite-Gaussian TEM_{01} beam and using the minimum of intensity in the beam profile to trap the atoms ([98]). Another method makes use of a lattice; the atoms are then trapped between its fringes. However, if the lattice's spacing is too small (which is the case for an usual lattice), the atomic cloud can end up being loaded on several fringes, and split into distinct clouds. In order to avoid that, we use an accordion, $i.e.$ a lattice whose interfringe is adjustable and can go up to several μm. The interfringe is then decreased after loading the cloud.

In order to implement this accordion, we follow a scheme initially proposed in [99]. Other similar approaches have been implemented in [100] and [101]. We separate a single 532 nm beam into two parallel beams that are later recombined with a small angle and interfere. The light is blue-detuned, which means that the optical field will act as a repulsive potential. The lattice spacing can be tuned by changing the angle between the two interfering beams. In practice, this is done thanks to a motorised translation stage: the initial beam passes through two cubes that separate it on two paths (see Fig. 2.2a). The position at which the beam enters the first cube determines the distance between the two paths after the cubes. As these two paths then pass through a lens, this distance determines the angle of interference, and thus the lattice spacing. The relative phase between the two beams, which determines the absolute position of the fringes, is controlled by a piezoelectric stack glued on the mirror reflecting the top beam. We can this way load and then compress the gas into one fringe of the accordion. The apparatus is presented in more details in [46].

Strictly speaking, the potential created by the accordion is sinusoidal. However, if the lattice is deep enough, we can approximate its minimum by a parabola, and atoms will mostly experience a harmonic potential of frequency:

$$\omega_z = \sqrt{\frac{2\pi^2 U}{m d^2}}, \tag{2.1}$$

where U is the maximum height of the lattice, m is the atomic mass, and d is the lattice's interfringe. When compressing the accordion, d decreases from 11 μm to 2 μm, and ω_z increases from 0.7 to 4 kHz, for a power of 0.75 W. As the relevant thermal ($k_B T$) and interaction energy scales (E_{int}) are smaller than the vertical confinement frequency $\hbar\omega_z$, the only state of the vertical potential that the atoms can reach is the lowest one. The vertical direction is frozen out and the system is effectively 2D.

2.1.4 *Tailoring uniform potentials*

Finally, we want to create a uniform in-plane trapping potential. For this purpose, we use a Digital Micro-mirror Device (DMD, Vialux DLP7000) consisting of an array of 1024×784 square mirrors whose orientations can be set in two states: either reflecting light towards the atomic cloud, or not. The same 532 nm laser[1] used for the accordion is used for sending some light (typically 0.7 W) on the DMD, which then propagates vertically to the atoms. We use the DMD in direct imaging: the pattern displayed on the DMD is directly imaged on the atomic plane, and the DMD only modulates the amplitude of the light. The image of the DMD on the atoms is done with a microscope objective of numerical aperture NA = 0.45, which enables us

1 We use AOMs in order to shift the beams frequencies to avoid interferences.

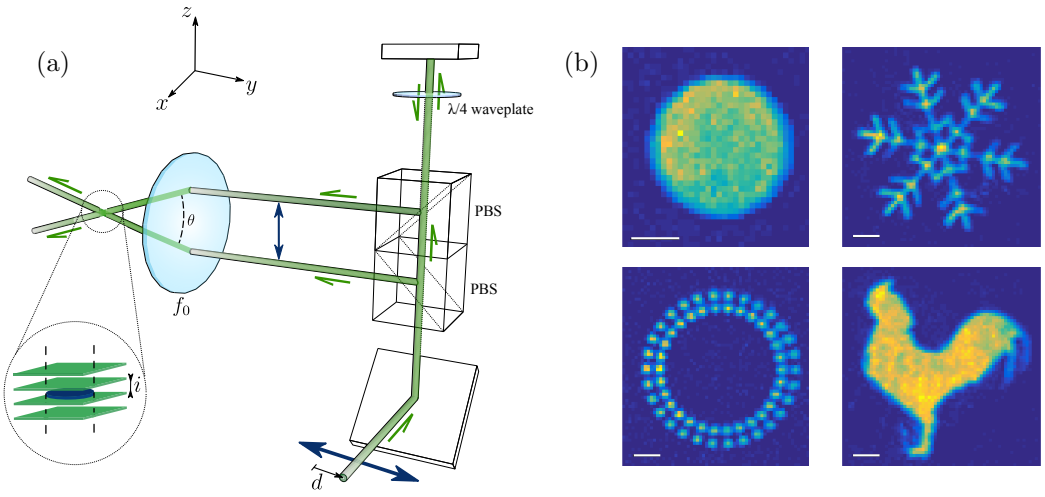

Figure 2.2: Left: optical accordion: by changing the impact position on the bottom right mirror, we can vary the interfringe from 11 μm to 2 μm. Figure taken from [76]. Right: absorption images of clouds for different boxes created by our DMD. The white lines represent 10 μm.

to reach optical resolutions of the order of the μm. This image creates the vertical repulsive walls of the box we trap our gas in. In total, we have 3 DMDs that we label:

- DMD1, the one used in this section to tailor box potentials,
- DMD2, also working at 532 nm and with around 0.2 W; we use it to add additional potentials on the atoms, for thermometry (see section 2.2.1) or for homogeneity corrections (chapter 3) for instance,
- DMD3, working with light between the D1 and D2 transition. We use it for Raman transitions in order to locally and coherently transfer atoms from $|1,0\rangle$ to $|2,0\rangle$.

There is a 1/70 magnification between the DMD and the atoms. One pixel of the DMD being 13.7 μm, this represents about 0.2 μm on the atoms, well below our imaging resolution of typically $\sim$ 1 μm. This means that pixellation effects on the atoms are negligible. Moreover, since we can independently chose the state of each mirror, we can basically draw any box we want, as long as this box is made out of 0 and 1. This is later referred to as our 'green box': the potential experienced by the cloud is flat inside the box (corresponding to the 0s of the DMD), and most of the atoms are too cold to reach the region of high potential created by the 1s of the DMD: the border between the two regions thus acts like a hard wall. Some examples are shown in Fig. 2.2b. A protocol for drawing more complex shapes will be discussed in chapter 3.

2.1.5 *Reaching 2D degeneracy*

Once the gas is loaded into the green box, two successive MW pulses transfer the atoms from $|1,-1\rangle$ to $|2,0\rangle$ and then to $|1,0\rangle$, in which we conduct most of the experiments that we do: it is magnetic insensitive, which means that we can ignore magnetic gradients acting on the atoms, and has a longer lifetime than $|2,0\rangle$ (tens of ms scale versus second scale). A detailed procedure for going from state to state is given in section 2.1.6.

The power of the green beams is then decreased to further evaporate the cloud. At this stage, we have a degenerate gas of about 1×10^5 atoms at 50 nK trapped in a 40×40 μm^2 box ($n_{2D} \simeq 70 \times 10^{12}$ m^{-2}). This corresponds to a PSD of about 50, well above the critical PSD of the BKT transition introduced in chapter 1 ($\mathcal{D}_c = 7.8$).

We can vary degeneracy and density by changing the evaporation level in the green box. A complementary possible procedure is to 'blast', *i.e.* remove some atoms. This is done by

transferring a certain fraction from $|1,0\rangle$ to $|2,0\rangle$ with a MW pulse, and then flashing the imager beam. The $|2,0\rangle$ atoms, which are resonant with the light, acquire a momentum due to the absorption of several photons, and get kicked out of the trap. We then let the remaining fraction thermalise for typically 0.5 s.

2.1.6 *Juggling between hyperfine states: MW transfer*

2.1.6.1 *When we need to perform two transitions*

In order to create a 2D degenerate gas, we need to be able to freely transfer atoms from one internal state to the other. The internal states that we manipulate are usually the $|1,0\rangle$, $|2,0\rangle$, and $|1,-1\rangle$ states. We present here the setup that allows us to juggle between these three states.

We use a MW antenna close to the atoms to perform these transitions. The output of a 6.8 GHz source (Nexyn NXPLOS 0680-02778) is mixed by an I-Q mixer (Pulsar IMOH 03-458) with a ~ 34 MHz signal coming from a function generator (Rigol DG4162). The signal generator sends two components in quadrature, so that only one sideband is produced. The resulting ~ 6.834 GHz signal is then amplified by a 10 W amplifier (Kuhne PA 7000) and sent to the antenna.

We usually perform at least two different MW transitions, and hence need several signals with different frequencies around 34 MHz. In practice, we use two generators to drive independently the two transitions $|1,-1\rangle \rightarrow |2,0\rangle$ (frequency f_1) and $|2,0\rangle \rightarrow |1,0\rangle$ (frequency f_2): the aforementioned Rigol (DG4162), and a Tektronix (AFG3052 2C). The instructions about the frequency, amplitude, and other such parameters of the signal we want to deliver are sent to the generators at the beginning of our sequence. At this moment, Cicero[2], the software that we use to control the experiment, sends the relevant information via a virtual RS232 port to a small Python script. As Cicero does not support USB communication, a virtual port was needed. This port is created with a program called com0com[3]. The python script then communicates with the generators via an USB cable, and the generators start delivering the signal. Finally, RF switches placed between the generators and the amplifier wait for a trigger, given later by Cicero, to irradiate the atoms with the MW. A scheme of this MW chain is presented in Fig. 2.3a.

2.1.6.2 *When we need to perform four transitions*

We often use more than these two frequencies. At one point of the sequence, the magnetic fields have to be changed to the final values needed for imaging, and this change is usually done during the evaporation of atoms in $|1,0\rangle$. In some experiments, we need a magnetic sensitive state (see section 2.2.3 for instance), which means that we have to transfer atoms back to $|1,-1\rangle$ after evaporation. However, as the magnetic fields have changed, f_1 and f_2 cannot perform the transitions back to $|1,-1\rangle$, and we cannot change them as we only communicate with the generators at the beginning of the sequence. To solve this problem, we use the sweep function of the generators which change f_1 into f_1' and f_2 into f_2'. Since the second transition only feels a quadratic Zeeman shift, we have $|f_2' - f_2| \ll |f_1' - f_1|$. In the case where we want to go back to $|1,-1\rangle$, let us note $t_i^{(\prime)}$ the irradiation times associated to $f_i^{(\prime)}$ and corresponding to $\pi-$pulses. We thus have 4 frequencies to deliver with 2 generators. The scheme is the following one, and is represented in Fig. 2.3b.

- Communication is done with the generators when the sequence starts. All relevant information about the next steps ($f_1,\ f_2,\ f_1',\ f_2'$, for instance) is given now. We start in state $|1,-1\rangle$. In our example, the Rigol generator operates the first and fourth transition, while the Tektronix generator operates the second and third ones.

2 A free software for atomic physics experiments, see http://akeshet.github.io/Cicero-Word-Generator/.
3 A free virtual port emulator, see http://com0com.sourceforge.net/.

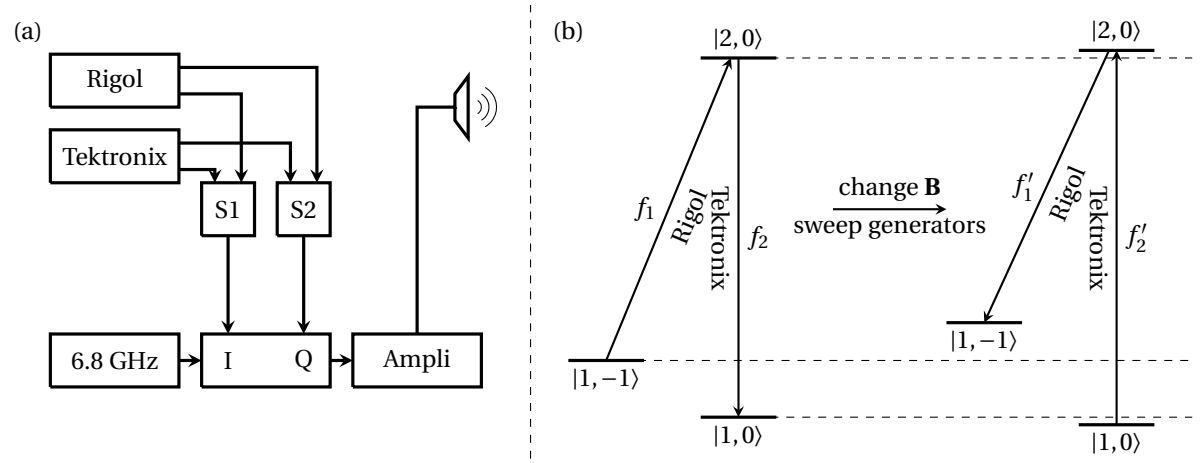

Figure 2.3: Left: scheme of the MW chain: each generator delivers two signals in quadrature that are mixed by an IQ mixer. Two switches S1 and S2 let either one or the other generator access to the IQ mixer. This is mixed with a 6.8 GHz source in order to create a signal at $\sim$ 6.834 GHz, which is then amplified and sent to the atoms. Right: scheme to perform 4 transitions: we first operate f_1 with Rigol and f_2 with Tektronix in order to arrive to $|1, 0\rangle$. The two generators are then swept to the new relevant frequencies f_1' and f_2' while the magnetic fields are changed to their final values. Then, Tektronix transfers atoms back to $|2, 0\rangle$ and Rigol transfers them back to $|1, -1\rangle$.

- A first trigger is sent to the generators, which makes them deliver sinusoidal signals at frequency f_1 and f_2. Two additional switches after each generators prevent the atoms from being irradiated by the MW.
- The switches open the Rigol channel for a time t_1 in order to realise a $\pi-$pulse, and then switch it back off. The atoms are now in state $|2, 0\rangle$. They then open the Tektronix channel for a time t_2 to transfer atoms to $|1, 0\rangle$ with a $\pi-$pulse.
- A second trigger instructs the generators to sweep to frequencies f_1' and f_2'. We have found that the minimal sweeping time is 5 ms. Below this time, the generators may not have the necessary time to sweep, and the next step will not work. We also vary the magnetic fields to their final values.
- Now that the outputs are sinusoidal signals at f_1' and f_2', we open the Tektronix channel for a time t_2' to transfer atoms back to $|2, 0\rangle$ with a $\pi-$pulse. The Rigol channel is then open for a time t_1' to transfer them back to $|1, -1\rangle$ with a $\pi-$pulse.

2.1.6.3 *When we need to perform more than four transitions*

In cases where we need to operate more transitions than we have available, the trick is to add a magnetic field in order to bring the magnetic sensitive state on resonance with one of the frequencies already used. To do this, we have several pairs of coils at our disposal. Some of these coils are used for cooling stages, some in order to create additional biases. We have:

- a pair of anti-Helmholtz coils that produce a gradient of 22 G/cm in plane; it is used for the MOT stage,
- a pair of anti-Helmholtz coils that produce a gradient of 240 G/cm in the vertical directions; it is used for our quadrupole trap,
- three pairs of Helmholtz coils along the three directions of space that produce biases of a few G, typically used for polarisation maintaining and/or MW transfer, as previously described.

This trick allows us to manipulate the internal state of atoms from the typical state we trap our atoms in initially ($|1,-1\rangle$) to non-magnetic sensitive states ($|1,0\rangle$, $|2,0\rangle$). Again, other states than these 3 are seldom used.

2.1.7 *Juggling between hyperfine states: Raman transfer - intensity lock*

As the radiation used in the MW scheme and described in the previous section has a centimetric wavelength far larger than the sample's size, it can only perform uniform transfers. This can be a limitation for some of the experiments we want to conduct. For instance, the demixing experiments discussed in Chapters 6 and 7 use protocols involving localised transfers. To implement this, Raman beams coherently transferring atoms from $|1,0\rangle$ to $|2,0\rangle$ were installed during my PhD. This setup has been covered extensively in [81]; let us simply say that a laser beam is split in two, each path being slightly detuned by an AOM (one arm also has an EOM). The total detuning is equal to the $|1,0\rangle \rightarrow |2,0\rangle$ transition frequency, which enables us to transfer atoms from one state to the other. Moreover, this scheme also performs a momentum transfer, which we can vary over a large range of momenta. This includes no momentum transfer at all, which will be the case throughout this thesis. In order to locally address the transition, the two beams are shone upon a DMD to spatially modulate the light, and the tailored profile is then sent onto the atoms.

Initially, the Raman beams' intensities were not locked. This proved to be an issue as the Raman π pulse was slowly drifting. In order to solve this problem, we decided to compensate for the fluctuations of the beams' powers using an mbed NXP LPC1768 (a programmable microcontroller), acting as a PID. The idea is not exactly to lock the beams' powers, but rather to counteract the long-time drifts typically caused by temperature changes along the day.

To do so, we added two control photodiodes (one on each arm of the Raman setup), which created the input signal of the loop, while the PID output was sent to the AOMs' drivers. For the loop's set point, a simple DC power supply was used. Each AOM has an individual downstream shutter, which acts as an extra security measure to prevent light from going to the atoms when the AOM's TTL is off. These shutters open 15 ms before the AOM switches on, and close immediately after it has been switched off.

As the duration of the Raman pulse is typically in the 10 μs range , while an mbed is a discrete system operating at a 50 μs cycle, an mbed acting as a conventional PID would not work as the available bandwidth for locking the beams would be too small. In order to circumvent this problem, we chose to lock the Raman power during a 5 ms window, 15 ms before actually sending light on the atoms. Figure 2.4 shows a sketch of the locking scheme that we use. The sequence is the following one:

- Initial state: no light anywhere. The AOMs' TTLs and the shutters' TTLs are off.
- Locking stage: light on the photodiodes in order to lock, but no light on the atoms. The AOM's TTL switches on during 5 ms. We lock the two beams independently with two mbeds.
- Memory stage: no light anywhere. The AOM's TTL switches back off, and the shutter's TTL switches on for 15 ms. The mbeds remember the last output $e_{1,2}$ they had to deliver at the end of the locking stage.
- Raman stage: light on the atoms. The AOM's TTL gets back to the on position and light is diffracted on the atoms for t_{Raman}. As the time lapse between the locking stage and the Raman stage is relatively short (15 ms), we can expect $e_{1,2}$ to still be relevant, and the voltages measured on the photodiodes to still be very close to the target.

Indeed, we find that this method works very well. Fig. 2.4 shows the drift over 90 minutes (locked beams) and 10 hours (unlocked beams) of the values measured by the photodiodes

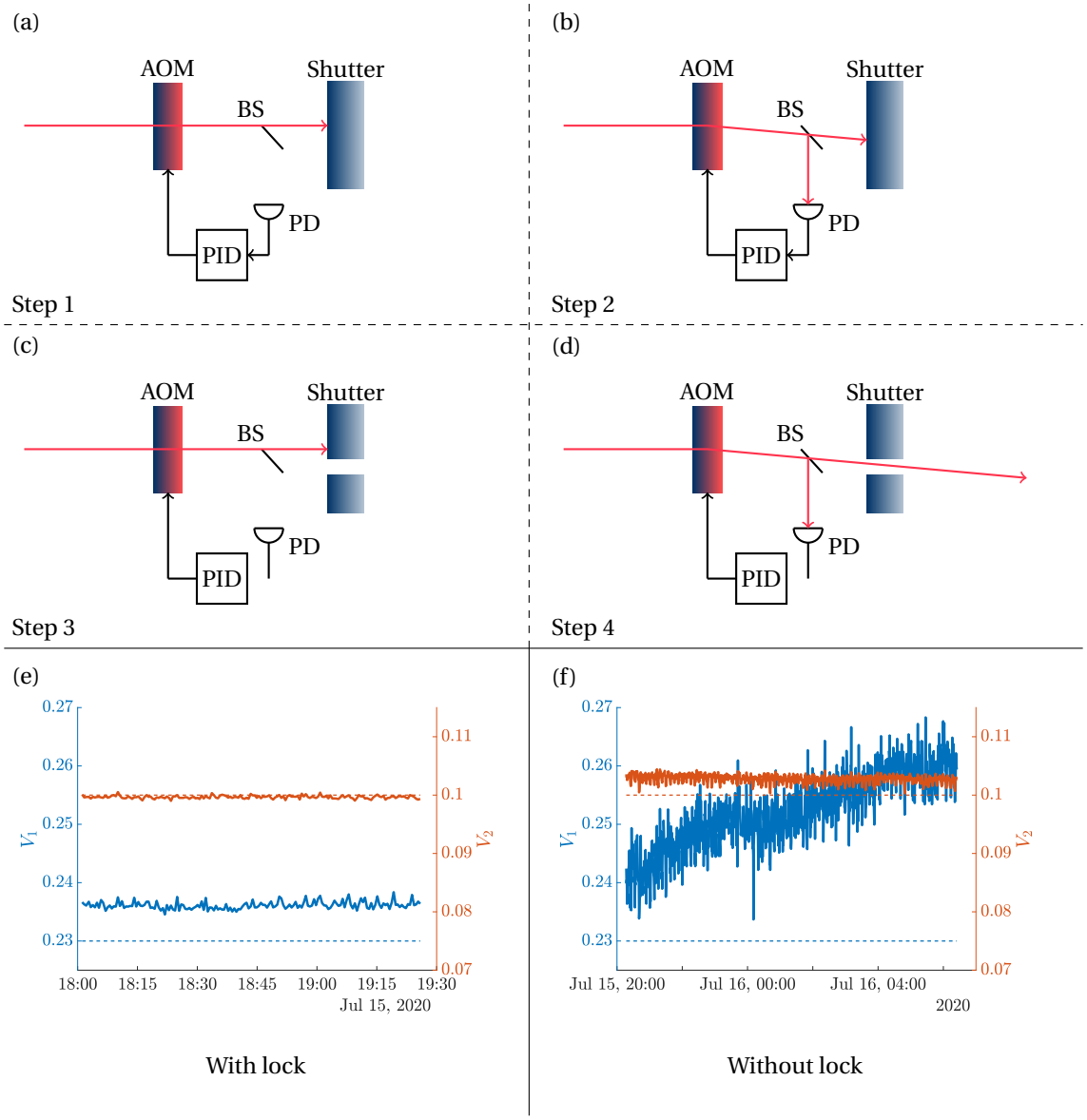

Figure 2.4: Top and middle: scheme of the intensity lock (a-d); for clarity, only 1 AOM is shown, but the scheme presented here is duplicated for the second AOM. At first, the AOM does not diffract and the shutter is closed (a). We make the AOM diffract during 5 ms during which we lock the intensity with a PID (b). At the end of this step, the output of the PID is frozen, and new information is not corrected. The AOM is then switched off while we take 15 ms to open the sutter (c). The AOM is then switched on for a time t_{Raman} and light goes to the atoms. Bottom (e-f): effect of the locking on the beams' intensities. Photodiode traces taken with lock for 90 minutes (e) and without lock for 10 hours (f). The set points are represented in dashed lines. We observe a clear improvement with the lock.

with and without the loop. Without correction, we observe a typical amplitude of fluctuation of 7 % for the first channel, and 2% for the second one, while these values are decreased to 0.8% with the lock. There is small constant shift between the set point (dashed line) and the trace, but as long as this shift remains constant (it does), it should not prove to be a problem.

2.2 MEASUREMENT OF THE GAS' PROPERTIES

2.2.1 *Measurement of the phase space density*

We have seen in the previous section that we could freely vary the degeneracy of our gas. We now want to measure how degenerate it is. The old Rubidium experiment used to create harmonically trapped 2D Bose gases, and measured their PSD by fitting the wings of the distribution in an in situ image. This of course, is not possible for uniform samples.

The typical way of measuring temperatures in 3D cold atoms experiments is to release the cloud from all trapping potentials and try to fit the wings of the thermal distribution after a time of flight. For condensed samples, one has to separate the condensed and the thermal part. It is then a good approximation to fix the chemical potential μ to 0: the shape of the saturated Bose function, used to fit the wings, depends thus only on T.

However, there is no saturation of the Bose function in 2D, which means that the shape of the wings will depend on both T and μ. Moreover, the size of our condensates is usually quite big, which requires longer TOF (and gives lower signals) than for harmonically trapped samples, where typical cloud sizes are smaller. These issues typically yield unreliable results.

However, other protocols are possible. Our group uses a method inspired by [102]. The idea is to add an extra potential of variable height with which we press on a small area of the cloud. The response of the atoms to this potential, or in other words, the OD[4] of this dip, gives us information on the degeneracy of the cloud. All that leaves to be done is to find a relation between the dip OD, which is related to the phase space density $\mathcal{D}$, and the extra potential, which is related to the chemical potential μ via the local density approximation. In other terms, we have to find a way to express the gas' equation of state.

As discussed in the previous chapter, there are two regimes ($\mathcal{D} \gg 1$ and $\mathcal{D} \ll 1$) in which the equation of state is known analytically, but there is no analytical expression of the full equation of state. There are, however, Monte-Carlo simulations ([40]) from which we can interpolate it. We can, from these points, construct a fitting function f that we use on our data.

Experimentally, we trap our atoms in a square of side 40 μm with DMD1 and add an extra potential V with DMD2 on a small disk of radius 5 μm. This size was chosen to be big enough to have signal, but to be small enough so that the perturbation remains negligible on the scale of the cloud. The local density approximation states that on this small zone, $\mu_{\text{loc}} = \mu_0 - V$. We separately calibrated the relationship between μ and the power of DMD2, which is common to all PSD measurements. We then plot the density n of the dip as a function of μ, and find the best rescaling parameter T so that $\mathcal{D} = nh^2/2\pi m k_B T$ as a function of $\beta\mu = \mu/k_B T$ is best fitted by f. A typical example of this procedure is given in Fig. 2.5. Importantly, we have seen in the previous chapter that because our system is scale invariant, $\mathcal{D}$ depends only on $\mu/k_B T$ and not on μ and T independently. It thus seems counter intuitive to extract T and not T/T_c, and this is possible only because we have previously calibrated μ.

Moreover, while both T and T_c depend on the atom number calibration, T/T_c does not, which makes its determination more reliable than the one of T. As the system is scale invariant, the PSD is only determined by T/T_c, and in most cases, so is the physics. When a measure of T is needed, however, it is important to have an exact calibration of the atomic density. This point is the topic of section 2.2.3.

4 See eq. 2.2 for a definition of the optical density.

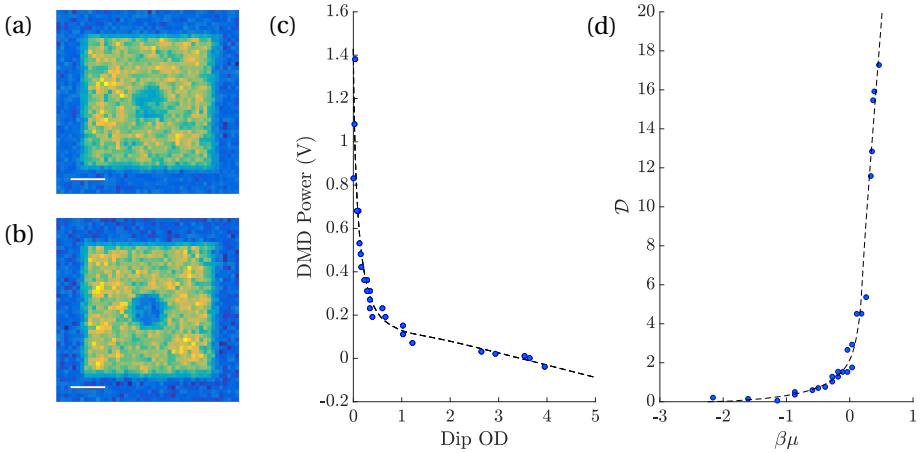

Figure 2.5: Left: absorption images of the cloud. At high DMD2 power (b), the dip created by the extra excitation is almost totally depleted, which is not the case at lower DMD2 power (a). The white line represents 10 μm. Middle: example of the fitting procedure (black dotted line) described above. For this example, we find $T/T_c = 0.43$ and $T = 125$ nK. Right: Same thing but the axis OD and DMD Power have been converted to $\mathcal{D}$ and $\beta\mu$, respectively.

2.2.2 *Imaging the atoms*

Imaging is done via an absorption imaging process. The imager beam is resonant with the $F = 2 \rightarrow F' = 3$ transition and collectively addresses all Zeeman states in $F = 2$. We usually image the atoms along two directions: the horizontal one (with a Pixelfly (pco.pixelfly usb)), and the vertical one (with a Princeton (Pixis 1024)). Typical absorption images are shown in Fig. 2.6.

According to the Beer-Lambert law, I/I_0 decreases exponentially with the thickness of the cloud. More precisely, accounting for the background intensity and defining the optical density OD, we have:

$$\mathrm{OD} \triangleq -\ln\left(\frac{I - I_{\mathrm{bgd}}}{I_0 - I_{\mathrm{bgd}}}\right) = \int \sigma n_{3\mathrm{D}}\,\mathrm{d}z = \sigma n_{2\mathrm{D}} \tag{2.2}$$

where we have defined the scattering cross section σ.

It is important to note that one of the hypothesis of Beer-Lambert's law is that the number of scattered photons per atom is proportional to I. This approximation is valid if I remains very low compared to the saturation intensity $I_{\mathrm{sat}} = \frac{\hbar\omega\Gamma}{2\sigma_0}$, where $\omega = 2\pi c/\lambda$, c is the speed of light, and Γ is the width of the excited level. This means that in order to trust the measured atom number, we need to always have $I \ll I_{\mathrm{sat}}$. Experimentally, we always use $I < 0.2 I_{\mathrm{sat}}$. Moreover, we also place ourselves in the regime where $\mathrm{OD} \lesssim 1$, otherwise, the light field might excite collective excitations of the gas, which can lead to a wrong result ([103],[104]). To abide by this condition, only some atoms are transferred from $|1, 0\rangle$ (invisible state) to $|2, 0\rangle$ (visible state) and imaged in order to avoid saturation.

The exact value of σ depends on a lot of factors: the polarisation of the imaging beam, the transitions involved, the magnetic fields present during the imaging step, and the detuning of the imaging beam. On resonance, we theoretically have $\sigma = \frac{7}{15}\frac{3\lambda^2}{2\pi}$, where the factor $7/15$ is an average of the Clebsch-Gordon coefficients for the transitions involved, and λ is the imaging wavelength. However, absorption images do not usually give accurate measurements of atom number, and previous independent measurements ([77], [43]) have shown that an extra 'fudge factor' $\mathcal{F}$ had to be added. We define it by $n_{\mathrm{real}} = \mathcal{F} n_{\mathrm{obs}}$ and usually have $\mathcal{F} \simeq 1.5$. The calibration of $\mathcal{F}$ is the topic of the next section.

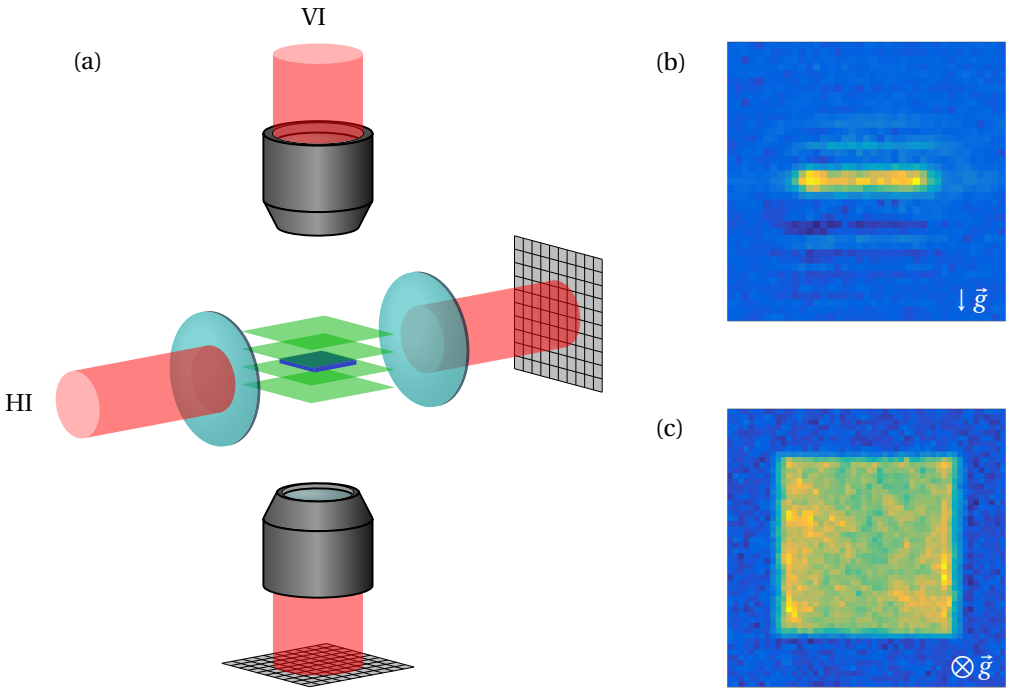

Figure 2.6: Imaging setup (a). HI stands for horizontal imaging (and gives image (b)), VI for vertical imaging (corresponding to (c)). The two microscope objectives are depicted in black, the accordion is depicted in green, and the atomic cloud is shown as a blue pancake.

2.2.3 *Calibration of the fudge factor*

The exact atom number calibration in cold atom experiments is usually complex, and people often introduce fudge factors in order to match absorption theory and experimental results. Typically, in our setup, this fudge factor mostly depends on magnetic fields present during imaging. Different sequences require different kinds of state manipulations, which in turn leads to different magnetic fields during the imaging procedure.

Our calibration is based on two results. The first one is the fact that for a 2D weakly-interacting Bose gas in a harmonic potential of pulsation ω, one has:

$$\ddot{E}_p = 2\omega^2 \left(E_k + E_i - E_p\right) \Rightarrow E_p(t) = \frac{E}{2} + \Delta E \cos(2\omega t) \tag{2.3}$$

where we have introduced E_p, E_k, E_i, and E, the respectively potential, kinetic, interaction, and total energies, and where $\Delta E = (E_p(0) - E_k(0) - E_i(0))/2$. This remarkable result is a consequence of the SO(2,1) symmetry of this particular system, and has been treated in more details in [81] and [43]. This means, of course, that the potential energy of the system is periodic. However, for certain specific initial clouds, not only is $E_p(t)$ periodic, but $\psi(\mathbf{r}, t)$ also has non trivial properties. In the case where the gas initially occupies an equilateral homogeneous triangle, for instance, the triangle reforms perfectly into another equilateral triangle at times $\ell T/4,\ \ell \in \mathbb{N}$, where $T = 2\pi/\omega$. For even ℓ, we regain the initial triangle. For odd ℓ, the triangle is inverted, and its size depends on $\tilde{g}N$, where N is the number of atoms in the triangle and $\tilde{g}$ the interaction parameter of the gas. This is the second result that we use for our calibration.

If we assume that the gas is in the Thomas-Fermi regime (meaning $E_i \gg E_k$), we have at $t = T/4$:

$$E_p(T/4) = \frac{E}{2} - \Delta E \simeq E_i(0). \tag{2.4}$$

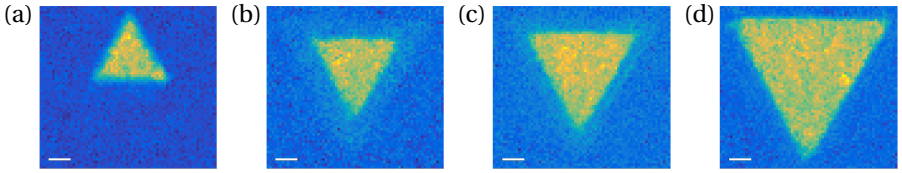

Figure 2.7: An equilateral triangle (a) gets transformed into another, inverted, scaled triangle (b), (c), (d) after a quarter of oscillation in a harmonic trap. The size of the inverted triangle depends on the initial triangle's parameter $\sqrt{\tilde{g}N}$. Here $\sqrt{\tilde{g}N} = 75.1$ (a) and (d), 45.6 (b) and 53.6 (c). The white line represents 10 μm.

Knowing that we start in a homogeneously filled equilateral triangle T of side L_i, and noting the side of the triangle we end up in L_f, we can then write:

$$\begin{cases} E_i(0) = \dfrac{\hbar}{2m}\tilde{g}\displaystyle\int_T |\psi|^4 \,\mathrm{d}^2 r = \dfrac{2}{\sqrt{3}}\dfrac{\hbar^2\tilde{g}}{mL_i^2}N^2 \\ E_p(T/4) = \displaystyle\int_T V(\mathbf{r})|\psi|^2 \,\mathrm{d}^2 r = \dfrac{1}{24}m\omega^2 L_f^2 N \end{cases} \Rightarrow \quad N = \frac{\sqrt{3}}{48}\frac{m^2\omega^2}{\hbar^2\tilde{g}}L_i^2 L_f^2. \tag{2.5}$$

This atom number only depends on parameters $(\omega,\ \tilde{g},\ L_{i,f})$ which we can access independently and with a good accuracy. In our case, the harmonic confinement is performed by the quadrupole trap whose zero is shifted by $z_0 \simeq 0.5$ mm along the vertical direction z. If we remain at distances r from the vertical axis such that $r \ll z_0$, the trapping potential is indeed harmonic:

$$V(x,y) = -g_F\mu_B|\mathbf{B}(x,y)| \simeq \frac{\mu_B b_0 z_0}{2} + \frac{\mu_B b_0}{16 z_0}r^2 = V_0 + \frac{1}{2}m\omega^2 r^2, \tag{2.6}$$

where we have introduced the Landé factor g_F, Bohr's magneton μ_B and the vertical gradient b_0 created by the quadrupole at the level of the coils' axis. In order to measure ω precisely, we place a small cloud of atoms close to the centre of the trap and monitor its evolution. Often, frequencies in both directions differ by a few Hz (out of typically 20 Hz). We correct this anisotropy by adding a small gradient with the MOT coils.

The interaction parameter $\tilde{g}$ is measured via parametric heating. We modulate the power of the accordion at a certain frequency. We then monitor the total number of atoms: when the modulation frequency f reaches two times the frequency of the vertical trapping f_z, we observe a dramatic loss of atoms. This way, we can calibrate the trapping frequency for different accordion powers, an deduce $\tilde{g} = 4\pi a\sqrt{\frac{mf_z}{\hbar}}$, with a being the scattering length.

Finally, L is measured directly on the absorption images by integrating the OD along one direction and fitting it with a line. The magnification between the atomic plane and the camera plane M_2 is calibrated by first loading the atoms in a lattice created by the DMD: this gives $M_1 \times M_2$, where M_1 is the magnification between the DMD plane and the atomic plane. Then, we compare this result with a measurement of an atomic TOF after a lattice has been flashed on the atoms: this Bragg diffraction experiment gives M_2/M_1. This point is treated in more details in [76].

In order to actually calibrate the fudge factor, we need magnetic sensitive states that can experience the magnetic harmonic confinement. Atoms in states $F = 2$ have a shorter lifetime than those in $F = 1$, so we chose the state $|1,-1\rangle$. Then, the exact procedure reads as follows.

- Following the scheme explained in section 2.1.6, we start with atoms in $|1,0\rangle$.
- We remove a variable amount of atoms and we let the remaining fraction thermalise for typically 0.5 s.

- During this time, the magnetic fields are changed to the particular parameters used for the cloud's dynamics.
- We transfer the atoms back to $|1, -1\rangle$.
- The green box is switched off and atoms can evolve in the harmonic potential. The vertical confinement remains on, but we usually decrease its strength in order to minimise defects created by the accordion.
- After a quarter of oscillation, we repump the atoms to $|2, 0\rangle$ and absorption image them. We typically take 5-10 images for each value of the atomic density.

When this is done for the chosen magnetic fields, we can multiply by a fudge factor $\mathscr{F}$ the observed atom number N^{obs}. Doing the same experiment with different magnetic fields might yield a different N^{obs}, and can simply perform a rule of three to compute the total fudge factor.

CONCLUSION

In conclusion, we have explained how we go from a 3D thermal gas of ^{87}Rb to a 2D uniform degenerate sample. The internal state of the atoms is controlled with MW transitions, and the shape of the cloud itself is chosen at whim thanks to the DMD creating the box walls. The cloud's phase space density is measured thanks to the addition of an extra potential that lets us travel on the gas' equation of state, and we use a method based on the dynamical symmetries of the harmonically trapped 2D Bose gas to calibrate the atomic number of our system.

Of course, using a DMD for designing the trap has limitations: we can only create potentials tailored with 0 and 1, and we can suffer from homogeneity defects, especially at low atomic density. However, the next chapter is devoted to overcoming these issues.

3

CONTROLLING THE 2D ATOMIC DENSITY

Historically, harmonic confinements have been the norm in most cold atom experiments due to their ease of implementation. In this case, the BEC phase transition is a local phase transition, and the condensate fraction will emerge where the density peaks, $i.e.$ at the centre of the trap. This makes measurement of certain BEC features, for instance phase coherence between two points, harder and less reliable. With the advent of new uniform trapping methods, experiments in flat potentials were made possible without having to resort to only probing small portions of the cloud or using the local density approximation ([105]). An example of one such method is the use of an axicon to create a hollow tube of light, which creates cylindrical walls for the atoms. Two more planes of light have then to be added to create a 3D uniform cylindrical box ([44]).

Another method consists in using Spatial Light Modulators, or SLMs, instead of an axicon ([45, 106]). Liquid crystals (LC) SLMs typically modulate the phase of a beam with a resolution depth of 8-12 bits, which is far superior than the 1 bit that a DMD can offer. However, they suffer from a very low (10-200 Hz) refresh rate, when a DMD can typically reach tens of kHz ([107]).

An SLM can be used as a phase or intensity modulator. An interesting feature of phase modulation is the ability to holographically correct unavoidable optical aberrations, which greatly improves the quality of the trapping ([108, 109])). For instance, in [109], authors have been able to reduce the aberrations from several λ to $\lambda/50$. Complex geometries of micro-traps ([110]) and arbitrary potential landscapes ([109]) have been created with this method. Both LC SLMs and DMD SLMs can be used for phase modulation, but the diffraction efficiency is dramatically lower for the second ones due to the inherent grating nature of DMDs that distribute power among several diffraction orders.

Our set-up, on the other hand, uses intensity modulation. Blue-detuned (repulsive) light is shone on a DMD whose pixels are set to deflect light in a certain region, thus creating a flat box potential. Nevertheless, as the DMD's pixels can only be set to 0 or 1, this method has limitations for tailoring more complex potentials.

In that regard, some teams make use of time-averaged potentials by periodically switching on and off pixels of different zones at different duty cycles [111]. If the main frequency is high compared to the other relevant frequency scales, the atoms will average the action of the potential and what is originally a discrete process will in effect be continuous. This is less relevant in 2D where one usually has a very high frequency trapping (several kHz) along one of the axis, invalidating this condition.

Some other teams use dithering algorithms ([112–114]) for the same purpose: the idea is to generate zones with different balances of 0 and 1 that locally average to zones with different tones of grey. This works if the effective size of the DMD pixels in the atomic plane is small enough so that the pixels are not resolved by the atoms; in this case, the potential is then averaged in space and not in time.

Alongside dithering, iterative methods are often implemented. For instance, in order to create an eighth-order super-Lorentzian flat-top beam, the algorithm used in [112] and [113] deterministically removes and adds pixels in regions of extremal intensity. By identifying at each step the regions containing the maximum and minimum of intensity, it retroacts on these regions by switching on and off pixels in order to flatten the general potential landscape. The protocol used in [115] is slightly different as it tries to retroact on all regions that differ from the

target, and not only on the most extremal ones. Finally, other algorithms consisting of random pixel changes also lead to interesting results, but need bigger computational power ([116]).

Precisely shaping the intensity of our beam is of great importance. One possible application is the ability to correct the homogeneity of our cloud. At low density, the gas is more sensitive to various optical defects present on the experiment, and the quality of the gas' homogeneity is worse. By retroacting on the light profile in order to have a very flat beam, we can circumvent this problem. Another possible application of precise beam shaping is the printing of a phase on the atoms. By flashing a potential U on the cloud, one transforms the wavefunction $\psi(x, y)$ into:

$$\psi'(x,t) = \psi(x,t) \times e^{iU(x,y)\tau/\hbar}, \tag{3.1}$$

where the flashing light τ is chosen small enough to prevent density excitations. By choosing a phase winding profile for U, one can hope to create a vortex ([117]). Finally, we could also use this beam shaping method in order to precisely control the shape of the zone that we transfer with the Raman DMD. We could, for instance, print a spin bubble with a solitonic shape and examine if its profile evolves with time.

We will first describe how our feedback works by presenting some general concepts about dithering and proportional-integral-derivative (PID) correction, and by introducing the notations that we use. We will then turn to simulations we made in order to better understand the operation of the loop and its limits. Finally, we will present the data that we took and discuss the limits of our system.

3.1 IMPLEMENTATION OF THE LOOP

Originally, we did not try to correct the homogeneity of the atomic cloud and only used DMD1 to create the box walls. This works very well at relatively high 2D densities ($n_{2D} \geqslant 50$ at/μm^2 typically) but imperfections and defects in the optical field tend to create inhomogeneities in the density distribution when decreasing n_{2D}. This is mostly believed to be caused by our vertical confinement: changing the power of the accordion beams dramatically affects the homogeneity of the gas.

In order to fix this issue, we have implemented a simple correction loop. We use DMD2 to add light on certain regions of the box in order to reach the desired landscape. For flat targets, this method compensates for optical defects by flattening high density regions, improving the homogeneity of the cloud. This protocol also allows us to create more arbitrary potentials (swimming pool bottoms, harmonic potential...), and corrects for defects that would appear in these landscapes.

We need two ingredients for this: a dithering algorithm, and a feedback loop. Theoretically, a loop is not a necessity: one could simply calculate what needs to be put on DMD2 to attain the target density. In real life, however, extra potentials created by optical fields (either intricate effects of coherent light like speckle, or defects due to imperfections of the beam) have to be precisely accounted for. The precise propagation of the dithered DMD plane on the atomic one is also hard to accurately calculate. Moreover, a one-step method assumes that a precise calibration of the DMD's effect on the atomic density has been performed. On the other hand, an iterative loop is easy to implement, and in the case of a PID loop, its parameters do not have to be chosen very precisely for the correction to work.

In our case, the dithering algorithm will be used to transform the image $\mathtt{s}_n$ outputted by the loop (with pixels continuously ranging from 0 to 1) to an image displayable on the DMD2 (with pixels being only 0 or 1). The feedback will correct the residual errors due to experimental defects and act on the pattern displayed on DMD2 so that the density distribution converges towards the chosen target.

3.1.1 *Dithering algorithm*

Dithering is a technique often used in image processing when one has to convert the colour palette of an image to a different, more limited one. The idea is to create the illusion of a colour depth by using the fact that the human eye groups neighbouring pixels together and interprets the local hue as an 'average' of the initial pixels. This way, one can simulate more colours than one actually has available. As our final image can only have black and white pixels, the dithered result will be referred as the 'grey level image' in the following.

Several type of ditherings exist. We will review three of the most used type of algorithms here.

A simple threshold operation is the easiest type of dithering one can imagine. Under this protocol, a pixel with value lower than the threshold is assigned to the value 0. In the other case, it is assigned to 1. The simplicity of this algorithm is counterbalanced by a big loss of contrast and contouring: for example, an underexposed (resp. overexposed) zone will be transformed into a black (resp. white) zone, resulting in detail loss.

Ordered dithering makes use of a 'dither matrix'. In this version, pixels remain independent from one another, and zones of the image are individually compared to a certain matrix. More precisely, a dithering matrix M of size n has to be defined. The original image A is divided into subzones A_p of size $n \times n$. These subzones are then compared to M: if $A_p(i,j) < M(i,j)$, the pixel (i,j) is assigned to value 0. Otherwise, it goes to 1. For instance, if we define:

$$M = \frac{1}{4}\begin{pmatrix} 0 & 2 \\ 3 & 1 \end{pmatrix}, \tag{3.2}$$

we will have to compare each 2×2 zone A_p of A to M, pixel by pixel. If $A_p(i,j) > M(i,j)$, then we put a 1 in position (i,j) of the dithered image; otherwise, we put a 0. This method is quicker to implement than other type of ditherings where one pixel influences its neighbours (like error diffusion, for instance), but it usually creates unwanted periodic patterns due to the shape of the dithering matrix.

Error diffusion dithering diffuses the quantisation error made on one pixel to its neighbours, with variable weights. Different types of error diffusion algorithms exist. First, one has to choose a kernel of weights used to spread the error. In the case of the Floyd-Steinberg dithering, the kernel is defined as:

$$M = \begin{pmatrix} & - & \star & \frac{7}{16} & \cdots \\ \cdots & \frac{3}{16} & \frac{5}{16} & \frac{1}{16} & \cdots \end{pmatrix}. \tag{3.3}$$

We browse the matrix from top to bottom and from left to right. For each pixel (i,j) (represented with a star), we compute the quantisation error $\varepsilon(i,j)$ defined as the difference between the original value and the closest value available in our palette scale. Each of the neighbouring pixels is then updated: for instance: $A(i,j+1) \leftarrow A(i,j+1) + \frac{7}{16}\varepsilon(i,j)$. This tends to reduce the global error that is made, but results in longer computation time.

A comparison between these three methods is shown in Fig. 3.1. As expected, threshold operation comes with a big loss of information. Ordered dithering creates repeatable patterns that we might want to avoid. Error diffusion, on the other hand, seems to give satisfactory result.

We can also have a look at the statistics of the dithered pixels. In order to avoid having only 2 possible values (0 and 1), we smoothen the dithered images by convolving it with a gaussian function. For this example, we take the gaussian width to be 15 pixels, for which the original image is still recognisable, and details have not been totally blurred out. Fig. 3.2 shows that

Figure 3.1: Result of dithering for different protocols. From left to right: original image, threshold dithering, ordered dithering (with the same matrix as described in the text), and error diffusion dithering (using a Floyd-Steinberg algorith). The threshold method loses a lot of information, while the ordered dithering one creates unwanted patterns. The error diffusion result, on the other hand, is quite pleasing to the eye (dithering might only appear if you zoom in). All images are of size 1920 $\times$ 1280 pixels.

both threshold and ordered dithering suffer from peaks in the pixels' value distribution. That is because these two methods only apply (local) thresholds on the images: a large overexposed zone, $e.g.$ the 'shade' of the windows on the wall, will be deterministically brought to the same value, which will peak in the histogram. Threshold dithering only offer 2 tones, and thus has two peaks around 0 and 1. Ordered dithering, using the matrix defined above, offers 4 different tones, and thus has 4 such peaks. While the first one fails at reproducing the initial distribution, the second one is better but struggles with low-values pixels. On the other hand, error diffusion tends to lower the quantisation error, and therefore addresses all regions more satisfactorily.

In conclusion, the error diffusion algorithm is an efficient way to reproduce an image with a more limited palette choice. In the rest of this work, we will stick to the Floyd-Steinberg error diffusion algorithm. As stated above, more recent and elaborate methods also exist: for instance, some methods based on random pixel changes perform better than error diffusion but need bigger computational power ([116]). However, we will see in the experimental section that the choice of an error diffusion algorithm is not the limiting factor for our setup.

3.1.2 *Feedback algorithm*

In order to compute what should be put on the DMD, we drew inspiration on PID controllers. This kind of feedback is widely used in control systems due to its simplicity and efficiency. Its mode of operation for a discrete case is defined as follows. Defining a set point T and a measured value e_n that we want to bring to the value T, we define the error as being $\varepsilon_n = e_n - T$. Setting the derivative part to 0, the output of the controller is then:

$$s_{n+1} = K_p \varepsilon_{n+1} + K_i \tau \sum_{k=0}^{n+1} \varepsilon_k = s_n + K_p(\varepsilon_{n+1} - \varepsilon_n) + K_i \tau \varepsilon_{n+1}. \tag{3.4}$$

PID controllers usually assume that the sampling time of the loop is fast compared to the response time. In our case, however, the response time of the system is instantaneous compared to the sample time, and the term $\varepsilon_{n+1} - \varepsilon_n$ can lead to oscillations. To better understand why, let us imagine an example where most of the convergence is done during one action of the loop. This means that $|\varepsilon_1|$, the error during the first step, is big compared to $|\varepsilon_2|$. Putting this into equation, we have:

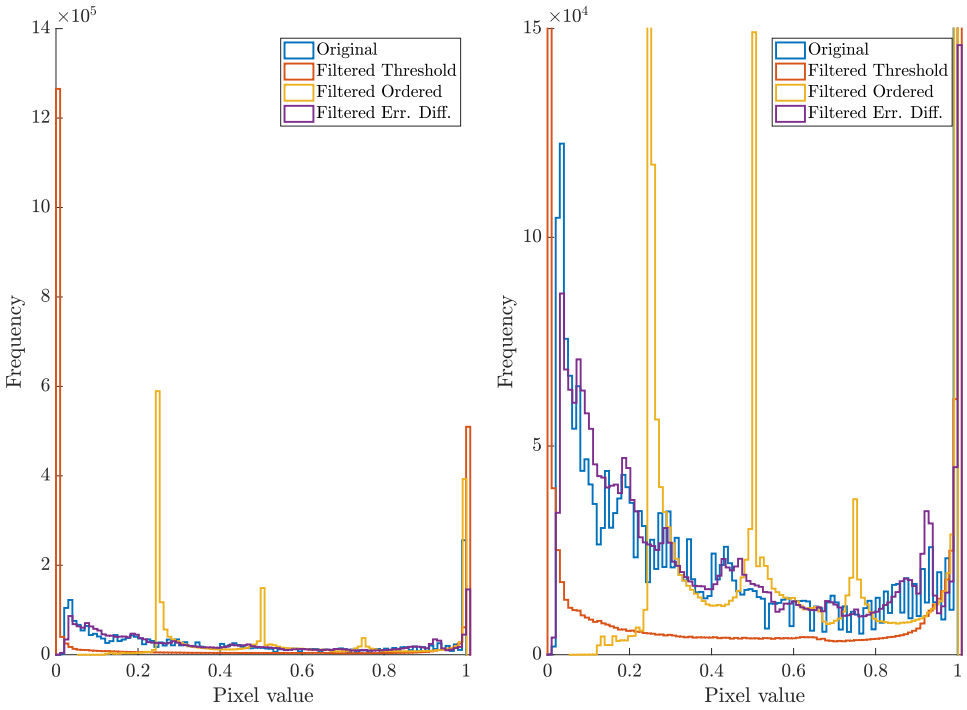

Figure 3.2: Statistics of dithered pixels for different algorithms. All the images have been convolved with a gaussian of width 15 pixels before being analysed. Left: histogram for original image, filtered threshold, filtered ordered, and filtered error diffusion ditherings. Right: enlarged version of the previous histogram. Threshold dithering is a method based on one threshold, and as such, produces two peaks on the histogram. Ordered dithering, with the previous matrix, is based on 3 thresholds, and thus creates four distinctive peaks on the histogram. Error-diffusion dithering, on the other hand, reproduces more faithfully the original distribution.

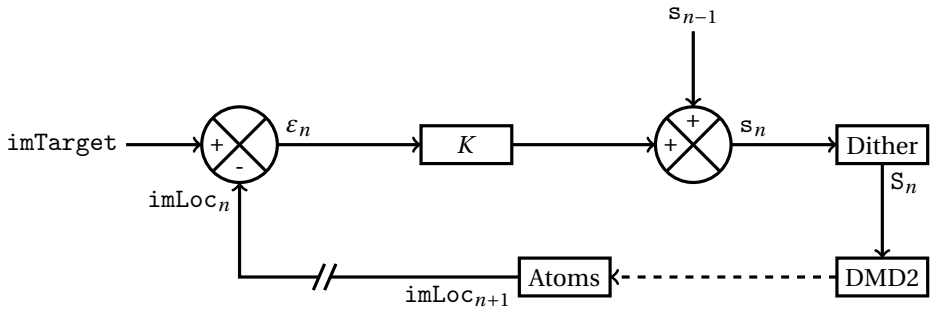

Figure 3.3: Scheme of the loop. We define a target `imTarget`, to which the absorption image at rank n $\mathtt{imLoc}_n$ is compared. The difference between these two images gives the error ε_n at rank n. An output $\mathtt{s}_n$ is then computed. This output is dithered into $\mathtt{S}_n$ and put on DMD2. We then measure the new absorption image $\mathtt{imLoc}_{n+1}$.

$$\begin{aligned} s_1 &= (K_p + K_i\tau) \times \varepsilon_1, \\ s_2 &= s_1 + K_i\tau\varepsilon_2 + K_p(\varepsilon_2 - \varepsilon_1). \end{aligned} \tag{3.5}$$

We see that as $|\varepsilon_2| < |\varepsilon_1|$, the integral term will be small compared to the negative proportional term, and the correction attained during step 1 will regress during step 2. The next step will try to overcorrect that, and the next one after this one will regress again. Therefore, for values of K_p close to values of $K_i\tau$, the system oscillates. An easy solution to this is to remove K_p altogether.

This is somewhat different from the PID textbook example where one adds K_p, and then K_i to the system. However, only keeping the K_i term in Eq. 3.4 actually makes sense in instantaneous systems: at rank $n+1$, we take the output s_n of the loop at rank n, and add it to what is left to correct at rank $n+1$ (modulo a multiplicative factor). As a consequence, we chose the following correction for our loop:

$$s_{n+1} = s_n + K\varepsilon_{n+1}. \tag{3.6}$$

We will keep these notations for the rest of this chapter.

3.1.3 *Correction loop*

We now have our two main ingredients to correct the atomic density: a feedback loop that tries to bring the cloud to a specific target, and a dithering algorithm that translates the output of this loop into an image that can be used by DMD2.

An important limitation of our method is the fact that we can only decrease OD. To better understand this, let us take the case where we want a uniform cloud, but where we observe a bit more atoms on the left. DMD1 is usually set to a basic, non-grey level image (a disk or a square mask, typically). This means that in a perfect world, there is already no light hitting the atoms on the left: all the mirrors inside the box are already off. Therefore, our only knob is to remove atoms in zones where the density is higher than average (here, on the left) by shining some light on these areas. As a consequence, the target's 'OD' has to be reasonably lower than the original 'OD'.

We then have four parameters that we need to define at each rank n of the loop:

- a target `imTarget`,
- an input $\mathtt{imLoc}_n$, here the absorption images that we take at the beginning of each loop iteration,
- an error $\varepsilon_n = \mathtt{imLoc}_n - \mathtt{imTarget}$, the difference between the input and the target,

- an output $\mathtt{s}_n$, that is dithered into $\mathtt{S}_n$ and fed to DMD2 in order to retroact on the input.

A scheme of the feedback is presented in Fig. 3.3. In order to quantify the effect of the loop, we also define a normalised figure of mérite $\mathcal{F}$:

$$\mathcal{F}_n = \frac{\sqrt{\left\langle (\mathtt{imLoc}_n - \mathtt{imTarget})^2 \right\rangle}}{< \mathtt{imTarget} >}. \tag{3.7}$$

Ideally, $\mathcal{F}$ should tend towards 0 when the loop has converged. We usually see that with a reasonable gain, $\mathcal{F}$ reaches a steady-state after 5-10 loop steps. This steady state is never exactly 0 and depends in part on the number N_r of images taken at each iteration. An example of the behaviour of $\mathcal{F}$ versus N_r is shown in Fig. 3.13. However, $\mathcal{F}$ is not only limited by this experimental noise. More fundamental limitations (on the DMD pixel size or the imaging resolution, for instance) also prevent $\mathcal{F}$ from going to zero. Understanding these limitations is one of the motivations for doing the simulations that we present next.

3.2 SIMULATIONS

It was not clear, at first, what exact type of feedback we would have to use, and to which level of accuracy this would bring us. The behaviour of our loop was also not so straightforward initially, and some simulations helped us to get a better understanding of our loop and of its limitations. These simulations are based on the local density approximation: adding light linearly translates into losing atoms.

3.2.1 *Protocol*

We first simulated the loop in a very basic manner. We did not take into account the gaussian nature of the beams, or the specific orientations of each different DMD that we use in the lab. We simply specified an atomic box of fixed size (about the one we experimentally have), on which a certain number of DMD pixels would retroact. The zone used on DMD2 to correct the atomic density was fixed to the one we use experimentally, but we varied the size ℓ of the DMD pixels. In other words, we fixed the size of the atomic box and varied the number $p = 1/\ell^2$ of DMD pixels available for each box pixel. Every length here is expressed in terms of atomic box pixels (1 pixel = 1.15 μm).

The atomic box that we defined was a square of side $L + 6$ pixels. Here, we took $L = 30$ pixels, which is the experimental size of the atomic box. Two rows and lines on each side were filled with zeros. This leaved us with a gas occupying a square of side $L + 2$. In order to avoid border effects, we took a subimage of side L of this zone on which we retroacted.

Because the loop output was only computed on this size L^2, we needed to continuously extend it on a grid of size $(L + 6)^2$ in order to retroact on the full box. We obtained this continuous extension by using Matlab's `interp2` function. This samples our output on the grid of size L^2 and finds an extrapolation of this sample up to a grid of size $(L + 6)^2$.

When this was done, we resized this output to the size of the area used on the DMD (a square of side $(L + 6)/\ell$ pixels where $\ell = 1/\sqrt{p} < 1$ is the size of a DMD pixel in terms of box pixels), and 'shone' it on the atoms. This resizing was implemented to mimic what happens experimentally: we have a magnification of approximately 70 on the setup, and this transforms DMD pixels of size 14 μm to pixels of size 0.2 μm on the atomic plane. As one camera pixel is about 1.15 μm in this plane, we have typically $\ell = 0.17$ pixels, which means $p = 33$.

A typical iteration of the loop works as follows.

- We started by looking at the $(L + 6)^2$-sized image $\mathtt{ImTot}_n$ measured at rank n. In order to avoid border effects, we took a subimage $\mathtt{imLoc}_n$ of $\mathtt{imTot}_n$. It was of size L^2 and was

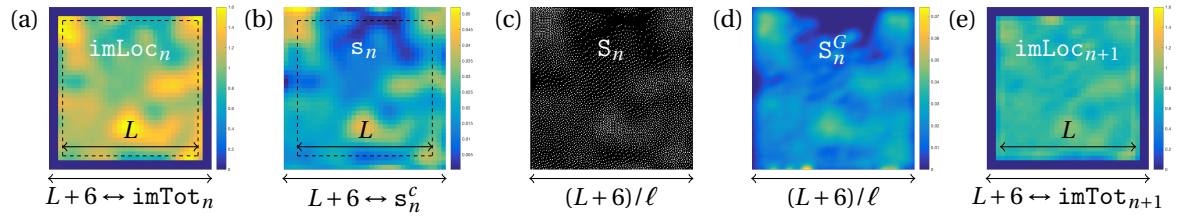

Figure 3.4: Example of a typical loop; here, the target is a flat cloud. We define an original image (a) that we try to compensate with the loop. This image has two rows of zeros and we only act on a subimage of side L. Once we have computed the output of the loop $\mathtt{s}_n$ on the dashed square and convolved it by a gaussian of fixed width, we continuously extend it on a square of side $L+6$ pixels (b). We then resize it and compute its dithered image (c). For this example, we used a very high gain in order to see some white pixels on the figure. An actual image usually has about 6 times less white pixels than here. Convolving (c) by a gaussian to mimic light propagation gives (d). Removing (d) from (a), we get the light corrected image (e).

the input of our loop at rank n. The initial non corrected images were noted $\mathtt{ImTot}_0$ and $\mathtt{imLoc}_0$.

- We then defined the output $\mathtt{s}_n$ (size L^2) of the loop at rank n. Error-diffusion usually adds some high-frequency noise to the dithered image. To avoid such artefacts being amplified iteration after iteration, we convolved $\mathtt{s}_n$ by a gaussian of width 1.5 pixel. This value was chosen to smoothen details without losing too much information.
- Taking the continuous extension of the convolved output to a size $(L+6)^2$, we got $\mathtt{s}_n^c$.
- We resized $\mathtt{s}_n^c$ to a size $\left(\frac{L+6}{\ell}\right)^2$ and took its dithered image $\mathtt{S}_n$.
- We defined $\mathtt{S}_n^G$, the convolution of $\mathtt{S}_n$ by a gaussian of standard deviation σ/ℓ pixel, in order to mimic the propagation of light from the DMD plane to the atoms. The experimental value of σ should be around 0.4. This corresponds to a low pass filter.
- We resized $\mathtt{imTot}$ (size $(L+6)^2$) to $\mathtt{ImTot}$ (size $\left(\frac{L+6}{\ell}\right)^2$).
- Finally, we simulated the action of the light by using the local density approximation and stating that in the Thomas-Fermi regime, we had:

$$\mathtt{ImTot}_n = \mathtt{ImTot}_0 - \alpha \mathtt{S}_n^G. \tag{3.8}$$

- We then resized $\mathtt{ImTot}_n$ to $(L+6)^2$ pixels, and started a new iteration.

The operations described above are illustrated in Fig. 3.4. The factor α represents the effect of the light on the atoms. It depends on the power of the light hitting the DMD and was experimentally calibrated to $\alpha = 15$. We will use this value in our simulations. A scheme of the whole loop is shown in Fig. 3.5. Compared to Fig. 3.3, it adds some convolution to the output of the loop, continuously extends it, and resizes it in order to fit the DMD size.

3.2.2 *First Tests*

We first simulated a simple flat target. The initial state of the box was a matrix of average 1 and standard deviation 0.2 obtained by adding some random noise on a uniform matrix and convolving it by a gaussian to get something smooth. We wanted to bring this image to a uniform target of value 0.7.

We computed 20 steps of the loop, varying the size ℓ of the pixels on the DMD, but keeping the number of pixels in the atomic box constant. Here, ℓ was varied between 0.09 and 0.35. For

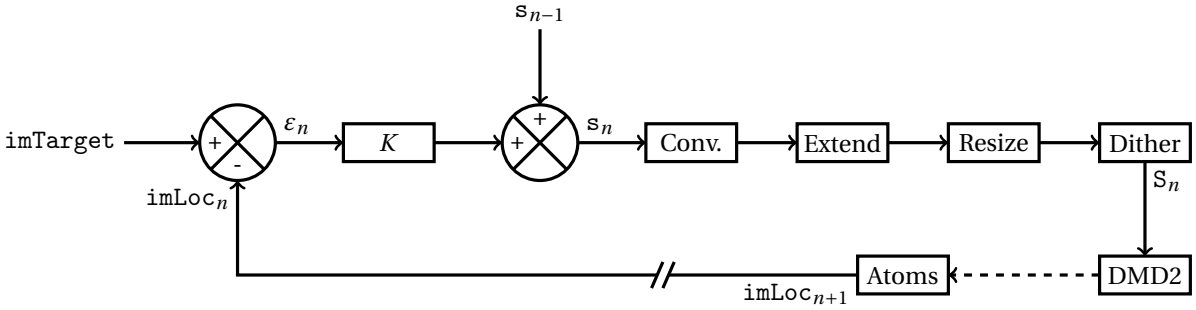

Figure 3.5: Scheme of the loop. The left part is identical to Fig. 3.3. Once the output $\mathtt{s}_n$ is calculated, it is convolved by a gaussian of width 1.5 pixels, continuously extended to retroact on the whole cloud, resized to fit the DMD size, and then dithered. This dithered image is put on DMD2. We then 'measure' the new 'absorption image' $\mathtt{imLoc}_{n+1}$.

the experimental results of the next section, $\ell = 0.17$. In order to propagate the effect of the DMD on the atoms, we also convolve the output of the loop by a gaussian of standard deviation σ. Typically, on the experiment, we have $\sigma = 0.5$ μm $= 0.4$ pixels.

At first, we did not consider any measurement noise. In other words, we did not simulate the photonic noise that we had on the experiment, which of course impacts the steady-state values of $\mathcal{F}$ in real life. The results of this section are presented in Fig. 3.6.

In a first round of simulations, we varied the gain K of the loop, keeping the convolution parameter σ and the DMD pixel size ℓ at the experimental level. The steady state value of $\mathcal{F}$ seems to be more or less independent of the gain. By removing the dithering, and then the convolution from the simulations, we estimated that about two thirds of the residual error could be attributed to the use of a dithering algorithm, while one third was due to the convolution losing some information.

The optimal gain, $K = 0.05$, was then chosen for the rest of the simulations. For lower gains, the convergence is very slow, and for larger gains, the system tends to be unstable. This is not so clear when looking at $\mathcal{F}$, where one only has the impression that the convergence is slower for higher gain. When looking at the OD, however, we clearly see oscillations. In effect, what happens is that for high gains, the system overshoots (the density is lower than the target) once every two times, and to compensate that, undershoots (the density is higher than the target) the remaining times. This distance between these two states and the target is approximately the same, meaning that this phenomenon does not lead to a big change in $\mathcal{F}$.

Mathematically, adding the pure dithered image (setting $\sigma = 0$ for the convolution) must lead to an increase of noise. This means that at too low σ, $\mathcal{F}$ should increase. However, a too large σ must lead to a blurring of the details that the loop is trying to correct. Thus, there must be an optimal σ which which the noise is kept at a decent level, but with which the loop corrects details with a relevant spatial scale. Experimentally, this convolution corresponds to a certain spatial filtering that is always done by the limited numerical aperture of the microscope objective. In other words, the question we are asking here is whether it is relevant to add an iris on the experiment to filter more (increase σ) than what we already do. In the end, we see in Fig. 3.6 that increasing σ, *i.e.* adding an iris, seems to improve $\mathcal{F}$, although the change is not dramatic. Here, we limited ourselves to a reasonable value of σ; a more complete study, however, should take into account the optimisation of this parameter.

Finally, keeping the optimal value $K = 0.05$ and the expected experimental value $\sigma = 0.4$, we turned ourselves to simulating a change of DMD resolution. As expected, $\mathcal{F}$ decreases when ℓ decreases.

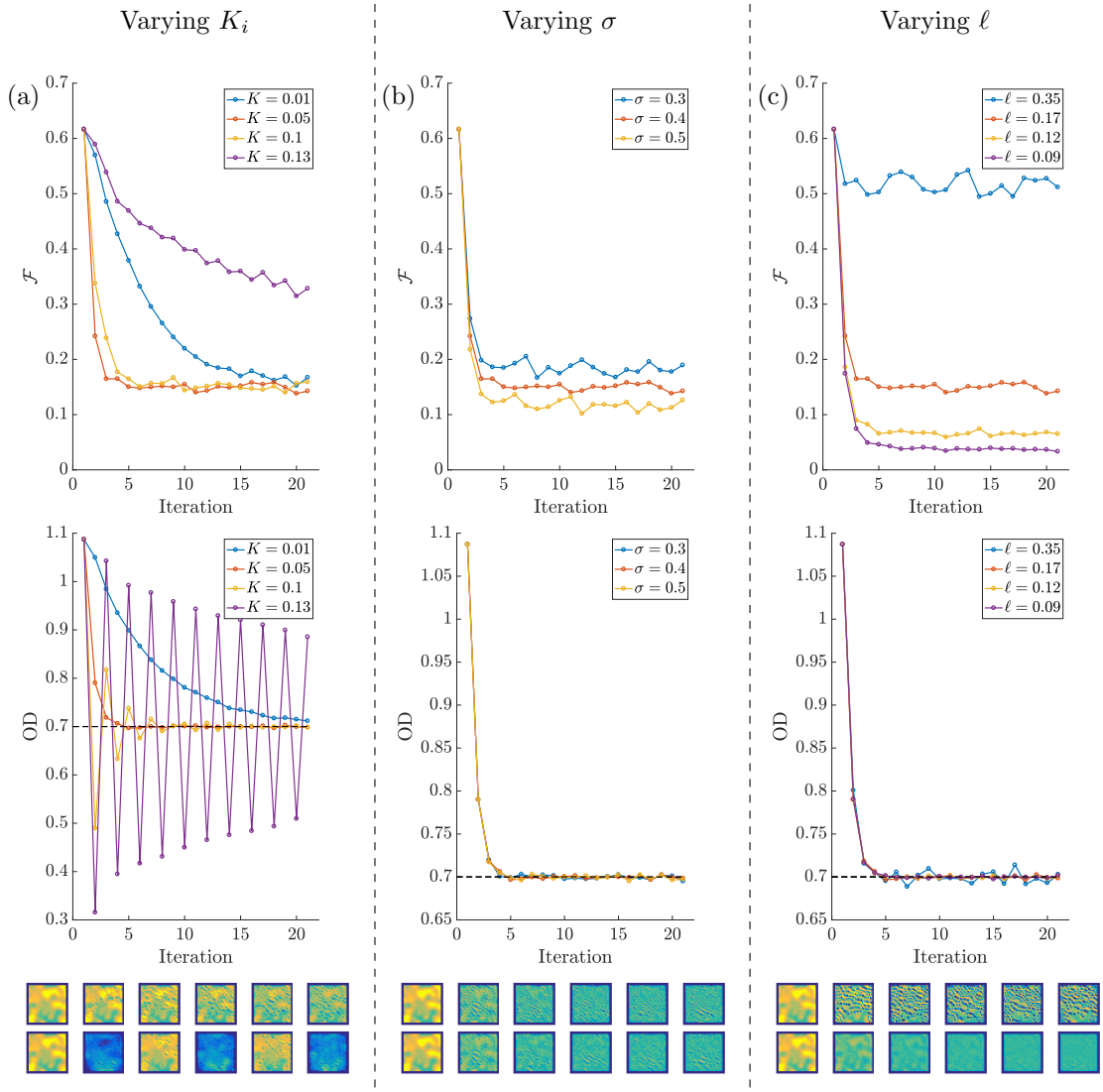

Figure 3.6: Evolutions of $\mathcal{F}$ (top) and mean 'OD' (bottom). The black lines correspond to the target 'OD'. Except for (a), all the 'OD' plots are superimposed. Left: we vary K while we fix $\sigma = 0.4$ pixel and $\ell = 0.17$. Middle: we keep $\ell = 0.17$, fix K to its optimum of 0.05, and vary σ. Right: we keep $K = 0.05$ and fix $\sigma = 0.4$ pixel while we vary ℓ. The images below the graphs are the 6 first simulated images, left to right, for the minimum (top) and maximum (bottom) varied parameter. For instance, the top left row corresponds to $K = 0.01$ and the bottom one to 0.13.

3.2.3 *Effect of the photonic noise*

We now take into account the detection shot noise. In other words, at rank n, we will duplicate $\texttt{imLoc}_n$ N_r times, add some noise to each of the N_r images, and average these images to compute the error and the output of the loop. Experimentally, this amounts to taking N_r different images and using the mean to feed the correction loop.

In order to determine the amplitude of the noise we should add, we follow the computations done in Laura Corman's thesis ([96]). Experimentally, we use an imaging beam in the low saturating regime: $I \ll I_{\text{sat}} = 1.6\ \text{mW/cm}^2$. We typically have a saturation parameter $s = I/I_{\text{sat}} = 0.2$, with an imaging pulse of duration $\tau = 10\ \mu\text{s}$. For the D_2 transition of ^{87}Rb, a camera pixel size of $1.15\ \mu\text{m}$, and taking into account the optical losses, this amounts to a number of counts per pixel $N_0 = 120$.

Moreover, neglecting the background intensity, we can write, for one pixel:

$$\text{OD} = \ln\left(\frac{N_0}{N}\right), \tag{3.9}$$

where N and N_0 correspond respectively to the number of counts received per pixel on the image with atoms and without atoms. As both N and N_0 follow a Poisson distribution, we have $\text{std}(N_0) = \text{d}N_0 = \sqrt{N_0}$, and the same goes for N. Moreover, $N = e^{-\text{OD}}N_0$, so $\text{d}N = \sqrt{e^{-\text{OD}}}\,\text{d}N_0$. We can now propagate the incertitude:

$$\begin{aligned}\text{dOD} &= \sqrt{\left(\frac{\text{d}N}{N}\right)^2 + \left(\frac{\text{d}N_0}{N_0}\right)^2} \\ &= \sqrt{\frac{1+e^{\text{OD}}}{N_0}}.\end{aligned} \tag{3.10}$$

This typically gives dOD = 0.16 which is the value that we use. To implement this on the simulations, we simply replace $\texttt{ImTot}_n$ in Eq. 3.8 by:

$$\texttt{ImTot}_n = \left\langle \texttt{ImTot}_0 - \alpha \text{S}_n^G + \text{dOD} \times R \right\rangle_{N_r} \tag{3.11}$$

where R is a normally distributed random matrix of average 0 and standard deviation 1 and we average on N_r events. Increasing N_r amounts to giving a more precise picture of the needed correction to the loop, while decreasing N_r blurs the information and expectedly leads to poorer results. For $N_0 \simeq 120$, normal and Poisson distribution are very close, hence the choice of a normal law.

We kept a gain of $K = 0.05$, which was the optimum gain found in the previous section, and used the experimental parameters $\sigma = 0.4$ pixel and $\ell = 0.17$. We then simulated the effect of varying N_r for four different values: $N_r = 4$, 6, 25 and 100. Results are presented in Fig. 3.7. As expected, $\mathcal{F}$ decreases with N_r. Plotting the result found in the last section, we see that it is comparable to the results at $N_r = 25$ and $N_r = 100$. In other words, above $N_r = 25$, the detection noise is negligible, and we are limited by the same issues that arose in the last section, the resolution of the DMD for instance.

We will use $N_r = 4$ and $N_r = 6$ in the next section ; let us just note that for our experimental parameters, we expect $\mathcal{F}_{N_r=4,6} \simeq 0.17$ for the steady state regime.

3.3 EXPERIMENTAL RESULTS

3.3.1 *Loop operation*

To operate the loop, we followed the steps detailed in the previous section. The value of each DMD2 pixel was determined by the grey-level algorithm, and we iterated this process until

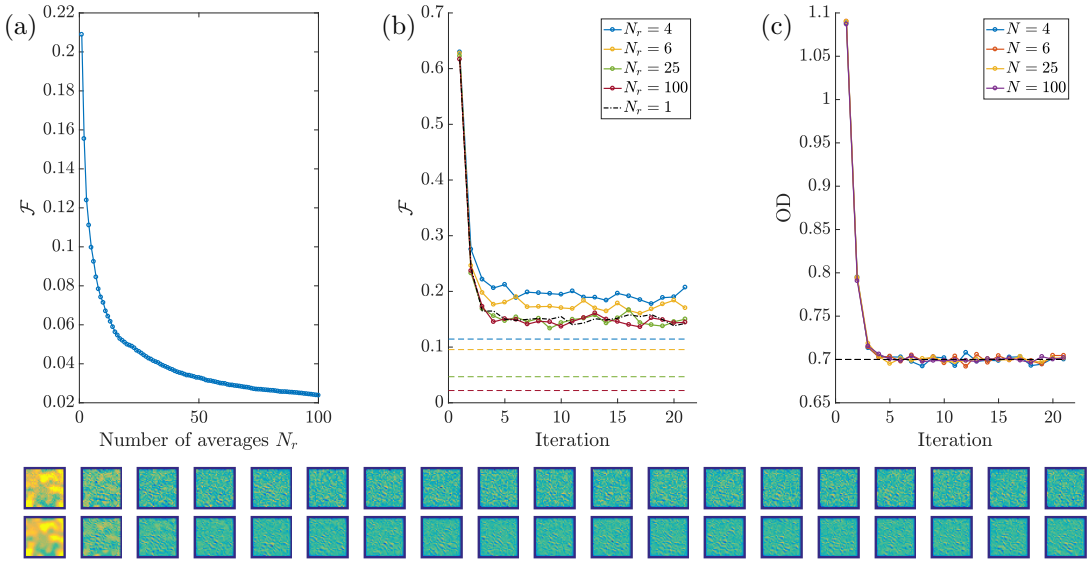

Figure 3.7: Simulations taking into account the detection noise. (a) We first compute $\mathcal{F}$ for the target image. This represents the lowest achievable $\mathcal{F}$ taking the measurement noise into account. (b) Then, we vary the number of fictive measurements between 4 and 100 and compute $\mathcal{F}$. The coloured lines are the values taken from (a) and reported for the corresponding N_r. We see that we never reach this level. The black line is the result of the previous section and corresponds to $N_r = 1$ but without photonic noise. (c) We also plot the evolution of the 'OD' for each parameter. The black line on the right plot represents the target OD. The images below the graphs are the first 19 simulated images for $N_r = 4$ (top) and $N_r = 100$ (bottom).

we reached an acceptable result. We realised that due to the finite size of the beam incident on DMD2, the correction was sometimes too weak on the edges of the cloud (where there was less available light). To fix this issue, we chose the gains of the loop to be inverse gaussian matrices rather than constants:

$$K(x, y) = K_0 \times \mathrm{e}^{2\frac{(x-x_0)^2+(y-y_0)^2}{w^2}}, \tag{3.12}$$

where $w = 28$ μm is the measured width of the DMD2 beam in the atomic plane. This way, the correction had more or less an equal action on all pixels, even the ones far away from the centre.

Concerning the number N_r of images we take for each loop step, we typically had $N_r = 5-10$. We experimentally needed around 20 loop steps, so for $N_r = 10$, this corresponded to almost 2 hours of data taking. Moreover, as the atomic box moves by about 2 pixels during the day due to thermal drifts, we also had to sometimes redefine the region of interest. Apart from that, we followed the steps described in section 3.2.2. An example of a typical loop is shown in Fig. 3.8.

3.3.2 *Qualitative examples*

All the images shown here were realised K around 0.1. Concerning the target image, we could almost chose it at whim, which offers a certain flexibility for tailoring arbitrary potentials. There were three main limitations: the target OD, the minimal typical length scale, and the resolution in terms of modulation depth:

- We could always remove atoms, which means that we could freely chose the target atomic density as long as it was reasonably lower than the initial one.
- In terms of spatial frequency, we were limited by our PSF. Typically, we could not hope to print details at the submicronic scale.

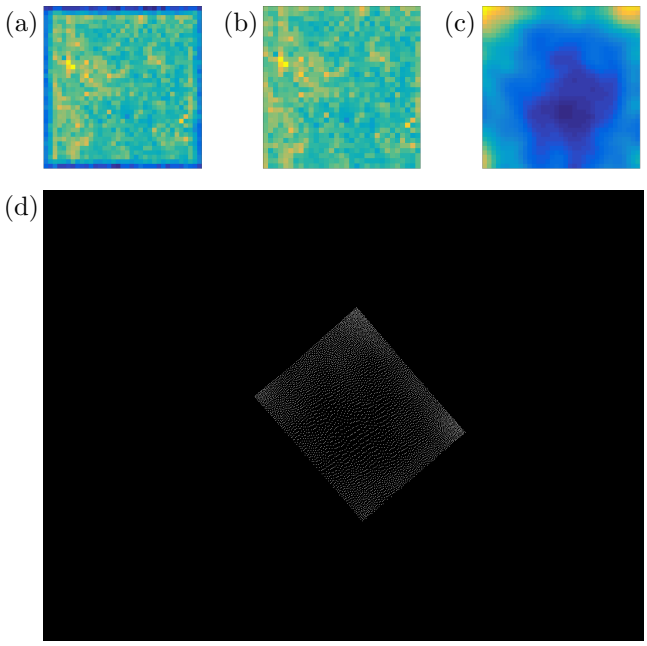

Figure 3.8: Example of a typical loop. The images shown are taken from the first iteration of the loop, and the target is a uniform density. With (a), we take an image $\texttt{imTot}_n$ slightly bigger than the box. In (b), we take a subimage $\texttt{imLoc}_n$ of (a) in order to avoid border effects. We then compute the output $\texttt{s}_n$ shown in (c); note that in order to compensate for the gaussian shape of the beam, the gain is higher on the edges than in center, resulting in an output also higher on the edges. Finally, we resize everything and create a grey-level image (d) that we load on the DMD. We can then reiterate.

- The available modulation depth mostly depended on the resolution of the DMD, so a higher resolution improved the number of grey tones we could use.

Fig. 3.9 shows some examples of such possibilities. Overall, the results are quite close to the targets.

3.3.3 *Quantitative exemples*

Quantitatively, we can compare $\mathcal{F}$ for corrected and non corrected clouds. The idea is to set a target OD and compare two protocols:

- we blast a fraction of the atoms away to reach this target density, and do not try to correct the homogeneity of the cloud,
- we use the grey level loop to reach this target density ; hopefully, the defects that appear get corrected along the way. In this case, we take $\mathcal{F}$ at the end of the loop, when it has reached a steady state.

The first protocol was tried for different targets, the second one was tried at a target close to maximum density. The result is shown in Fig. 3.10. We took the same number of images ($N_r = 6$) for each of the two protocols, in order to be able to compare their respective $\mathcal{F}$. For the grey-level correction, we find $\mathcal{F} = 0.19$, which is very close to the simulated value of $\mathcal{F} = 0.17$. We can see in Fig. 3.10 that for this target, the grey-level correction does more or less the same thing than the blasting protocol. If this efficiency is independent of the target OD, this would represent a two fold decrease of $\mathcal{F}$ for low targets. However, this study does not look at the images' spectra, which could be used to quantify the efficiency of the correction. A more detailed study could look at the noise's typical length scale in order to compare the two protocols: we suspect that the grey level procedure adds a lot of high frequency noise compared to the blasting method.

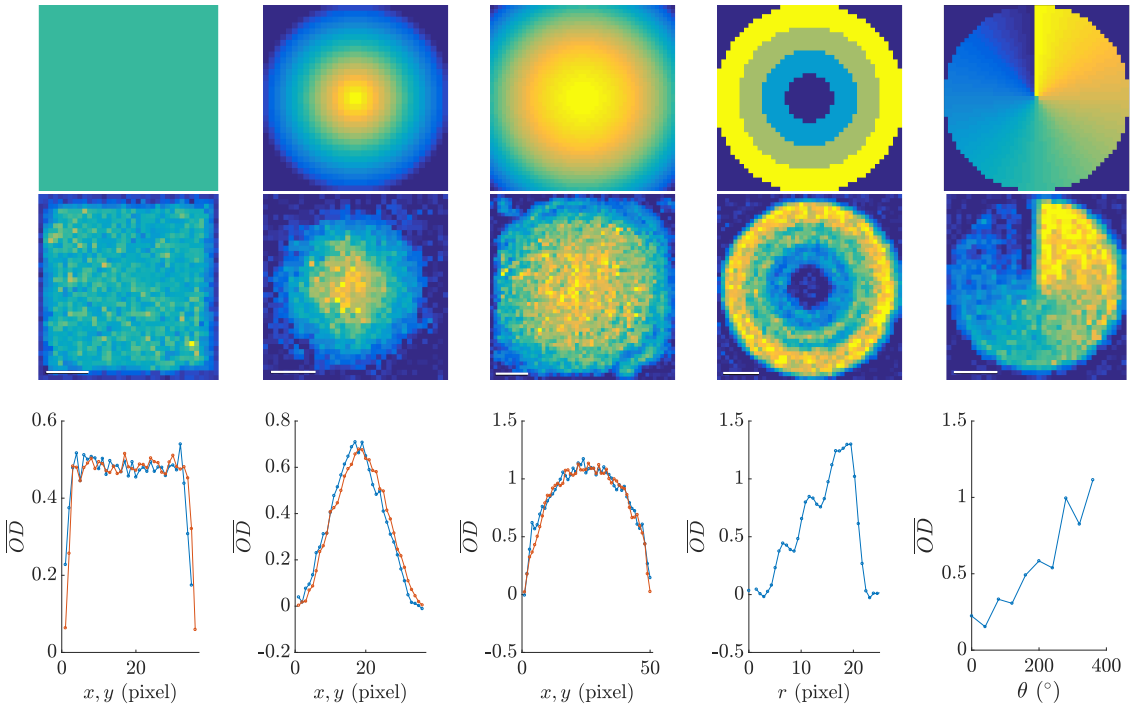

Figure 3.9: Exemples of images realised thanks to the correction algorithm. All these images are averaged over typically 7 iterations. The white line represents 10 μm. From top to bottom: target image, loop corrected image, and mean OD along the two directions for corrected image (radial and azimuthal average for the Hanoi towers and phase winding pattern respectively).

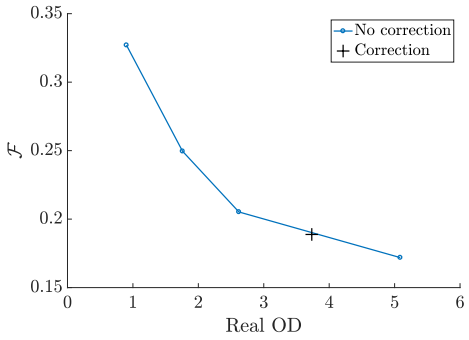

Figure 3.10: Homogeneity parameter for different non corrected blastings (blue), and what we reach after the loop (black).

We will now focus on the swimming pool pattern, and we will analyse the convergence of the loop by looking at $\mathcal{F}$. As the actual value of this parameter depends on the number N_r of images that we take to compute a mean image, we limit ourselves to $N_r = 4$ to keep the duration of the optimisation reasonable. At the end of one of the loops, we tried to vary N_r up to 16, and computed, for this step of this loop, the values of $\mathcal{F}^{(N_r)}$ as a function of N_r. As expected, we see a decrease of $\mathcal{F}$ with N_r: Fig. 3.13 also displays a fit of the data by a square-root function. Moreover, the steady-state values that we find for $\mathcal{F}$ are quite close to the simulated ones.

N_r being fixed, we tried 5 different integral gains: $K = 0.05$, 0.1, 0.15, 0.20 and 0.25. Fig. 3.11 shows an example of the evolution of the atomic density along the loop for different gains. As expected, increasing the gain speeds up the convergence (iteration 3 has hardly changed compared to iteration 1 for the lowest gain), but leads to oscillations. This is very clear in Fig. 3.11: for $K = 0.25$, the algorithm removes too many atoms at iteration 3 and tries to correct this by removing too few atoms at iteration 4, only to remove too many atoms again at iteration 5. Fig. 3.12 shows the whole evolution of the run with the highest gain.

Fig. 3.13 shows the convergence of the loop for 5 gains between 0.05 and 0.25. We can quantitatively see the effect of the gain on the speed of convergence. The optimal gain seems to be $K = 0.10$ as it combines fastest convergence speed and lowest steady state $\mathcal{F}$. We also see that the steady-state value of $\mathcal{F}$ depends on the gain. This counterintuitive result can be explained by the persistence of long lived local density oscillations. For instance, for the highest gain, we can see in Fig. 3.12 that as the loop overshoots and undershoots repeatedly, some zones exchange atoms with a period of 2 loop steps. As the distance that we use involves squares and the two processes are symmetric around the target, $\mathcal{F}$ does not change significantly from iteration 3 onwards. This however hides two positive terms:

$$\mathcal{F} = \mathcal{F}_\infty + \mathcal{F}_{\text{osc}}, \tag{3.13}$$

where $\mathcal{F}_\infty$ is the optimal reachable $\mathcal{F}$ while $\mathcal{F}_{\text{osc}}$ depicts the effect of the local oscillations. For higher gains, there tends to be more local oscillations, which increase $\mathcal{F}_{\text{osc}}$, and in turn change the steady state value of $\mathcal{F}$. One could look at local $\mathcal{F}$s within different regions of an image in order to detect such oscillations; however, these phenomena correspond to high gain regimes which we did not explore too much, and a further analysis of these oscillations was deemed unnecessary.

CONCLUSION

In conclusion, we have explained how we can mitigate the inhomogeneity defects that inevitably appear at relatively low densities. The use of a dithering algorithm, in parallel with a feedback loop, allows us to greatly improve the flatness of out cloud. This method can also be used in order to tailor specific potentials that might be of use for other kind of experiments: vortex imprinting, or solitonic bubbles shaping, for instance.

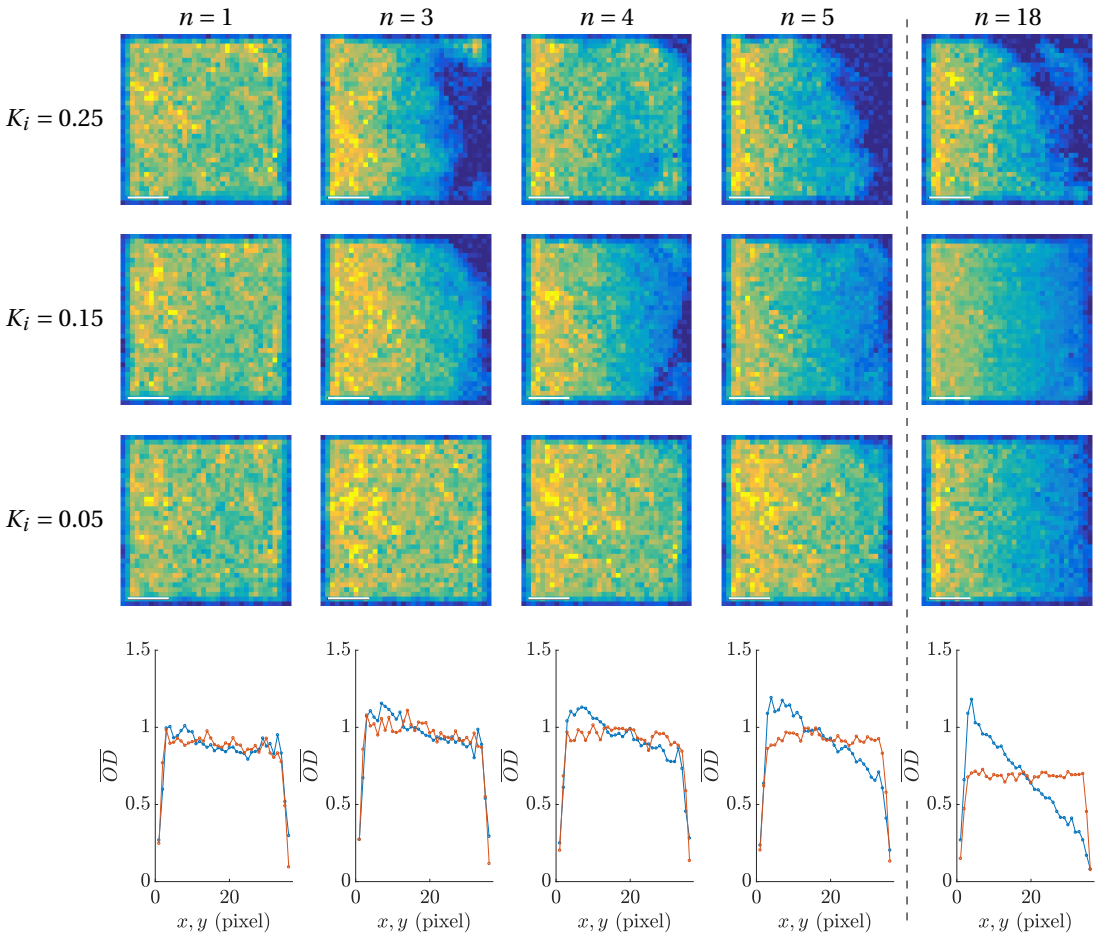

Figure 3.11: Examples of swimming pool potentials realised with gains $K = 0.25$ (top), 0.15 (middle top) and 0.05 (middle bottom). The bottom row is an average along both space directions for the run with lowest gain. All these images are averaged over typically 4 iterations. The white lines represent 10 μm. From left ro right, the images are: cloud at iteration 1 (no correction), 3, 4, 5, and 18 (optimum for these 3 runs). Convergence is slow for the middle bottom row, and too fast for the top one, leading to local oscillations of density.

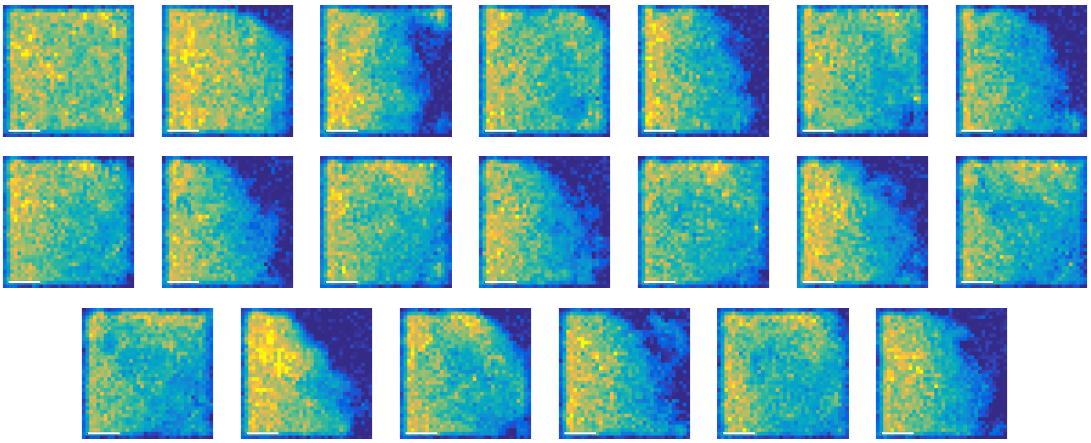

Figure 3.12: Evolution of the atomic density along the loop, for $K = 0.25$. Iterations are going from left to right, then from top to bottom. We see that even if $\mathcal{F}$ seems to have reached a steady state at iteration 3, in effect, some regions overshoot and some others undershoot, leading to a more or less constant $\mathcal{F}$.

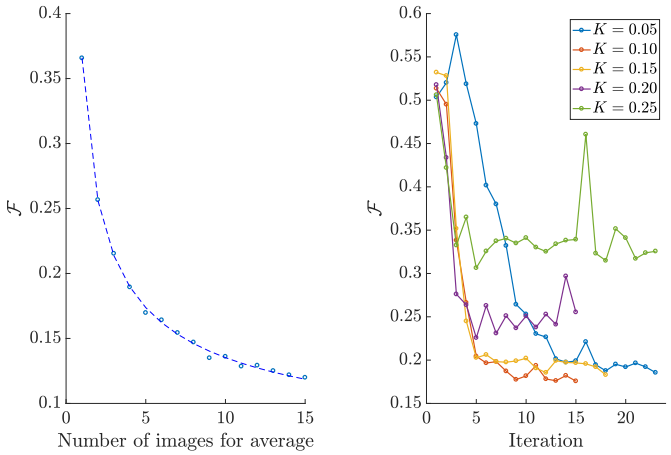

Figure 3.13: Left: decrease of $\mathcal{F}$ with the number N_r of images taken. The dashed line is a square-root fit. Right: figures of mérite correponding to gains $K = 0.05 - 0.25$.

II

Demixing phenomena in 2D uniform boxes

The seed is strong.

—Jon Arryn

4

DEMIXING PHENOMENA: THEORETICAL CONSIDERATIONS

INTRODUCTION

Demixing is an everyday life phenomenon that takes place when different species with strong enough repulsive interactions are brought together: because the mixed state is unstable, a hydrodynamical instability develops, which tends to spatially segregate the two immiscible species. From the separation of oil and vinegar in a vinaigrette, to the tears of wine observable in a glass filled with alcohol, hydrodynamical instabilities are encountered in many mundane situations. However, the description of cold atoms gases by hydrodynamic-like equations shows that these phenomena are also relevant for such systems. In this chapter, we will first introduce the concept of hydrodynamical instability in classical physics, then apply it to quantum gases. Finally, we will review the state of the research in this field, and give some numerical results for our system.

4.1 ROLE OF INSTABILITIES IN CLASSICAL DEMIXING PHENOMENA

4.1.1 *An example of immisicibility-induced dynamics*

Mixtures are ubiquitous in physics, and are observed in day to day life. A mixture of two species 1 and 2 can either be miscible (1 and 2 can coexist in the same phase), or immiscible (in which case 1 and 2 phase separate, and the system demixes). Ultimately, the miscibility of two species has energetic origins: if it is energetically more favourable to create domains (for instance if the inter species repulsion is stronger than the intra species one), the two components will spatially separate.

In this case, the steady state of the system is expected to have two well separated phases, for instance species 1 at the centre and species 2 forming a shell around it. This steady-state vision can however be quite far from what happens experimentally when an overlapping mixture is prepared and let to evolve. For instance, in a vinaigrette, when the stirring stops, the homogenous system will quickly form phase separated droplets, but one will not immediately end up with only two domains.

An interesting example of dynamics induced by immiscibility can be found in [118, 119]. As anyone knows, oil and water do not mix. Because of surface tension, a drop of water deposited on a bath of oil takes a curved shape like the one of a convex lens, and does not expand. Alcohol and oil, however, do mix: a drop of alcohol will quickly expand on an oil surface, followed by a quick evaporation. Then, what happens with a mixture of alcohol and water deposited on the same surface?

Of course, the result depends on the balance between alcohol and water. Above a certain alcohol threshold, the oil surface is wettable by the mixture, and the droplet starts expanding. However, alcohol quickly evaporates and the mixture eventually crosses the threshold: the droplet stops expanding. One would then expect the system to come back to the initial lenticular shape. Instead, the receding front leaves on its border a multitude of droplets (see Fig. 4.1). This is caused by an accumulation of liquid on the edge of the droplet, in turn creating a Plateau-Rayleigh-like instability that breaks up this bulge into several smaller droplets. This process continues until the alcohol has totally evaporated.

Thus, in order to grasp the dynamics of phase separation, and the characteristic scales of the domains created, it is crucial to correctly understand the physics of hydrodynamical instabilities.

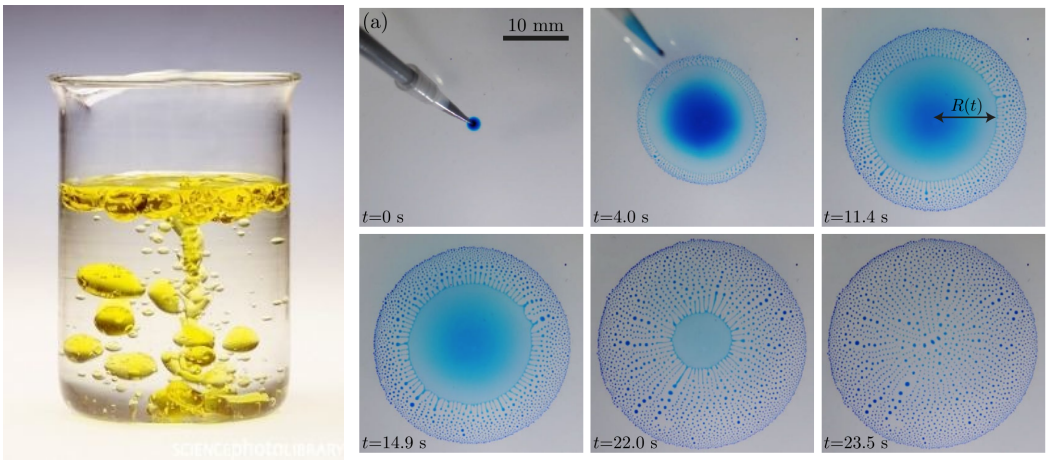

Figure 4.1: Oil and water are immiscible (left). However, when alcohol is added to water in sufficient quantity (right), the situation changes dramatically: such a droplet quickly expands over the oil surface, before receding due to alcohol evaporation. As the layer is thicker in the centre, the alcohol tends to evaporate faster on the edge. This translates into a gradient of surface tension towards the rim, which causes an accumulation of liquid there. Due to a Plateau-Rayleigh-like instability, this bulge collapses into a multitude of small droplets, whose exact size depends on the concentration of alcohol in the mixture. Figure taken from [118].

This is the topic of the next section. This framework of thinking is general and will also be applied to ultracold atomic gases.

4.1.2 *Example of hydrodynamical instability: the Rayleigh-Taylor instability*

The formation and growth of domains in an unstable mixture is well explained by the study of hydrodynamical instabilities, and is a classical example in hydrodynamic lectures. A whole zoology of instabilities exists: the Rayleigh-Taylor instability, for instance, describes the deformation of an interface between a heavier fluid placed above a lighter one. In this example, one finds that the points where the heavier fluid penetrates the other can initially form an approximately periodic pattern (see Fig. 4.2). The periodicity of the interface's deformation is a general result for hydrodynamical instabilities.

Other types of instabilities exist, like the Rayleigh-Plateau or the Kelvin-Helmholtz instabilities, both shown in Fig. 4.2. The first one describes how a stream of fluid breaks into several periodically spaced domains when the typical extension of the stream reaches a critical value, and is observed in water running from a faucet, for instance. The second one occurs between two layers of fluids travelling at different speeds: this creates specific periodic deformations at the interface and describes, for instance, how waves are created at the surface of the ocean. Its manifestation for clouds can also be observed, although it is rarer.

As can be seen, the deformation of an interface caused by a hydrodynamical instability creates periodic patterns that are, at first glance, quite counter intuitive. Where does this periodicity come from? We reproduce here a simple argument given in [120] to explain this phenomenon.

In the case of the Rayleigh-Taylor instability, the deformation of the interface is ultimately caused, as in many cases in physics, by the competition between two effects. While gravity tends to push the heavier fluid down, the surface tension opposes any penetration of one fluid into the other, as this would increase the interface area.

Let us consider a thin film of initial thickness e_0 placed in an unstable configuration. For instance, the experiment can consist in creating a film of glycerol on a surface, and then flipping this surface upside down so that the denser fluid (the glycerol) is placed above the lighter one (the air). For simplicity, we will here perform a 1D analysis, and will not take into account what happens in the transverse dimension, where the size of the sample is w. Let us examine

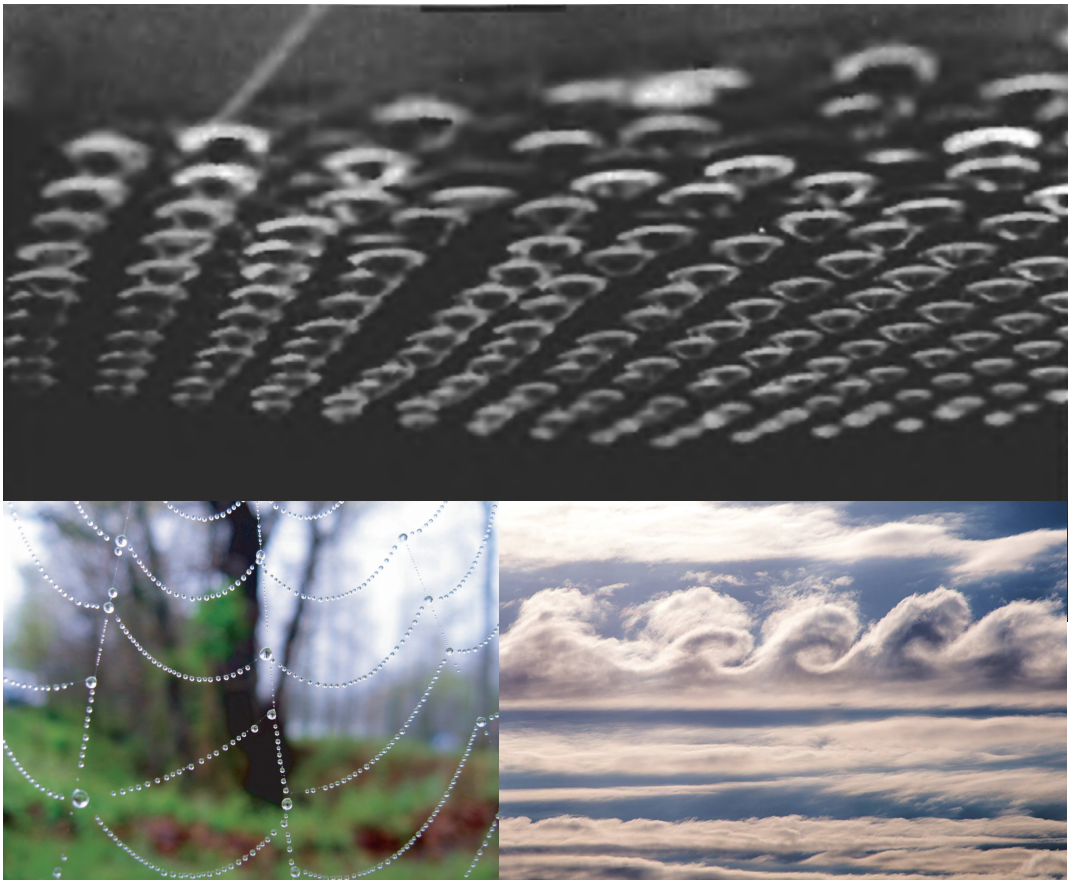

Figure 4.2: Top: Example of a Rayleigh-Taylor instability: the droplets can be formed by condensation or destabilisation of a liquid film (figure taken from [120]). Bottom left: example of a Rayleigh-Plateau instability where water forms droplets on a cobweb (photo via Ensnaria). Bottom right: example of a Kelvin-Helmholtz instability seen in clouds above New York state (photo via Paul Chartier).

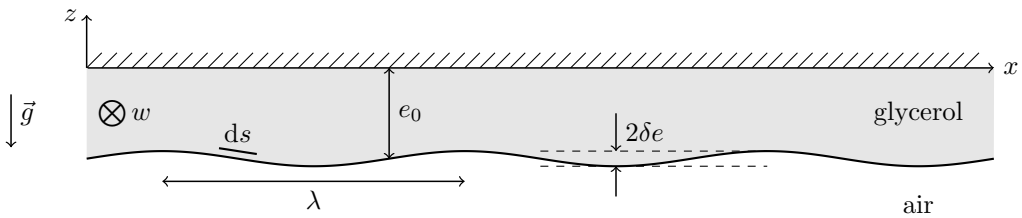

Figure 4.3: A dense fluid (here, glycerol) is placed on top of a less dense fluid (air in this example). The interface deforms and we examine how a modulation of the thickness $e = e_0 + \delta e \cos(kx)$ evolves. Here, $k = 2\pi/\lambda$.

how a modulation of the thickness $e = e_0 + \delta e \cos(kx)$, with $\delta e \ll e_0$, evolves with time (see Fig. 4.3 for notations). We note v the velocity of an element of volume of the fluid, and p the dynamic pressure applied on that same element of volume. For our film, the velocities involved in the problem cannot be very large, and one can write the Navier-Stokes equation for an incompressible fluid, neglecting the inertial term:

$$\eta \frac{\partial^2 v}{\partial z^2} = \frac{\partial p}{\partial x}, \tag{4.1}$$

where we have introduced the fluid's dynamical viscosity η. The velocity goes from 0 on the solid surface to v at the fluid/air interface, and one typically has:

$$\eta \frac{v}{e_0^2} \sim \frac{\partial p}{\partial x}, \text{ while } Q = e_0 w v \;\Rightarrow\; Q \sim \frac{e_0^3}{\eta} w \frac{\partial p}{\partial x}, \tag{4.2}$$

where we have introduced the fluid's flow rate Q. In our case, one can show that the exact numerical factor is $1/3$.

Now, we want to see how e deforms with time. One can use the volume conservation equation:

$$\frac{\partial Q}{\partial x} = -w \frac{\partial e}{\partial t}. \tag{4.3}$$

In our case, $\partial p/\partial x$ has two components: the element related to the hydrostatic pressure $\rho g \frac{\partial e}{\partial x}$, and the force induced by the surface curvature $-\gamma \frac{\partial^3 e}{\partial x^3}$. This yields:

$$\dot{\delta e} = \delta e \frac{\gamma e_0^3}{3\eta} k^2 (\kappa^2 - k^2), \tag{4.4}$$

where we have introduced the capillary length of the denser fluid $\kappa^{-1} = \sqrt{\gamma/\rho g}$. Interestingly, for $k < \kappa$, the solutions of this equation grow exponentially, and the patterns form at a rate:

$$\tau_k^{-1} = \frac{\gamma e_0^3}{3\eta} k^2 (\kappa^2 - k^2) = \tau_0^{-1} \left(\frac{k}{\kappa}\right)^2 \left[1 - \left(\frac{k}{\kappa}\right)^2\right] \text{ where } \tau_0^{-1} = \frac{\gamma e_0^3 \kappa^4}{3\eta}. \tag{4.5}$$

The maximum of τ_k^{-1} is reached for a certain $\lambda_f = 2\pi\sqrt{2}/\kappa$, as shown in Fig. 4.4. This means that while there is a whole range of unstable ks, there is one mode k_f that will grow faster than the others, and that will imprint its pattern on the system, which explains why the observed deformations are periodic and quasi-monomode. We will see that the same kind of argument will be used for patterns arising in ultracold atomic gases. Of course, it should be noted that δe cannot physically diverge. At one point, this perturbative analysis ceases to be valid, and the dynamics will stop following this simple prediction.

Quantum gases also abide by hydrodynamical equations, and we will now apply the same kind of arguments to this field in order to predict the typical length and time scales of two ultracold demixing gases.

4.2 THEORETICAL DESCRIPTION FOR ULTRACOLD ATOMIC GASES

4.2.1 *Demixing criterion*

We have mentioned that for classical fluids, the miscibility of two species, or lack thereof, is governed by the nature of interactions between the two components. In an ultracold atomic gas, this role is played by the inter and intracomponent s-wave scattering lengths a_{ij}. We aim here at finding a quantitative criterion for when demixing happens.

Let us take two species 1 and 2 with repulsive interactions. We suppose that $T = 0$ and that the system is uniform. We reproduce here a simple energy argument developed in [121]: we

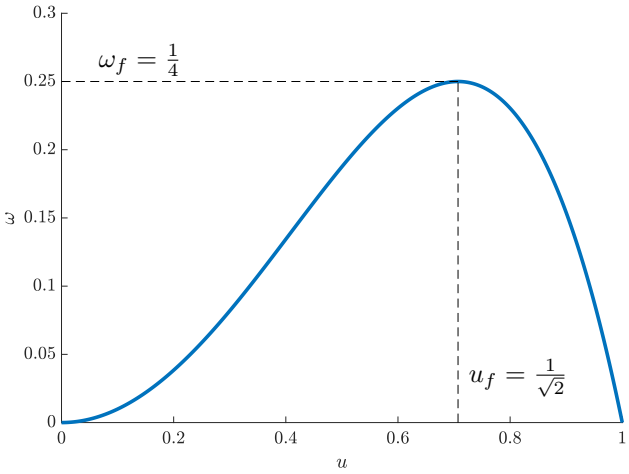

Figure 4.4: Evolution of the normalised rate $\omega = \tau_0/\tau_k$ versus the normalised wave vector $u = k/\kappa$. The maximum is reached in (u_f, ω_f).

take the naive picture where the gas separates into two parts, 1 to the centre, 2 forming a shell around 1 (the right image of Fig. 4.5, for instance). The N_1 atoms of 1 occupy a volume αV while the N_2 other atoms take the remaining space, *i.e.* $(1-\alpha)V$, V being the size of the system. Among these two parts, the density is uniform, and drops at the border on a length scale of the order of the healing length ξ. The surface kinetic and interaction energies are thus negligible in the thermodynamical limit compared to the volume interaction energy:

$$E_{\text{int}} = \frac{N_1^2 g_1}{2\alpha V} + \frac{N_2^2 g_2}{2(1-\alpha)V} \quad \text{with} \quad g_i = \frac{4\pi\hbar^2}{m} a_{ii}. \tag{4.6}$$

When minimising this energy over α, we find that the demixed configuration has an energy:

$$E_{\text{demix}} = \frac{1}{2V}\left(N_1^2 g_1 + N_2^2 g_2 + 2N_1 N_2 \sqrt{g_1 g_2}\right). \tag{4.7}$$

The spatially uniform configuration, however, has an energy:

$$E_{\text{unif}} = \frac{1}{2V}\left(N_1^2 g_1 + N_2^2 g_2 + 2N_1 N_2 g_{12}\right) \quad \text{with} \quad g_{12} = \frac{4\pi\hbar^2}{m} a_{12}. \tag{4.8}$$

Hence, if $g_{12} > \sqrt{g_1 g_2}$, the demixed configuration has a lower energy than the overlapping system. Demixing is thus expected to happen for such interaction parameters. One should keep in mind that this criterion assumes a $T = 0$ uniform system. The relevant criterion for when the two species phase separate might be different for non uniform systems where it might depend on atom number ([122]), while the finite temperature could lead to large modifications of spin dynamics and to the appearance of a phase transition ([123]).

Another important point is that in the work we present later, we do not investigate this equilibrium state. Rather, we quench the system into a mixture of immiscible spin states that are initially overlapping. While the totally separated phase configuration is expected to be the system's ground state, what happens en route to this ground state is not described by this simple energy argument. This will be the focus of the next section.

Finally, it should be noted that the energy difference per particle between the two aforementioned configurations is extremely small. Considering a mixture with equal number of atoms: $N_1 = N_2 = N/2$, and a total density of $n = 70\ \mu\text{m}^{-2}$, one has:

$$\Delta E = n(g_{12} - \sqrt{g_1 g_2}) \simeq k_B \times 1.5\,\text{nK} \ll k_B T, \tag{4.9}$$

which makes the obtention of this equilibrium hard to observe experimentally.

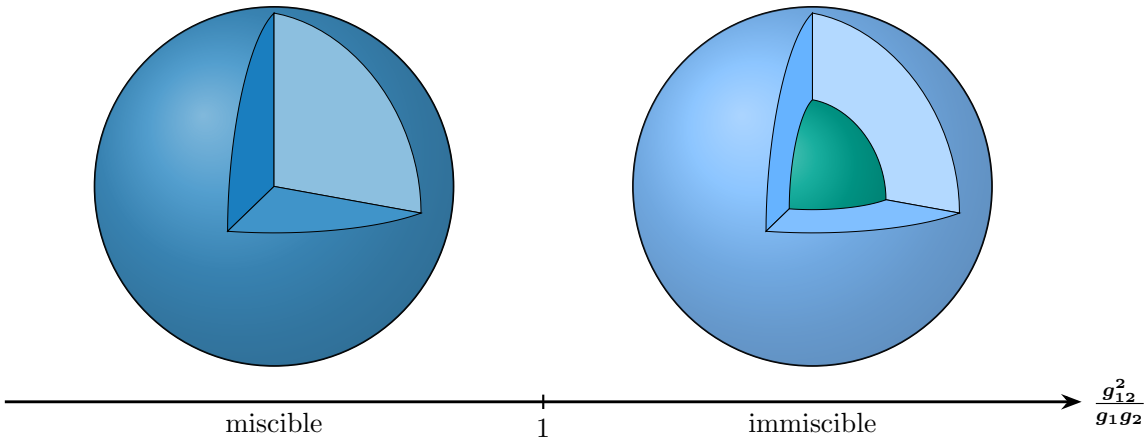

Figure 4.5: Phase diagram: the relative strength of interactions will render the system either miscible or immiscible. State 2 is represented in light blue, state 1 in green (a miscible mixture is represented in dark blue). The expected ground state of the system is shown for different parameters of $\Delta = g_{12}^2/g_1 g_2$: in the immiscible case, the atoms of 1 and 2 are totally separated.

4.2.2 *Bogoliubov-de Gennes analysis*

In this section (mostly based on [61]), we want to discuss the dynamics of demixing phenomena. We previously had a glimpse of what the stationnary state of a demixed system was, but we have not discussed its dynamics. What actually happens is that when the mixture is quenched out of the miscible regime, an instability develops and separates the system into different domains. As for the classical case, we investigate the existence of unstable modes, and look for a maximum rate of formation for such modes.

Let us consider a BEC with two components 1 and 2. For the sake of simplicity, our calculations are done in a 3D infinite uniform system. Let us note φ_j the wave functions of our two condensates. Unless specified otherwise, j will be either 1 or 2 here. In order to go beyond last section's simple energy argument, we have to take into account the system's kinetic and chemical energy, and link them to its time evolution. For this purpose, we use the Gross-Pitaevskii equation that gives the temporal evolution of a weakly interacting Bose gas' wave functions. We add an inter-species interaction term and obtain:

$$\begin{cases} i\hbar\dot{\varphi}_1 &= -\dfrac{\hbar^2}{2m}\nabla^2\varphi_1 + g_1|\varphi_1|^2\varphi_1 - \mu_1\varphi_1 + g_{12}|\varphi_2|^2\varphi_1, \\ i\hbar\dot{\varphi}_2 &= -\dfrac{\hbar^2}{2m}\nabla^2\varphi_2 + g_2|\varphi_2|^2\varphi_2 - \mu_2\varphi_2 + g_{12}|\varphi_1|^2\varphi_2, \end{cases} \tag{4.10}$$

where μ_j is the chemical potential of component j. We now want to study small perturbations of φ_j compared to its non perturbed value and we write:

$$\varphi_j(\mathbf{r},t) = \sqrt{n_j(\mathbf{r},t)}e^{i\theta_j(\mathbf{r},t)} = \varphi_j^0(\mathbf{r},t) + \delta\varphi_j(\mathbf{r},t). \tag{4.11}$$

We equivalently have:

$$\begin{cases} n_j(\mathbf{r},t) &= n_j^0 + 2\delta n_j(\mathbf{r},t) \quad \text{with} \quad \delta n_j \ll n_j^0, \\ \theta_j &= \theta_j^0 + \delta\theta_j(\mathbf{r},t) \quad \text{with} \quad \delta\theta_j \ll \theta_j^0. \end{cases} \tag{4.12}$$

Noting that $\varphi_j \approx \varphi_j^0(1 + \delta n_j/n_j^0 + i\delta\theta_j)$, we obtain:

$$i\hbar\left[\frac{\delta\dot{n}_1}{n_1^0} + i\delta\dot{\theta}_1\right] = -\frac{\hbar^2}{2m}\left[\frac{1}{n_1^0}\nabla^2\delta n_1 + i\nabla^2\delta\theta_1\right] + 2g_1\delta n_1 + 2g_{12}\delta n_2. \tag{4.13}$$

We can then identify real and imaginary parts in order to obtain the equations for density and phase fluctuations:

$$\begin{cases} \hbar\delta\dot{n}_1 &= -n_1^0\dfrac{\hbar^2}{2m}\nabla^2\delta\theta_1, \\ -\hbar\delta\dot{\theta}_1 &= -\dfrac{\hbar^2}{2m}\dfrac{1}{n_1^0}\nabla^2\delta n_1 + 2g_1\delta n_1 + 2g_{12}\delta n_2, \end{cases} \tag{4.14}$$

of which we can take the time derivative:

$$\begin{cases} \hbar^2\delta\ddot{n}_1 &= -\left(\dfrac{\hbar^2}{2m}\right)^2\nabla^4\delta n_1 + 2\dfrac{\hbar^2}{2m}\left[g_1 n_1^0\nabla^2\delta n_1 + g_{12}n_1^0\nabla^2\delta n_2\right], \\ \hbar^2\delta\ddot{\theta}_1 &= -\left(\dfrac{\hbar^2}{2m}\right)^2\nabla^4\delta\theta_1 + 2\dfrac{\hbar^2}{2m}\left[g_1 n_1^0\nabla^2\delta\theta_1 + g_{12}n_2^0\nabla^2\delta\theta_2\right]. \end{cases} \tag{4.15}$$

In order to find how different modes $\mathbf{k}$ behave, we then develop the density and phase perturbations on a plane wave basis:

$$\begin{cases} \delta n_j(\mathbf{r},t) &= A_j(\mathbf{k})e^{i(\mathbf{k}\cdot\mathbf{r}-\omega(\mathbf{k})t)} + \text{c.c.} \\ \delta\theta_j(\mathbf{r},t) &= B_j(\mathbf{k})e^{i(\mathbf{k}\cdot\mathbf{r}-\omega(\mathbf{k})t)} + \text{c.c.} \end{cases} \tag{4.16}$$

We now want to find an equation on ω. We can inject eq. 4.16 into eq. 4.15 and its counterpart for species 2:

$$\begin{cases} \omega^2 A_1(\mathbf{k}) &= \dfrac{k^2}{2m}\left[\left(\dfrac{\hbar^2k^2}{2m} + 2g_1n_1^0\right)A_1(\mathbf{k}) + 2g_{12}n_1^0A_2(\mathbf{k})\right], \\ \omega^2 A_2(\mathbf{k}) &= \dfrac{k^2}{2m}\left[\left(\dfrac{\hbar^2k^2}{2m} + 2g_2n_2^0\right)A_2(\mathbf{k}) + 2g_{12}n_2^0A_1(\mathbf{k})\right], \end{cases} \tag{4.17}$$

$$\begin{cases} \omega^2 B_1(\mathbf{k}) &= \dfrac{k^2}{2m}\left[\left(\dfrac{\hbar^2k^2}{2m} + 2g_1n_1^0\right)B_1(\mathbf{k}) + 2g_{12}n_2^0B_2(\mathbf{k})\right], \\ \omega^2 B_2(\mathbf{k}) &= \dfrac{k^2}{2m}\left[\left(\dfrac{\hbar^2k^2}{2m} + 2g_2n_2^0\right)B_2(\mathbf{k}) + 2g_{12}n_1^0B_1(\mathbf{k})\right]. \end{cases} \tag{4.18}$$

For non trivial solutions to exist, each system determinant must be 0, which brings the same condition for both systems:

$$\Omega_\pm^2(k) = \frac{\omega_1^2 + \omega_2^2}{2} \pm \frac{1}{2}\sqrt{(\omega_1^2 - \omega_2^2)^2 + 4g_{12}^2k^4n_1^0n_2^0/m^2}, \tag{4.19}$$

where we have defined $\hbar^2\omega_j^2 = \dfrac{\hbar^2k^2}{2m}\left(\dfrac{\hbar^2k^2}{2m} + 2g_jn_j^0\right)$, which is the single-component Bogoliubov dispersion relation. We can rewrite this expression by defining:

$$c_\pm^2 = \frac{1}{2}(c_1^2 + c_2^2) \pm \frac{1}{2}\sqrt{(c_1^2 - c_2^2)^2 + 4g_{12}^2c_1^2c_2^2/(g_1g_2)}, \tag{4.20}$$

where $c_j^2 = g_j n_j^0/m$ are the Bogoliubov speeds. We can thus rewrite this dispersion relation with a more compact form:

$$\Omega_\pm^2 = k^2 c_\pm^2 + \left(\frac{\hbar k^2}{2m}\right)^2. \tag{4.21}$$

We see that $c_-^2 < 0$ for $g_{12}^2 > g_{11}g_{22}$, which is the same criterion found in the last section. In this case, there is a range of k for which $\Omega_-^2 < 0$, meaning that $\Omega_- \in i\mathbb{R}$. As a consequence, these modes will correspond to unstable modes, while the other modes will be dynamically stable. Let us take the case where $A_j(\mathbf{k}) \in \mathbb{R}$ (*i.e.* $\delta n \in \mathbb{R}$). Using eq. 4.16, we see that an imaginary Ω_- indeed corresponds to unstable, exponentially growing modes:

$$\delta n_j(\mathbf{r}, t) = A_j(\mathbf{k}) e^{i(\mathbf{k}\cdot\mathbf{r} - \Omega_- t)} + \text{c.c.} = 2A_j(\mathbf{k}) \cos(\mathbf{k}\cdot\mathbf{r}) \times e^{|\Omega_-|t}, \tag{4.22}$$

while this equation shows that if $\Omega_- \in \mathbb{R}$, δn_j simply oscillates with a fixed amplitude.

It is then easy to take the derivative of eq. 4.21 with respect to k in order to find that the maximum growth rate is reached for $k_f = \sqrt{2}m|c_-|/\hbar$, and corresponds to a typical time $\tau_f = |\Omega_{-,k_f}|^{-1} = \hbar/(m|c_-|^2)$. According to the argument developed in section 4.1.2, we thus expect to see a pattern of wavelength $\lambda_f = 2\pi/k_f$ emerging after a typical time τ_f.

Finally, the relative amplitudes $A_{j,\pm}$ and $B_{j,\pm}$ can also be determined:

$$A_{2,\pm} = A_{1,\pm}\frac{mc_\pm^2 - g_1 n_1^0}{g_{12} n_1^0} = A_{1,\pm}\frac{g_{12} n_2^0}{mc_\pm^2 - g_2 n_2^0} \text{ and } B_{1,\pm} = -i\frac{A_{1,\pm}}{n_1^0}\frac{2m\omega_\pm}{\hbar k^2}. \tag{4.23}$$

We can now see how this model applies to cold atomic systems, what has been done in the field, and what time and length scale we can expect for the states of ^{87}Rb that we use.

4.3 ULTRACOLD DEMIXING EXPERIMENTS

4.3.1 *Examples in cold atom experiments*

Thanks to their high versatility, cold atomic systems are ideal candidates for studying mixtures physics. The first experiment that involved mixtures of two cold atoms species was realised in [47] and involved two hyperfine states of ^{87}Rb, where the repulsion between these two states was observed thanks to a displacement of the condensed part of species 1 when species 2 was present. When species 2 was absent, there was no repulsive force exerted and condensate 1 occupied the centre of the thermal cloud. Other experiments then quickly followed, involving different hyperfine levels ([124]), spinor condensates ([48, 49]), and later, mixtures of different atomic species ([52]), or mixtures of bosons and fermions ([125]).

In such systems, the miscibility parameter, which depends on the scattering lengths of both species, can often be controlled via Feshbach resonances ([52, 53]), or by the addition of a dressing MW field that couples both states ([54–56]). These very powerful tools are then used to study the different behaviours of the system in the miscible and immiscible regimes.

In the immiscible regime, spontaneous pattern formations have been reported when half of a single component gas was transferred to another state immiscible with the first one ([58, 59]), or when the miscibility parameter was tuned from miscible to immiscible with a Feshbach resonance ([60]). Usually, these experiments first observe a regime of quick initial pattern growth ([58, 126]), followed by a regime where the patterns do not evolve anymore and a steady state has been reached. For instance, in [58], the authors initially prepared a quasi 1D gas of ^{87}Rb in an equal superposition of states $|\downarrow\rangle = |F = 1, m_F = -1\rangle$ and $|\uparrow\rangle = |F = 1, m_F = 1\rangle$. This superposition is dynamically unstable and slowly evolves into separated spin domains in typically 1 s (see Fig 4.6). At longer times, the BEC starts losing atoms and domains can no longer maintain a full spin polarisation. This enables domains of state $|\uparrow\rangle$ to cross into domains

of state $|\downarrow\rangle$ to coalesce with other domains of state $|\uparrow\rangle$ (and vice versa), thus decreasing the number of domains.

Interestingly, the formation of such domains in a 1D elongated gas can pin the system and prevent it from moving when an m_F-dependent magnetic gradient is applied: if the system is given time to phase separate, and then a magnetic gradient is applied, the gradient will have very little effect on the gas, while the species easily flow and separate in the other case ([62]).

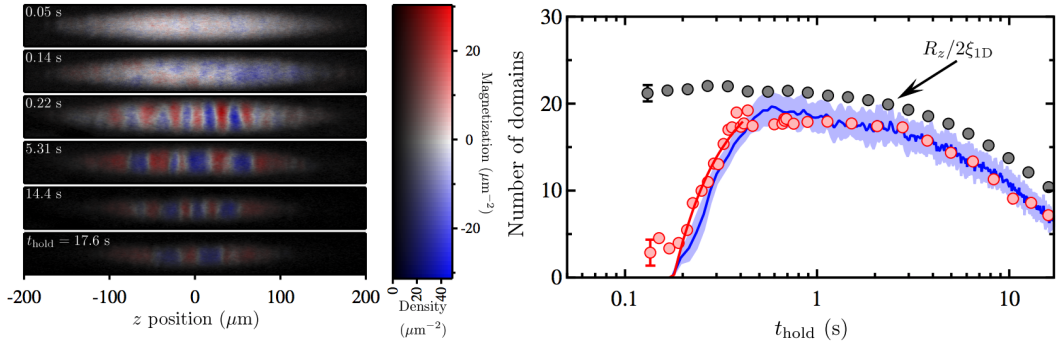

Figure 4.6: Left: a quasi 1D BEC of ^{87}Rb is initially prepared in an equal superposition of the 2 immiscible spin states $|F = 1, m_F = \pm 1\rangle$. The number of spin domains quickly increases, before slowly decreasing (see right): because of atomic losses, eventually, small domains cannot maintain a total polarisation and they coalesce into bigger domains. Right: number of domains with time. The red points are the experimentally observed values (typical uncertainty plotted on the leftmost point), the red line is an exponential fit, the blue line is a Gross-Pitaevskii simulation (with uncertainties denoted by the blue band), and the grey points correspond to the ratio $R_z/2\xi$ where R_z is the Thomas-Fermi radius of the gas, and ξ the healing length. Considering that the system is of total size $2R_z$ and that the domains have a typical size of 4ξ, this ratio gives an estimate of the number of domains present in the system. Both figures are taken from [58].

There are other ways to prepare a metastable state: in [63] for instance, the authors let the system reach a phase separated state before applying a state-selective force displacing the domains and forcing them to re-equilibrate; while in [64], the authors let an immiscible system demix for a certain time before transferring one component to another state in order to get a miscible system. Other experiments include the study of superfluid currents ([65]), counterflow dynamics ([66]), the stabilisation of droplets by beyond mean field effects ([67, 68]), or the propagation of sound ([127]). Finally, there is a variety of articles numerically studying instabilities in these systems: reference [71] showed the appearance of Rayleigh-Taylor instabilities when the interatomic interaction or the trap frequency is varied, while authors in [69, 70] studied Kelvin-Helmholtz and counter-superflow instabilities at an interface of two condensates moving relative to each other.

4.3.2 *Parameters for our experiment*

In order to be insensitive to stray magnetic fields, the immiscible states that we use are the $|1, 0\rangle$ (state 1) and $|2, 0\rangle$ (state 2) hyperfine states of ^{87}Rb. This corresponds to s-wave scattering lengths of $a_1 = 100.9\ a_0$, $a_2 = 94.9\ a_0$, and $a_{12} = 98.9\ a_0$ where a_0 is Bohr's radius (in this chapter, we use values for the a_{ij} taken from [128]; there are, however, several other estimates ([129, 130]) for these parameters). This gives a miscibility parameter of $\Delta = a_{12}^2/a_1 a_2 = 1.022$: we are slightly immiscible. As shown in Fig. 4.7, Ω_- is quite sensitive to a small change of a_{12}: a good determination of the interspecies scattering lengths is thus very important.

There is no Feshbach resonance between the states that we use, which prevents us from tuning the miscibility parameter at whim. There are, however, other knobs that we can act upon in order to change the emerging pattern's characteristics. To do so, we can vary the atomic

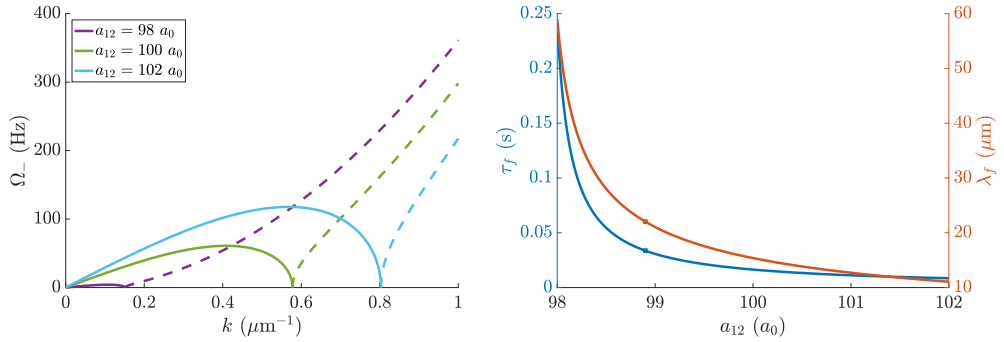

Figure 4.7: Left: evolution $\Omega_-(k)$ with a_{12} for a balanced mixture while the density is fixed at 50 μm^{-2}. Notice that Ω_- is extremely sensitive to a small change in a_{12}.The solid line represents the zone where $\Omega_- \in i\mathbb{R}$ (any seed gets exponentially amplified), while the dashed line is the zone where $\Omega_- \in \mathbb{R}$ (any seed simply oscillates). Right: corresponding appearing wavelength λ_f and characteristic growth time τ_f. The small squares represent the value that we take for a_{12}.

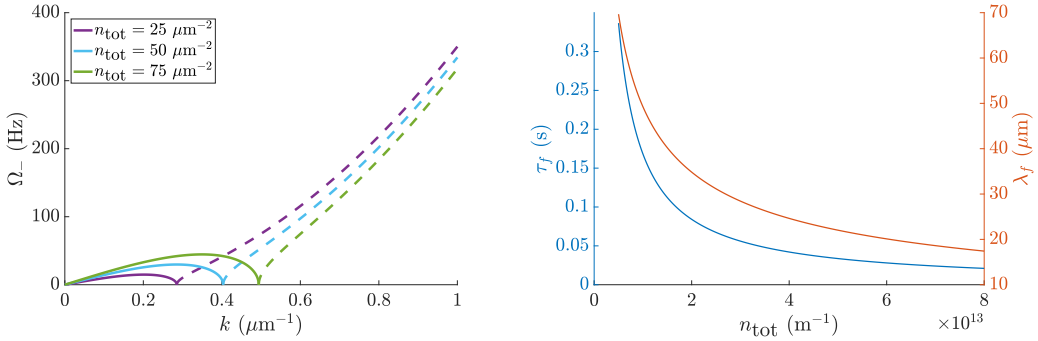

Figure 4.8: Left: evolution $\Omega_-(k)$ with n_{tot} for a balanced mixture while a_{12} is fixed at 98.9 a_0. As before, Ω_- is purely imaginary where the line is solid and real when it is dashed. Right: corresponding appearing wavelength λ_f and characteristic growth time τ_f.

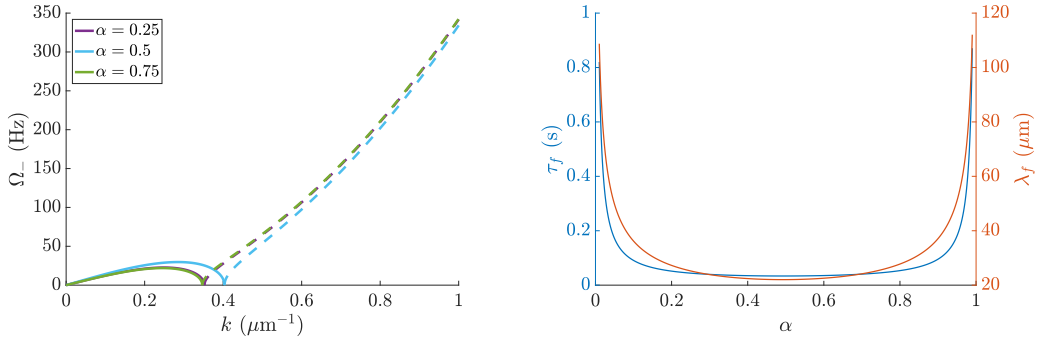

Figure 4.9: Left: evolution of $\Omega_-(k)$ with α while n_{tot} and a_{12} are fixed at 50 μm^{-2} and 98.9 a_0, respectively. As before, Ω_- is purely imaginary where the line is solid and real when it is dashed. Right: corresponding appearing wavelength λ_f and characteristic growth time τ_f.

density n_{tot}, which impacts the Bogoliubov speeds c_1 and c_2, which in turn change τ_f and λ_f. The behaviour of Ω_-, τ_f, and λ_f versus n_{tot} is shown in Fig. 4.8. For instance, for a typical value of $n_{\text{tot}} = 75$ μm^{-2}, we expect that the appearing pattern will be set by the fastest growing mode ($k \simeq 0.35$ μm^{-1}) and will grow with a typical rate of ~ 44.5 Hz. We thus expect to see a periodic pattern of period ~ 18 μm arise in typically ~ 22 ms. A lower density results in slower growth, and in patterns with larger wavelengths.

Another possibility is to change the relative population between components 1 and 2. If we note $n_1 = \alpha n_{\text{tot}}$ and $n_2 = (1-\alpha)n_{\text{tot}}$, we can express Ω_- as a function of α. The behaviour of Ω_-, τ_f, and λ_f versus α is shown in Fig. 4.9. In particular, we see that the curves of τ_f and λ_f as functions of α are extremely flat. For instance, in order to observe a growth twice slower than at $\alpha = 1/2$, one needs to go at $\alpha \simeq 0.14$ or $\alpha = 0.85$, which implies a very small signal to noise ratio. Note that the curves are not exactly symmetric with respect to $\alpha = 1/2$ due to the small differences between the a_i.

A last possibility could be to change the geometry of the system. All the calculations above were done for a 3D infinite system. However, it is easily understandable that strict boundary conditions must have an effect on the symmetry of the spin domains. We will see in the following chapters that this is actually the case: demixing in a square box gives rise to patterns with a square geometry, while the same experiment in a ring produces patterns with a circular symmetry.

CONCLUSION

In this chapter, we have derived a criterion that determines the miscibility of an ultracold atomic mixture: if $g_{12} > \sqrt{g_1 g_2}$, then, the system is immiscible, and an initial overlap of the two species will result in the rise of a hydrodynamical instability that will phase separate the system. A Bogoliubov analysis shows that when this criterion is met, the solutions of the dispersion relation take purely imaginary values for a certain range of wave vectors. Any seed with such k will be exponentially amplified; for a random seed, we expect to see a periodic pattern emerge corresponding to the wave vector for which the appearing rate is maximal. Moreover, we can study this kind of phenomena with a balanced mixture of Rb atoms in $|1,0\rangle$ and $|2,0\rangle$: this will be the topic of the next three chapters.

5

COUPLED GROSS-PITAEVSKII EQUATIONS: NUMERICAL SIMULATIONS

Simulations are a powerful tool to better understand a physical system. After some preliminary experimental tests, we turned to numerics to help us get a better grip on the dynamics of demixing. In particular, we wanted to check the dispersion relation calculated in [61] and see how it was modified in a box. In this chapter, part of a 2D gas initially in component $|1,0\rangle$ (state 1) is suddenly transferred into another component $|2,0\rangle$ (state 2), immiscible with the first one. In order to mimic what will be done experimentally, the transfer can either be uniform ('natural demixing') or localised ('seeded demixing'):

- in the first case, half of the atoms are suddenly and uniformly transferred to the other state, typically with a MW pulse,
- in the second case, the transfer is non uniform and we seed a pattern on the atomic density, using our Raman beams. This seed is always a monochromatic periodic perturbation.

In order to benchmark our simulations with the prediction from [61], we performed simulations for a 2D box with periodic boundary conditions (PBC). However, in order to compare the numerical results with the experimental data, we also ran simulations for the same box with strict boundary conditions (SBC). An interesting way to merge these two aspects of the problem is, as we will do in chapter 6, to work with rings: in addition of having a 1D system with PBC, we also get access to more modes for the same used area. For this purpose, we also ran some simulations for rings (Semi-Strict Boundary Conditions, or SSBC). A table summarising the different type of demixings (natural or seeded), and different type of simulations (PBC, SBC, or SSBC) is presented on Table 5.1. A similar table completed with a summary of this chapter's main results is presented on Table 5.2. We will first expose the principle of the algorithm that we use, and then compare our results with the 3D infinite theory developed in Chapter 4.

5.1 SIMULATION ALGORITHM

5.1.1 *Dimensionless Gross-Pitaevskii equations*

We aim here at simulating the evolution of a system of wave functions (φ_1, φ_2) following coupled Gross-Pitaevskii equations. We use a $N_g \times N_g$ 2D grid to simulate our system, and unless specified, the total density of the system under scrutiny is n_{tot}.

We first define some parameters in order to render the Gross-Pitaevskii equations dimensionless:

$$\begin{cases} t_0 &= \frac{mL^2}{\hbar N_g^2}, \\ x_0 &= \frac{L}{N_g} = n_0^{-1/2}, \\ V_0 &= \frac{\hbar^2 n_0}{m}. \end{cases} \tag{5.1}$$

These parameters have respectively the dimensions of a time, a distance, and an energy. This allows us to work with dimensionless variables:

	PBC	SBC	SSBC
Natural		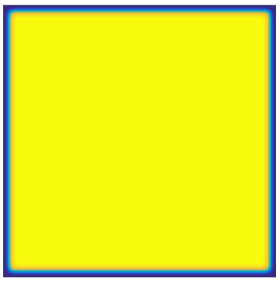	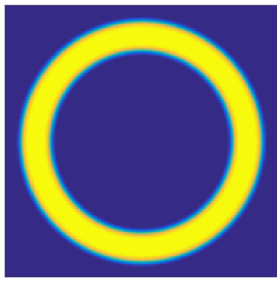
Seeded	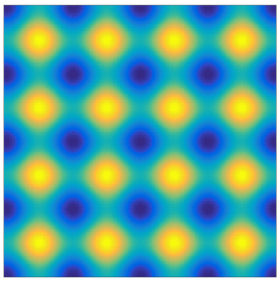	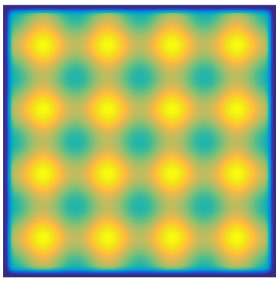	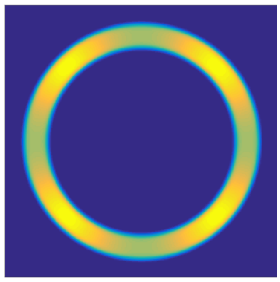

Table 5.1: Summary of the different type of simulations. Represented in each case is the initial density of atoms in state 2.

$$\begin{cases} \widetilde{t} &= t/t_0, \\ \widetilde{\nabla} &= x_0 \nabla, \\ \widetilde{\varphi_i} &= x_0 \varphi_i, \\ \widetilde{V} &= V/V_0, \end{cases} \tag{5.2}$$

Thus, the coupled Gross-Pitaevskii equations read:

$$\begin{cases} i\dot{\widetilde{\varphi}}_1 &= \left(-\frac{1}{2}\widetilde{\nabla}^2 + \widetilde{V} + \widetilde{g}_1|\widetilde{\varphi}_1|^2\right)\widetilde{\varphi}_1 + \widetilde{g}_{12}|\widetilde{\varphi}_2|^2\widetilde{\varphi}_1, \\ i\dot{\widetilde{\varphi}}_2 &= \left(-\frac{1}{2}\widetilde{\nabla}^2 + \widetilde{V} + \widetilde{g}_2|\widetilde{\varphi}_2|^2\right)\widetilde{\varphi}_2 + \widetilde{g}_{12}|\widetilde{\varphi}_1|^2\widetilde{\varphi}_2, \end{cases} \tag{5.3}$$

where $\widetilde{g}_{ij} = \sqrt{8\pi}a_{ij}/l_z$ as defined in chapter 1[1]. Throughout this chapter, the wave functions are normalised to their respective atomic number:

$$\iint |\widetilde{\varphi}_i|^2 \, \mathrm{d}\widetilde{x} \, \mathrm{d}\widetilde{y} = N_i. \tag{5.4}$$

We will drop the $\widetilde{\ }$ notation in the following for clarity.

1 Throughout this chapter, we take the same values as in [131] and we fix $a_1 = 100.9\, a_0$, $a_2 = 94.9\, a_0$, and $a_{12} = 98.9\, a_0$, with a_0 the Bohr's radius. The exact values of these parameters is not important here; we mostly want to compare the Bogoliubov analysis found in [61] to what happens when the system is trapped in a box.

5.1.2 *Time-Splitting Algorithm*

An interesting scheme to solve this kind of equations is the time-splitting technique ([132, 133]). As there is no common basis in which we can compute the kinetic part on one hand, and the interaction and potential parts on the other hand, the idea is to split the two contributions by first applying the kinetic part of the hamiltonian in Fourier space where it is diagonal, and then the interaction and potential parts in real space. This method relies on separating exponentials of operators, and neglects all terms with commutators appearing in the Baker-Campbell-Hausdorff formula:

$$e^{\hat{A}}e^{\hat{B}} = e^{\hat{Z}} \text{ with } \hat{Z} = \hat{X} + \hat{Y} + \frac{1}{2}\left[\hat{X},\hat{Y}\right] + \frac{1}{12}\left[\hat{X},\left[\hat{X},\hat{Y}\right]\right] - \frac{1}{12}\left[\hat{Y},\left[\hat{X},\hat{Y}\right]\right] + \dots \tag{5.5}$$

It is thus only valid if dt is small enough. In other words, in order to solve the equation:

$$\frac{\partial\varphi}{\partial t} = \hat{A}\varphi + \hat{B}\varphi \tag{5.6}$$

one approximates the solution $\varphi(t_l + dt) = e^{(\hat{A}+\hat{B})dt}\varphi(t_l)$ by $\varphi(t_l + dt) = e^{\hat{A}dt}e^{\hat{B}dt}\varphi(t_l)$. This assumption is thus valid if $1/dt$ is typically larger than any energy scale appearing in the problem.

For the the kinetic part of the hamiltonian, we first solve:

$$\begin{cases} i\dot{\varphi}_1 &= -\dfrac{1}{2}\nabla^2\varphi_1, \text{ for } t_l < t \leqslant t_l + dt \\ i\dot{\varphi}_2 &= -\dfrac{1}{2}\nabla^2\varphi_2, \end{cases} \tag{5.7}$$

with initial condition $\varphi_i(t_l)$ being the result φ_i^l of iteration l and $i = 1, 2$. Going to Fourier space replaces the ∇^2 by a diagonal term which enables us to solve this set of equations exactly. The second step is then to Fourier inverse these solutions and to solve:

$$\begin{cases} i\dot{\psi}_1 &= \left(V + g_1|\psi_1|^2\right)\psi_1 + g_{12}|\psi_2|^2\psi_1, \text{ for } t_l < t \leqslant t_l + dt \\ i\dot{\psi}_2 &= \left(V + g_2|\psi_2|^2\right)\psi_2 + g_{12}|\psi_1|^2\psi_2, \end{cases} \tag{5.8}$$

with initial condition $\psi_i(t_l) = \varphi_i(t_{l+1})$. The solution of these equations is then the result φ_i^{l+1} of iteration $l + 1$.

5.1.3 *Choice of the grid's geometry*

Throughout this chapter, we chose to simulate our system on a 2D square grid with N_g sites on each side. While this choice is natural for PBC and SBC, it might not be optimal for simulations of a ring-shaped cloud, where a lot of the grid area is occupied with zero-valued pixels. A possibility could be to simulate the system on a rectangular thin grid, with SBC on the long sides, and PBC on the short ones. However, for simplicity and because the gain in time was not so important, we decided to keep a 2D grid for this case. Moreover, unwrapping the ring on a rectangular grid suppresses possible curvature effects. These effects might be of small magnitude for the size of rings that we use, but subtle effects might still emerge.

For these reasons, it was deemed more reasonable to keep a 2D grid even for ring geometries. In effect, what is changed between SBC and SSBC is simply the shape of the potential in which the cloud evolves, as we will see in the next section (this potential is set to 0 for PBC). For PBC and SBC, the physical size of the box was fixed at 38 μm, while it was set at the slightly higher value of 45 μm for SSBC in order to accommodate the whole ring.

5.1.4 *Calculation of the ground state*

In order to simulate the time evolution of a system, one has first to choose the initial state in which one places the system. Either for natural or seeded demixing, and in order to mimic the experimental sequence, we first need to compute the ground state of the one-component system before the transfer: all the atoms then share the same wave function.

To calculate the system's ground state, a widespread method consists in applying an imaginary time evolution to the system: in the general case, starting from a Schrödinger equation with hamiltonian H, one can write:

$$\frac{\partial \varphi}{\partial t_i} = -\hat{H}\varphi. \tag{5.9}$$

where we have introduced $t_i = it/\hbar$. Interestingly, for an eigenfunction φ_p of $\hat{H}$ associated to the energy E_p, one has:

$$\frac{\partial \varphi_p}{\partial t_i} = -\hat{H}\varphi = -E_p\varphi_p \;\Rightarrow\; \varphi_p(t) = \varphi(0)e^{-t_i E_p}. \tag{5.10}$$

Decomposing φ on the φ_p, and ordering the φ_p so that E_0 is the lowest energy state (we assume that the ground state is not degenerate), one thus has:

$$\varphi(t_i) = \sum_p c_p\varphi_p(t_i) = \sum_p e^{-E_p t_i} c_p\varphi_p(0) \propto c_0 e^{-t_i E_0}\varphi_0(0). \tag{5.11}$$

In other words, excited states decay more rapidly than the ground state, and for a long enough imaginary time evolution, $\varphi(t_i)$ is to a good approximation and up to a renormalisation factor, the state of the system with the lowest energy. This means that we can imaginary time evolve an ansatz in order to compute the system's ground state: we simply need to replace t by it in the algorithm detailed in the previous section; in particular, we will use the same value for dt. The number of iterations N_{im} is chosen so that the computed wave function is to a good approximation the system's ground state; the exact number of iterations needed to do so is discussed in section 5.2.3. The ansatz that we choose must be relatively 'close' to the real ground state for fast convergence, and we thus opt for a homogeneous matrix of real value $\sqrt{n/n_0}$ everywhere:

$$\varphi^0_{\text{im}} = \sqrt{\frac{n}{n_0}}. \tag{5.12}$$

5.1.4.1 *Case of a box geometry*

We can either work with SBC, in which case the wavefunction vanishes at the edge of the grid, or with PBC, where it does not. In the PBC case, we set $V = 0$: eq. 5.12 is already the ground state of the system, and no imaginary time evolution is needed. For SBC, $V \neq 0$, and the ground state's profile is affected by the exact shape that we take for V. We settle for a double erf function, which is represented in Fig. 5.1b:

$$V = 2V_0\left[1 - \left(\frac{\operatorname{erf}\left(\frac{x}{l}\right)}{2} + \frac{\operatorname{erf}\left(\frac{L-x}{l}\right)}{2}\right)\left(\frac{\operatorname{erf}\left(\frac{y}{l}\right)}{2} + \frac{\operatorname{erf}\left(\frac{L-y}{l}\right)}{2}\right)\right],\ x, y \in [0, L], \tag{5.13}$$

where l represents the typical length scale on which the potential varies an is set by the imaging resolution of the system. We can approximate our point spread function by a gaussian of standard deviation 0.5 μm, which in terms of erf function, corresponds to typically $l = 4x_0$ ($x_0 = 0.15$ μm for $N_g = 256$). We settle on this value for every simulation run presented here.

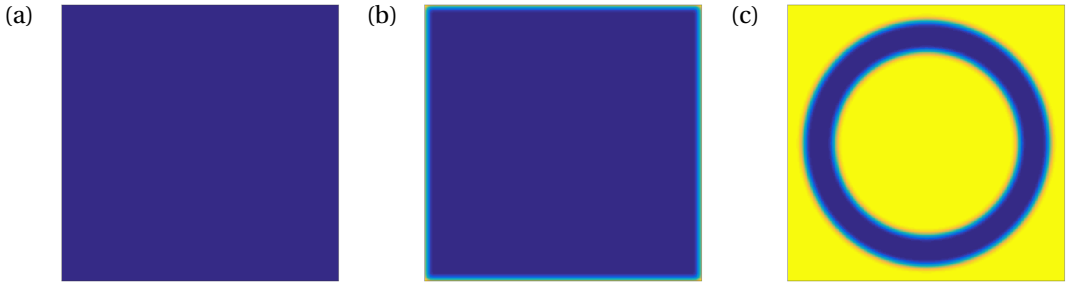

Figure 5.1: Values of the potential V for the PBC scheme (a), the SBC scheme (b), and the SSBC scheme (c). In the first case, the potential is zero everywhere, while it varies on a length scale l for (S)SBC.

As for V_0, it is the typical height of the potential on the edges, corners excepted[2], and we choose $V_0 = 5E_{\text{int}}$. The box potential is represented in Fig. 5.1.

After having imaginary time evolved the ansatz defined on eq. 5.12, we have obtained a matrix φ_{im}: for PBC, this result is totally uniform (and thus the specific parameters that we chose for the imaginary time evolution are not very relevant), while for SPC, φ_{im} goes to zero on a scale of a few pixels. This physically corresponds to the healing length ξ on which the wavefunction varies[3], or to l if $l \gtrsim \xi$.

5.1.4.2 *Case of a ring geometry*

For a ring, the same procedure applies, and the only change is the exact shape of V. To mimic the experimental data, we chose to work with an annulus of inner and outer radii $r_1 = 15$ μm and $r_2 = 20$ μm, respectively. The definition of V is then chosen as:

$$V = \frac{2 + \operatorname{erf}\left(\frac{r-r_2}{l}\right) - \operatorname{erf}\left(\frac{r-r_1}{l}\right)}{2} V_0, \; r \in \left[0, \frac{L}{2}\right]. \tag{5.14}$$

The box potential is represented in Fig. 5.1c.

5.1.5 *Definition of the initial state*

5.1.5.1 *Natural demixing*

Here, we are interested in what happens when a uniform superposition of two immiscible states is created, *i.e.* a situation with no seed. We define the initial state as a superposition of states 1 and 2, sharing the same spatial wavefunction φ_{im}:

2 The value of the function defined in eq. 5.13 is twice as big on the 4 corners of the box than on its straight edges.

3 As a_1, a_2 and a_{12} are very close to each other, so are the different healing lengths involved. As this length scale mostly appears as an order of magnitude, the exact choice of a for the calculation of ξ does not really matter. To fix things, we will consider here that $\xi = 1/\sqrt{2g_1 n}$.

$$\begin{cases} \varphi_1^0 &= \frac{1}{\sqrt{2}}\varphi^{\text{im}} \\ \varphi_2^0 &= \frac{1}{\sqrt{2}}\varphi^{\text{im}} \end{cases} \tag{5.15}$$

It should be noted that while the result of the imaginary time evolution is a ground state of the system before the transfer (up to the convergence of the algorithm), the new state is not a ground state of the superposition as it is not phase separated and our two states are immiscible. For instance, for SBC, the difference between a_1 and a_2, and the addition of an inter-component interaction term a_{12} changes the lengths on which each φ_i^0 vanishes on the edges of the box, and as we will see, this difference in ξ is a motor for the demixing dynamics.

5.1.5.2 *Seeded demixing*

Here, we suppose that we do seed the system with a monomode perturbation of wave vector k, which we also represent by its mode number $m = k_m L/2\pi$ ($m = \bar{R}k_m$ for SSBC, $\bar{R}$ being the average radius of the ring). The idea is to see whether this perturbation grows with time (*i.e.* is dynamically unstable), or simply oscillates at a fixed amplitude (dynamically stable). In order to seed an eigenmode of the system, we define φ_i^0 using eq. 4.16 of the previous chapter: we write $\varphi_i^0 = \varphi^{\text{im}}(1 + \delta\varphi_i) = \varphi^{\text{im}}(1 + \delta n_i/n_i + i\delta\theta_i)$, with:

$$\begin{cases} \delta n_j(\mathbf{r}) &= A_j(\mathbf{k})e^{i(\mathbf{k}\cdot\mathbf{r})} + \text{c.c.} \\ \delta\theta_j(\mathbf{r}) &= B_j(\mathbf{k})e^{i(\mathbf{k}\cdot\mathbf{r})} + \text{c.c.} \end{cases} \tag{5.16}$$

Choosing a normalised, dimensionless perturbation amplitude δA, we can write the coefficients A_i and B_i as:

$$\begin{cases} A_1 &= \delta A \\ A_2 &= A_1 \frac{m^2(c_-^2 - c_1^2)}{g_{12}\hbar^2 \frac{n_{\text{tot}}}{2}} \end{cases} \qquad \begin{cases} B_1 &= \frac{-2im\Omega_-(k)}{\hbar k^2} A_1 \\ B_2 &= \frac{-2im\Omega_-(k)}{\hbar k^2} A_2 \end{cases} \tag{5.17}$$

We then use the matrix φ^{im}:

$$\begin{cases} \varphi_1^0 &= \frac{1}{\sqrt{2}}\varphi^{\text{im}}\left(1 + A_1 f + iB_1 f\right), \\ \varphi_2^0 &= \frac{1}{\sqrt{2}}\varphi^{\text{im}}\left(1 + A_2 f + iB_2 f\right). \end{cases} \tag{5.18}$$

For PBC and SBC[4], the function f is defined as $f = \frac{1}{2}\left(\cos(kx) + \cos(ky)\right)$, while for SSBC, it is $f = \cos(m\theta)(H - V)/H$, with θ the azimuthal angle. An example of initial states is shown for each case in Fig. 5.2.

These equations do not exactly correspond to equation 5.16. For instance, in the SBC case, the form taken by equation 5.16 orders the modulation patterns diagonally, which is incompatible with the square box's geometry. Moreover, f creates patterns along two directions, while equation 5.16 only creates lines. The choice of this shape for f stems from the fact that we intuitively wanted to seed modes that looked like what happened for natural demixing, and thus, that had the same symmetry as the box (see Fig. 5.10 for instance). A more thorough justification of this choice is given in Appendix A; overall, this does not change the prediction from [61].

4 The exact value of k is changed between PBC and SBC in order to take into account the real size of the atomic cloud, which is affected by the healing length and is thus a bit smaller than L for SBC.

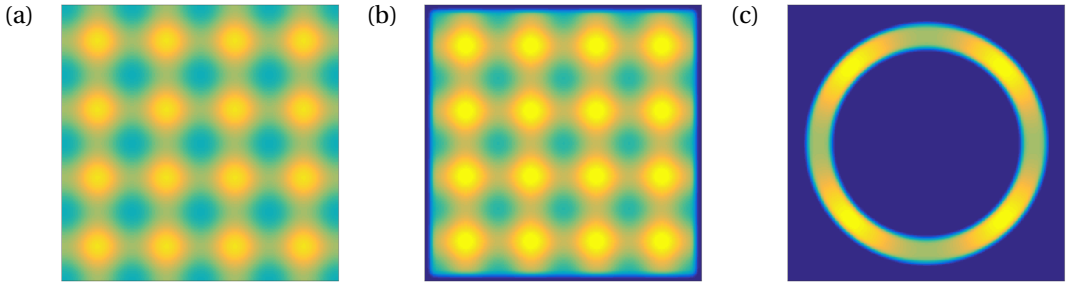

Figure 5.2: Initial density in state 2 for $\delta A = 0.1$ for the PBC scheme (a), the SBC scheme (b), and the SSBC scheme (c). The seeded mode is $m = 4$ for the 3 cases, however, at this density, this corresponds to a stable k_m for (a) and (b), while it is unstable for (c).

We can now perform numerical simulations and compare them to theoretical results. To do so, we first need to define the observables that we will use. Moreover, it can be reassuring to run some tests in order to explore for which parameters our algorithm gives a physical result. This is the aim of the next section.

5.2 PRELIMINARY TESTS

5.2.1 *Choice of observables*

The idea here is to understand in which range of the simulation parameters (dt or N_g typically) do the numerics give a physical result. One can check this by varying these parameters and see when the results deviate from the physical expected behaviour for a simple case. The idea is for instance to seed a certain mode in the system ($\delta A \neq 0$) and compare the mode's oscillation period (if the mode is stable) or its growth time (if it is unstable) to the theoretical prediction.

To do a simple test, we chose here to simulate the evolution of a seeded density perturbation corresponding to the mode 4 of the box. We will work at $n_{\text{tot}} = 30\ \mu\text{m}^{-2}$, in PBC, and keeping other parameters constant, we:

- vary the time step dt,
- vary the number of grid sites N_g,
- vary the total imaginary time evolution T_i (if this simulation is conducted in (S)SBC, where the initial ansatz and the limit of the algorithm are different).

We are then interested in the value of each of these parameters that minimises computation time, while still giving an accurate result. For instance, we look at the minimum value of N_g that we can use before the simulations start missing details at too small length scale, where the computation outcome becomes flawed.

5.2.1.1 *Observables in a box geometry*

As for the choice of an observable, mode 4 is supposed to be stable at this density. We can thus look at the population of this mode, and fit its oscillatory behaviour to extract a period. This

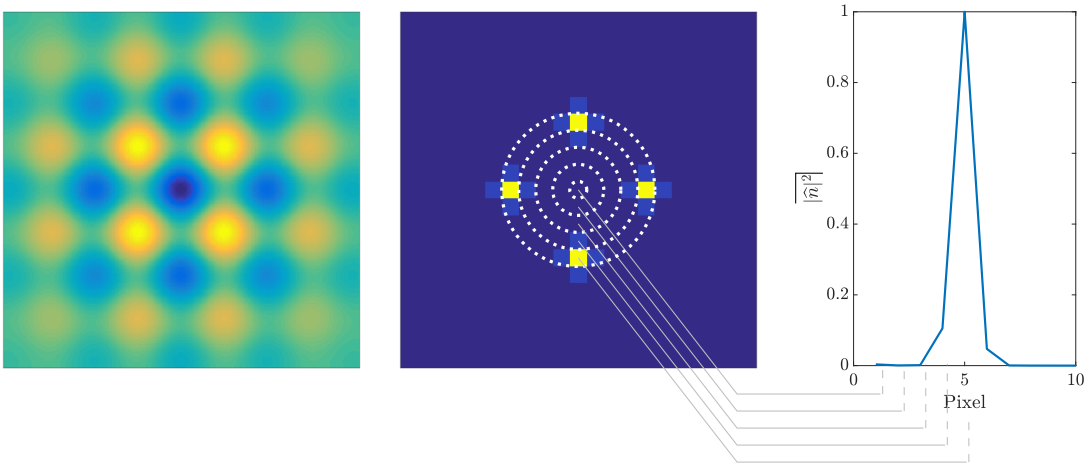

Figure 5.3: Example of our procedure for box geometries. The images shown here do not correspond to numerical simulations. Left: we start from a matrix representing an atomic density. Middle: we then compute the modulus square of its Fourier transform (zoom in the central part; the original matrix has 256 × 256 pixels). Right: we finally compute a radial sum of this quantity (zoom to the low k region). The mode that we observe on the left is approximately the mode 4 of the box (4 maxima), and thus, we observe a peak in the Fast Fourier Transform (FFT) 5 pixels away from the centre, and on the 5$^{\text{th}}$ element of $\overline{|\widehat{n}|^2}$.

period is then compared to the prediction from [61]. To compute our observable, we look at the density of atoms in state 2[5]:

$$n(x, y, t) = |\varphi_2(x, y, t)|^2, \tag{5.19}$$

of which we take the Fourier transform $\widehat{n}$. The derivation from [61] only uses the modulus k of the appearing perturbation, and we thus need to define an observable which adresses all modes (k_x, k_y) with a constant modulus. We chose to work with the radial sum of all elements being at distance k of the continuous: we define the operator $\overline{\cdot|}$ acting on a matrix M in the following way:

$$\overline{M|} = \int_k^{k+dk} M \ \mathrm{d}^2k. \tag{5.20}$$

In other words, $\overline{M|}$ is a 1D vector with element 1 corresponding to the sum of all elements within a certain radius dk, while element 2 corresponds to the sum of all elements in an annulus $[dk, 2dk]$, and so on. A scheme of this procedure is shown in Fig. 5.3.

As $\overline{\widehat{n}|}$ is a complex quantity, we chose to look at $\overline{|\widehat{n}|^2|}(k_m, t)$: for a fixed k_m, this should either oscillate or grow exponentially with time, and we will fit it by either $t \to Ae^{\Omega t}$ (unstable mode) or by $t \to A\cos(\Omega t + \phi)$ (stable mode). Thus, even if we plot the Ωs for stable and unstable modes on the same graph, it physically corresponds to two different things: either a growth rate, or a period.

Finally, due to the squaring, all timescales will be doubled: an oscillation at τ actually means that the original signal oscillates at 2τ. In the results that we show here, this has already been taken into account: all the timescales that we present on this thesis' figures have been divided by

5 The choice of $|2, 0\rangle$ instead of $|1, 0\rangle$, or of $|2, 0\rangle - |1, 0\rangle$, is a bit arbitrary. It is however motivated by the fact that experimentally, we usually only take images of $|2, 0\rangle$. Thus, this definition will enable us to compare simulations and experimental data. Moreover, except on the edges of the box, the densities in $|1, 0\rangle$ and $|2, 0\rangle$ have, to a good approximation, a constant sum everywhere, as can be seen in Fig. 5.10, meaning that there is the same information in both components.

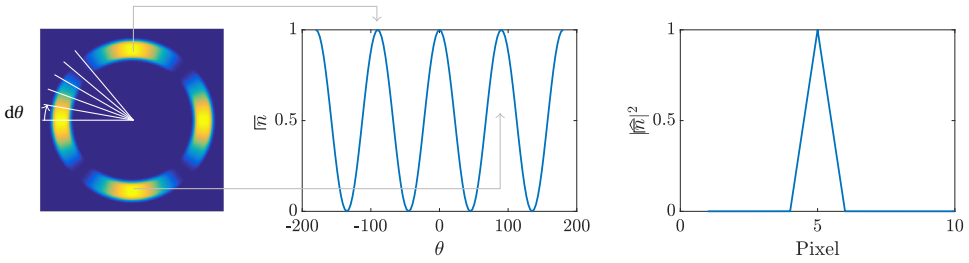

Figure 5.4: Example of our procedure for ring geometries. Left: we start from a 2D matrix with $m = 4$. Middle: for each cone $[\theta, \theta + \mathrm{d}\theta]$, we compute an average of all pixels present in the cone. Pixels outside of the annulus are excluded from the average. The position of two of the maxima in (a) are reported on (b). Right: we finally compute the FFT of this azimuthal sum (zoom to the low k region). The mode that we observe on the left is approximately the mode 4 of the ring (4 maxima), and thus, we observe a peak in the FFT 5 pixels away from the centre.

two. This, however, is not the case when we show plots of $\overline{|\widehat{n}|^2}(t)$. For instance, in Fig. 5.8, the top row shows the evolution of the bare $\overline{|\widehat{n}|^2}(t)$, without any corrective factors. The observed period, $T = 22.3$ ms, corresponds to an actual period of $T_R = 44.6$ ms, which gives $\Omega_- = 2\pi/T_R \simeq 141$ Hz, as can be seen on the bottom row of Fig. 5.8.

5.2.1.2 *Observables in a ring geometry*

For the SSBC case, since the geometry of the system is different, it is more convenient to first transform the 2D matrix into a 1D vector *before* performing a Fourier transform. This is done with an azimuthal average comparable to what is done with the radial sum procedure. First, one defines a region of interest (ROI) in which the atomic density is non zero. Then, an average of all pixels of this ROI between angles $[\theta, \theta + \mathrm{d}\theta]$ is performed. In other terms, we define the operator $\overline{\cdot}$ as:

$$\overline{M} = \frac{\displaystyle\int_{\theta}^{\theta+\mathrm{d}\theta} M \ \mathrm{d}^2k}{\displaystyle\int_{\theta}^{\theta+\mathrm{d}\theta} \mathrm{d}^2k}. \tag{5.21}$$

We obtain an oscillatory signal, which we Fourier transform in order to extract a frequency. A scheme of the whole procedure is shown in Fig. 5.4.

5.2.2 *Choice of the simulation parameters - PBC case*

For the simulations to give reliable results, there are conditions that dt and N_g have to fulfil. For this section, we fix $\delta A = 10^{-3}$; we will see later that with this choice, non linear effects caused by the fact that we look at the square quantity of eq. 5.18 should be negligible.

Conserved quantities: It is sometimes hard to be sure that the result of a simulation corresponds to the question that was asked. The parameters might be wrong, or there might be some mistakes in the code. An easy way to eliminate possible errors is to check for the conservation of some conserved physical quantities. In our case, we check that the total atom number N and the total energy E of the system are conserved throughout the time evolution simulation. Due to numerical rounding errors, it is never exactly the case, but with relative variations of 10^{-10} for E and 10^{-13} for N in the case of periodic boundary conditions (see Fig. 5.5), we can safely assume that this is not an issue.

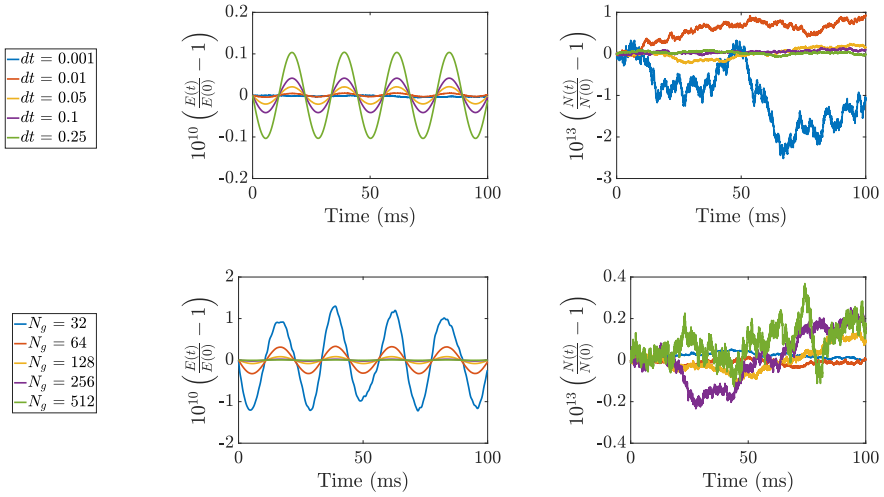

Figure 5.5: Variations of E (left) and N (right) during the real time evolution for varyious dt (top) and N_g (bottom) (PBC, $n_{\text{tot}} = 30\ \mu\text{m}^{-2}$). Both observables are normalised to their first values and compared to one. Note the 10^{10} and 10^{13} prefactors.

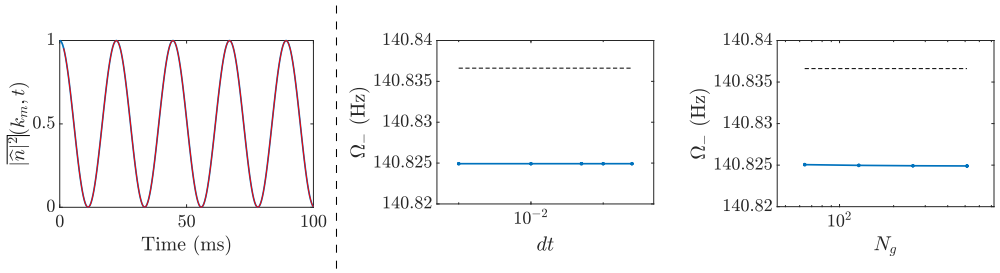

Figure 5.6: Left: Evolution of $\overline{|\widehat{n}|^2}(k_m, t)$ for $m = 4$, $dt = 0.05$, $N_g = 256$, and $\delta A = 10^{-3}$ (the red line is a cosine fit). The function looks very monochromatic, and the same thing goes for all the other dt and N_g that were explored. Middle: From the fit, we extract a pulsation Ω that we plot versus dt. The same thing is done for N_g on the right graph. The dashed black lines are the prediction from [61]. Note the values on the y-scale.

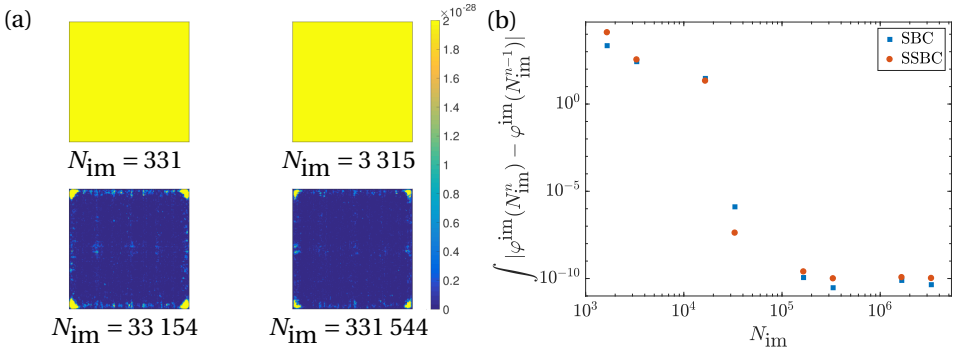

Figure 5.7: Evolution of the calculated ground state for different number of imaginary time steps N_{im} ranging from ~ 70 to $\sim 7 \times 10^5$: (a), modulus of the difference in φ^{im} between two consecutive parameters N_{im}^n and N_{im}^{n-1} in the SBC case (the SSBC case is similar); (b): sum of all pixels value of (a) for SBC (blue squares) and SSBC (red disks). There is no real change from $N_{\text{im}} = 3 \times 10^4$ onwards, and we fix $N_{\text{im}} = 33\,154$ for the rest of discussion.

Condition on dt: as stated above, this method works if dt is small enough, as this technique separates the different parts of the hamiltonian and neglects the commutators. For the time evolution to be exact, one must have $1/dt$ large compared to the energy scales involved in the system. This corresponds to $k^2 dt/2 \ll 1$, $V dt \ll 1$ and $g|\varphi|^2 dt \ll 1$. For a typical atomic density of 30 μm^{-2}, the first term is preponderant and this corresponds to typically $dt \ll 0.2$. For periodic boundary conditions, we actually observe no significant change for $dt < 0.25$ (see Fig. 5.6). Above $dt = 0.3$, however, a numerical problem arises during the simulation and E and N are no longer conserved. We fix $dt = 0.05$ for the rest of the discussion.

Condition on N_g: in order to have a good spatial resolution on the spin dynamics, we need the grid step to be small compared to the spin healing length $\xi_s \sim 1.3$ μm. When working with strict boundary conditions, the gas' healing length $\xi \sim 0.3$ μm should also be resolved, but this more stringent condition comes with a big computational cost. In the end, we settle for $N_g = 256$, except when stated otherwise. For periodic boundary conditions, we actually observe no significant effect of N_g (see Fig. 5.6).

5.2.3 *Condition on T_i - (S)SBC case*

For PBC, the ansatz defined in eq. 5.12 is already a ground state and no imaginary time evolution is needed. For SBC however, this is not the case, and one needs to evolve this ansatz for a certain number of iterations N_{im}.

To choose N_{im}, we kept $N_g = 256$, set $dt = 10^{-2}$, and we varied the total number of steps time N_{im} from ~ 70 to $\sim 7 \times 10^5$. The idea is to stop when the wave function has reached a steady state, while minimising the computation time.

The results are shown in Fig. 5.7. We look at the absolute difference in wave function between two consecutive parameters (Fig. 5.7a), and to the sum of this absolute difference (Fig. 5.7b). The result quickly drops above 7 000 steps, and above 33 000 steps, it has reached a plateau. We thus fix $N_{\text{im}} \simeq 33\,000$ for SBC runs.

Now that we have isolated the parameters for which we have a good accuracy and a reasonable computation time, we want to compare the modes' evolution times to what is predicted in [61]. Unless stated otherwise, dt and N_g are set to the aforementioned values.

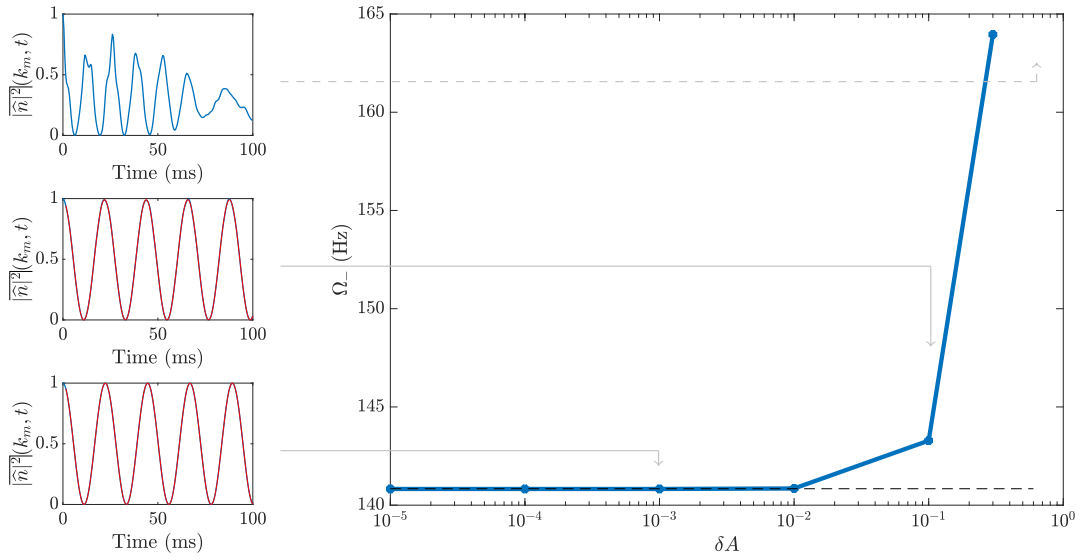

Figure 5.8: Left: we seed the mode 4 of the box (PBC, $n_{\text{tot}} = 30\ \mu\text{m}^{-2}$) and look at $\overline{|\widehat{n}|^2}(k_4, t)$, normalised to its initial value, for different amplitudes: $\delta A = 10^{-3}$ (bottom), $\delta A = 0.1$ (middle), and $\delta A = 0.6$ (top). We then fit this signal to extract a period showed on the right graph (for the first two graphs, the red line is a cosine fit). When the seed's amplitude becomes too large, non-linearities start appearing, which lead to a non monomode signal. The 3D infinite prediction is shown in dashed lines.

5.3 RESULTS

5.3.1 *Periodic boundary conditions*

For this section, there is no need for imaginary time evolution and we fix $N_{\text{im}} = 0$.

5.3.1.1 *Natural demixing*

We first do a simple test: we compute the numerical evolution of a seedless system. In this case, nothing happens, and there is no demixing: this underlines the importance of inhomogeneities (box edges, seed, noise...) as a trigger of the dynamics that we see experimentally. Even if the mixed state is unstable, without a seed, played for instance by the imbalance created by the difference in ξ for SBC, the system's dynamics are frozen.

5.3.1.2 *Seeded demixing*

We want to investigate the influence of the seed's amplitude on the measured period. Indeed, the theoretical model found in [61] assumes that the modulation depth is negligible compared to 1. As a consequence, this model must fail for relatively large seed amplitudes. We can explore the limits of δA for which the model is still applicable by varying this value from 10^{-5} to 0.6 (δA close to 1 corresponds to a full contrast, although the exact value depends on $\Omega_-(k)$ because of the weights B_i). The effect of various δA on the measured period of oscillation is shown in Fig. 5.8. In the end, we fix $\delta A = 10^{-3}$ for this section, for which non linear effects should be negligible. We then seed several modes at an amplitude $\delta A = 10^{-3}$, at two different densities. We recover perfectly the 3D infinite prediction (see Fig. 5.9).

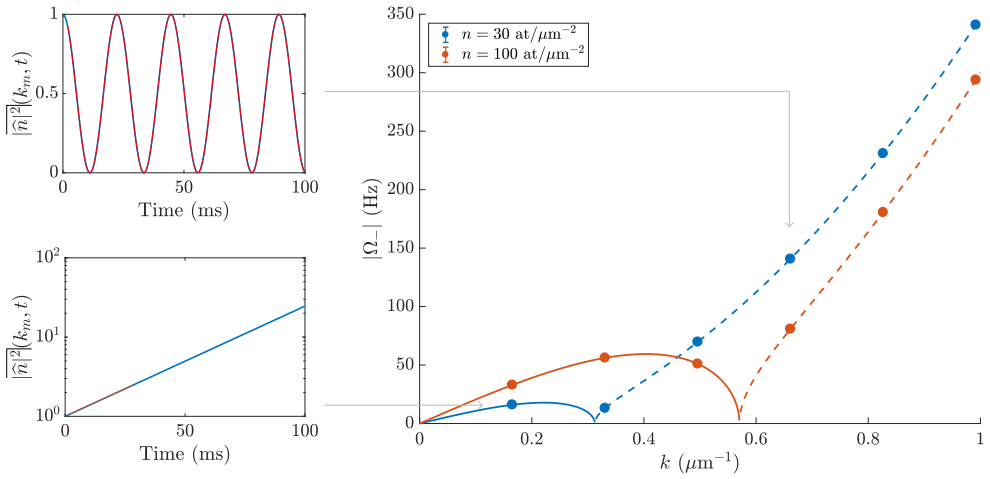

Figure 5.9: Left: example of the time evolution for a stable (top, $m = 4$) and an unstable (bottom, $m = 1$) mode. The red lines are respectively a cosine and an exponential fit. Right: $|\Omega_-|$ for different k at two different atomic densities (PBC, $\delta A = 10^{-3}$). The regions where $\Omega_- \in i\mathbb{R}$ are represented with solid lines, while the regions where $\Omega_- \in \mathbb{R}$ are in dotted lines.

In conclusion, the PBC case strictly follows the theoretical prediction, at least for small seeds. As there is no more physical ingredient in [61] than in the Gross-Pitaevskii code, this is somewhat expected. However, this remains an important benchmark for our simulations, and we can now confidently look at the SBC case. As the seeded modes are no longer eigemodes of the system in this case, the naive prediction from [61] will probably no longer apply, but the numerical study will give us some insight on what happens experimentally.

5.3.2 *Strict boundary conditions*

5.3.2.1 *Natural demixing*

In a box, the edges are where the demixing starts. This is due to the difference in scattering lengths between the two states, which translates into a small difference in healing length. As we compute the ground state for state 1 only, upon transfer to 2, the corresponding wave function tries to adapt its shape and starts showing differences with φ_1 on the edges. This small imbalance is sufficient to trigger the demixing dynamics that then progress from the box edges towards its centre. A typical time evolution is presented in Fig. 5.10. We clearly see wavelets appearing at the limit of the cloud, increasing in amplitude and decreasing in k as times increases: while for $n = 30$ μm^{-2}, the mode present at $t = 20$ ms is approximately $m = 4$, this decreases to $m = 2$ after 50 more ms. This cascade effect is particular to SBC and will also be observed on the experimental data.

As we now have some pixels outside the atomic cloud, we need to exclude them from our observables as to not pollute the signal by adding high frequency artefacts. As a consequence, we chose to remove 10 pixels in each direction starting from the box borders, and we work on the corresponding submatrix, which is totally immersed in the atomic box. Interestingly, the observed behaviour of the different mode populations is no longer exponential or oscillatory, and all modes initially start growing, even those that the 3D infinite model predicts to be stable. Nevertheless, at a k-dependent point that happens quicker for higher k than smaller ones, the modes stop growing, collapse, and further oscillate. Such behaviour is shown in Fig. 5.11.

In order to analyse the typical mode that appears in our system, it is thus practical to look to the average mode present at each time:

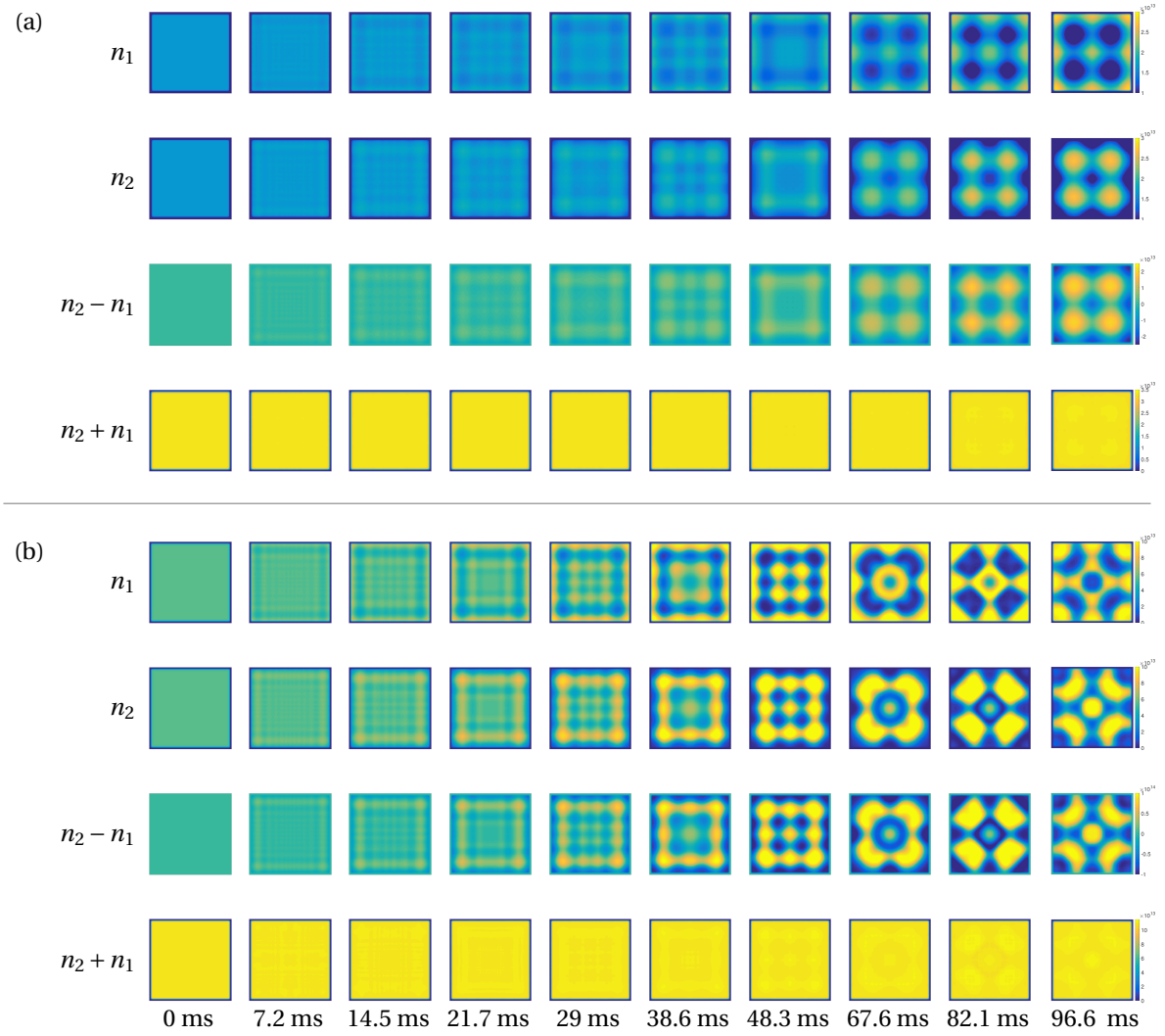

Figure 5.10: Demixing simulation in a box with no seed for $n_{\text{tot}} = 30\ \mu\text{m}^{-2}$ (a) and $n_{\text{tot}} = 100\ \mu\text{m}^{-2}$ (b).

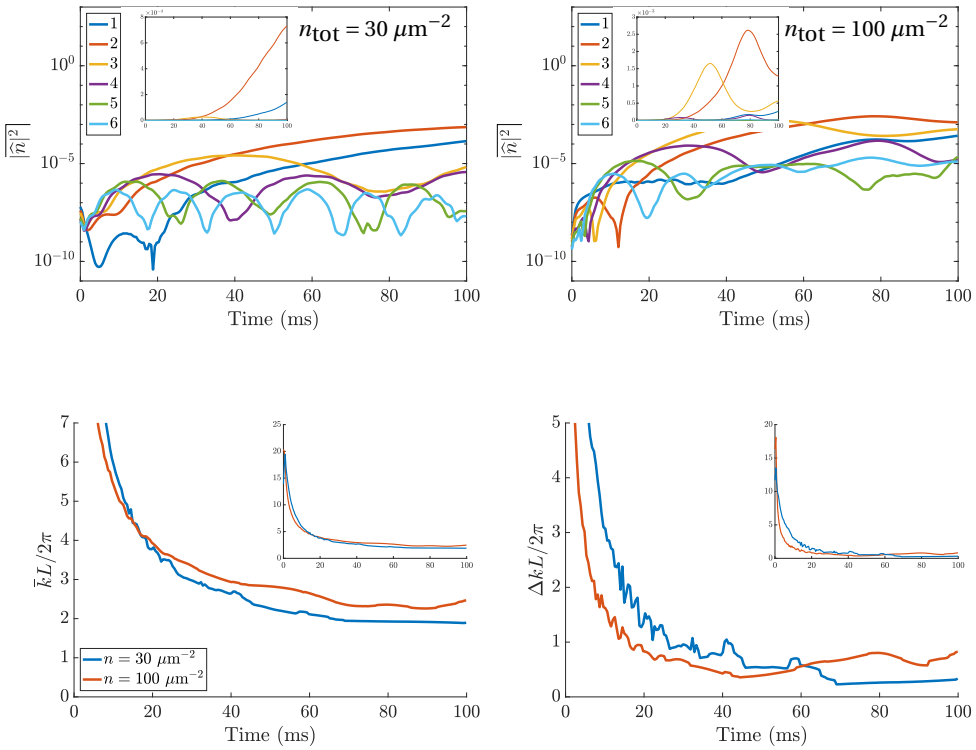

Figure 5.11: Simulation of demixing in a box with no seed. Top: evolution of each mode population $\overline{|\hat{n}|^2}(k_m, t)$ versus time for $n_{\text{tot}} = 30\ \mu\text{m}^{-2}$ (left) and $n_{\text{tot}} = 100\ \mu\text{m}^{-2}$ (right), for $m \in [1, 6]$. The data is shown in semilog scale, while the insets show the same data in a linear scale. Bottom: evolution of $\bar{k}(t)$ (left) and $\Delta k(t)$ (right) in dimensionless units for the same two runs (the insets are the same non-zoomed data). The 3 first graphs show a cascade from high k to smaller k during time evolution, which is also visible in Fig. 5.10.

$$\bar{k} = \frac{\sum_{ij} \sqrt{k_i^2 + k_j^2} |\hat{n}_{ij}|^2}{\sum_{ij} |\hat{n}_{ij}|^2}. \tag{5.22}$$

We also define the standard deviation of the distribution of k:

$$\Delta k = \sqrt{\frac{\sum_{ij} \left(\sqrt{k_i^2 + k_j^2} - \bar{k}\right)^2 |\hat{n}_{ij}|^2}{\sum_{ij} |\hat{n}_{ij}|^2}}. \tag{5.23}$$

However, for a non perfect signal, this definition suffers from a pollution from high values of $\sqrt{k_i^2 + k_j^2}$: because of noise, the contributions from these areas are non negligible, and on experimental images, we observed that $\bar{k}$ could be up to quadrupled. We thus chose to ignore all values in $|\hat{n}_{ij}|^2$ lower than a tenth of its maximum. The average and standard deviation of k with time are presented in Fig 5.11, where the cascade effect is very clear.

5.3.2.2 *Seeded demixing*

We seem to have lost the simple exponential and oscillatory behaviours when we added a potential. There is a way, however, to recover some of the simple predictions of the previous

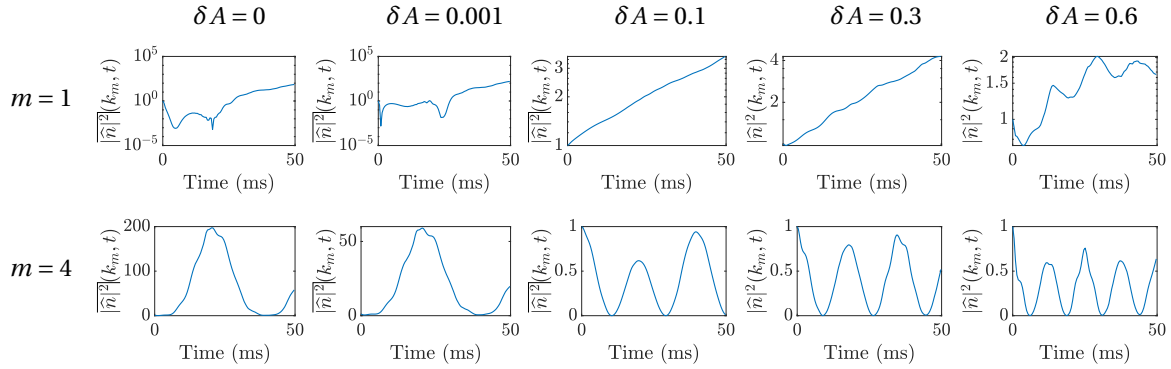

Figure 5.12: Population of the seeded mode for different amplitudes of seed ($n_{\text{tot}} = 30\ \mu\text{m}^{-2}$, SBC). Top row: we seed $m = 1$ and vary δA from 0 to 0.6. We recover an exponential behaviour for a large enough seed, but this behaviour is lost again when δA is increased too much (the graphs are in semi-log scale). Bottom row: same thing for $m = 4$. For too small a seed ($\delta A = 0.001$ for instance), the modulation is amplified before collapsing (see the (linear) scale), but this behaviour is quite different from the oscillatory nature observed for larger δA.

model. For a seed with a large enough δA, the other modes lose of their importance and the seeded mode behaves as expected. The corresponding growth rate or oscillation period does not follow exactly the 3D infinite prediction, even if the prediction gives the correct order of magnitude.

We show in Fig. 5.12 two such examples. For $n_{\text{tot}} = 30\ \mu\text{m}^{-2}$, mode 1 is supposed to grow exponentially. If the seed is too small ($\delta A < 0.01$ typically), its effect is negligible. If it is too large ($\delta A > 0.3$), there is not more 'space' left to grow in, and the mode population stagnates or can even decrease with time. In between the two, we recover an exponential growth with a growth rate of the same order of magnitude as the 3D infinite prediction, although the exact rate depends on the seed's amplitude. Something similar happens for mode 4, which is supposed to be stable: if the seed is too small, the natural demixing is preponderant and this mode (along with all others) starts growing; otherwise, we are able to observe oscillations with about the right time scale. The other modes also grow, but up to the time that we looked (100 ms), the seeded mode remained the most populated one.

Fig. 5.14 sums up the differences between SBC and PBC. For PBC, we took the values from Fig. 5.9: we seed modes $m = 1 - 6$ at an amplitude $\delta A = 0.001$ and extract $\Omega_-(k_m)$. For SBC, we chose to work at $\delta A = 0.1$, an amplitude where exponential and oscillatory behaviour are recovered for most modes. However, for modes with small $|\Omega_-|$ (typically those close to the stable/unstable border), this amplitude is not large enough to recover a clear-cut behaviour (see Fig. 5.13): the time scale of evolution for these modes is too small compared to the natural demixing time, and it is not possible to extract Ω_-. This is the case for mode 2 at $n_{\text{tot}} = 30\ \mu\text{m}^{-2}$, and for modes 3 and 4 at $n_{\text{tot}} = 100\ \mu\text{m}^{-2}$: they were not fitted and the corresponding points do not appear on Fig 5.14. For other modes, we recover something close to the 3D infinite prediction.

In conclusion, the SBC case differs from the PBC case on various points: first, the edges play an important role as they trigger the dynamics that then propagate to the centre. In contrast with the PBC case, all modes initially start growing, and the physics is totally multimode. While these dynamics are richer than in the PBC case, this of course complicates the analysis as we lose the previous exponential and oscillatory behaviours. Secondly, seeding the box with a predetermined mode can be used to recover an approximately monomode system, but the amplitude of the seed needs to be sufficiently large to counterbalance the edges dynamics which

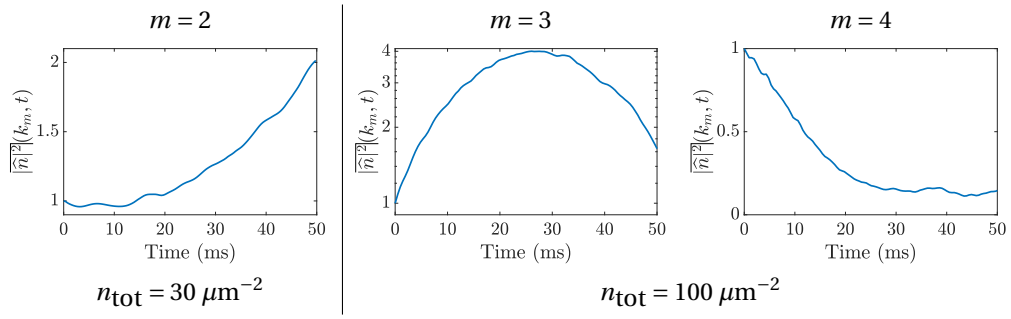

Figure 5.13: For modes too close to the stable/unstable border, the associated evolution time is large compared to the demixing time, and natural demixing takes over. Left: seeding of $m = 2$ for $n_{\text{tot}} = 30\ \mu\text{m}^{-2}$; this mode is supposed to oscillate. Middle: seeding of $m = 3$ for $n_{\text{tot}} = 100\ \mu\text{m}^{-2}$; this mode is supposed to grow exponentially. Right: seeding of $m = 4$ for $n_{\text{tot}} = 100\ \mu\text{m}^{-2}$; this mode is supposed to oscillate.

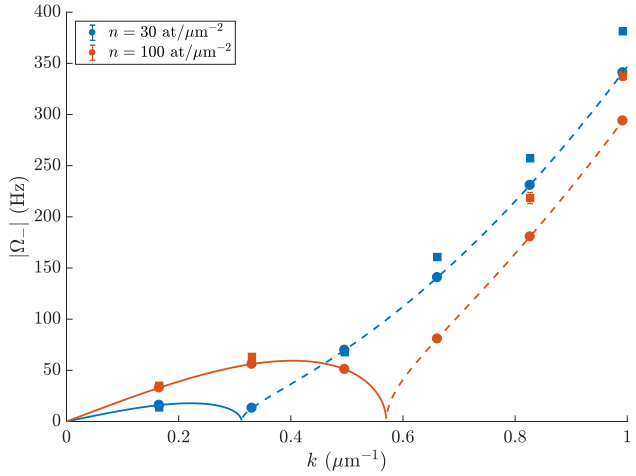

Figure 5.14: Comparison of $\Omega_-(k)$ between PBC (circles, $\delta A = 0.001$) and SBC (squares, $\delta A = 0.1$) at two different densities. For SBC, the mode 2 at $n_{\text{tot}} = 30\ \mu\text{m}^{-2}$ and the modes 3 and 4 at $n_{\text{tot}} = 100\ \mu\text{m}^{-2}$ were excluded as their behaviour was neither really exponential nor oscillatory. The error bars, determined by the fitting procedure, are too small to be seen.

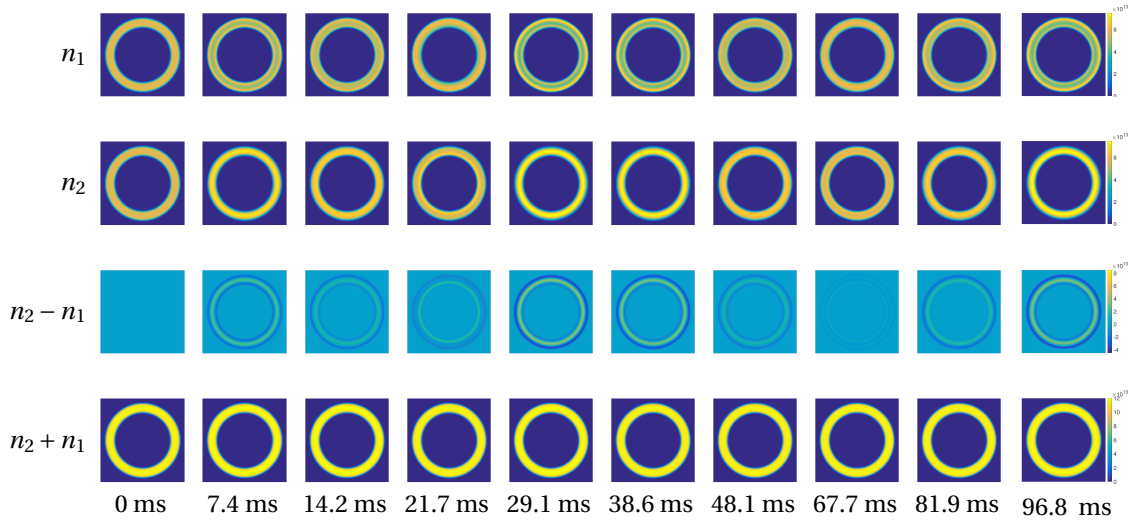

Figure 5.15: Simulation of demixing in SSBC with no seed for $n_{\text{tot}} = 30\ \mu\text{m}^{-2}$. Only radial dynamics with small amplitudes take place up to 100 ms.

would otherwise prevail. Of course, the next question that comes to mind is to know whether the SSBC system is more PBC-like or SBC-like.

5.3.3 *Semi Strict Boundary Conditions*

5.3.3.1 *Natural demixing*

We have seen that in the PBC case, nothing happens for natural demixing as there is no seed on which the instability can grow, while for SBC, the instability starts at the edges of the box and propagates towards the centre. For SSBC, we could be tempted to use the same argument and predict a radial demixing phenomenon consisting of concentring rings. Nevertheless, the annulus only has a width of 5 μm, while the expected demixing length scales are typically[6] $\lambda_f = 28\ \mu$m and $\lambda_f = 16\ \mu$m at $n_{\text{tot}} = 30$ and $100\ \mu\text{m}^{-2}$, respectively. This means that the corresponding instability simply does not have enough space to grow in this direction, and that radial demixing is essentially frozen.

As can be seen in Fig. 5.15, some radial dynamics do develop a bit, but simply do not reach the same amplitude as what happens for SBC. Without the help of an additional trigger (noise, in the experimental case), nothing more happens, and there is no azimuthal demixing.

5.3.3.2 *Seeded demixing*

We can now try to seed different modes in a ring and see if we recover the theoretical dispersion relation. We first check at what amplitude we can seed the system. It appears that while there is no lower limit for stable modes, an unstable mode seeded with too low an amplitude only grows marginally, and way slower than what is expected (see Fig. 5.16). The reason for this is not very clear. Moreover, for stable modes, there is a small discrepancy between the theoretical prediction and the observed period (see Fig. 5.17). This is likely to be due to an ambiguity in the definition of $k_m = m/\bar{R}$: for $\bar{R}$, we took the average of the inner and the outer radii, *i.e.* $\bar{R} = 17.5\ \mu$m. However, the actual size involved might not be exactly that one. The typical error in Ω is 5 %, while the change in $\bar{R}$ necessary to recover the theoretical prediction is 0.35 μm. This effect is more visible for large m, which might explain why it is more pronounced for stable modes (see Fig. 5.18).

6 The length scale λ_f and time scale t_f of the instability are the ones defined in the previous chapter.

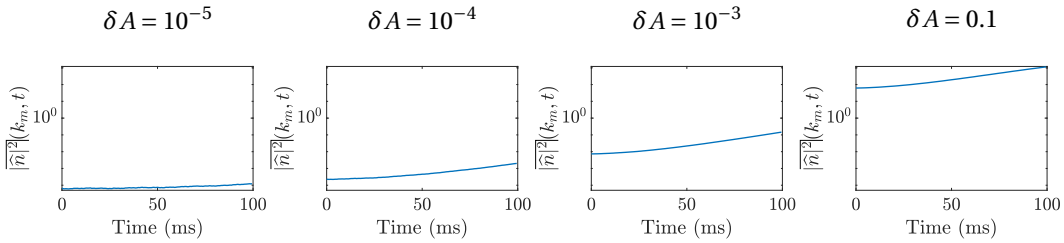

Figure 5.16: For unstable modes, below typically $\delta A = 10^{-4}$, the seed only grows marginally, with a growth rate lower than what is expected. Here, we seed $m = 4$ and look at its population with time. Because of the radial edges, the seed is not exactly an eigenmode of the system, and the initial growth is not exactly exponential as the system needs some time to adjust. When the growth has become exponential (here, when the graph looks like a line), we see that the growth rate for $\delta A = 10^{-5}$ (the slope of the curve at long times) is much lower than for $\delta A = 10^{-3}$.

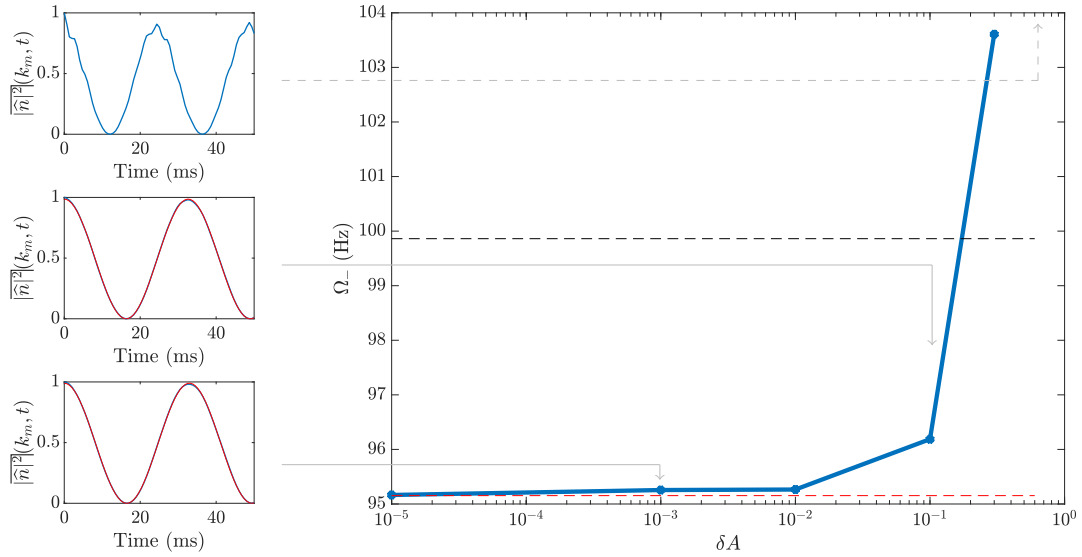

Figure 5.17: Left: we seed mode 10 for $\delta A = 10^{-3}$ (bottom), $\delta A = 0.1$ (middle), and $\delta A = 0.6$ (top). For stable modes, there is no minimal excitation threshold, and we recover something very similar to the PBC case. Right: effect of δA on Ω_-. The theoretical prediction is shown in black for $\bar{R} = 17.5$ μm, and in red for $\bar{R} = 17.85$ μm. The discrepancy between what we expect and what we observe is typically 5 %.

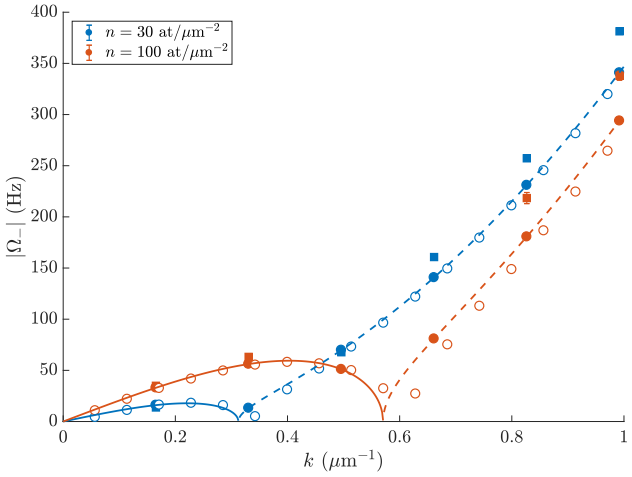

Figure 5.18: Comparing $\Omega_-(k)$ between PBC (filled circles, $\delta A = 0.001$), SBC (filled squares, $\delta A = 0.1$), and SSBC (open circles, $\delta A = 0.1$) at two different densities. For SBC, the mode 2 at $n_{\text{tot}} = 30$ μm^{-2} and the modes 3 and 4 at $n_{\text{tot}} = 100$ μm^{-2} were excluded as their behaviour was neither really exponential nor oscillatory.

In the end, we chose to keep $\delta A = 0.1$, where we should to a good extent recover the prediction from [61]. We then seed the system with modes $m = 1 - 17$ at the two usual densities. We mostly recover the theoretical prediction, up to a few percents.

CONCLUSION

In conclusion, we are able to recover the 3D infinite prediction for periodic boundary conditions at relatively low seeding amplitudes. For strict boundary conditions, however, the edges of the box take a more important role. For natural demixing, we observe patterns appearing at the edges of the box that propagate towards its centre; this is associated with a cascade of both $\bar{k}$ and Δk that will be observed experimentally in the next chapters. For seeded demixing, a very small seed has basically no impact, but we recover an exponential or oscillatory behaviour for important δA. However, the associated time scale deviates from the theoretical prediction. Finally, in the SSBC case, nothing is observed azimuthally for natural demixing, while seeded dynamics abide, to a good extent, by the theoretical prediction. A summary is presented on Table 5.2.

	PBC 💡: $\overline{\lvert\widehat{n}\rvert^2}$	SBC 💡: $\overline{\lvert\widehat{n}\rvert^2}$	SSBC 💡: $\lvert\overline{\widehat{n}}\rvert^2$
Natural	 👁: $\emptyset$	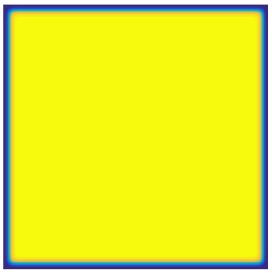 👁: - All k grow - Growth $\neq$ exp	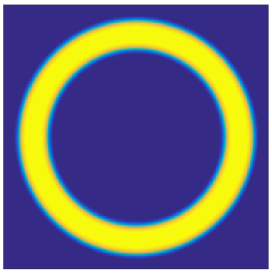 👁: - Radial dynamics - $\emptyset$ Azimuthally
Seeded	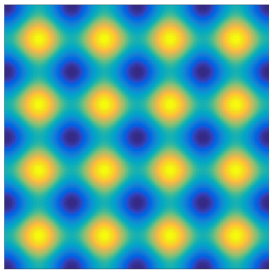 👁: - Exp if unstable - Osc if stable	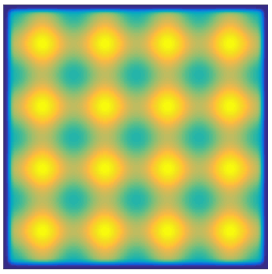 👁: - Exp/osc is δA large enough	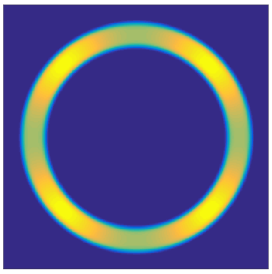 👁: - Exp if $\delta A > \delta A_{\text{crit}}$ - Osc $\forall\ \delta A$

Table 5.2: Summary of the different type of simulations, with 💡 standing for the chosen observable and 👁 for what is observed.

6

DEMIXING IN RING GEOMETRIES

We have seen in Chapter 4 that in the case of an immiscible mixture, a system phase separates with a certain length and time scale predicted in [61]. However, this model assumes an infinite system with periodic boundary conditions, which is of course hard to implement experimentally. In order to realise periodic boundary conditions, we confine our atoms on a ring, and look at what happens for both natural demixing and seeded dynamics. This also has the advantage of involving larger length scales for a given surface in the atomic plane, which in turn means that we have access to lower k. We will first describe the preparation of our sample, then treat the case of natural demixing, and then finish with the seeded case.

6.1 DATA TAKING AND ANALYSIS STRATEGY

6.1.1 *Preparation of the atomic box*

In order to have a good atomic density, simply flashing a ring pattern on DMD1 was not optimal, and we used a movie to increase the loading efficiency of the ring. To do so, we created N different images and had DMD1 flash them one after the other, with a time dt between two images. The first image was a disk of radius R_i, and from the second image onward, we created a hole in the centre of the disk that would increase in size, while R_i would decrease to reach the final value R_f that we wanted. If dt is small enough (basically if the 'speed' of the disk front is small compared to the speed of sound), the atoms see a continuous change and adapt to the decreasing box size by increasing their density. As the green box's potential is kept at a low value during this process, any excess of energy is dissipated through evaporation, and the temperature remains constant. In the end, we chose $N = 20$ and $dt = 10$ ms. The images that were used to compose the movie are shown in Fig. 6.1.

We tried different values of R_i and settled on the one that maximised the final OD. This value depends on the desired radius R_f; an example for $R_f = 20$ μm showing the optimisation of R_i is depicted in Fig. 6.1.

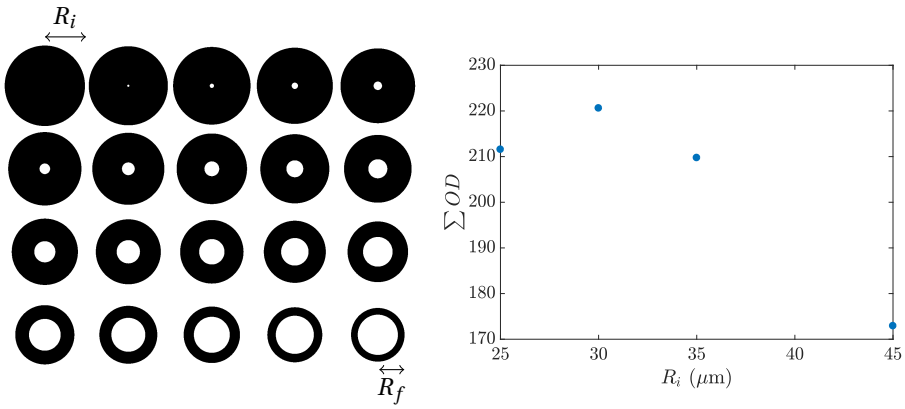

Figure 6.1: Left: images used for the movie: a disk of initial radius R_i is transformed into a ring of outer radius $R_f = 20$ μm (the inner radius here is 15 μm). Right: effect of R_i on the ring's loading: we vary R_i and compute in each case the sum of all the pixels' OD. We find that for this R_f, it is maximal for $R_i = 30$ μm.

We worked with 3 kind of 'shapes' for this chapter: small ring, large ring, and cut ring. The large ring had external and internal radii of 20 and 15 μm, while they were 15 and 10 μm for the small one. As for the cut ring, it was a large ring open by 4 μm on one side. We used it to see what happened when we reintroduced strict boundary conditions in the system: this cut, which acted as a seed for the demixing dynamics, basically set the phase of the appearing patterns, as we will see later.

6.1.2 *Initial state imprinting*

For these experiments, we tried two different protocols. We could either let the system demix naturally by performing a 50/50 MW transfer, or seed the system with a certain wave vector k using our Raman beams. In order to spatially modulate the Raman transfer, we used a grey-levelled DMD3 to modulate the light intensity that we sent on the atoms, and thus the fraction transferred from $|1,0\rangle$ to $|2,0\rangle$.

As we have done during the previous chapter, we would like to imprint a density modulation:

$$n(x,y) = n_{\text{tot}}\left(\frac{1}{2} + A\cos(m\theta)\right), \quad \text{where } \theta = \arg(x+iy) \text{ and } m \in \mathbb{N}. \tag{6.1}$$

Moreover, the transferred fraction can be written as $F(x,y) = \sin\left(\frac{\pi}{2}\frac{t_R}{T(x,y)}\right)^2$ with t_R the time during which the Raman are flashed, and T the time necessary for a π-pulse. This time is inversely proportional to the intensity sent by the DMD, so that with a pattern $P(x,y)$ on DMD3:

$$P(x,y) = \frac{2}{\pi}\text{asin}\left(\sqrt{\frac{1}{2} + A\cos(\theta m)}\right), \tag{6.2}$$

we end up with the desired density modulation.

It is important to note that here, we cannot seed an eigenmode as defined in eq. 5.18 as we have no control over the phase of the wave function. This corresponds to taking $B_i = 0$ and $A_1 = -A_2$ in eq. 5.18. Moreover, we can only define a modulation in density here, and not in wave function, as was the case for the previous chapter. In particular, we defined δA as:

$$\varphi_i = \varphi_i^0(1 + \delta A f) \Rightarrow n_i = n_{\text{tot}}\left(\frac{1}{2} + \delta A f + \frac{\delta A^2}{2}f^2\right), \tag{6.3}$$

where n_i is the atomic density of component i but $n_{\text{tot}} = n_1 + n_2$ represents the total atomic density. For small modulations, this leads to $\delta A \simeq A$, but to this relation does not stand at larger ones. In the rest of this thesis, we choose to work with the experimental parameter A, instead of the theoretical parameter δA.

In the end, we conducted experiments for various densities ranging from typically 10 to 80 μm^{-2}, for different amplitudes ($A = 0$ to $A = 0.5$), and for different seeded modes ($m = 3$ to $m = 12$, defined as modes of wave vectors $k_m = 2\pi m/\bar{L} = m/\bar{R}$, where $\bar{L}$ and $\bar{R}$ correspond respectively to the annulus' average circumference (the ring's middle line) and to the average radius (average of the inner and outer radii)).

6.1.3 *Analysis strategy*

For each demixing time, we typically have 10 different iterations, which we would naturally like to average. For non-cut rings, however, we cannot start by taking the mean of the different shots as the patterns are not phase-locked and do not always appear at the same position. We thus need an intermediate operation.

We opted for the following procedure for each run (cut or non cut): first, we need to transform our OD matrix (mostly non-zero on a ring) into a 1D vector that we can Fourier-analyse. As for

the previous chapter, we thus start by azimuthally averaging our OD[1] matrix. Each point of this vector $\overline{n}$ corresponds to the average of a 'ring arc' of extension $\mathrm{d}\theta = 2\pi/N_b$, where N_b is the number of bins used.

We then take the squared modulus of the Fourier transform's of $\overline{n}$, and average this $|\widehat{\overline{n}}|^2$ over different iterations for better signal to noise ratio. We finally look at the evolution of each mode population $\langle|\widehat{\overline{n}}|^2\rangle(k_m, t)$ with time (we will drop the $\langle\cdot\rangle$ notation from now on).

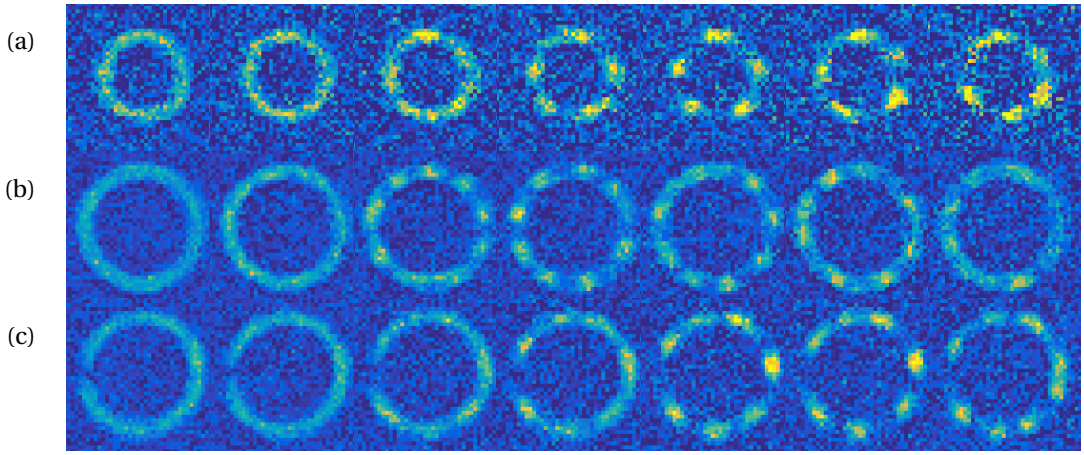

Figure 6.2: Examples of natural demixing experiments in rings of inner and outer radii 10 and 15 μm (top), and 15 and 20 μm (middle/bottom). The bottom ring is cut on its left side. No average has been performed as the blob's locations are not fixed for the top and middle row.

Now that we have defined our observables, the easiest experiment that comes to mind is to prepare an atomic ring and simply let it demix. In this case, we have seen that no demixing happens in a perfect $T = 0$ system. However, we can see in Fig. 6.2 that this is clearly not the case here, meaning that here, the demixing is triggered by the noise present in the system. Moreover, we can wonder whether the dynamics are different when we reintroduce strict boundary conditions. In other words, do open rings and closed ones behave differently?

6.2 NATURAL DEMIXING

In this section, we create a 50/50 mixture with MW. Raman beams are not used at all. We typically varied the atomic density between 15 and 80 $\mu\mathrm{m}^{-2}$ and looked at the density dependence of the appearing mode.

6.2.1 *Phase analysis*

As seen in Chapter 5, the role of edges is important in demixing: the dynamics start there and then propagate towards the centre. In a thin ring, however, the system has no edge[2], and the position of the pattern will be set by small, randomly located density defects. On the other hand, in a cut ring, the dynamics start at the cut and propagate like waves towards the point symmetrically opposed to it. This sets the pattern's phase.

1 Throughout this chapter, we only look at the density n of atoms in $|2, 0\rangle$. We seldom image $|1, 0\rangle$ as this doubles the time needed for data taking; however, we did check on several occasions that a maximum of $|2, 0\rangle$ do correspond to a minimum in $|1, 0\rangle$, and vice versa.

2 The radial edges do not count that much as the thickness of the ring is smaller than the typical appearing length scale, which prevents radial demixing. In this sense, the radial dynamics are essentially frozen and everything happens azimuthally.

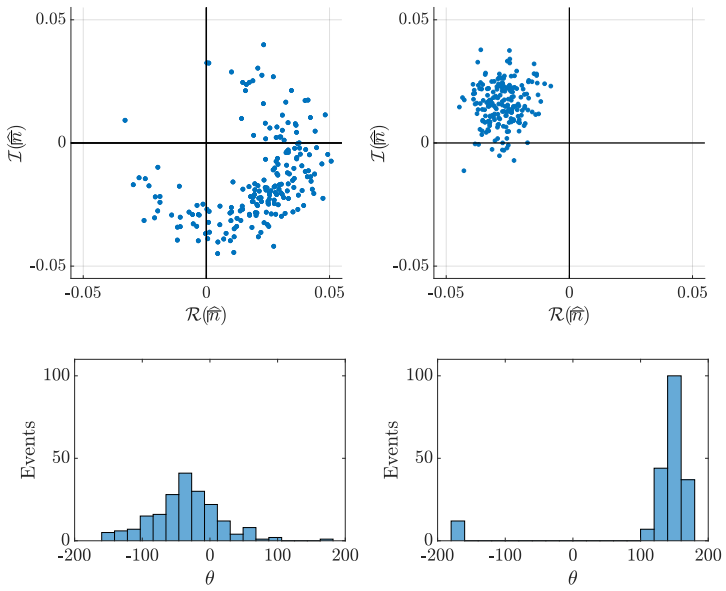

Figure 6.3: Phase distribution for non cut (left) and cut (right) rings. The density of the ring is $n_{\text{tot}} \simeq 38\ \mu\text{m}^{-2}$. The time of observation is chosen so that the patterns are the most visible, in this case $t = 70$ ms. We plot the results in two different fashions: the top row shows the Fourier component of the largest populated mode drawn in the complex plane. If the pattern's phase is truly random, we expect to see a ring: we see that this is more or less the case for a non cut ring (although the distribution is not totally uniform as some constant ring inhomogeneity always seed the dynamics), while for a cut ring, the points are way more localised, illustrating the role played by the borders. The bottom row displays the same data as a phase histogram: we can see that the width of the distribution is far larger in the non cut case than in the cut one.

This can be seen by choosing the time where the pattern is the most visible and accumulating data about the blobs' locations for a cut and a non cut ring. More precisely, we let a ring with $n_{\text{tot}} \simeq 38\ \mu\text{m}^{-2}$ demix for a time $t = 70$ ms before imaging it, and we accumulate 200 images for each configuration. At this time, the most populated mode is the mode $m = 7 - 8$ for the non cut ring. We can thus look at $\widehat{|n|}(k_m)$: if the locations of the blobs are not fixed, the phase of this number should be random, and we should see an annulus of equally distributed points in the complex plane. If, however, the phase is set by some constraints, like an opening in the ring, the cloud of points should be more localised.

This can be seen in Fig. 6.3: for a non cut ring, the cloud's distribution is more random than for a cut one, although there is a lack of points in the top left corner. This is due to a residual inhomogeneity of the ring: that day, there was always a bit more atoms on the top of the ring, which broke the symmetry of the system. To remedy this problem, we tried to go to smaller disks, where such problems might be less preponderant, and we also tried to lower the power of the vertical confinement, whose defects were believed to be the origin of the inhomogeneity. This, however, did not really give more satisfying results. Nevertheless, even with these homogeneity issues, the result of Fig. 6.3 remains very clear, and shows that having edges in the azimuthal direction does result in a spatially locked pattern.

6.2.2 *Individual mode analysis*

We now try to recover the exponential behaviour discussed in the previous chapters, and we look at $|\widehat{n}|^2(k,t)$. Fixing k, we can perform exponential fits on our observables, and extract a characteristic growth time scale for each mode (see Fig 6.4). As modes do not indefinitely grow and eventually collapse, the fits should be stopped at a certain time. However, the signal can be

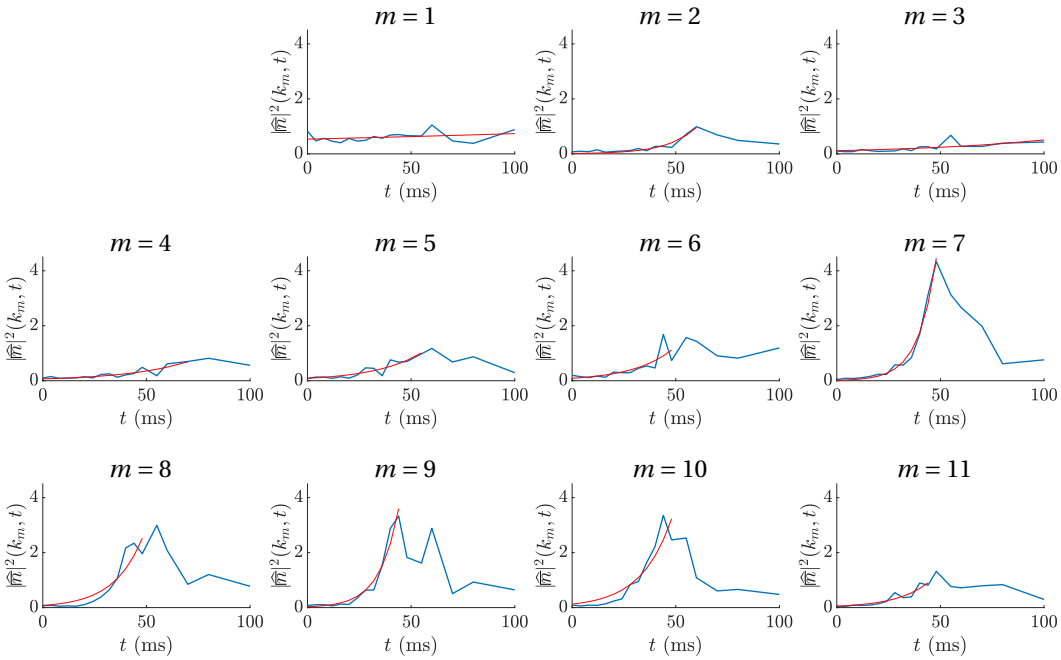

Figure 6.4: Example for the highest density run performed in a large ring. We fit each $|\widehat{\overline{n}}|^2(k_m = m/\bar{R}, t)$, with $m \in \mathbb{N}$, by an exponential (in red), and extract a characteristic time scale. In this example, only modes 7-10 get significantly populated.

a bit noisy, and it is not always obvious where to stop. To have an unbiased choice, we chose to smoothen our signals by performing a moving average on 3 pixels, and by defining the stoping point as the time when this smoothed vector reached its maximum. The fits are then performed on the original, non smoothed vectors.

Performing the aforementioned transformations and looking at the growth rates for each k and for each run, we summarise in Fig. 6.5 our results for each configuration (large, small, or cut rings). As we can see, there are discrepancies between the model and the data: for instance, modes that should be stable still grow marginally, especially for cut rings. This is not a surprise as a result from the previous chapter was that edges usually complicate the simple PBC prediction, and that even stable modes tend to grow in this case.

Moreover, the exact position of $|\Omega_{\text{max}}|$ is not very well predicted, even if its value shows the correct behaviour. This is particularly true for cut rings, where a lot of 'stable' modes still grow. This would tend to designate the cut, creating the aforementioned demixing 'waves', as responsible for this discrepancy.

We can also extract the maximal growth rates for each run. The result is presented in Fig. 6.6, along with the prediction from [61]. On the left, we plot the theoretical prediction with the values from [131] for the s-wave scattering lengths: $a_{11} = 100.9\ a_0$, $a_{22} = 94.9\ a_0$, and $a_{12} = 98.9\ a_0$. However, the agreement with the data is not optimal. Keeping a_{11} and a_{22} fixed, and extracting the slope of $|\Omega_{\text{max}}|(n)$ with a linear fit, yields $a_{12} = 99.3\ a_0$. As one can see, the difference between the value from [131] and what this method gives is relatively small.

Now that we know what mode naturally appears, we want to see if we can force another mode to be populated instead. As for the previous chapter, the idea is to seed a certain mode and see how it evolves with time.

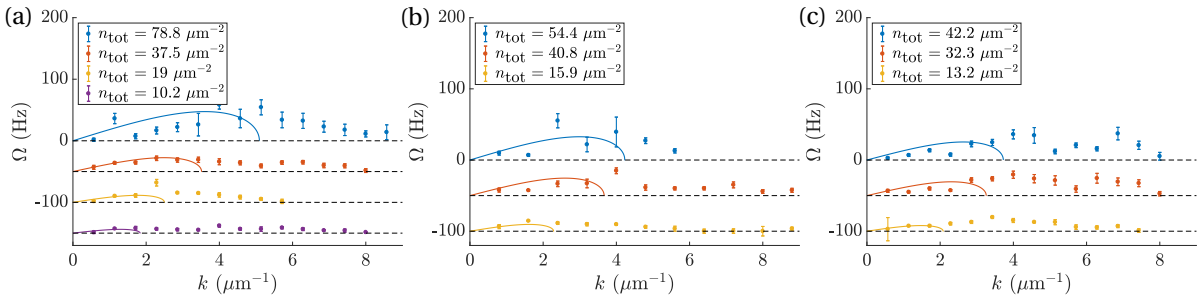

Figure 6.5: Summary of the growth rates for the natural demixing experiments. Figure (a) treats of the large rings case, (b) of the small rings, and (c) of the cut rings. As usual, the solid line represents the theoretical prediction (no free parameter, values from [131]) when $\Omega_- \in i\mathbb{R}$, and the dashed line corresponds to $\Omega_- \in \mathbb{R}$. All the experimental points showed here represent exponential fits: no oscillatory behaviour for the region where $\Omega_- \in \mathbb{R}$ were detected. For clarity, the plots are shifted vertically by 50 Hz each, and the base line is indicated in black dashed lines; the blue plots are not shifted at all.

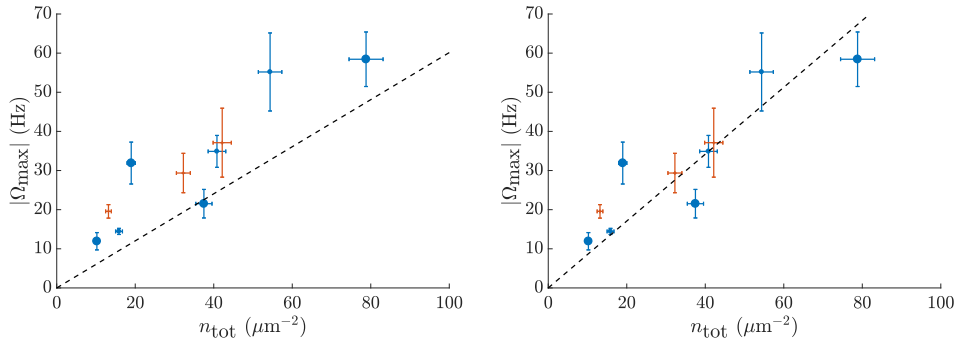

Figure 6.6: Maximum growth rates vs atomic density with the value from [131] (left), and with a fit on the value of a_{12} (right), fixing a_{11} and a_{22} to the values from [131]. This fit yields $a_{12} = 99.3\ a_0$. The black dashed line represents the theoretical prediction. For each plot, a large circular marker represents a run taken for a large ring; a small marker represents a small ring; a red cross represents a cut ring.

6.3 SEEDED DYNAMICS

6.3.1 *Preliminary tests*

6.3.1.1 *Unstable modes*

For this section, we only worked with large rings at one density, $n \simeq 24 \pm 5$ at/μm^2. We first chose to investigate the effect of the seeding amplitude on the evolution of the seeded mode. Typically, numerical simulations performed in the previous chapter showed that for unstable modes, there exists a threshold under which the seeded modulation is not strong enough to drive the system. This minimal amplitude is typically in the 10^{-4} range. Except for $A = 0$, we are always above it, and should not expect to observe such an effect, while the presence of noise should anyway make this prediction inapplicable.

By seeding mode 4 (an unstable mode at this density), we can check whether A has an effect on the mode's growth rate. The results are shown in Fig. 6.7, where the amplitude A is varied from 0 to 0.5.

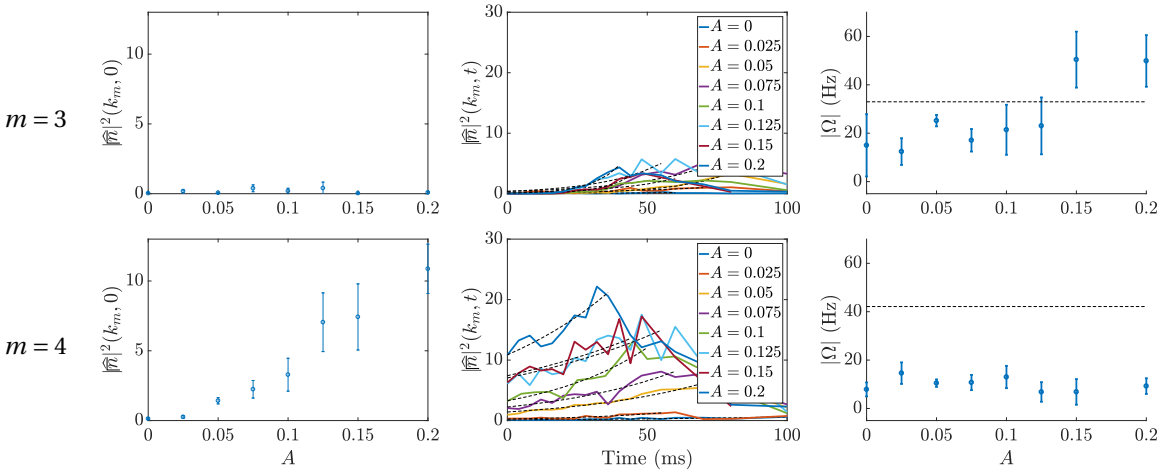

Figure 6.7: Left: Initial mode population for different values of the seed A. The curves for modes $m \neq 4$ is quite flat, and loosely populated, in opposition with the $m = 4$ case: the perturbation that we seed is quite monomode. Middle: time evolution of the modes' populations for different seeds A. Only mode 4 gets macroscopically populated. From this graph, we can extract a growth rate plotted on the right row: on the explored range, $|\Omega|$ seems more or less independent of A for the seeded mode. The black dashed lines correspond to the prediction from [61] with the values from [131].

First, we see that the seeding is quite monomode, as seeding $m = 4$ does not populate other m ($m = 3$ for instance): while the initial population of mode 4 increases as we increase A, the initial population of mode 3 is essentially constant.

Second, when measuring the growth rate of mode 4 for different seeds (see right row), we see that the results are more or less independent of the seed's amplitude: having a large seed merely gives a head start for mode 4, without influencing its growth rate. This is also the case for $A = 0$. The absence of a threshold in this case can be explained by the fact that the experimental system presents some inherent noise absent from the simulations, which can help start the dynamics. As the result does not really depend on the seed's amplitude, we will fix an intermediate value of $A = 0.1$ when working with unstable modes.

6.3.1.2 *Stable modes*

For stable modes, the story is a bit different. As can be seen in Fig. 6.8, below a certain amplitude, the seeded mode does not oscillate and simply collapses. For higher A, we recover a small revival, which we can try to fit by a cosine function. However, for large amplitudes, the excitation is no longer monomode, and we also seed neighbouring modes $m \pm 1$, which oscillate at their own frequencies. Because this oscillation is often even clearer than the one from the seeded mode, we also fit the evolution of these neighbouring modes to extract their periods.

This difference between what we observe and numerical simulations is probably, again, due to the presence of noise. In a noisy system, all modes are initially seeded with a non-zero amplitude, and the most unstable mode (mode 4, here), will rapidly take over. To be able to oscillate, a seed needs to be stronger than mode 4 and get a head start, explaining the need for a large A.

We conclude that we need an amplitude around 0.5 to detect the oscillation of the seeded mode: below this, the oscillation of the seeded mode is almost invisible, and anyways not exploitable. We thus fix $A = 0.5$ for the rest of the chapter when dealing with stable modes.

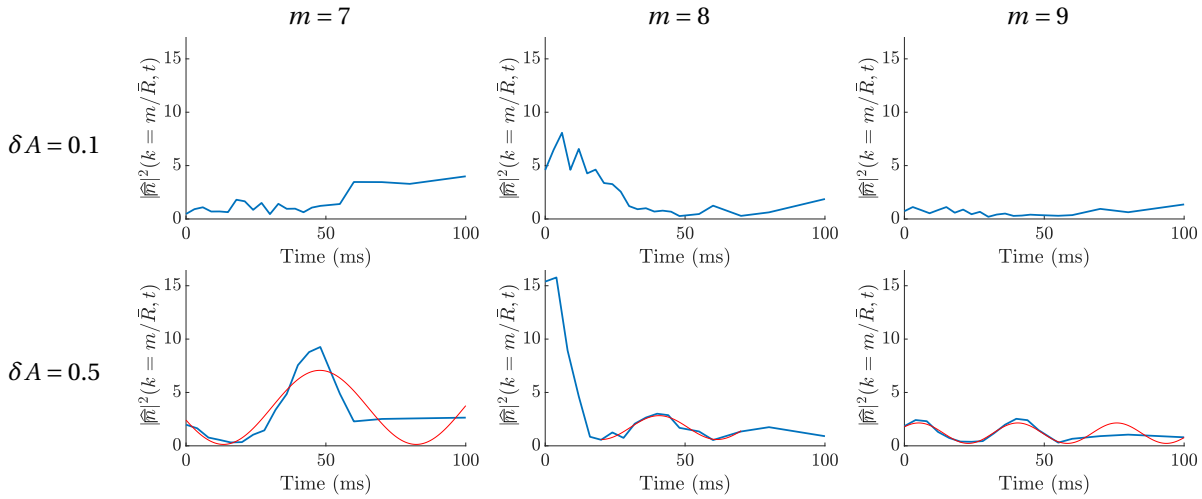

Figure 6.8: We seed mode $m = 8$, which is supposed to oscillate at this density, and observe the populations of modes $m = 7, 8, 9$ for $A = 0.1$ (top) and $A = 0.5$ (bottom). For the lowest amplitude, we simply observe a collapse of the seeded mode, its energy being redistributed to other modes. When increasing A, we observe some oscillations for the main and the neighbouring modes, that we fit by a cosine function (red) to extract the growth rate.

6.3.2 *Dispersion relation*

We can now seed each mode independently and look at their growth rate (for unstable modes) or oscillation periods (for stable ones). As mentioned above, we fix $A = 0.1$ for unstable modes (here corresponding to modes $m = 1 - 6$) and $A = 0.5$ for stables ones ($m > 6$). The result is presented in Fig. 6.9. Because each run has a slightly different density, there is an uncertainty on this parameter, translating into an uncertainty on $|\Omega|$, corresponding to the shaded area. In particular, mode 6 is at the border between the stable and the unstable regions. Experimentally, we saw it grow, and we thus decided to analyse it as such.

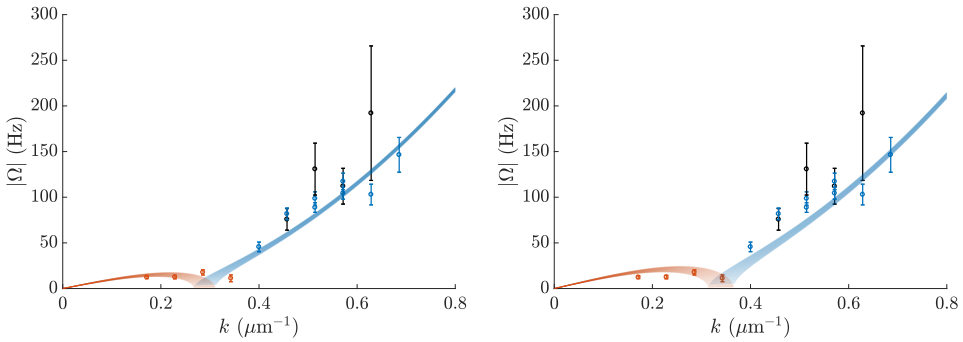

Figure 6.9: Dispersion relation for seeded modes 3-12 at typically $n_{\text{tot}} = 24\ \mu\text{m}^{-2}$. The left graph's theoretical prediction is plotted for $a_{12} = 98.9\ a_0$ (value from [131]), while the right one's correspond to $a_{12} = 99.3\ a_0$ (coming from a fit of Fig. 6.6). The shaded areas indicate the uncertainty in density. The shaded red (blue) region indicates the zone where $\Omega_- \in i\mathbb{R}$ ($\Omega_- \in \mathbb{R}$). Points in red behaved as unstable modes and were fitted with exponentials, while points in blue and black behaved as stable ones and were fitted with a cosine. The black points represent the seeded modes, which give a poor signal. For high A, however, neighbouring modes are also seeded. These modes correspond to the blue points. The uncertainties represented here are the 95 % uncertainties given by the fitting procedure.

For stable modes, we plot both the seeded mode m (in black), and the two neighbouring modes $m \pm 1$ (in blue). As the signal is clearer on these modes, and the fits more accurate, it

can be tempting not to take into account the black points. In this case, we recover something very close to the theoretical prediction. The results from the previous chapter tend to show that at this amplitude, there should not be a large gap between the observed values and the model from [61]. The discrepancies that we see could be explained by errors in the density calibration, or in the value of a_{12} used, as we have seen in Chapter 4 that $\Omega_-(k)$ is extremely sensitive to this parameter. Moreover, the applicability of [61] is debatable here: we do not have an infinite system, and the presence of thermal noise complicates the analysis.

CONCLUSION

In conclusion, we have studied the case of natural and seeded demixing in ring geometries. This geometry is interesting as the demixing dynamics take place in the azimuthal direction, with periodic boundary conditions in the case of a non-cut ring.

Although we do not exactly recover the result from [61], the qualitative predictions are respected: we observe growing modes for low k, oscillatory ones for high k, and the associated timescales vary as expected with density.

It should be noted that the choice of a_{12} can impact a lot the agreement with the model found in [61]. While [131] gives a value of $a_{12} = 98.9\ a_0$, the value 99.3 a_0 gives more accurate results. This is not to much of a stretch; however, a spectroscopy measurement that we performed more recently ([86]) yields $a_{22} = 93.9\ a_0$ and $a_{12} = 100.3\ a_0$, assuming $a_{11} = 100.9\ a_0$, as is detailed in the Outlooks. With these values, and although the mismatch is on the order of the %, the agreement with [61] is very poor. It is not exactly clear where this difference stems from.

Interestingly, the numerical study in the case of a non seeded SSBC system does not predict azimuthal demixing, and we are here in the case where the dynamics are entirely triggered by density noise. Although this has not been tested, an interesting idea would thus be to look at the effect of T on the demixing, or to try to inject additional density noise with the help of a DMD to see how the dynamics are changed.

7

DEMIXING IN SQUARE GEOMETRIES

INTRODUCTION

The 1D case treated during the last chapter was interesting as it enforced PBC in an experimental system. We now want to turn to a more complex system, namely a 2D box. As we have seen in Chapter 5, the physics for this system is fundamentally multimode, and the model from [61] does not easily apply. In this richer system, the analysis that we can conduct is essentially qualitative. However, we will try to outline some general ideas that connect with the naive model.

One of this model's main result is the density's influence on the demixing length and time scales, and we can first check whether this prediction is also verified for a finite box. As the model is written in an infinite system, it can also be interesting to investigate a possible influence of the box's finite size on the appearing dynamics. Finally, all the data presented up to now was essentially taken at zero temperature. While demixing is expected to happen when the temperature's effect is negligible, the scale of the demixing energy remains very small compared to $k_B T$, and the importance of the phase separation dynamics is supposed to fade in a hotter system.

In order to explore these effects, we will first examine the influence of both density and box's size on natural demixing. As there is no simple observable for the natural demixed system, we will try to synthesise the effect of each of these parameters on the appearing pattern, using an average mode number analysis. We will then explore the $T \neq 0$ case before turning to seeded demixing.

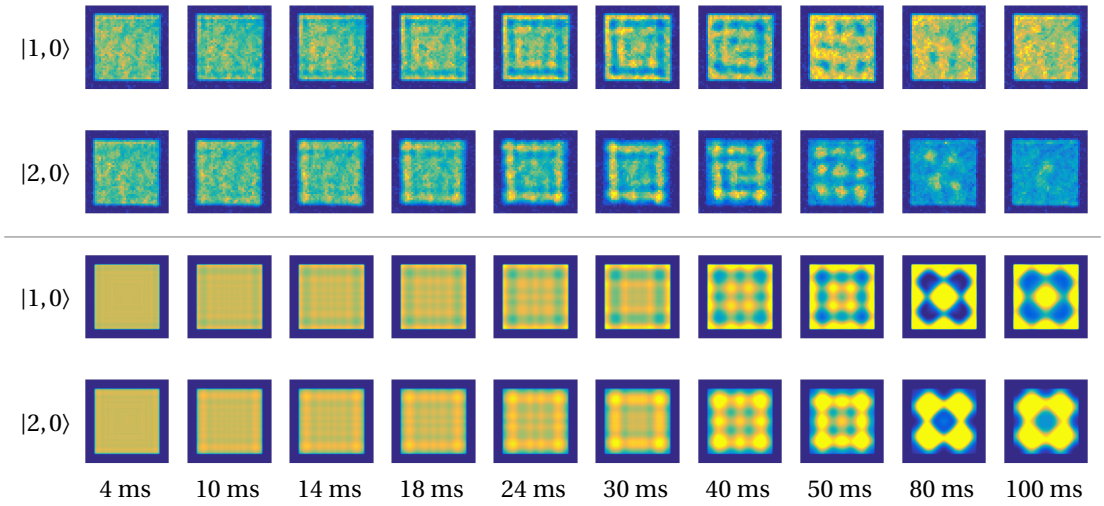

Figure 7.1: The top rows correspond to experimental data and show average images of population $|1,0\rangle$ and $|2,0\rangle$ for a total density initial $n_{\text{tot}} = 67\ \mu\text{m}^{-2}$. The box's size is $40\ \mu\text{m} \times 40\ \mu\text{m}$. We see that the two populations are complementary; as a consequence, we will only work with $|2,0\rangle$ from now on. Bottom rows: simulation images performed for the same density show a very similar behaviour up to typically 50 ms. After that time, the demixing in the experimental system fades away due to both thermal noise and atomic losses.

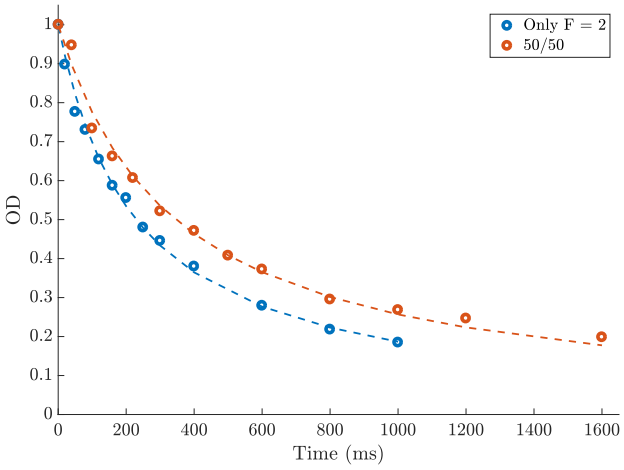

Figure 7.2: Evolution of the OD in $|2,0\rangle$ with time for atoms in an initial 50/50 superposition of $|1,0\rangle$ and $|2,0\rangle$ (red), and for atoms initially in $|2,0\rangle$ only (blue). In both cases, the OD is normalised to its first value. The dashed lines are two-body loss fits ($t \to (1+t/\tau)^{-1}$), yielding respectively $\tau = 345$ and 230 ms. As one can see, the atomic losses depend on the initial density in $|2,0\rangle$, and thus vary from run to run.

7.1 NATURAL DEMIXING

7.1.1 *Varying the atomic density*

Experimentally, the easiest parameter to vary is the atomic density. In this case, [61] predicts that increasing n_{tot} results in a higher k appearing at an earlier time. Is this also the case for an experimental finite box?

In this section, we varied the total atomic density from 17 to 88 μm^{-2}, while the box's side L was fixed at 40 μm. We worked at the lowest temperature possible, which in our case was typically $T = 90$ nK (the exact value varied from run to run). This corresponds to T/T_c ranging from 0.16 to 0.86.

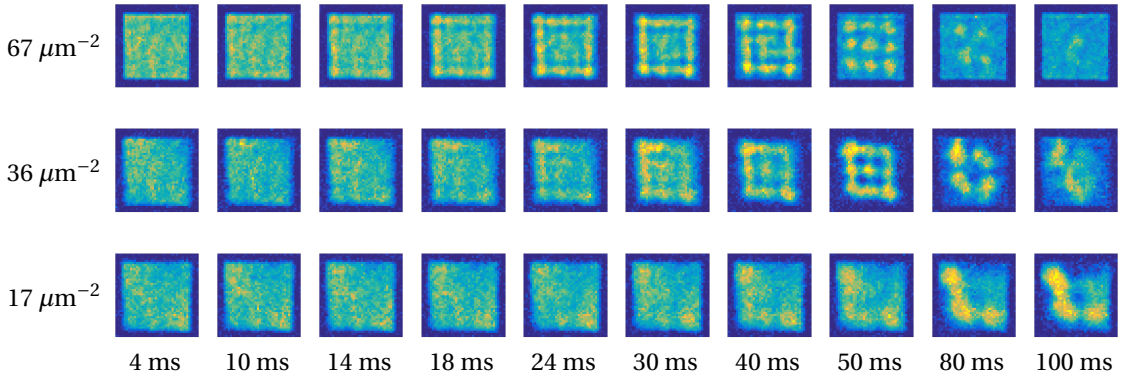

Figure 7.3: Average images of $|2,0\rangle$ populations for total atomic densities $n_{\text{tot}} = 67$ (top), 36 (middle), and 17 μm^{-2} (bottom). The box's size is 40 μm$\times$40 μm, while T is typically set at 90 nK. We see that the higher the density, the faster the patterns appear, and the higher the mode.

As we have seen in Chapter 5, in the case of a box with strict boundary conditions, we do not expect the prediction from [61] to stand, and instead of having one well defined mode, we

should observe a multimode system with many modes present, and a cascade of k from higher to lower values.

Some experimental shots are visible in Fig. 7.1 and 7.3. The first figure shows very clearly four things.

- All the images shown here are averages over typically 10 iterations, and yet, the patterns are very clear. In other words, the blobs do not move from shot to shot, and as for rings, having hard edges locks the position of the patterns.
- Second, as seen with the numerical simulations, the demixing dynamics first appear on the box's borders, and then propagate towards the centre.
- Third, a maximum of $|1,0\rangle$ corresponds to a minimum of $|2,0\rangle$ and vice-versa: imaging one state or the other gives the same information. In the following, and except if stated otherwise, we only use the density in $|2,0\rangle$.
- Fourth, upon apparition, the typical mode number present in the system decreases with time; for instance, the $|2,0\rangle$ density displays approximately $m = 4$ at 40 ms, while this has decayed to $m = 3$ at 50 ms and $m = 2$ at 80 ms. This cascade effect is observed for all parameters.

Overall, the agreement between the observed and simulated densities is very good up to $t \simeq 50$ ms. After this time, the noise present in the experimental system starts to kick in, while the simulations, being conducted at $T = 0$, keep evolving undisturbed. There is also another effect at play: the numerical study conducted in Chapter 5 does not take into account any effect related to atomic losses. However, the lifetime of atoms in $|2,0\rangle$ is smaller than in $|1,0\rangle$, leading to a typical loss of 30 % of the atoms after 100 ms (see Fig. 7.2). This also plays a role in the decay of the demixing contrast, explaining the increasing discrepancy between data and simulations after 50 ms.

Fig. 7.3 shows the time evolution for atoms in $|2,0\rangle$ for different densities. We observe that when the density is increased, the apparition time decreases, while the mean mode number that initially appears increases. This is in agreement with the naive picture where:

$$k_f = \sqrt{2}m|c_-|/\hbar, \text{ and } \tau_f = \hbar/m|c_-|^2 \text{ with } c_- \propto \sqrt{gn/m}. \tag{7.1}$$

This simple model, however, does not explain the observed cascade effect, which is a signature of the system's multimode nature, as observed in the numerical simulations. In this case, many modes initially start growing, which is related to the fact that the patterns only appear on the edges initially, indicating a large $\bar{k}$. The modes then collapse one by one, as can be seen in Fig. 7.4. Modes with larger k collapse faster, so that overall, a cascade of modes, from high k to low k is observed. We can still try to fit each mode's growth by an exponential, however, we find that there is a large difference between the obtained $\Omega(k)$ and the infinite system prediction, as was found in the numerical study. It is thus more convenient to drop the individual mode analysis and focus on a mean mode one.

In this picture, we compute for each time and each iteration i the average wave vector $\bar{k}_i$ present in the system, along with its standard deviation Δk_i, using the matrix $|\hat{n}^{(i)}_{pq}|^2$ as a weight (pq represent the elements of the matrix)[1]:

$$\bar{k}_i = \frac{\sum_{pq} \sqrt{k_p^2 + k_q^2}|\hat{n}^{(i)}_{pq}|^2}{\sum_{pq} |\hat{n}^{(i)}_{pq}|^2} \text{ and } \Delta k_i = \sqrt{\frac{\sum_{pq} \left(\sqrt{k_p^2 + k_q^2} - \bar{k}_i\right)^2 |\hat{n}^{(i)}_{pq}|^2}{\sum_{pq} |\hat{n}^{(i)}_{pq}|^2}}. \tag{7.2}$$

1 This is equivalent to what has been done in the numerical study with $i = 1$.

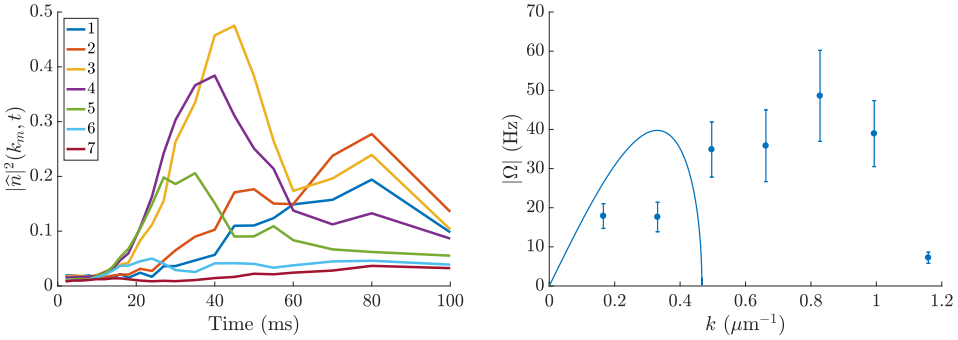

Figure 7.4: Left: evolution of each mode's population $\overline{|\widehat{n}|^2}(k_m, t)$ for $n_{\text{tot}} = 67\ \mu\text{m}^{-2}$, and $L = 40\ \mu$m. As can be seen in Fig. 7.1, each mode grows before collapsing. Modes with a higher k collapse before modes with lower ones, causing a cascade of k on experimental images. Right: we can try to fit these modes's growths with exponentials; however, in this case, the obtained $\Omega(k)$ is very different from what is expected in an infinite system (blue line). This naive picture is no longer applicable, and in order to better understand the system's important features, we decide to focus on a simpler observable: we look at the pattern's average mode number instead of performing this individual mode analysis.

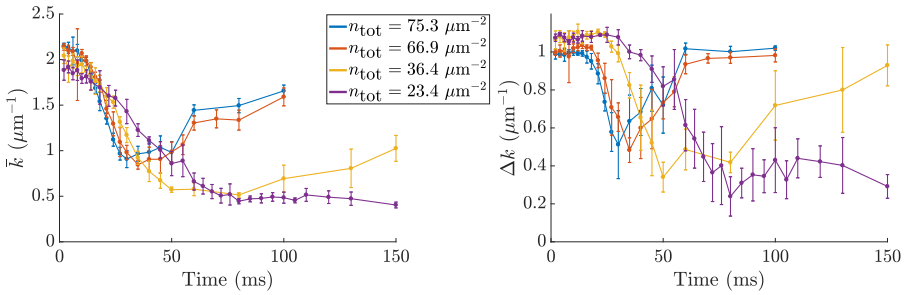

Figure 7.5: Evolution of the mean wave vector $\bar{k}$ present in the system (left), and its standard deviation Δk (right) with time, for boxes of sides $L = 40\ \mu$m and various densities. Each value is averaged over typically 10 iterations; the error bars are the resulting standard deviations over these $\simeq 10$ iterations.

We then take the averages of $\bar{k}_i$ and Δk_i over typically 10 iterations to define our observables $\bar{k}$ and Δk:

$$\bar{k} = \langle \bar{k}_i \rangle_i \ \text{ and } \ \Delta k = \langle \Delta k_i \rangle_i. \tag{7.3}$$

The uncertainty on these observables is defined as the corresponding standard deviation over the 10 iterations.

The evolutions of $\bar{k}$ and Δk with time are presented in Fig. 7.5. Overall, we do observe the expected cascade, up to a certain point: after a time corresponding to the time t_* where Δk is minimal, $\bar{k}$ starts growing again.

This can be explained by the presence of noise in the system. At t_*, the demixing dynamics have reached their apex, and a well defined mode has emerged, explaining the minimum of Δk. After that time, the fact that the cloud is not at $T = 0$ becomes preponderant and the system slowly lapses back to a patternless configuration. In order to correctly reconstruct the system, a lot of modes are needed, which explains why $\bar{k}$ increases again. For smaller densities, this happens at longer times, and for some runs, we even stopped taking data before t_*.

Finally, it should be noted that the lower the density, the lower the chemical potential, and the more homogeneity problems we have. This is not an issue for high density runs; however, this effect is more pregnant for low densities. For instance, on the bottom row of Fig. 7.3, these

fluctuations in n seed the dynamics on the box's top left and bottom right corners, producing a pattern slightly twisted. We will also see this effect when the temperature is increased.

7.1.2 *Varying the box's size*

As we have seen in the numerical study, the effect of the box's edges are of paramount importance as they are the features where the demixing starts in a finite system. It is then natural to wonder whether L plays an important role in the observed dynamics. Particularly, does $\bar{k}$ depend on L?

In this section, we kept the density and the temperature constant and varied the box's side L between[2] 20 μm and 40 μm. We typically have $n_{\text{tot}} = 82\ \mu\text{m}^{-2}$.

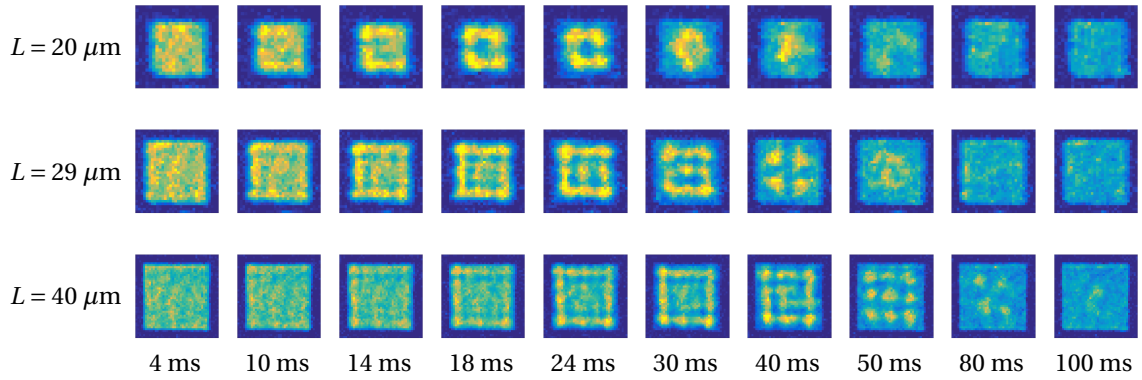

Figure 7.6: Time evolution of the $|2, 0\rangle$ density for $L = 20$, 29, and 40 μm. All the densities are close to each other (typically 82 μm^{-2}). We observe more or less equivalent k at equivalent times.

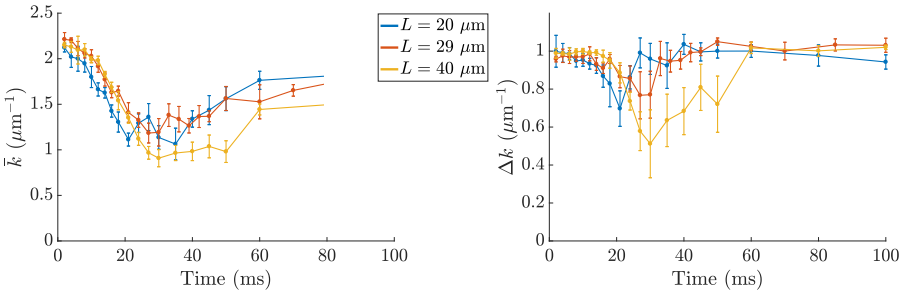

Figure 7.7: Evolution of the mean wave vector $\bar{k}$ present in the system (left), and its standard deviation Δk (right) with time, for boxes of sides $L = 20$, 29, ans 40 μm. The total density is typically 80 μm^{-2}. Each value is averaged over typically 10 iterations; the error bars are the resulting standard deviations over these 10 iterations.

Fig. 7.6 shows the patterns' evolution in each box, while Fig. 7.7 shows the variations of $\bar{k}$ and Δk with time. We observe small differences between the three runs which might be due to small density variations or experimental noise. Typically, the smallest box having the highest density, it is the one that displays the fastest dynamics, while as expected, for the biggest box, as n is decreased, the dynamics are a bit slower. Overall, the differences seem small and we can conclude that the box's size has a negligible effect: even though the number of lobes observed is different, the emerging k is more or less the same.

2 We also tried a box with $L = 55\ \mu$m; however, the box's filling was less optimal in that case, leading to density typically halved. In order to study the effect of L alone, we chose not to take this run into account here.

7.1.3 *Visibility analysis*

As the physics is now multimode and as the prediction from [61] has failed, there is no naive length or time scale that we can naturally define. The idea is thus to define a parameter replacing τ_f and λ_f in order to synthesise our previous results.

In order to measure the changes in the dynamics due to variations of the experimental parameters, we could look at the time t_* for which Δk is minimal, and the associated $k_* = \bar{k}(t_*)$. This choice is motivated by the fact that while τ_f is not a relevant parameter here, t_* is still a typical time associated with the apparition of demixing, while k_* represents the most visible mode. In the dynamical instability picture, this would correspond to the most unstable mode associated to the wave vector k_f. In the case when t_* is the last time observed, we do not take the corresponding run into account as we cannot be sure whether Δk would keep on decreasing after t_* or not.

The evolution of t_* and k_* with density is presented in Fig. 7.8, along with the t_f and k_f related to an infinite system (throughout this chapter, we use the values from [131] for the a_{ij}). Although, t_* and k_* are not the scales associated with the demixing dynamics in PBC, one can see that they still follow the PBC tendencies.

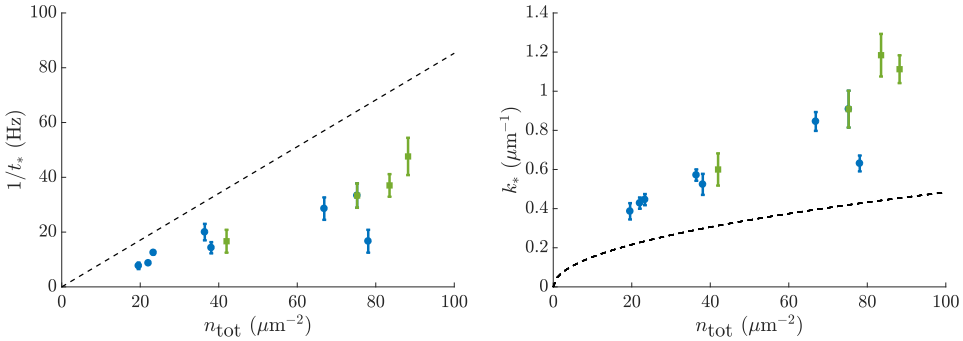

Figure 7.8: Evolution of t_* (left) and k_* (right) for various densities. The blacked dashed lines represent the prediction from [61] for $1/t_f$ and k_f. Runs at the coldest temperature performed in a $L = 40$ μm box (corresponding to section 1.1) are shown as blue circles, and runs at the coldest temperature performed in box with various L (section 1.2) are shown as green squares.

7.1.4 *Demixing in a $T \neq 0$ system*

All the data presented so far corresponded to the $T = 0$ case. As has been noted in Chapter 4, the typical difference in energy between the phase separated configuration and the uniform one is extremely small:

$$\Delta E = n(g_{12} - g_1 g_2) \simeq k_B \times 1.5 \text{ nK} \ll k_B T. \tag{7.4}$$

This points at the fact that demixing dynamics can only be a transient phenomenon in a real physical system: if $T \neq 0$, the temperature will ultimately destroy the appearing patterns. Of course, one can then wonder at what happens when the temperature is varied: can we completely kill the demixing dynamics by increasing T?

In this section, we vary the cloud's temperature T between typically 78 et 415 nK (corresponding to T/T_c between 0.3 and 1.35). The box's size is fixed at $L = 40$ μm while the density for runs considered in this section is in average $n_{\mathrm{tot}} = 58 \pm 5$ μm^{-2}. As for the low density case, we have an increasing density noise when T is increased, which makes the last run's signal a bit worse than the others.

As can be seen in Fig. 7.9 and 7.10, increasing the temperature causes a smaller m to appear, although the typical appearance time seems less sensitive to a variation of T. The naive model

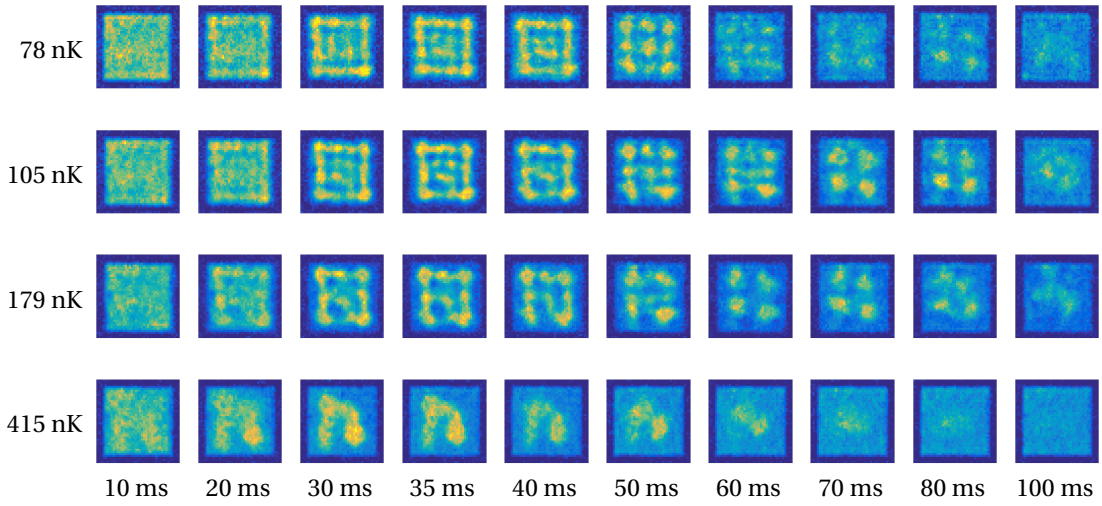

Figure 7.9: Time evolution of the $|2,0\rangle$ density for $T = 78$, 105, 179, and 415 nK, while the total density is kept at about 58 μm^{-2}. For these pictures, $L = 40$ μm. As the temperature is increased, the number of lobes created decreases, although the time of appearance is more or less constant.

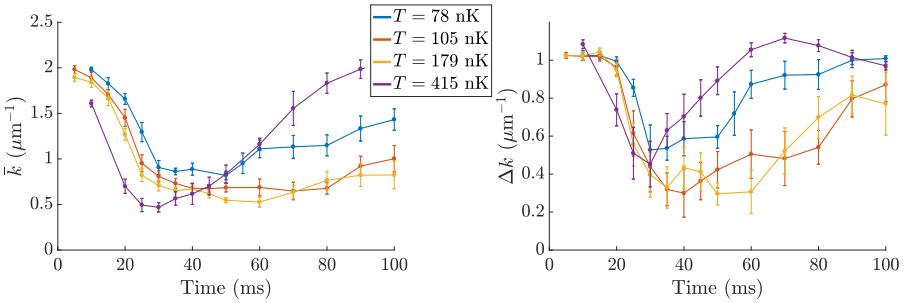

Figure 7.10: Evolution of the mean wave vector $\bar{k}$ present in the system (left), and its standard deviation Δk (right) with time, for a box of side $L = 40$ μm and temperatures $T = 78$, 105, 179, and 415 nK. The total density is typically 58 μm^{-2}. Each value is averaged over typically 10 iterations; the error bars are the resulting standard deviations over these $\simeq 10$ iterations.

from [61], being conducted in a $T = 0$ system, does not give any insight of possible temperature effects. However, for this density, the most unstable mode in the infinite system is around $m = 2$. It is possible that the noise added by the increased temperature simply prevents other weaker modes to grow, shortcutting the cascade to let only k_f appear. We indeed see in Fig. 7.11 that while we started afar from k_f for the coldest sample, we approach this value when increasing T.

Although this system exhibits richer physics that what the infinite model suggests, we have seen in Chapter 5 that a way to approximately recover the naive prediction was to seed the system with a large enough amplitude. We now turn to seeded dynamics to see what happens in this case.

7.2 SEEDED DEMIXING

7.2.1 *Excitation protocol*

For the rest of the discussion, we set $L = 40$ μm and we go to the smallest temperature accessible. We have seen in the previous chapter that in order to imprint a stable mode, the seed needs

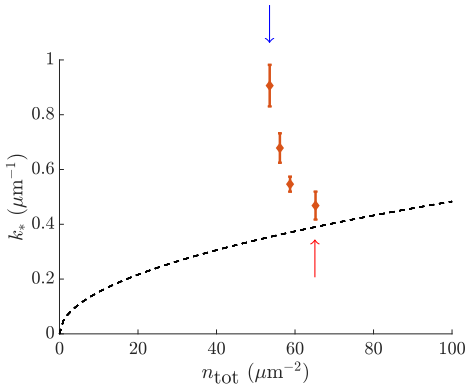

Figure 7.11: Evolution of k_* for temperatures ranging from 78 to 415 nK. The blue arrow denotes the coldest point, and the red arrow the hottest one. The dashed black line represents the prediction from [61] for k_f. We see that in this case, increasing T decreases significantly k_*.

to be relatively important as otherwise, natural demixing takes over. This is no different here: as can be seen in Fig. 7.12, seeding too low an amplitude does not yield an oscillation for a stable mode. On the other hand, seeding an unstable mode with too high an initial population makes it only grow marginally as it is already close to its acme, and it then quickly collapses. Of course, this makes the extraction of a characteristic growth rate more delicate.

As a consequence, we will work with $A = 0.05$ for unstable modes, and $A = 0.5$ for stable ones. When this condition is enforced, we see that modes behave as they should, as can be seen in Fig. 7.13: unstable modes grow with time, while stable modes simply oscillate. We can then extract a growth time in the first case, and a period in the second, in order to extract $\Omega(k)$.

7.2.2 *Varying the density*

For this section, we took data at three different total densities : around 32, 23 and 12 μm^{-2}. Due to drifts in the atomic density, each run has a slightly different n_{tot}; the deviation is typically $\pm 15\,\%$. For each density, we seeded modes 1-5 with an amplitude corresponding to their (un)stable behaviour. The result is presented in Fig. 7.14.

Overall, the agreement with [61] is quite good, especially for stable modes, and we are again in the case where we can recover the infinite system prediction by forcing an oscillation with a large enough seed. The picture is a bit different for unstable modes, where the growth rate deviated from the one observed in an infinite system, indicating that in this case, the seed's growth is hindered by the natural demixing.

In particular, for the densest sample, mode 3 is supposed to be stable. However, we observe a growing behaviour, and no oscillations. While the difference in growth rates predicted by [61] and the observed ones can be explained by the nature of our system which is not infinite, the (un)stable character of a mode is usually well predicted by the naive model. However, mode 3 is not too far from the stable/unstable border, and a mistake in a_{ij} or in the density calibration might lead to an important shift of this border, without changing too much the high k part of the dispersion relation, as this part is less sensitive to experimental parameters.

CONCLUSION

In conclusion, and as the numerical study suggested, demixing in a square box is richer than in an infinite system. For natural demixing, the system is totally multimode, and one has to shift from an individual mode analysis to a mean mode one, for which a decay of $\bar{k}(t)$ is observed for every density, temperature, or box's size under scrutiny. Even if the naive model can no longer apply, the appearance time and length scales still follow the expected tendencies. As for

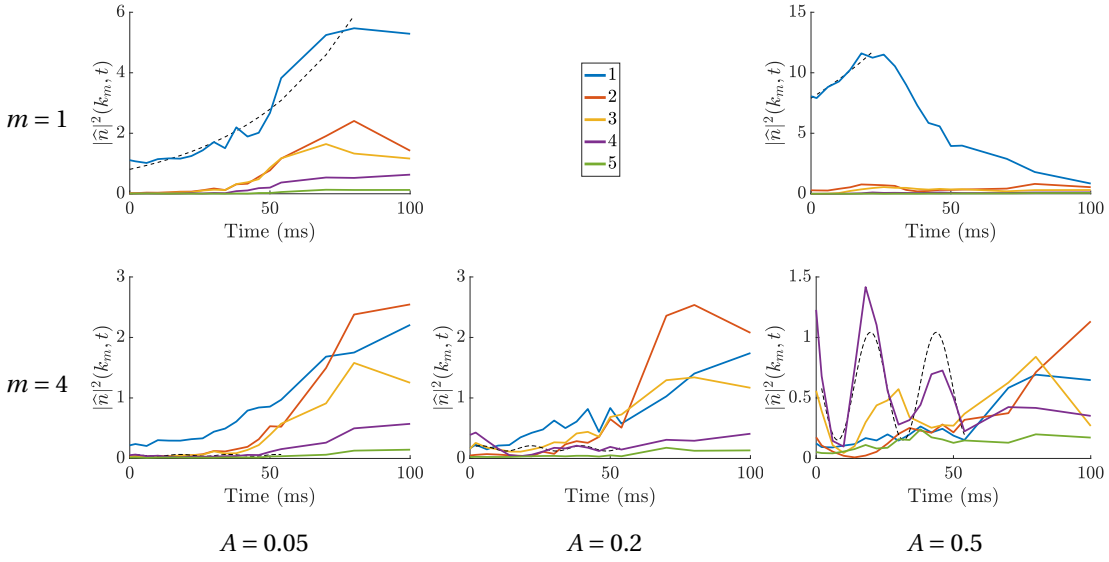

Figure 7.12: Behaviour of $\overline{|\widehat{n}|^2}(k_m, t)$ for different seeds. Top: we seed $m = 1$, which is an unstable mode for this density. For too large a seed, the mode only marginally grows before collapsing, making it hard to extract reliably a growth rate. Bottom: we seed $m = 4$, which is a stable mode at this density. Below $A = 0.5$, we hardly see any oscillation. This incited us to use large A when seeding a stable mode, and small A for unstable ones.

1D systems, there is a way to recover the naive prediction: to counterbalance natural demixing, one has to seed the system with a non-zero amplitude. Typically, for stable modes, the seed needs to be strong in order to observe oscillations. When this condition is met, the finite system has a behaviour close to the infinite one.

Some experimental issues, typically homogeneity or imprinting problems, limit the quality of the signal. Although this was not tried, we could use the grey-level loop presented in Chapter 3 to correct either of this defects. In particular, this might improve the signal in the unstable part of the spectrum, where one is typically more vulnerable to random noise triggering other modes than the seeded one. We might this way enhance the quality of the data, especially for runs presenting an inherent high noise, like low density or high temperature runs.

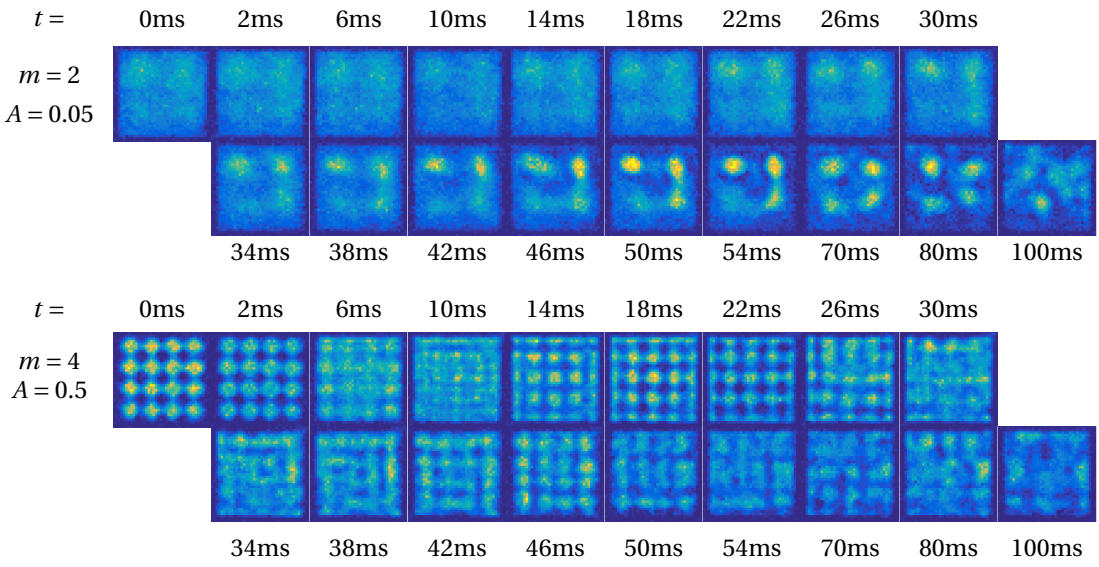

Figure 7.13: Time evolution of two seeded modes of different nature. Top: we seed $m = 2$ at a low amplitude ($A = 0.05$) as this mode, for this density, is unstable. The initial perturbation grows with time. Bottom: we seed $m = 4$ with a large amplitude ($A = 0.5$) as for this density, this mode is stable. We see the pattern oscillate: the density perturbation vanishes around 10 ms before reappearing, inverted, around 20 ms. We typically observe a full cycle before the signal disappears.

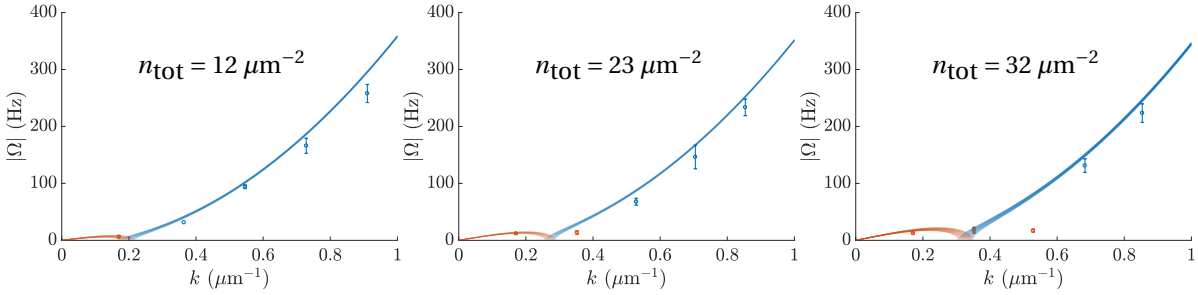

Figure 7.14: Dispersion relations for three different densities : 12 μm^{-2} (left), 23 μm^{-2} (middle) and 32 μm^{-2} (right). We seed modes 1-5 with $A = 0.05$ for unstable modes (red points) and $A = 0.5$ for stables ones (blue points). The prediction for an infinite system is shown in red when $\Omega_- \in i\mathbb{R}$ and in blue when $\Omega_- \in \mathbb{R}$. Each run has a slightly different density (the standard deviation in density within each graph is typically 15 % of the mean), which gives rise to the corresponding shaded areas.

Conclusion

CONCLUSION

In this thesis, we have explored the physics of 2D Bose gases: we have detailed the production of bidimensional uniform clouds, and explored the demixing dynamics that occur in an immiscible mixture of such fluids.

The first part of this manuscript detailed the specifics of our experimental setup, including an iterative procedure that can be used to control the cloud's homogeneity, or more generally, the profile in intensity of a laser beam. This is a very powerful tool as it can be used to correct for homogeneity defects that inevitably appear in the gas, and more importantly, can also be a way to improve the Raman imprinting that is used on several projects. For instance, with this procedure, we could transfer a spatially-shaped solitonic bubble from $|1,0\rangle$ to $|2,0\rangle$ and see how this impurity evolves with time. The evolution of such bubbles with gaussian shapes is an ongoing project in our team, where we observe the gaussians to expand below a certain critical atom number N_c, and contract above. However, this gaussian shape is not the system's ground state, and even when the atom number is very close to N_c, we do not observe a stabilised, stationary bubble. Being able to correctly and accurately imprint a solitonic ground state was, without this correction loop, beyond our reach. We can now hope for a better imprinting, and hopefully, an observation of a stationary state.

The second part of this manuscript presented a study of demixing in 2D Bose gases, first from a numerical point of view, and then with experimental data. Demixing phenomena have previously been observed in 3D and/or harmonically trapped system, but comprehensive studies in 2D uniform systems are rare. With our setup, we could compare a Bogoliubov approach ([61]), first to simulations, and then to experimental data. The numerics showed that although the model could be applied to a system with periodic boundary conditions, the presence of edges complicated a lot this naive picture, since in the case of an initially uniform superposition, demixing waves would start there and then propagate towards the centre. Thus, for a system naturally demixing in a box, the physics was multimode, and all k, not only those that [61] deemed unstable, initially grew; moreover, this growth had a different behaviour than what was predicted for an edgeless system. This result was then verified for an experimental system, where the prediction from [61] effectively failed.

Another possibility was then to operate a spatially dependant transfer, where a certain mode would be seeded in the system, and let to evolve. Overall, for this evolution to be compliant with the naive model, the seed's amplitude needed to be relatively large in order to prevent natural demixing from happening. For stable modes, we could neatly recover the dispersion relation found in [61]; for unstable modes, however, the numerics abided by the model from ([61]), but the experimental agreement was relatively poor. These differences could in part be attributed to small mismatches in the chosen scattering lengths values, and more importantly, to the probable inapplicability of the simple model in a real experimental system: due to the presence of edges, the studied modes are no longer eigenmodes of the system, and the multimode character of the system renders this model irrelevant.

Some leads that were not or little explored during this thesis include the temperature dependance of these dynamics, and the fundamental role of noise in our experiments. The numerical study showed that in the case of a ring, for instance, radial dynamics are frozen by the thinness of the system, and there is no real demixing. Nevertheless, this is not the case for a real system, where we did see azimuthal demixing when performing the experiment. This tends to show that the presence of noise in the system is critical in getting the dynamics started. Adding some extra noise, with the help of a DMD for instance, could thus have an influence on the observed modes' growths, while simulations on this issue could help intuiting the exact mechanics that trigger the demixing. Additionally, performing experiments at different temperatures can also

lead to interesting results: the difference in energy between the phase separated and the uniform configuration is on the order of the nK, far smaller than the temperature of the system. Thus, at high temperature, the transient demixing dynamics that we observe should totally disappear. Although we did not see this effect up to typically 400 nK, this could be an interesting path to follow.

Outlook

Spectroscopy of the clock transition

As we have seen, a small mismatch in the values of the inter and intraspecies scattering lengths involved in the problem can lead to dramatic changes. In the case of demixing dynamics, this is due to the fact that all the a_{ij} are close to one another, while t_f and k_f are set by variables depending on their difference. This prompted us to accurately measure these parameters with a spectroscopic measurement.

In the mean-field picture, single-particle levels of energy are shifted when dealing with more than one atom: for a one component system, the shift in energy is known to be proportional to $g\bar{n}$. For two components, one also has to add the interspecies contribution, and for a 2D $T = 0$ gas, one ends up with a shift of the transition frequency compared to the single atom case ([95]):

$$\Delta\nu \propto \bar{n}\big(a_{22} - a_{11} + (2a_{12} - a_{11} - a_{22})f\big), \tag{7.5}$$

where $\bar{n}$ is the average 2D density, and f is the imbalance between the two states: $f = (n_1 - n_2)/(n_1 + n_2)$. When $T \neq 0$, $\Delta\nu$ can be expressed with the help of a 'normalised' Tan's contact:

$$\frac{C}{C_0} \propto \frac{\partial E}{\partial a} \propto \frac{1}{\bar{n}}\frac{\Delta\nu}{\Delta a}, \tag{7.6}$$

where E is the gas's internal energy. As we have seen in Chapter 1, under certain conditions, this quantity is related to $g_2(0)$. For an ideal gas, $g_2(0)$ varies from 2 to 1 when one goes from $\mathcal{D} \ll \mathcal{D}_c$ to $\mathcal{D} \gg \mathcal{D}_c$, and one thus expects a similar variation of C across the transition. For an interacting gas, however, $g_2(0)$ is ill-defined as its $T = 0$ contribution is singular ([85]). One can however relate the contact to the thermal contribution of g_2:

$$\frac{C}{C_0} = 1 + g_2^{T\neq 0}(0). \tag{7.7}$$

Interestingly, this variation of the contact with degeneracy can be observed using Ramsey interferometry. As the shift in energy is typically of the order of the Hz, it can only reasonably be performed on our clock transition, and we chose to work with the magnetic insensitive states $|1, 0\rangle$ and $|2, 0\rangle$.

With this scheme, we could observe the contact go from 1 in the very degenerate regime to ~ 1.7 at $\mathcal{D} \simeq 5$, *i.e.* above the critical point ([85]). Additionally, we also measured $a_{11} - a_{22} = 7\, a_0$ and $a_{11} - a_{12} = 3.4\, a_0$ for a magnetic field perpendicular to the atomic plane. The value found for a_{12} is slightly larger than what is expected and comes from a correction due to magnetic dipole-dipole interactions between the two species ([86]).

Vortex generation

As we have seen in Chapter 1, the decrease of $g_2(0)$ to 1 at large degeneracies is associated to a reduction of density fluctuations, leading to a frozen density with phase fluctuations, and translating into a superfluid gas. An interesting feature of superfluid systems is their ability to create vortices when injected with angular momentum, instead of simply rotating, as usual fluids do. These vortices have been observed for a 3D superfluid ([9]), and their arrangements into lattices have also been investigated ([10]).

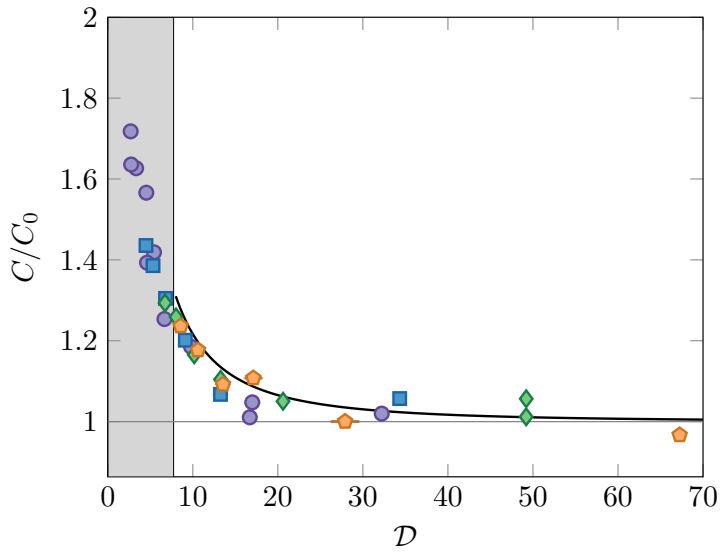

Figure 7.15: variation of C/C_0 with the phase-space density $\mathcal{D}$, the non-superfluid regime corresponding to the grey area. The different densities that were used are $\bar{n} = 10.4, 21, 31.5$, and 42 μm^{-2}, and correspond respectively to violet disks, blue squares, green diamonds, and orange pentagons. The black line is a Bogoliubov prediction. Figure taken from [85].

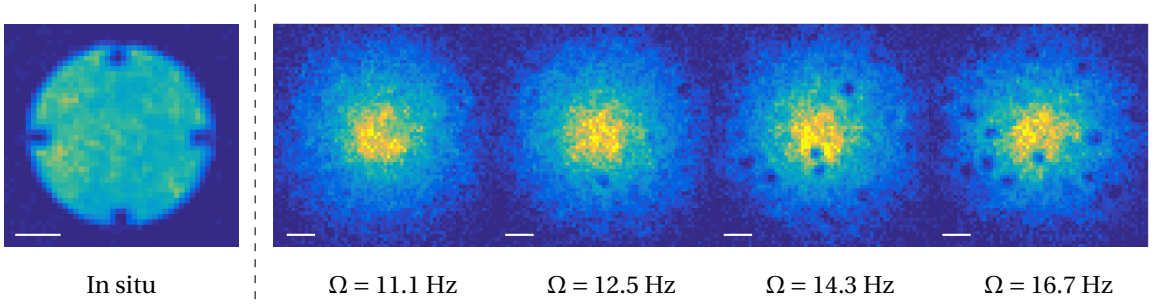

Figure 7.16: Left: stirring created by DMD2 (in situ image). The four teeth rotate at certain frequency in order to inject angular momentum in the cloud. Right: after 10 turns, we image the vortices with a time of flight measurement. The number of vortices grows as we increase the injected angular momentum. The white lines represent 10 μm.

Our goal in revisiting these experiments was the perspective to study Fractional Quantum Hall Effect physics, using the fact that a rotation of neutral particles essentially simulates the effect of an artificial magnetic field on electrons. To do so, we needed to study the system's ground state at large rotation speeds, and we expected to see a nice vortex lattice.

In order to perform these experiments, we took a very cold sample and stirred it with a small perturbation produced by DMD2. We set this DMD output to be the negative image of a gearwheel (see Fig. 7.16), and had the four teeth rotate at a set frequency for a certain time before performing the time of flight measurement. In the end, we could reproduce the historical experiments in our flat bottom system, but we did not manage to have a nice vortex lattice (see Fig. 7.16). This topic is for the moment an ongoing study, as we are still trying to understand why we do not see a periodic arrangement of the vortices. This might be due an excess of entropy, possibly related to our experimental protocol which could create some unwanted excitations; we plan on investigating this in the near future.

Future projects

A last path our team could pursue in the future would be to go from our weakly interacting regime to a strongly interacting one, using dipole-dipole interactions between Rydberg states to reach the desired regime. We could then trap our bosons in custom shaped clouds and investigate interesting transport properties. This might be explored in the following years.

Appendix

A

APPENDIX

In this appendix, we aim at explaining the differences between the chosen shape for the density and phase modulations, and the theoretical one, defined by the eq. 5.16 in Chapter 5:

$$\begin{cases} \delta n_j(\mathbf{r}) &= A_j(\mathbf{k})e^{i\mathbf{k}\cdot\mathbf{r}} + \text{c.c.} \\ \delta\theta_j(\mathbf{r}) &= B_j(\mathbf{k})e^{i\mathbf{k}\cdot\mathbf{r}} + \text{c.c.} \end{cases} \tag{A.1}$$

Choosing a normalised, dimensionless perturbation amplitude δA, we wrote the coefficients A_i and B_i as:

$$\begin{cases} A_1 &= \delta A, \\ A_2 &= A_1 \frac{m^2(c_-^2 - c_1^2)}{g_{12}\hbar^2 \frac{n_{\text{tot}}}{2}}, \end{cases} \qquad \begin{cases} B_1 &= \frac{-2im\Omega_-(k)}{\hbar k^2} A_1, \\ B_2 &= \frac{-2im\Omega_-(k)}{\hbar k^2} A_2. \end{cases} \tag{A.2}$$

Let us first note that for $\delta A \in \mathbb{R}$, eq. A.2 shows that $A_2 \in \mathbb{R}$. Moreover, for stables modes, $B_i \in i\mathbb{R}$ while for unstable ones, $B_i \in \mathbb{R}$. This makes the phase modulation defined in A.1 sometimes a $\cos$, and sometimes a $\sin$, while the density modulation is always a $\cos$. To makes things simpler, we wanted to replace these two functions by a unique real one. The non trivial point is then to go from the shape taken by eq. A.1 to the one that we chose:

$$\begin{cases} \varphi_1^0 &= \varphi_1^0\left(1 + \delta n_1 + i\delta\theta_1\right) = \varphi_i^0\left(1 + A_1 f + iB_1 f\right), \\ \varphi_2^0 &= \varphi_2^0\left(1 + \delta n_2 + i\delta\theta_2\right) = \varphi_i^0\left(1 + A_2 f + iB_2 f\right), \end{cases} \tag{A.3}$$

with $f = \frac{1}{2}\left(\cos(kx) + \cos(ky)\right)$ for PBC and SBC, and $f \propto \cos(m\theta)$, for SSBC, with θ the azimuthal angle.

We treat here the SBC case. The SSBC case is its 1D equivalent. The demonstration is based on the fact that one can choose different shapes for the modulation defined in eq. A.1 without changing the dispersion relation or eq. A.2. Indeed, any function verifying $\ddot{f} = -\omega^2 f$ and $\nabla^2 f = -k^2 f$ will give the same dispersion relation, and the same weights A_i and B_i. In particular, choosing $e^{i\mathbf{k}\cdot\mathbf{r}} + \text{c.c.}$, or $\cos(\mathbf{k}\cdot\mathbf{r})$ for both δn and $\delta\theta$ is equivalent in that regard.

However, a modulation in $\cos(\mathbf{k}\cdot\mathbf{r})$ does not respect the symmetry of our square box, since it creates diagonally ordered maxima as can be seen in Fig. A.1. Moreover, we intuitively wanted to recreate something close to the natural demixing patterns that we observed experimentally, which ordered spin domains in a 2D 'Manhattan' fashion. The demonstration of the equivalence of these two forms is based on the linearity of our equations, and on the infinite, isotropic character of the model.

As the theoretical model describes an infinite system, we can freely rotate the perturbation without consequence: all the modulations shown in Fig. A.2 share the same k and grow the same way. Moreover, since we have linearised the Gross-Pitaevskii equations to obtain the dispersion relation, the sum of the two modulations also grows the same way. It then suffices to compute this sum to find the desired pattern, as is shown in Fig. A.3. This is exactly the shape taken by f.

In conclusion, the initial modulation given by eq. A.1 and the final one that is obtained in Fig. A.3 are totally equivalent in the eyes of the dispersion relation, and we can freely use one definition or the other.

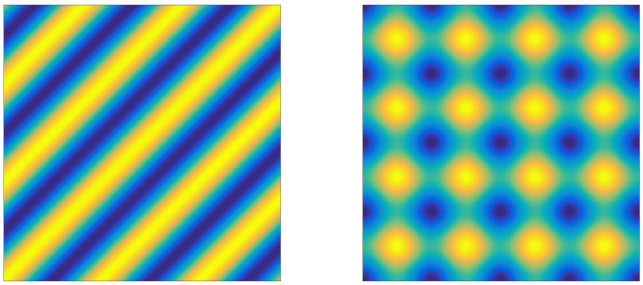

Figure A.1: Left: shape taken by a $\cos(\mathbf{k}\cdot\mathbf{r})$ modulation. Right: instead of diagonally ordered patterns, we want something that respects the symmetry of the box, has a modulation in both directions, and resembles what happens for natural demixing: we thus use the shape given by f.

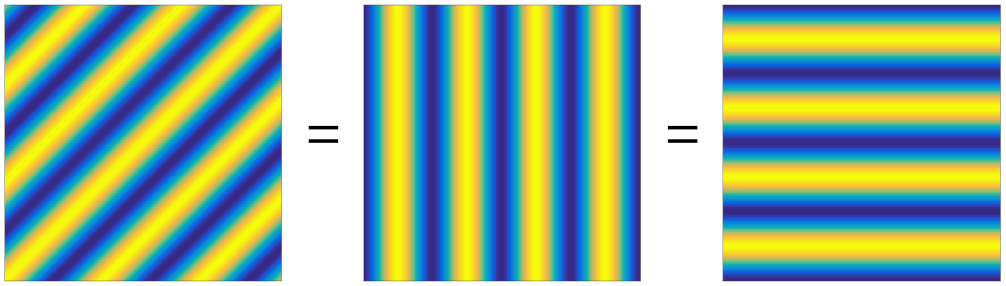

Figure A.2: As the system is infinite, we can rotate the modulation given by Fig. A.1 to get vertical and horizontal stripes with the same k: each of these perturbations grows the same way.

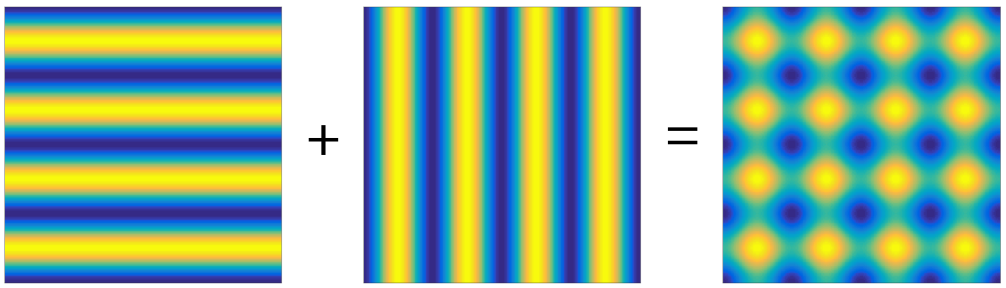

Figure A.3: It then suffices to add the vertical and the horizontal modulations to get the desired shape.

Publications

Featured in Physics

Sound Propagation in a Uniform Superfluid Two-Dimensional Bose Gas

J. L. Ville, R. Saint-Jalm, É. Le Cerf, M. Aidelsburger,* S. Nascimbène, J. Dalibard, and J. Beugnon†
Laboratoire Kastler Brossel, Collège de France, CNRS, ENS-PSL University, Sorbonne Université, 11 Place Marcelin Berthelot, 75005 Paris, France

(Received 5 April 2018; published 3 October 2018)

In superfluid systems several sound modes can be excited, such as, for example, first and second sound in liquid helium. Here, we excite running and standing waves in a uniform two-dimensional Bose gas and we characterize the propagation of sound in both the superfluid and normal regimes. In the superfluid phase, the measured speed of sound is in good agreement with the prediction of a two-fluid hydrodynamic model, and the weak damping is well explained by the scattering with thermal excitations. In the normal phase we observe a stronger damping, which we attribute to a departure from hydrodynamic behavior.

DOI: 10.1103/PhysRevLett.121.145301

Propagation of sound waves is at the heart of our understanding of quantum fluids. In liquid helium, the celebrated two-fluid model was confirmed by the observation of first and second sound modes [1,2]. There, first sound stands for the usual sound appellation, namely, a density wave for which normal and superfluid fractions oscillate in phase. Second sound corresponds to a pure entropy wave with no perturbation in density (normal and superfluid components oscillating out of phase), and is generally considered as conclusive evidence of superfluidity.

Sound wave propagation is also central to the study of dilute quantum gases, providing information on thermodynamic properties, relaxation mechanisms, and superfluid behavior. In ultracold strongly interacting Fermi gases, the existence of first and second sound modes in the superfluid phase was predicted [3] and observed in experiments [4,5], with a behavior similar to liquid helium. In three-dimensional (3D) weakly interacting Bose-Einstein condensates (BECs), one still expects two branches of sound with speeds $c^{(1)} > c^{(2)}$ but the nature of first and second sound is strongly modified because of their large compressibility [6]. At zero temperature the gas is fully superfluid and the only relevant mode corresponds to Bogoliubov excitations, i.e., density oscillations. At nonzero temperature, an isothermal density perturbation is expected to excite mostly the second sound mode, propagating at a velocity approximately proportional to the square root of the superfluid fraction [6,7]. This contrasts to the usual picture for liquid helium where second sound is excited via local heating [1,2]. Sound waves in an elongated 3D BEC were observed in Refs. [8–10] in a regime where the sound speed remains close to the Bogoliubov sound speed.

The study of sound propagation can be very insightful for two-dimensional (2D) Bose fluids, where superfluidity does not result from a Bose-Einstein condensation, but occurs instead via a Berezinskii-Kosterlitz-Thouless (BKT) transition [11]. This transition is associated with a jump of the superfluid density but as the transition is of infinite order, the jump cannot be revealed by the thermodynamic properties of the fluid. However, the presence of a superfluid component is predicted to lead to two distinct sound modes, whose velocities $c_{\mathrm{HD}}^{(1)}$ and $c_{\mathrm{HD}}^{(2)}$ were calculated within a hydrodynamic model in Refs. [12,13]. These velocities are functions of the superfluid density and thus both exhibit a discontinuity associated with the superfluid jump at the critical point. In particular, the second sound velocity is expected to remain nonzero just below the critical point of the superfluid to normal transition and to disappear just above. Experimentally, 2D Bose fluids were first realized with liquid helium films adsorbed on a substrate [14]; in this case the presence of the substrate blocks the motion of the normal component and thus prevents the investigation of such phenomena.

In this Letter, we report on the first observation of sound propagation in a 2D Bose fluid. We observe a single density sound mode both in the superfluid and normal regimes. Deep in the superfluid regime, the measured sound speed agrees well with the Bogoliubov prediction. We measure a weak damping rate compatible with Landau damping, a fundamental mechanism for the understanding of collective modes of superfluids at finite temperature [15]. For higher temperatures, we observe a decrease of the sound velocity consistent with the second sound speed variation predicted in Ref. [12] from two-fluid hydrodynamics. The damping of sound increases with temperature and, above the critical point, we still observe strongly damped density waves with no discernable discontinuity at the critical point. The discrepancy with the two-fluid model predictions could be due to a departure from hydrodynamic behavior.

Our experimental setup has been described in Refs. [16,17] and more details can be found in Ref. [18]. Briefly, we confine ^{87}Rb atoms in the $|F = 1, m = 0\rangle$ ground state into a 2D rectangular box potential

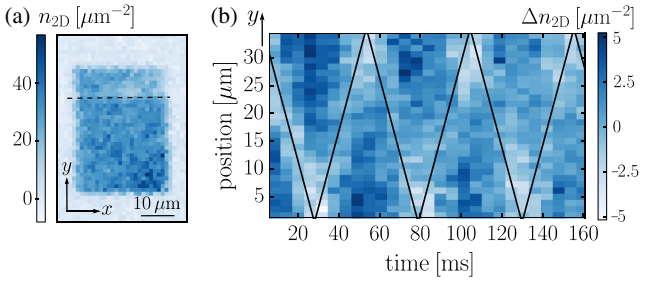

FIG. 1. Experimental protocol and observation of propagating waves. (a) Absorption image of the cloud perturbed by a local additional potential. The excitation is delimited by the horizontal dashed line and depletes the atomic density by a factor around 1/3. (b) Example of time evolution of the variation of the density profile n_{2D} with respect to its spatial mean value (integrated along x) obtained after abruptly removing the additional potential. For this example $T/T_c = 0.37(12)$ and $n_{2D} = 29(3)$ μm^{-2}. The position of the dip is fitted by a triangle function (black solid line) which gives, $c = 1.49(3)$ mm/s.

of size $L_x \times L_y = 30(1) \times 38(1)$ μm [see Fig. 1(a)]. The confinement along the vertical z direction can be approximated by a harmonic potential of frequency $\omega_z/(2\pi) = 4.59(4)$ kHz. We always operate in the quasi-2D regime where interaction and thermal energies are smaller than $\hbar\omega_z$. The gas is characterized by the effective coupling constant $g = \hbar^2\tilde{g}/m = (\hbar^2/m)\sqrt{8\pi}a_s/\ell_z$, where a_s is the s-wave scattering length, $\ell_z = \sqrt{\hbar/(m\omega_z)}$, and m the atomic mass [11]. We operate here in the weakly interacting regime: $\tilde{g} = 0.16(1)$. In the quasi-2D regime and for a given $\tilde{g}$, the equilibrium state of the cloud is only characterized by a dimensionless combination of T and n_{2D}, thanks to an approximate scale invariance [11]. In the following we use the ratio T/T_c, where $T_c = 2\pi n_{2D}\hbar^2/[mk_B \ln(380/\tilde{g})]$ is the calculated critical temperature for the BKT phase transition [25]. In this work, we study Bose gases from the highly degenerate regime ($T/T_c \approx 0.2$) to the normal regime ($T/T_c \approx 1.4$).

We first investigate propagating waves which we excite by a density perturbation. Prior to evaporative cooling in the box potential, we apply to the cloud a repulsive potential, which creates a density dip on one side of the rectangle [see Fig. 1(a)]. The extension of this dip is about 1/4 of the length of the box and its amplitude is chosen so that the density in this region is decreased by a factor of 1/3. After equilibration, we abruptly remove the additional potential and monitor the propagation of this density dip. We show in Fig. 1(b) a typical time evolution of the density profile integrated along the transverse direction to the perturbation for a strongly degenerate gas. In this regime, the density perturbation propagates at constant speed and bounces several times off the walls of the box. Using the calibrated size of the box, we extract a speed $c = 1.49(3)$ mm/s. This value is slightly lower than the Bogoliubov sound speed $c_B = \sqrt{gn_{2D}/m} = 1.6(1)$ mm/s expected at zero temperature for the measured density $n_{2D} = 29(3)$ μm^{-2}. The measured speed is also close to the second sound mode velocity $c_{HD}^{(2)} = 1.4(1)$ mm/s, estimated from two-fluid hydrodynamics at our experimental value of $T/T_c = 0.37(12)$ [12]. The first sound, expected to propagate at a much higher speed $c_{HD}^{(1)} = 3.3(3)$ mm/s [12], does not appear in our measurements that feature a single wave front only. The absence of first sound in our experiments can be explained by its very small coupling to isothermal density excitations in a weakly interacting gas [12].

In order to probe the role of the cloud degeneracy on the sound wave propagation, we vary both n_{2D} and T. For each configuration, we excite the cloud with the protocol described above, while adjusting the intensity of the depleting laser beam to keep the density dip around 1/3 of nonperturbed density. At lower degeneracies, sound waves are strongly damped and the aforementioned measurements of the density dip position become inadequate. We thus focus on the time evolution of the lowest-energy mode [26]. We decompose the density profiles integrated along x as

$$n(y,t) = \bar{n} + \sum_{j=1}^{\infty} A_j(t)\ \cos(j\pi y/L_y), \qquad (1)$$

where $\bar{n}$ is the average density along y and the A_j are the amplitudes of the modes. The choice of the cosine basis ensures the cancellation of the velocity field on the edges of the box. Our excitation protocol mainly couples to the lowest energy modes. We keep the excitation to a low value to be in the linear regime while still observing a clear signal for the lowest-energy mode, which in return provides a too weak signal for a quantitative analysis of higher modes [27]. For each duration of the evolution, we compute the overlap of the atomic density profile with the lowest-energy mode. Examples of the time evolution of the normalized amplitude $\tilde{A}_1(t) = A_1(t)/A_1(0)$ for different degrees of degeneracy are shown in Fig. 2. We observe damped oscillations with a damping rate increasing with T/T_c. We fit the experimental data by an exponentially damped sinusoidal curve $e^{-\Gamma t/2}[\Gamma/2\omega \sin(\omega t) + \cos(\omega t)]$ to determine the energy damping rate Γ and the frequency ω [28]. We then determine the speed of sound $c = L_y\omega/\pi$ and the quality factor of this mode $Q = 2\omega/\Gamma$.

We consolidate all our measurements of speed of sound and quality factors in Fig. 3. To facilitate comparison with theory, we show in Fig. 3(a) the values of c normalized to c_B. The non-normalized results are reported in Ref. [18] for completeness. In the temperature range $T \lesssim 0.9T_c$, we measure weakly damped density oscillations, corresponding to a well-defined sound mode ($Q \gtrsim 10$). In this regime, we observe a significant decrease by about ≈25% of the sound velocity for increasing values of T/T_c. The

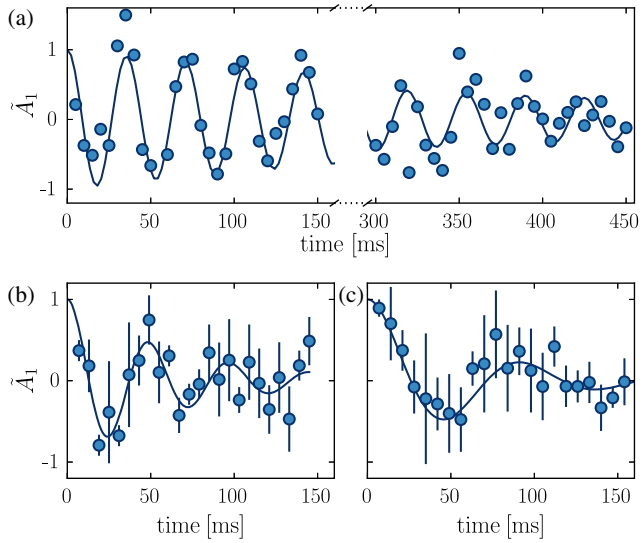

FIG. 2. Time evolution of the normalized amplitude of the lowest-energy mode for (a) $T/T_c = 0.21(11)$, (b) $T/T_c = 0.95(5)$, (c) $T/T_c = 1.38(18)$. The solid line is a fit of an exponentially damped sinusoidal oscillation. For (b) and (c) graphs, each data point is the average of three measurements and the error bars represent the associated standard deviation. In (a) each point corresponds to a single measurement.

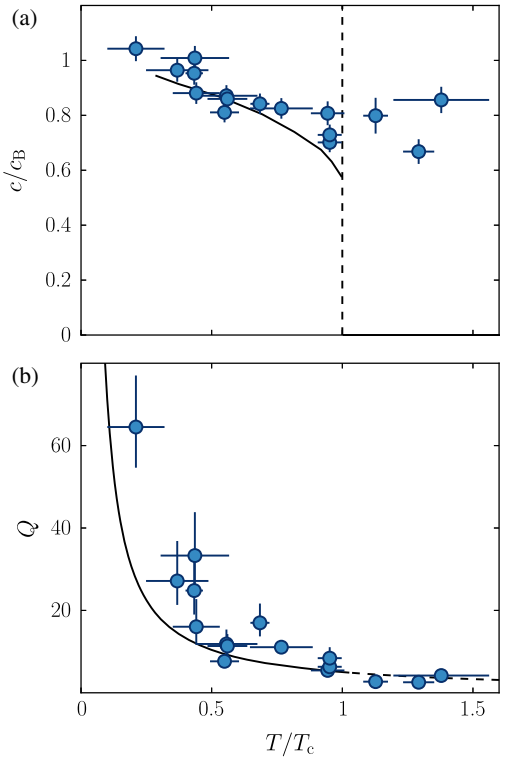

FIG. 3. Speed of sound and quality factor. (a) Measured speed of sound c normalized to c_B. The vertical dashed line shows the position of the critical point. The solid line shows the result from the two-fluid hydrodynamic model applied to the 2D Bose gas [12]. A fit to the data points below T_c by this hydrodynamic model with a free multiplicative factor shows that the measurements are globally 3% above the theoretical prediction. This could correspond to a 6% systematic error in the calibration of n_{2D} used to determine $c_B \propto n_{2D}^{1/2}$. Our estimated uncertainty on n_{2D} is on the order of 11% (see Ref. [18]) and our measurements are thus compatible with the predicted value of the speed of second sound $c_{HD}^{(2)}$. (b) Quality factor $Q = 2\omega/\Gamma$ of the lowest-energy mode. The solid line is the prediction for Landau damping [30] (continued as a dashed line for $T > T_c$). For both graphs, the error bars represent the statistical uncertainty extracted from the fitting procedures used to determine c, Γ and T/T_c.

measured velocities agree well with the prediction from two-fluid hydrodynamics [12] combined with the equation of state of the 2D Bose gas [29]. According to the analysis of Ref. [12] for weakly interacting gases, the change of speed of sound is mainly due to the variation of the superfluid fraction f_s from ≈ 1 at $T = 0$ to ≈ 0.5 close to $T = T_c$ with the approximate scaling $c_{HD}^{(2)} \propto f_s^{1/2}$ [13]. We note the absence of a discernable discontinuity of sound velocity at T_c, in disagreement with the two-fluid hydrodynamic approach.

In order to explain this disagreement, we first note that collective excitations in ultracold Bose gases can be of different nature depending on the relative amplitude of mean-field effects and collisions between particles [9,31,32]. In the very degenerate regime $T \ll T_c$, the system is naturally described within quantum hydrodynamics [33], where interactions between particles occur via a mean-field energy E_{int}. This is valid for $\omega \ll E_{int}/\hbar$, which is satisfied for our setup. In this regime we expect sound waves propagating at c_B, as observed in the experiment. For larger temperatures, but still below T_c, the normal fraction becomes significant. In order to use an hydrodynamic two-fluid model in that case, the local equilibrium condition also requires $\omega \ll \Gamma_{coll}$, where $\Gamma_{coll} = \hbar\tilde{g}^2 n/(2m)$ is the collision rate [34]. The same condition holds for the single fluid case above T_c. The opposite "collisionless" regime has been recently studied in Refs. [35,36]. It also leads to the existence of a sound mode, originating solely from mean-field interactions described, e.g., by a Landau-Vlasov kinetic equation. For $T \gtrsim T_c$ this collisionless sound mode has a velocity notably smaller than the hydrodynamic result and close to the prediction of Ref. [12] for the second sound velocity at T_c. For our data above T_c we estimate Γ_{coll}/ω to be in the range 1.6–3.4, which indicates that we are in a crossover between these limiting hydrodynamic and collisionless regimes.

The distinction between the quantum hydrodynamics regime and the crossover regime ($\Gamma_{coll} \sim \omega$) is supported by the study of the measured quality factors [see Fig. 3(b)]. For $T \ll T_c$, damping can be described at first order by the decay of low-lying collective excitations via scattering on thermal excitations [15,37], the so-called Landau damping

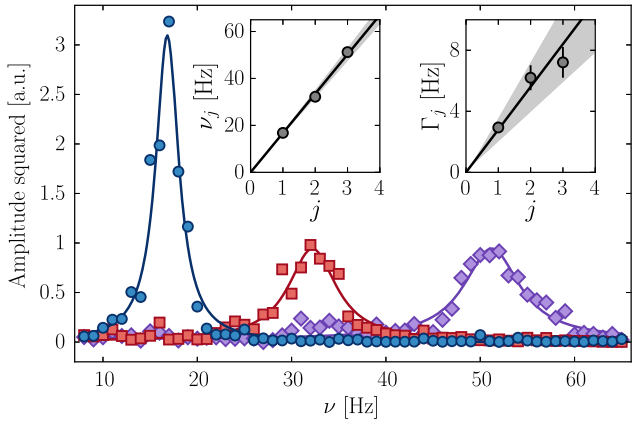

FIG. 4. Observation of standing waves in the box potential. Contribution of the three lowest-energy modes to the amplitude of the density modulation: $j = 1$ (circles), $j = 2$ (squares), $j = 3$ (diamonds). The solid lines are Lorentzian fits. The two insets show the resonance frequencies ν_j and the full widths at half maximum Γ_j resulting from these fits. The solid lines in the insets are linear fit to the data and the shaded areas represent the uncertainty on the fitted slope. From the slope $c/(2L_y)$ of the fit to the resonance frequencies, we find $c = 1.90(9)$ mm/s. For this specific experiment, the length of the cloud is $L_y = 57(1)$ μm and the degree of degeneracy is $T/T_c = 0.41(7)$.

mechanism. It predicts an increase of the quality factor when decreasing temperature due to the reduction of the number of thermal excitations available for scattering with the sound mode [38]. This perturbative approach is meaningful for large enough quality factors and does not take into account interactions between phonon modes. The solid line in Fig. 3(b) corresponds to Landau prediction for a 2D system [30]. It shows an overall good agreement with our data, even close to T_c, where it gradually looses its validity. Finally, above T_c, we measured low quality factors, showing that the observed sound mode is strongly damped, in agreement with the predictions of the collisionless sound mode [35].

In the highly degenerate regime, the low damping rate allows us to observe standing waves. To study them, we modulate sinusoidally the amplitude of the potential creating the dip of density on one edge of the box [39]. After $\approx$1 s we extract, for each frequency ν of the excitation, the amplitude of the (time-dependent) density modulation induced on the cloud (see Ref. [18] for details). We show in Fig. 4 the contribution of the three lowest-energy modes to the amplitude of the modulation as a function of the excitation frequency. For each mode j we observe a clear resonance peak centered at a frequency ν_j. We display in the insets the resonance frequencies and width of the modes. The ν_j's are equally spaced, as confirmed by the linear fit. In addition, the right inset shows the widths of the peaks. They also increase approximately linearly with j [40], meaning that the quality factor associated with these peaks is almost the same, as expected for Landau damping.

We focus in this work on a weakly interacting Bose gas which features a large compressibility compared to liquid helium or strongly interacting Fermi gases. A natural extension of this work would thus be to investigate second sound propagation for increasing interactions [13]. It would also be interesting to investigate first sound, e.g., by applying a localized temperature excitation [5]. During the completion of this work we were informed that a related study with a homogeneous 3D Fermi gas was currently performed at MIT [41].

This work is supported by DIM NanoK and ERC (Synergy UQUAM). This project has received funding from the European Union's Horizon 2020 research and innovation programme under the Marie Skłodowska-Curie Grant Agreement No. 703926. We thank S. Stringari, L. Pitaevskii, M. Ota, N. Proukakis, F. Dalfovo, F. Larcher, and P. C. M. Castilho for fruitful discussions, M. Villiers for experimental assistance, and F. Gerbier, R. Lopes, and M. Zwierlein for their reading of the manuscript.

J. L. V. and R. S. J. contributed equally to this work.

*Present address: Fakultät für Physik, Ludwig-Maximilians-Universität München, Schellingstr. 4, 80799 Munich, Germany.
†beugnon@lkb.ens.fr

[1] R. J. Donnelly, The two-fluid theory and second sound in liquid helium, Phys. Today **62**, 34 (2009).
[2] S. Balibar, The discovery of superfluidity, J. Low Temp. Phys. **146**, 441 (2007).
[3] E. Taylor, H. Hu, X.-J. Liu, L. P. Pitaevskii, A. Griffin, and S. Stringari, First and second sound in a strongly interacting Fermi gas, Phys. Rev. A **80**, 053601 (2009).
[4] J. Joseph, B. Clancy, L. Luo, J. Kinast, A. Turlapov, and J. E. Thomas, Measurement of Sound Velocity in a Fermi Gas Near a Feshbach Resonance, Phys. Rev. Lett. **98**, 170401 (2007).
[5] L. A. Sidorenkov, M. K. Tey, R. Grimm, Y.-H. Hou, L. Pitaevskii, and S. Stringari, Second sound and the superfluid fraction in a Fermi gas with resonant interactions, Nature (London) **498**, 78 (2013).
[6] A. Griffin and E. Zaremba, First and second sound in a uniform Bose gas, Phys. Rev. A **56**, 4839 (1997).
[7] A. Griffin, T. Nikuni, and E. Zaremba, *Bose-Condensed Gases at Finite Temperatures* (Cambridge University Press, Cambridge, England, 2009).
[8] M. R. Andrews, D. M. Kurn, H.-J. Miesner, D. S. Durfee, C. G. Townsend, S. Inouye, and W. Ketterle, Propagation of Sound in a Bose-Einstein Condensate, Phys. Rev. Lett. **79**, 553 (1997).
[9] D. M. Stamper-Kurn, H.-J. Miesner, S. Inouye, M. R. Andrews, and W. Ketterle, Collisionless and Hydrodynamic Excitations of a Bose-Einstein Condensate, Phys. Rev. Lett. **81**, 500 (1998).

[10] R. Meppelink, S. B. Koller, and P. van der Straten, Sound propagation in a Bose-Einstein condensate at finite temperatures, Phys. Rev. A **80**, 043605 (2009).
[11] Z. Hadzibabic and J. Dalibard, Two-dimensional Bose fluids: An atomic physics perspective, Riv. Nuovo Cimento **34**, 389 (2011).
[12] T. Ozawa and S. Stringari, Discontinuities in the First and Second Sound Velocities at the Berezinskii-Kosterlitz-Thouless Transition, Phys. Rev. Lett. **112**, 025302 (2014).
[13] M. Ota and S. Stringari, Second sound in a two-dimensional Bose gas: From the weakly to the strongly interacting regime, Phys. Rev. A **97**, 033604 (2018).
[14] D. J. Bishop and J. D. Reppy, Study of the Superfluid Transition in Two-Dimensional ^{4}He Films, Phys. Rev. Lett. **40**, 1727 (1978).
[15] L. P. Pitaevskii and S. Stringari, Landau damping in dilute Bose gases, Phys. Lett. A **235**, 398 (1997).
[16] J. L. Ville, T. Bienaimé, R. Saint-Jalm, L. Corman, M. Aidelsburger, L. Chomaz, K. Kleinlein, D. Perconte, S. Nascimbène, J. Dalibard, and J. Beugnon, Loading and compression of a single two-dimensional Bose gas in an optical accordion, Phys. Rev. A **95**, 013632 (2017).
[17] M. Aidelsburger, J. L. Ville, R. Saint-Jalm, S. Nascimbène, J. Dalibard, and J. Beugnon, Relaxation Dynamics in the Merging of N Independent Condensates, Phys. Rev. Lett. **119**, 190403 (2017).
[18] See Supplemental Materials at http://link.aps.org/supplemental/10.1103/PhysRevLett.121.145301 for methods and complementary results, which includes [19–24].
[19] L. Corman, J. L. Ville, R. Saint-Jalm, M. Aidelsburger, T. Bienaimé, S. Nascimbène, J. Dalibard, and J. Beugnon, Transmission of near-resonant light through a dense slab of cold atoms, Phys. Rev. A **96**, 053629 (2017).
[20] K. Hueck, N. Luick, L. Sobirey, J. Siegl, T. Lompe, and H. Moritz, Two-Dimensional Homogeneous Fermi Gases, Phys. Rev. Lett. **120**, 060402 (2018).
[21] A. Ramanathan, S. R. Muniz, K. C. Wright, R. P. Anderson, W. D. Phillips, K. Helmerson, and G. K. Campbell, Partial-transfer absorption imaging: A versatile technique for optimal imaging of ultracold gases, Rev. Sci. Instrum. **83**, 083119 (2012).
[22] M. F. Riedel, P. Böhi, Y. Li, T. W. Hänsch, A. Sinatra, and P. Treutlein, Atom-chip-based generation of entanglement for quantum metrology, Nature (London) **464**, 1170 (2010).
[23] V. Pastukhov, Damping of Bogoliubov excitations at finite temperatures, J. Phys. A **48**, 405002 (2015).
[24] P. C. Hohenberg and P. C. Martin, Microscopic theory of superfluid helium, Ann. Phys. (N.Y.) **34**, 291 (1965).
[25] N. Prokof'ev, O. Ruebenacker, and B. Svistunov, Critical Point of a Weakly Interacting Two-Dimensional Bose Gas, Phys. Rev. Lett. **87**, 270402 (2001).
[26] N. Navon, A. L. Gaunt, R. P. Smith, and Z. Hadzibabic, Emergence of a turbulent cascade in a quantum gas, Nature (London) **539**, 72 (2016).
[27] The study of the second spatial mode gives oscillation frequencies that are in good approximation twice larger than the lowest-energy mode and thus results in very similar speeds of sounds. However, the damping rate of this mode is also larger (see Fig. 4) and we cannot robustly estimate its lifetime for our deliberately weak excitation protocol.
[28] The choice of this oscillating function ensures a null derivative of the amplitude of the mode at $t = 0$, when the potential creating the density dip is removed. This behavior is expected from the continuity of the wave function and of its derivative describing the state of the gas at $t = 0$.
[29] N. Prokof'ev and B. Svistunov, Two-dimensional weakly interacting Bose gas in the fluctuation region, Phys. Rev. A **66**, 043608 (2002).
[30] M.-C. Chung and A. B. Bhattacherjee, Damping in 2D and 3D dilute Bose gases, New J. Phys. **11**, 123012 (2009).
[31] A. Griffin, Wen-Chin Wu, and S. Stringari, Hydrodynamic Modes in a Trapped Bose Gas above the Bose-Einstein Transition, Phys. Rev. Lett. **78**, 1838 (1997).
[32] D. Guéry-Odelin, F. Zambelli, J. Dalibard, and S. Stringari, Collective oscillations of a classical gas confined in harmonic traps, Phys. Rev. A **60**, 4851 (1999).
[33] L. Pitaevskii and S. Stringari, *Bose-Einstein Condensation and Superfluidity*, Vol. 164 (Oxford University Press, 2016).
[34] D. S. Petrov and G. V. Shlyapnikov, Interatomic collisions in a tightly confined Bose gas, Phys. Rev. A **64**, 012706 (2001).
[35] M. Ota, F. Larcher, F. Dalfovo, L. Pitaevskii, N. P. Proukakis, and S. Stringari, Collisionless Sound in a Uniform Two-Dimensional Bose Gas, following letter, Phys. Rev. Lett. **121**, 145302 (2018).
[36] A. Cappellaro, F. Toigo, and L. Salasnich, Collisionless Dynamics in Two-Dimensional Bosonic Gases, arXiv: 1807.02541 [Phys. Rev. A (to be published)].
[37] R. Meppelink, S. B. Koller, J. M. Vogels, H. T. C. Stoof, and P. van der Straten, Damping of Superfluid Flow by a Thermal Cloud, Phys. Rev. Lett. **103**, 265301 (2009).
[38] Note that Beliaev damping, another mechanism for the decay of low-lying excitations, is absent for the first spatial mode of the box. Indeed, it corresponds to a decay of a low-lying excitation into two excitations with lower energies and thus does not exist for the lowest energy mode.
[39] Y.-H. Wang, A. Kumar, F. Jendrzejewski, R. M. Wilson, M. Edwards, S. Eckel, G. K. Campbell, and C. W. Clark, Resonant wave packets and shock waves in an atomtronic SQUID, New J. Phys. **17**, 125012 (2015).
[40] Because of the finite duration of the excitation (1 s), the width of the peaks is Fourier limited at a typical width of 1 Hz, which should be taken into account for a more quantitative analysis.
[41] M. Zwierlein (private communication).

Dynamical Symmetry and Breathers in a Two-Dimensional Bose Gas

R. Saint-Jalm, P. C. M. Castilho, É. Le Cerf, B. Bakkali-Hassani, J.-L. Ville, S. Nascimbene, J. Beugnon, and J. Dalibard*

Laboratoire Kastler Brossel, Collège de France, CNRS, ENS-PSL University, Sorbonne Université, 11 Place Marcelin Berthelot, 75005 Paris, France

(Received 19 March 2019; published 21 May 2019)

A fluid is said to be *scale invariant* when its interaction and kinetic energies have the same scaling in a dilation operation. In association with the more general conformal invariance, scale invariance provides a dynamical symmetry which has profound consequences both on the equilibrium properties of the fluid and its time evolution. Here we investigate experimentally the far-from-equilibrium dynamics of a cold two-dimensional rubidium Bose gas. We operate in the regime where the gas is accurately described by a classical field obeying the Gross-Pitaevskii equation, and thus possesses a dynamical symmetry described by the Lorentz group SO(2,1). With the further simplification provided by superfluid hydrodynamics, we show how to relate the evolutions observed for different initial sizes, atom numbers, trap frequencies, and interaction parameters by a scaling transform. Finally, we show that some specific initial shapes—uniformly filled triangles or disks—may lead to a periodic evolution corresponding to a novel type of breather for the two-dimensional Gross-Pitaevskii equation.

DOI: 10.1103/PhysRevX.9.021035

Subject Areas: Atomic and Molecular Physics, Nonlinear Dynamics, Superfluidity

I. INTRODUCTION

Symmetries play a central role in the investigation of a physical system. Most often, they are at the origin of conserved quantities, which considerably simplify the study of the equilibrium states and the evolution of the system. For example, spatial symmetries associated with translation and rotation lead to the conservation of linear and angular momentum. More generally, it is interesting to determine the dynamical (or hidden) symmetries of the system under study, which can lead to more subtle conserved quantities. These symmetries are described by the group of all transformations of space and time that leave the action, therefore, the equations of motion, invariant. A celebrated example is the $1/r$ potential in three dimensions, where there exists a dynamical symmetry described by the group $O(4)$ for the bounded orbits [1]. When treated by classical mechanics, it leads to the conservation of the Laplace-Runge-Lenz vector from which one deduces that the bounded orbits are actually closed trajectories.

Among the systems that display rich dynamical symmetries are the ones whose action is left invariant by a dilation transformation of space and time. Such scale-invariant systems were initially introduced in particle physics to explain scaling laws in high-energy collisions [2]. We consider here the nonrelativistic version of scale invariance, which applies to the dynamics of a fluid of particles. We consider the simultaneous change of length and time coordinates of each particle according to the scaling

$$\boldsymbol{r} \to \boldsymbol{r}/\lambda, \qquad t \to t/\lambda^2. \tag{1}$$

In this dilation, the velocity of a particle is changed as $\boldsymbol{v} \to \lambda \boldsymbol{v}$. Therefore, the kinetic energy of the fluid scales as $E_{\mathrm{kin}} \to \lambda^2 E_{\mathrm{kin}}$, which ensures that the corresponding part of the action ($\propto \int E_{\mathrm{kin}} dt$) remains invariant in the transformation (1). If the interaction energy has the same scaling $E_{\mathrm{int}} \to \lambda^2 E_{\mathrm{int}}$, the total action of the fluid is invariant in the dilation. The simplest example of such a fluid is a collection of nonrelativistic particles, either noninteracting ($E_{\mathrm{int}} = 0$) or with pairwise interactions described by a $1/r^2$ potential. A scale-invariant fluid possesses remarkably simple thermodynamic properties: For example, its equation of state depends only on the ratio of chemical potential to temperature instead of being an independent function of these two variables.

Most physical systems exhibiting scale invariance also possess a more general conformal invariance, where time and space are modified by conformal transformations instead of the simple dilations given in Eq. (1) [3]. In the nonrelativistic domain, this conformal invariance exists for the Schrödinger equation describing the motion of the two systems mentioned

*jean.dalibard@lkb.ens.fr

above, free particles [4,5] and particles interacting with a $1/r^2$ potential [6]. In both cases, the dynamical symmetry group associated with this scale and conformal invariance is the Lorentz group SO(2,1). This is also the case for the three-dimensional pseudo-spin-1/2 Fermi gas in the unitary regime (for a review, see, e.g., Ref. [7]). There, the scattering length between the two components diverges, ensuring the required disappearance of a length scale related to interactions. In addition to the existence of a universal equation of state, this dynamical symmetry leads to a vanishing bulk viscosity [8,9] and also to general relations between the moments of the total energy and those of the trapping energy in a harmonic potential [10].

In this article, we consider another example of a scale- and conformal-invariant fluid with the SO(2,1) dynamical symmetry, the "weakly interacting" two-dimensional (2D) Bose gas. The concept of "weak interaction" means in this context that the state of the gas is well described by a classical field $\psi(\boldsymbol{r}, t)$. This field is normalized to unity ($\int |\psi|^2 d^2r = 1$) so that the density of the gas reads $n(\boldsymbol{r}, t) = N|\psi(\boldsymbol{r}, t)|^2$ where N is the number of particles. In the scaling of positions, the 2D matter-wave field changes as $\psi(\boldsymbol{r}) \to \lambda\psi(\lambda\boldsymbol{r})$, which guarantees that the norm is preserved and that the dynamical part of the action $\propto i\hbar \int dt \int d^2r \psi^* \partial_t \psi$ is invariant. The interaction energy of the gas then reads for contact interaction

$$E_{\mathrm{int}} = \frac{N^2\hbar^2}{2m}\tilde{g}\int |\psi(\boldsymbol{r})|^4 d^2r, \tag{2}$$

where m is the mass of a particle, and $\tilde{g}$ the dimensionless parameter characterizing the strength of the interaction. One can immediately check that E_{int} obeys the λ^2 scaling required for scale invariance, which can be viewed as a consequence of the dimensionless character of $\tilde{g}$. The classical field description used here is valid if one restricts to the case of a small coupling strength $\tilde{g} \ll 1$ [11]. This restriction is necessary because of the singularity of the contact interaction $(\hbar^2/m)\tilde{g}\delta(\boldsymbol{r})$ in 2D when it is treated at the level of quantum field theory. Note that the condition $\tilde{g} \ll 1$ does not constrain the relative values of the interaction and kinetic energies. Actually, in the following we often consider situations where $E_{\mathrm{int}} \gg E_{\mathrm{kin}}$ (Thomas-Fermi regime).

So far, the scale and conformal invariance of the weakly interacting 2D Bose gas has been mainly exploited to measure its equation of state [12,13]. Also, one of its dynamical consequences in an isotropic 2D harmonic potential of frequency ω has been explored: The frequency of the breathing mode was predicted to be exactly equal to 2ω for any $\tilde{g}$ [14–16], as tested in Refs. [17,18]. Note that in the presence of a harmonic potential, the whole system is not scale invariant anymore, but it still possesses a dynamical symmetry described by the group SO(2,1), as shown in Ref. [15]. Recently, deviations from this prediction for $\tilde{g} \gtrsim 1$, an example of a *quantum anomaly* [19], have been observed [20,21].

The purpose of our work is to go beyond static properties of the weakly interacting 2D Bose gas and its single-mode oscillation in a harmonic potential and to reveal more general features associated with its dynamical symmetry. To do so, we study the evolution of the gas in a 2D harmonic potential of frequency ω, starting from a uniformly filled simple area (disk, triangle, or square). Here, we use $\tilde{g} \leq 0.16$ so that the classical field description is legitimate. We first check (Sec. II) the prediction from Ref. [15] that $E_{\mathrm{kin}} + E_{\mathrm{int}}$ should have a periodic evolution in the trap with the frequency 2ω. We then investigate the transformations linking different solutions of the equations of motion. These transformations are at the heart of the dynamical symmetry group SO(2,1). In practice, we first link the evolution of clouds with the same atom number and homothetic initial wave functions in harmonic potentials with different frequencies (Sec. III). Then, restricting to the case where superfluid hydrodynamics is valid, we derive and test a larger family of transformations that allows one to connect the evolutions of two initial clouds of similar shapes with different sizes, atoms numbers, trap frequencies, and interaction strengths (Sec. IV). Finally, in Sec. V we explore a property that goes beyond the symmetry group of the system and that is specific to triangular and disk-shaped distributions in the hydrodynamic limit: We find numerically that these distributions evolve in a periodic manner in the harmonic trap, and we confirm this prediction over the accessible range for our experiment (typically, two full periods of the trap $4\pi/\omega$). These particular shapes can therefore be viewed as two-dimensional breathers for the Gross-Pitaevskii (nonlinear Schrödinger) equation in the hydrodynamic limit [22]. They also constitute a novel example of universal dynamics in a quantum system prepared far from equilibrium [23–25].

II. EVOLUTION OF POTENTIAL ENERGY

Our experiment starts with a 3D Bose-Einstein condensate of ^{87}Rb that we load around a single node of a vertical (z) standing wave created with a laser of wavelength 532 nm. The confining potential along z is approximately harmonic with a frequency $\omega_z/(2\pi)$ up to 4.9 kHz. The interaction parameter is $\tilde{g} = \sqrt{8\pi}a_s/\ell_z$, where a_s is the 3D s-wave scattering length and $\ell_z = (\hbar/m\omega_z)^{1/2}$. The interaction energy per particle and the residual temperature are both smaller than $\hbar\omega_z$ so that the vertical degree of freedom is effectively frozen [26]. The initial confinement in the horizontal xy plane is ensured by "hard walls" made with a light beam also at 532 nm. This beam is shaped using a digital micromirror device (DMD), and a high-resolution optical system images the DMD pattern onto the atomic

plane [27], creating a box potential on the atoms. The cloud fills uniformly this box potential, and it is evaporatively cooled by adjusting the height of the walls of the box. For all data presented here, we keep the temperature low enough to operate deep in the superfluid regime with $T/T_c < 0.3$, where T_c is the critical temperature for the Berezinskii-Kosterlitz-Thouless transition. At this stage, the atoms are prepared in the $F = 1$, $m_F = 0$ hyperfine (ground) state, which is insensitive to magnetic field.

Once the gas reaches equilibrium in the 2D box, we suddenly switch off the confinement in the xy plane and simultaneously transfer the atoms to the field-sensitive state $F = 1$, $m_F = -1$ using two consecutive microwave transitions. Most of the experiments are performed in the presence of a magnetic field that provides the internal state $F = 1$, $m_F = -1$ with an isotropic harmonic confinement in the xy plane, with $\omega/2\pi$ around 19.5 Hz. We estimate the anisotropy of the potential to be $\lesssim 2\%$. We let the cloud evolve in the harmonic potential for an adjustable time before making an *in situ* measurement of the spatial density $n(\boldsymbol{r}) = N|\psi(\boldsymbol{r})|^2$ by absorption imaging.

The measurement of $n(\boldsymbol{r})$ gives access to both the interaction energy (2) and the potential energy in the harmonic trap

$$E_{\mathrm{pot}} = \frac{N}{2} m\omega^2 \int r^2 |\psi(\boldsymbol{r})|^2 d^2 r. \tag{3}$$

Since the gas is an isolated system, we expect the total energy $E_{\mathrm{tot}} = E_{\mathrm{kin}} + E_{\mathrm{int}} + E_{\mathrm{pot}}$ to be conserved during the evolution, where the kinetic energy E_{kin} reads

$$E_{\mathrm{kin}} = \frac{N\hbar^2}{2m} \int |\boldsymbol{\nabla}\psi|^2 d^2 r. \tag{4}$$

The SO(2,1) symmetry for a 2D harmonically trapped gas brings a remarkable result: $E_{\mathrm{kin}} + E_{\mathrm{int}}$ and E_{pot} should oscillate sinusoidally at frequency 2ω [15]. More precisely, using the 2D Gross-Pitaevskii equation, one obtains the relations

$$\frac{dE_{\mathrm{pot}}}{dt} = -\frac{d(E_{\mathrm{kin}} + E_{\mathrm{int}})}{dt} = \omega W, \tag{5}$$

$$\frac{dW}{dt} = 2\omega(E_{\mathrm{kin}} + E_{\mathrm{int}} - E_{\mathrm{pot}}), \tag{6}$$

where we define $W = \omega m \int \boldsymbol{r} \cdot \boldsymbol{v} n d^2\boldsymbol{r}$ and the velocity field $\boldsymbol{v}(\boldsymbol{r}) = (\hbar/m)\mathrm{Im}[\psi^*(\boldsymbol{r})\boldsymbol{\nabla}\psi(\boldsymbol{r})]/|\psi(\boldsymbol{r})|^2$. Initially, the gas is prepared in a steady state in the box potential so that $\boldsymbol{v} = 0$; hence, $W(0)$ is also null. Therefore, the potential energy evolves as

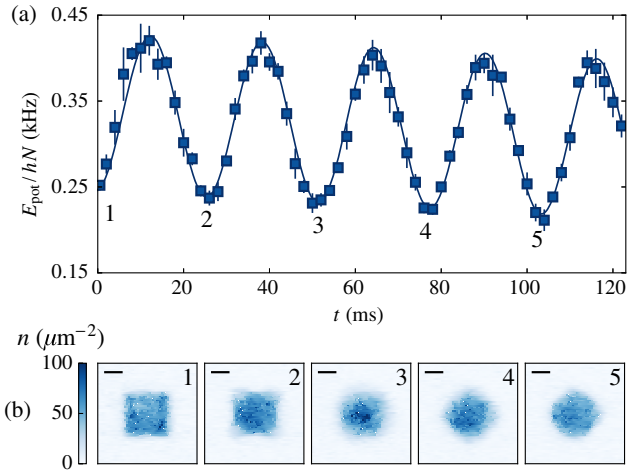

FIG. 1. Time evolution of the potential energy per particle of a 2D gas of ^{87}Rb atoms in an isotropic harmonic potential of frequency ω for a square of side length 27.6(5) μm with $4.1(2) \times 10^4$ atoms. (a) Evolution of the potential energy per particle. Each point is an average of seven to ten realizations, and the error bars indicate the standard deviation of these different realizations. The frequency of the trap is measured with the oscillation of the center of mass: $\omega/2\pi = 19.3(1)$ Hz. The oscillations of E_{pot} are fitted with a cosine function and an additional linear slope (continuous line). This slope is $-0.25(4)$ Hz/ms and accounts for the loss of particles from the trap. The fitted frequency is 38.5(1) Hz, which is compatible with ω/π, as predicted by the SO(2,1) symmetry of the gas. (b) Density distribution of an initially uniform gas after the evolution in a harmonic potential at times $\omega t = 0, \pi, 2\pi, 3\pi, 4\pi$, corresponding to the first periods of the potential energy indicated by the labels from 1 to 5. The horizontal black lines represent 10 μm.

$$E_{\mathrm{pot}}(t) = \frac{1}{2} E_{\mathrm{tot}} + \Delta E \cos(2\omega t), \tag{7}$$

where $\Delta E = \frac{1}{2}[E_{\mathrm{pot}}(0) - E_{\mathrm{kin}}(0) - E_{\mathrm{int}}(0)]$ can be positive or negative. A similar result holds for the sum $E_{\mathrm{kin}} + E_{\mathrm{int}}$ (with ΔE replaced by $-\Delta E$) but not for the individual energies E_{kin} or E_{int}.

We show in Fig. 1(a) the evolution of the potential energy per particle for an initially uniformly filled square. Although the density distribution is not periodic [see Fig. 1(b)], the potential energy E_{pot} evolves periodically and is well fitted by a cosine function with a period that matches the 2ω prediction and the expected zero initial phase. For a better adjustment of the data, we add a (small) negative linear function to the fitting cosine. Its role is likely to account for the residual evaporation rate of atoms from the trap (approximately 0.1 s^{-1}).

This simple dynamics can be viewed as a generalization of the existence of the undamped breathing mode at frequency 2ω that we mention in the Introduction [14,15]. We emphasize that this result is a consequence of the SO(2,1) symmetry and does not hold for the Gross-Pitaevskii equation in 1D or 3D.

III. GENERAL SCALING LAWS

An important consequence of the dynamical symmetry of the 2D Gross-Pitaevskii equation is the ability to link two solutions $\psi_{1,2}$ of this equation corresponding to homothetic initial conditions: One can relate $\psi_1(\boldsymbol{r},t)$ and $\psi_2(\boldsymbol{r}',t')$, provided they evolve with the same parameter $\tilde{g}N$ and the same trap frequency $\omega_1=\omega_2$. By using a simple scaling on space and time, this link can be further extended to the case $\omega_1\neq\omega_2$.

The general procedure is presented in the Appendix, and we start this section by summarizing the main results. Consider a solution of the Gross-Pitaevskii equation $\psi_1(\boldsymbol{r},t)$ for the harmonic potential of frequency ω_1:

$$i\hbar\frac{\partial\psi_1}{\partial t}=-\frac{\hbar^2}{2m}\boldsymbol{\nabla}^2\psi_1+\frac{\hbar^2\tilde{g}N}{m}|\psi_1|^2\psi_1+\frac{1}{2}m\omega_1^2\boldsymbol{r}^2\psi_1. \quad (8)$$

Using scale and conformal invariance, we can construct a solution $\psi_2(\boldsymbol{r}',t')$ of the Gross-Pitaevskii equation with the frequency $\omega_2=\zeta\omega_1$ using

$$\psi_2(\boldsymbol{r}',t')=f(\boldsymbol{r},t)\psi_1(\boldsymbol{r},t), \quad (9)$$

where space is rescaled by $\boldsymbol{r}'=\boldsymbol{r}/\lambda(t)$ with

$$\lambda(t)=\left[\frac{1}{\alpha^2}\cos^2(\omega_1 t)+\alpha^2\zeta^2\sin^2(\omega_1 t)\right]^{1/2}, \quad (10)$$

and the dimensionless parameter α is the homothetic ratio between the initial states. The relation between the times t and t' in frames 1 and 2 is

$$\tan(\omega_2 t')=\zeta\alpha^2\tan(\omega_1 t), \quad (11)$$

and the multiplicative function f is

$$f(\boldsymbol{r},t)=\lambda(t)\exp\left(-i\frac{m\dot{\lambda}\boldsymbol{r}^2}{2\hbar\lambda}\right), \quad (12)$$

where $\dot{\lambda}\equiv[(d\lambda)/(dt)]$. The two solutions $\psi_{1,2}(t)$ correspond to the evolution of two clouds with the same parameter $\tilde{g}_1N_1=\tilde{g}_2N_2$. At $t=0$, these two wave functions correspond to the ground states of the Gross-Pitaevskii equation in the box potentials with characteristic lengths $L_{1,2}$, with $L_2=\alpha L_1$. Both initial wave functions $\psi_{1,2}(0)$ can be chosen real, and the scale invariance of the (time-independent) 2D Gross-Pitaevskii equation ensures that they are homothetic: $\alpha\psi_2(\alpha\boldsymbol{r},0)=\psi_1(\boldsymbol{r},0)$. For example, in the limit $E_{\rm int}\gg E_{\rm kin}$, $\psi(0)$ corresponds to a uniform density in the bulk and goes to zero at the edges on a scale given by the healing length $\xi\equiv[N\hbar^2/(2mE_{\rm int})]^{1/2}$. For two box potentials of homothetic shapes filled with the same number of particles, the ratio ξ_2/ξ_1 is equal to the ratio L_2/L_1.

We explore experimentally this mapping between two evolutions in the particular case $L_1=L_2$ and $\omega_1\to 0$, i.e., $\alpha=1$ and $\zeta\to+\infty$. We thus compare the evolution of clouds with the same shape and the same size either in a harmonic potential or in free (2D) space. The choice of the initial shape is arbitrary; here we start from a uniform triangle of side length 40.2(3) μm with $3.9(3)\times10^4$ atoms and let it evolve either in a harmonic potential of frequency $\omega_2/(2\pi)=19.7(2)$ Hz or without any potential ($\omega_1=0$). In both cases, we record images of the evolution, examples of which are given in Figs. 2(a) and 2(b). These two evolutions should be linked via Eq. (9). The relation (11) between t and t' reads

$$\tan(\omega_2 t')=\omega_2 t, \quad (13)$$

and the relation (10) becomes

$$\lambda(t)=(1+\omega_2^2t^2)^{1/2}. \quad (14)$$

The relation (13) indicates that the scaling transformation maps the first quarter of the oscillation period in the harmonic trap $\omega_2 t'\leq\pi/2$ onto the ballistic expansion from $t=0$ to $t=\infty$. In the absence of interactions, this result has a simple physical interpretation: After the ballistic expansion between $t=0$ to $t=\infty$, the asymptotic position distribution reveals the initial velocity distribution of the gas, whereas the evolution in the harmonic trap during a quarter of oscillation period exchanges initial positions and initial velocities. We emphasize that the mapping (13) also holds for an interacting system as a consequence of the SO(2,1) symmetry underlying the 2D Gross-Pitaevskii equation [28].

In order to reconstruct the scaling laws (13) and (14) from the measured evolutions, we compare each image $n_1(\boldsymbol{r},t)$ for the free evolution with the set of images $n_2(\boldsymbol{r}',t')$ obtained for the in-trap evolution. More precisely, we start by defining the overlap $\mathcal{O}[n_1,n_2]$ between two images in the following way:

(i) We introduce the scalar product $(n_1|n_2)$ between two images

$$(n_1|n_2)=\int n_1(\boldsymbol{r})n_2(\boldsymbol{r})d^2r \quad (15)$$

and the norm of an image $\|n_1\|=\sqrt{(n_1|n_1)}$.

(ii) In order to relate two images that differ by a spatial scaling factor λ, we introduce the quantity

$$p[n_1,n_2,\lambda]=\frac{(n_1^{(\lambda)}|n_2)}{\|n_1^{(\lambda)}\|\|n_2\|}, \quad (16)$$

where $n_1^{(\lambda)}(\boldsymbol{r})=\lambda^2 n_1(\lambda\boldsymbol{r})$ is the image rescaled from $n_1(\boldsymbol{r})$ by the factor λ, with the same atom number:

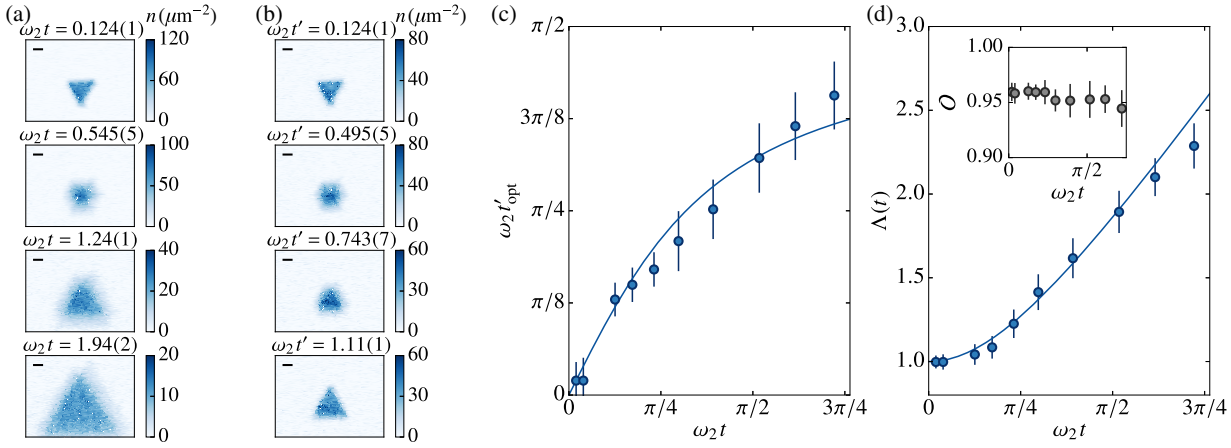

FIG. 2. Evolution of a gas with triangular shape [side length 40.2(3) μm, 3.9(3) $\times$ 10^4 atoms] for two different values of the harmonic trapping frequency. (a),(b) Averaged images of the density distribution after a variable evolution time in the harmonic potential of frequency $\omega_1 = 0$ and $\omega_2/2\pi = 19.7(2)$ Hz, respectively. The images are an average over five to ten realizations, and the horizontal black lines represent 10 μm. Pairs of images with approximately corresponding evolution times are shown. (c) Optimal time $t'_{\mathrm{opt}}(t)$ for which the overlap between images of the first and the second evolutions is maximum. (d) Optimal rescaling factor between the corresponding images $n_1(t)$ and $n_2(t'_{\mathrm{opt}})$. In the two graphs (c) and (d), the solid lines are the theoretical predictions given by Eqs. (13) and (14). The inset of (d) presents the overlap between the corresponding images of the two series. In (c) and (d), the error bars indicate the confidence intervals within 2 standard deviations of the fits used to reconstruct the scaling laws.

$N_1 = \int n_1(\boldsymbol{r}) d^2 r = \int n_1^{(\lambda)}(\boldsymbol{r}) d^2 r$. Note that the definition of the norm given above entails $\|n_1^{(\lambda)}\| = \lambda \|n_1\|$. By construction, the quantity $p[n_1, n_2, \lambda]$ is always smaller or equal to 1, and it is equal to 1 only when the image $n_1^{(\lambda)}$ is identical to n_2 up to a multiplicative factor.

(iii) Finally, for a couple of images (n_1, n_2), we vary λ and define their overlap as

$$\mathcal{O}[n_1, n_2] = \max_{\lambda} p[n_1, n_2, \lambda]. \tag{17}$$

In practice, for each image $n_1(t)$ acquired at a given time t, we determine the time t'_{opt} where the overlap between $n_1(t)$ and $n_2(t')$ is optimal. We denote $\Lambda(t)$ as the value of the scaling parameter λ for which the value $\mathcal{O}[n_1(t), n_2(t'_{\mathrm{opt}})]$ is reached (see the Supplemental Material [30] for more details). Since the center of the images may drift during the evolution, we also allow for a translation of n_2 with respect to n_1 when looking for the optimum in Eqs. (16) and (17).

The result of this mapping between the two evolutions is shown in Figs. 2(c) and 2(d). In Fig. 2(c), we plot t'_{opt} as a function of t. The prediction (13) is shown as a continuous line and is in good agreement with the data. In Fig. 2(d), we show the variation of the corresponding optimal scaling parameter $\Lambda(t)$. Here again, the prediction (14) drawn as a continuous line is in good agreement with the data. The overlap between the density distributions at the corresponding times is shown in the inset of Fig. 2(d) and is always around 0.95, confirming that these density distributions have very similar shapes. Indeed, the overlap between two images averaged over a few experimental realizations taken in the same conditions ranges from 0.98 to 0.99 due to experimental imperfections.

Finally, we note that here we connect solutions of the Gross-Pitaevskii equation (8) with the same atom number $N_1 = N_2$. Actually, the results derived above also apply to pairs of solutions with $\tilde{g}_1 N_1 = \tilde{g}_2 N_2$, since only the product $\tilde{g}N$ enters in the Gross-Pitaevskii equation (8).

IV. SCALING LAWS IN THE HYDRODYNAMIC REGIME

In the previous section, we link the evolution of two clouds with the same atom number N (or the same $\tilde{g}N$). We show now that it is also possible to link evolutions with different N's and $\tilde{g}$'s, provided we restrict to the so-called hydrodynamic (or Thomas-Fermi) regime, where the healing length ξ is very small compared to the size of the gas.

A. General formulation

The Gross-Pitaevskii equation (8) can be equivalently written in terms of the density and the velocity fields as

$$\partial_t n + \boldsymbol{\nabla} \cdot (n\boldsymbol{v}) = 0, \tag{18}$$

$$m\partial_t \boldsymbol{v} + \boldsymbol{\nabla}\left(\frac{1}{2}mv^2 + \frac{\hbar^2}{m}\tilde{g}n + \frac{1}{2}m\omega^2 r^2 + P(n)\right) = 0, \tag{19}$$

where $P(n) = -\hbar^2/2m(\boldsymbol{\nabla}^2\sqrt{n})/\sqrt{n}$ is the so-called quantum pressure. When the characteristic length scales over

which the density and velocity vary are much larger than the healing length ξ, one can neglect the contribution of the quantum pressure in Eq. (19):

$$m\partial_t \boldsymbol{v} + \boldsymbol{\nabla}\left(\frac{1}{2}m\boldsymbol{v}^2 + \frac{\hbar^2}{m}\tilde{g}n + \frac{1}{2}m\omega^2 r^2\right) = 0. \quad (20)$$

This approximation corresponding to the Thomas-Fermi limit leads to the regime of quantum hydrodynamics for the evolution of the density n and the irrotational velocity field $\boldsymbol{v}$ [31]. It enriches the dynamical symmetries of the problem, as we see in the following. For our experimental parameters, this approximation is legitimate since the healing length is a fraction of a micrometer only, much smaller than the characteristic size of our clouds (tens of micrometers).

We consider two homothetic shapes, e.g., two boxlike potentials with a square shape, with sizes $L_{1,2}$ and filled with $N_{1,2}$ atoms. We assume that we start in both cases with the ground state of the cloud in the corresponding shape so that the initial velocity fields are zero. Note that contrary to the case of Sec. III, the ratio between the healing lengths ξ_2/ξ_1 is not anymore equal to L_2/L_1 so that the initial wave functions are not exactly homothetic, but this mismatch occurs only close to the edges over the scale of $\xi_{1,2} \ll L_{1,2}$. As before, at time $t = 0$ we switch off the potential creating the shape under study and switch on a harmonic potential with frequency $\omega_{1,2}$. Our goal is to relate the two evolutions with parameters $(\tilde{g}_1 N_1, L_1, \omega_1)$ and $(\tilde{g}_2 N_2, L_2, \omega_2)$.

The general transformation involves three dimensionless constant parameters μ, α, ζ:

$$\tilde{g}_2 N_2 = \mu^2 \tilde{g}_1 N_1, \qquad L_2 = \alpha L_1, \qquad \omega_2 = \zeta\omega_1, \quad (21)$$

and reads

$$\tilde{g}_2 n_2(\boldsymbol{r}', t') = \lambda^2\mu^2\tilde{g}_1 n_1(\boldsymbol{r}, t), \quad (22)$$

$$\boldsymbol{v}_2(\boldsymbol{r}', t') = \lambda\mu\boldsymbol{v}_1(\boldsymbol{r}, t) - \mu\dot{\lambda}\boldsymbol{r} \quad (23)$$

with $\dot{\lambda} = [(d\lambda)/(dt)]$. The spatial variables are rescaled as $\boldsymbol{r}' = \boldsymbol{r}/\lambda(t)$ with the function λ now given by

$$\lambda(t) = \left[\frac{1}{\alpha^2}\cos^2(\omega_1 t) + \left(\frac{\zeta\alpha}{\mu}\right)^2 \sin^2(\omega_1 t)\right]^{1/2}, \quad (24)$$

and the relation between the times t and t' in frames 1 and 2 is

$$\tan(\omega_2 t') = \frac{\zeta\alpha^2}{\mu}\tan(\omega_1 t). \quad (25)$$

With a calculation similar to that detailed in the Appendix, one can readily show that if $(n_1, \boldsymbol{v}_1)$ is a solution of the hydrodynamic equations (18) and (20) for the frequency ω_1, then $(n_2, \boldsymbol{v}_2)$ is a solution for the frequency ω_2. If $\mu = 1$, these equations also apply beyond the Thomas-Fermi limit, as we show in Sec. III. More strikingly, they show that in the quantum hydrodynamic regime, the evolution of any cloud is captured by a universal dynamics that depends only on its initial geometry.

B. Connecting evolutions with a fixed trap frequency, a fixed size, and different $\tilde{g}N$

We present here the experimental investigation of the scaling described above, focusing on the case $L_1 = L_2$ and $\omega_1 = \omega_2$, i.e., $\alpha = \zeta = 1$. In other words, we compare the evolution of two clouds with the same initial shape and density distribution, different atom numbers, and different interaction strengths in a given harmonic trap. For simplicity, we consider the result of the evolution at times t and t' such that $\omega_1 t = \omega_2 t' = \pi/2$, which satisfies the constraint (25). In this case, $\lambda(t) = 1/\mu$ so that the general scaling (22) reads

$$\tilde{g}_2 n_2(\mu\boldsymbol{r}, t'_{\pi/2}) = \tilde{g}_1 n_1(\boldsymbol{r}, t_{\pi/2}). \quad (26)$$

We start with a cloud in a uniform box potential with the shape of an equilateral triangle of side length $L = 38.2(3)$ μm. At $t = 0$, we transfer the atoms in the harmonic trap of frequency $\omega/2\pi = 19.6$ Hz and remove the box potential. At $t = \pi/(2\omega)$, we image the cloud. We perform this experiment for different values of $\tilde{g}$ (and slightly different atom numbers) corresponding to the product $\tilde{g}N$ between 200 and 4000. This leads to a ratio ξ/L always smaller than 0.03, ensuring that we stay in the quantum hydrodynamic regime. The variation of $\tilde{g}$ is achieved by changing the intensity I of the laser beams creating the vertical confinement with $\tilde{g} \propto I^{1/4}$. The values of $\tilde{g}$ are obtained from the measurement of the vertical frequency ω_z (see Supplemental Material [30]).

We analyze the series of images using the same general method as in Sec. III. We select arbitrarily one image as a reference point (here, the one corresponding to $\tilde{g}N \approx 2000$ shown as a red square on Fig. 3). Then, we calculate the best overlap between this reference point and all other images obtained for different $\tilde{g}N$'s, and extract an optimal scaling parameter Λ. The results of this analysis are displayed on Fig. 3. The inset shows that the overlap is close to 1 for all values of $\tilde{g}N$, indicating that the clouds all have the same shape, as expected from Eq. (26). On the main graph of Fig. 3, we show the variations of Λ^{-2} with $\tilde{g}N$. The scaling law (24) predicts that $\Lambda^{-2} = \mu^2 \propto \tilde{g}N$, which is indicated by the solid line passing by the origin and the reference point. Here again, this prediction is in excellent agreement with the data, apart from the point for the largest $\tilde{g}N$. We attribute this discrepancy to the fact that the local defects of the vertical confinement play a more significant role at larger powers of the vertical confining laser beam.

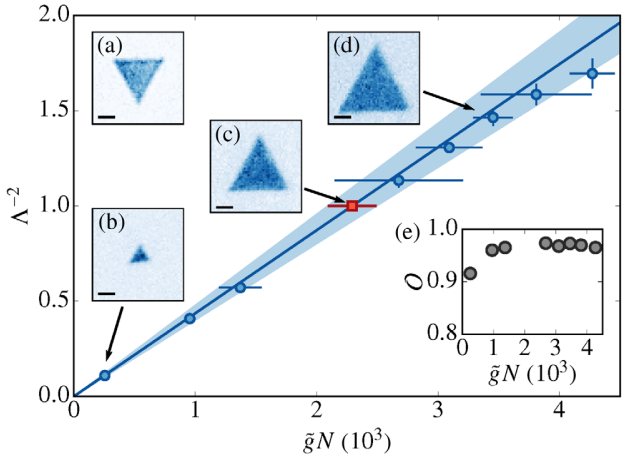

FIG. 3. Scaling factor at $\omega t = \pi/2$ for different values of $\tilde{g}N$. (a) Initial density distribution of the cloud. (b)–(d) Density distributions of the cloud after an evolution during $t = \pi/(2\omega)$ in the harmonic trap for different values of $\tilde{g}N$. For (a)–(d), the horizontal black lines represent 10 μm. Main graph: Best scaling factor Λ^{-2} as a function of $\tilde{g}N$. The red square corresponds to the reference image and its ordinate is fixed to 1. The solid line represents the prediction (26). The shaded area represents its uncertainty due to the one in the atom number of the reference point. The vertical error bars represent the precision at 2 standard deviations of the fit that determines Λ^{-2}. (e) Value of the overlap between the density distributions and the reference point. The error bars due to the fit are smaller than the black points.

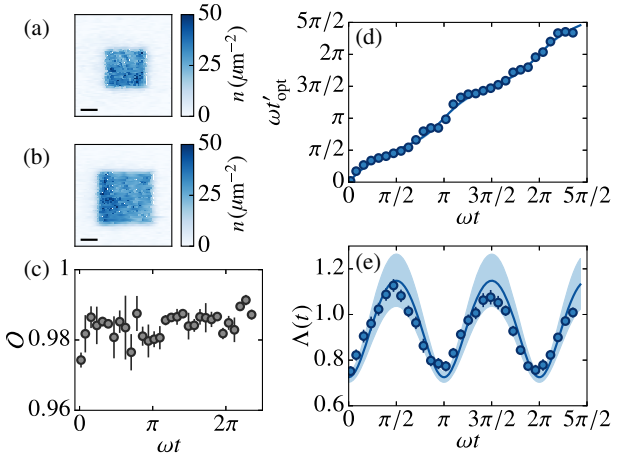

FIG. 4. Mapping between two clouds with the same shape, different sizes, and different atom numbers. (a),(b) Initial density distribution of the two clouds. The horizontal black lines represent 10 μm. (c) Best overlap between each image of the first series of images and the images of the second one. (d) Optimal time $t'_{\rm opt}$ of the second evolution as a function of the time t of the first evolution. (e) Optimal scaling factor $\Lambda(t)$ between the first and second evolutions. In (d) and (e), the solid lines are the predictions (25) and (24) where the values of the parameters α and μ are measured independently. The uncertainty of these values is represented as a shaded area. In (d), this area is too narrow to be discernable. In (c)–(e), the error bars indicate the confidence intervals within 2 standard deviations of the fit that we use to reconstruct the scaling laws. They are too small to be seen on (d).

Interestingly, the shape for $t' = \pi/(2\omega)$, i.e., $t = \infty$ for an evolution without any trap, is close to a uniformly filled triangle but inverted compared to the initial one (see insets of Fig. 3). The emergence of such a simple form after time-of-flight is reminiscent of the simple diamondlike shape obtained for the 3D expansion of a uniform gas initially confined in a cylindrical box [32]. Note that we also observe such a diamondlike shape at $t = \pi/(2\omega)$ starting from a square box, albeit with a nonuniform density (see Supplemental Material [30]).

C. Connecting evolutions with a fixed trap frequency, different sizes, and different $\tilde{g}N$

Finally, we compare the evolution of two clouds with homothetic shapes and α, $\mu \neq 1$, $\zeta = 1$, which means clouds with different initial sizes, different atom numbers, and evolving in the same harmonic trap. We perform an experiment where the initial shape is a square with a uniform density. The first cloud has a side length $L_1 = 27.0(5)$ μm, contains $N_1 = 3.7(3) \times 10^4$ atoms, and its initial density distribution is shown on Fig. 4(a). The second one has a side length $L_2 = 36.8(5)$ μm and contains $N_2 = 5.4(3) \times 10^4$ atoms [Fig. 4(b)]. The ratio ξ/L is around 0.01 for these two clouds. We let them evolve in the same harmonic potential described above and with the same interaction parameter $\tilde{g}$ and take pictures after different evolution times. We expect that the two evolutions $n_1(\boldsymbol{r}, t)$ of the first cloud and $n_2(\boldsymbol{r}', t')$ of the second cloud are linked via Eqs. (22), (24), and (25), with parameters $\alpha = L_2/L_1 = 1.36(4)$ and $\mu = \sqrt{N_2/N_1} = 1.21(8)$. We analyze the two series of images with the same procedure as in Sec. III and determine the scaling laws that link the two evolutions one to the other. The best overlaps between the images of the first and second series are shown in Fig. 4(c). They are all above 0.97, indicating that the two evolutions are indeed similar. The relation between the time t' of the second frame and the corresponding time t of the first frame is shown on Fig. 4(d), and the best scaling factor $\Lambda(t)$ is shown on Fig. 4(e). The solid lines show the theoretical predictions (25) and (24), which are in very good agreement with the experimental data.

With the three experiments described in Secs. III and IV, the scaling laws (22)–(25) are tested independently for the three parameters α, μ, and ζ, demonstrating that in the quantum hydrodynamic regime, the evolution of a cloud initially at rest depends only on its initial shape, up to scaling laws on space, time, and atom density.

V. TWO-DIMENSIONAL BREATHERS

In Sec. II, we have shown that due to the SO(2,1) symmetry, the evolution of the potential energy $E_{\rm pot}$ is

periodic with period $T/2 \equiv \pi/\omega$ for an arbitrary initial state $\psi(\boldsymbol{r}, 0)$ [see Eq. (7)]. Of course, the existence of this periodicity does not put a strong constraint on the evolution of $\psi(\boldsymbol{r}, t)$ itself. Because of the nonlinear character of the Gross-Pitaevskii equation, the evolution of ψ is not expected to be periodic, as illustrated in Fig. 1(b) for a square initial shape. When looking experimentally or numerically at various initial shapes like uniformly filled squares, pentagons, or hexagons, we indeed observe that even though $E_{\mathrm{pot}}(jT/2) = E_{\mathrm{pot}}(0)$ for integer values of j, the shapes $n(\boldsymbol{r}) = N|\psi(\boldsymbol{r})|^2$ at those times are notably different from the initial ones. We find two exceptions to this statement, which are the cases of an initial equilateral triangle and a disk. This section is devoted to the study of these very particular states that we call "breathers".

In the present context of a fluid described by the Gross-Pitaevskii equation, we define a breather as a wave function $\psi(\boldsymbol{r}, t)$ that undergoes a periodic evolution in an isotropic harmonic trap of frequency ω (for a generalization to different settings, see, e.g., Refs. [22,33]). According to this definition, the simplest example of a breather is a steady-state $\psi_{\mathrm{S}}(\boldsymbol{r})$ of the Gross-Pitaevskii equation, e.g., the ground state. Other breathers are obtained by superposing ψ_{S} with one eigenmode of the Bogoliubov–de Gennes equations resulting from the linearization of the Gross-Pitaeveskii equation around ψ_{S}. In principle (with the exception of the breathing mode [15]), the population of this mode should be vanishingly small to avoid damping via nonlinear mixing. Extending this scheme to the superposition of several modes in order to generate more complex types of breathers seems difficult. Indeed, the eigenmode frequencies are, in general, noncommensurable with each other; therefore, the periodicity of the motion cannot occur as soon as several modes are simultaneously excited [34]. Note that for a negative interaction coefficient $\tilde{g}$ in 1D, a bright soliton forms a stable steady state of the Gross-Pitaevskii equation (even for $\omega \to 0$) and thus also matches our definition. In that particular 1D case, a richer configuration exhibiting explicitly the required time periodicity is the Kuznetsov-Ma breather, which is obtained by superposing a bright soliton and a constant background (see, e.g., Ref. [37] and references therein).

Here, we are interested in 2D breathers that go well beyond a single-mode excitation, and we start our study with the uniform triangular shape. In this case, for experiments performed with a gas in the Thomas-Fermi regime, we find that the evolution of the shape is periodic with period $T/2$ within the precision of the measurement. As an illustration, we show in Fig. 5(a) four images taken between $t = 0$ and $T/2$. The scalar product $(n(0)|n(t))$ between the initial distribution and the one measured at times $T/2$, T, $3T/2$, and $2T$ shown in Fig. 5(b) is indeed very close to 1. We can reproduce the same result for various initial atom numbers.

We did not find an analytical proof of this remarkable result, but we can confirm it numerically by simulating the evolution of a wave function $\psi(\boldsymbol{r}, t)$ with the Gross-Pitaevskii equation [38]. We show in Fig. 6(a) a few snapshots of the calculated density distribution and in Fig. 6(b) the evolution of the modulus of the (usual) scalar product $|\langle\psi(0)|\psi(t)\rangle|$ between the wave functions at times 0 and t. The calculation is performed on a square grid of

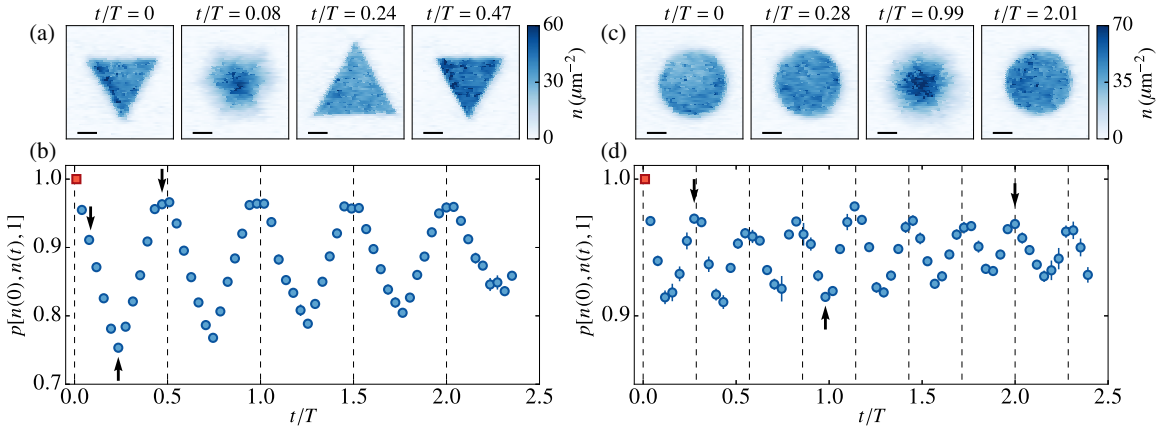

FIG. 5. (a) Density distributions of an initially triangular-shaped cloud at $t/T = 0$, $t/T = 0.08$, $t/T \approx 1/4$, and $t/T \approx 1/2$. The first and last distributions are close to each other. (b) Scalar product between the initial density distribution of a triangular-shaped cloud (red square) and the density distributions during its evolution in the harmonic trap. The first point is fixed at 1. The dashed lines indicate where t/T is a multiple of $1/2$. The shape seems to be periodic of period $T/2$. (c) Density distributions of an initially disk-shaped cloud at $t/T = 0$, $t/T \approx 2/7$, $t/T \approx 1$, and $t/T \approx 2$. The first two and the last distributions are close to each other. (d) Scalar product between the initial density distribution of a disk-shaped cloud (red square) and the density distributions during its evolution in the harmonic trap. The first point is fixed at 1. The dashed lines indicate where t/T is a multiple of $2/7$. The shape seems to be periodic of period $2/7$. In (a) and (c), the horizontal black lines represent 10 μm. In (b) and (d), the black arrows indicate the point corresponding to density distributions shown in (a) and (c), respectively. The error bars represent the statistical error of the measurement.

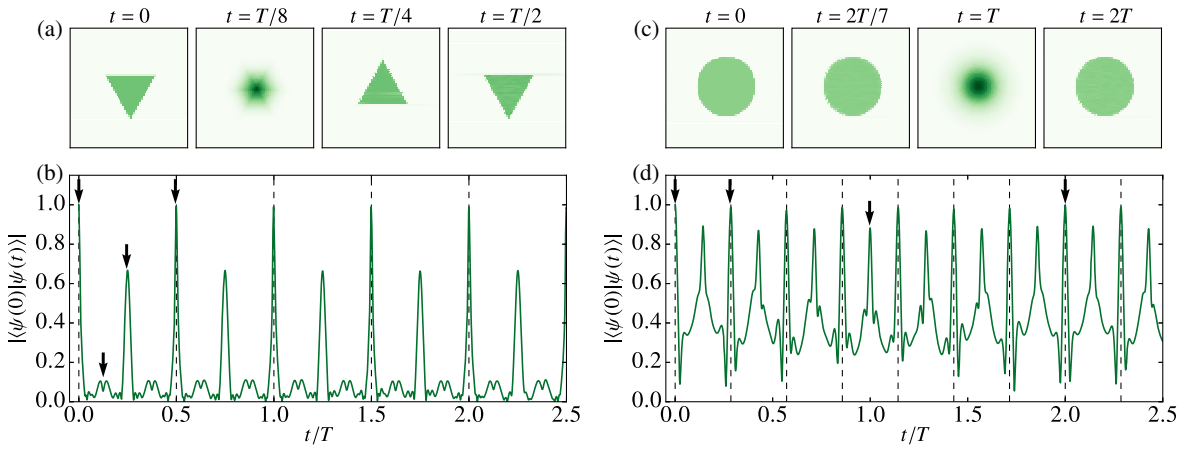

FIG. 6. (a) Calculated density distributions at times $t/T = 0, 1/8, 1/4, 1/2$ and (b) calculated time evolution of $|\langle\psi(0)|\psi(t)\rangle|$ starting from the ground state in a triangular box. The numerical integration of the Gross-Pitaevskii equation is performed on a 512×512 grid. The triangle is centered on the grid, with a side length equal to half the grid size. We choose $\tilde{g}N = 25\,600$ corresponding to an initial healing length $\xi \approx \ell$, where ℓ is the grid step. (c) Calculated density distributions at times $t/T = 0, 2/7, 1, 2$ and (d) calculated time evolution of $|\langle\psi(0)|\psi(t)\rangle|$ starting from the ground state in a disk-shaped box. The numerical integration of the Gross-Pitaevskii equation is performed on a 512×512 grid. The disk is centered on the grid, with a diameter equal to half the size of the grid. We choose $\tilde{g}N = 12\,800$ leading to an initial healing length $\xi \approx 2\ell$, where ℓ is the grid step. In (b) and (d), the black arrows indicate the times corresponding to the snapshots presented in (a) and (c).

size $N_s \times N_s$ with $N_s = 512$. The initial wave function is the ground state of a triangular box with the side length $N_s/2$ centered on the grid, obtained by imaginary time evolution for $\tilde{g}N = 25\,600$. Note that by contrast to the "scalar product between images" introduced above, the quantity $|\langle\psi(0)|\psi(t)\rangle|$ is also sensitive to phase gradients of the wave functions. Its evolution shows clear revivals approaching unity for t close to multiples of $T/2$.

We show in Fig. 7(a) the finite-size scaling analysis of the value of the first maximum of this scalar product occurring at $t_{\max} \approx T/2$ for increasing grid sizes $N_s = 64, \ldots, 1024$. The product $\tilde{g}N$ is adjusted such that the healing length $\xi = [N\hbar^2/(2mE_{\text{int}})]^{1/2} = a\ell$, where ℓ is the grid spacing and $a^2 = 0.5$, 1, 2, 4, 8. The condition $a \ll N_s$ ensures that ξ is much smaller than the size of the triangle (Thomas-Fermi regime), while having $a \gtrsim 1$ provides an accurate sampling of the edges of the cloud. The overlap between $|\psi(0)\rangle$ and $|\psi(t_{\max})\rangle$ increases with the grid size and reaches 0.995 for the largest grid.

In the simulation, the trapping frequency ω is adjusted such that $|\Delta E| \ll E_{\text{tot}}$ in Eq. (7); the cloud then keeps an approximately constant area over time, which is favorable for the numerics. Note that this choice does not restrict the generality of the result, since the scaling laws seen in Sec. III allow one to connect the evolution of a given $\psi(\boldsymbol{r}, t = 0)$ in traps with different frequencies. In particular, if the evolution starting from $\psi(\boldsymbol{r}, 0)$ in a trap of frequency ω_1 is periodic with period π/ω_1, the evolution in another trap with frequency ω_2 will be periodic with period π/ω_2 [see Eq. (11)].

Two simulations with the same ratio $a/N_s \propto \xi/L$, where $L = \ell N_s/2$ is the size of the initial cloud, describe the same physical system with a better accuracy as a and N_s are increased. For the results in Fig. 7(a), increasing the number of pixels N_s for a fixed a/N_s makes the scalar product closer to 1. If this result could be extended as such to arbitrary large values of N_s, this would demonstrate that the ground state of a triangular box evolves periodically in a harmonic potential. However, a closer look at the results of this finite-size scaling analysis seems to indicate that a should either be kept constant or increased at a slower rate than N_s to have the scalar product approaching 1 in an optimal way. Of course this conjecture deduced from our numerical analysis needs to be further explored with analytical tools, which is out of the scope of the present paper.

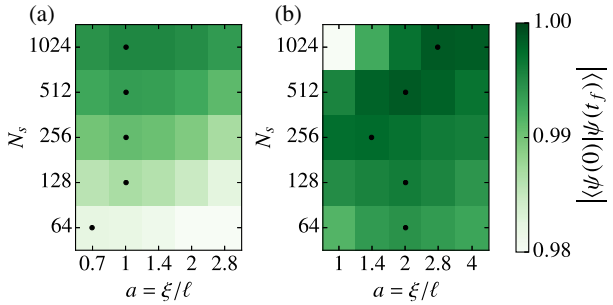

FIG. 7. Finite-size scaling for the numerical simulations. (a) Scalar product $|\langle\psi(0)|\psi(T/2)\rangle|$ for an initial triangular shape. The size of the grid N_s and the sampling of the healing length $a \equiv \xi/\ell$ are varied. The highest value is 0.9953 obtained for $N_s = 1024$, $a = 1$. (b) Scalar product $|\langle\psi(0)|\psi(2T)\rangle|$ for an initial disk shape. The highest value is 0.9986 obtained for $N_s = 1024$, $a = 2.8$. On both figures, the black dots indicate the highest value of the scalar product for each line.

The requirement for the Thomas-Fermi regime ($\xi/L \ll 1$) is necessary for obtaining a periodic evolution of the shape with period $T/2$. Indeed, in the ideal gas case ($\tilde{g} = 0$), the evolution over $T/2$ corresponds to an inversion of the initial shape with respect to the origin, i.e., a triangle pointing upwards for the case of interest here [Fig. 5(a)]. One may then wonder about the existence of a periodicity T for the triangular shape, irrespective of the product $\tilde{g}N$. Indeed this periodicity holds in both limiting cases $\tilde{g} = 0$ (ideal gas) and $\tilde{g}N$ large (Thomas-Fermi regime). However, numerical simulations show unambiguously that the evolution is not periodic in the intermediate case.

We also run the same simulations for other simple regular polygons (square, pentagons, hexagon). We do not observe a similar revival of the initial wave function over the time period $(0, 5T)$ (see Supplemental Material [30] for details).

Finally, we turn to the case of a disk-shaped initial cloud [Fig. 5(c)]. The experiment is performed with a cloud prepared such that $|\Delta E| \ll E_{\mathrm{tot}}$ in Eq. (7), so that the potential energy is approximately constant over time. In this particular case, the experimental result shown in Fig. 5(d) seems to indicate a periodicity of approximately $2T/7$ for the evolution of the overlap between $n(\boldsymbol{r}, 0)$ and $n(\boldsymbol{r}, t)$. To illustrate this, Fig. 5(c) displays four density distributions at times between 0 and $2T$. Let us assume that this periodicity $2T/7$ is exact when $\Delta E = 0$. For a disk-shaped initial distribution with any value of ΔE, the evolution cannot be $2T/7$ periodic. Indeed, the potential energy of the cloud is only $T/2$ periodic, which is not a submultiple of $2T/7$. However, all the disk-shaped clouds should have a $2T$ periodicity, which is the least common multiple of $T/2$ and $2T/7$. As we show now, this $2T$ periodicity is well supported by a numerical analysis.

We show in Fig. 6(c) snapshots of the calculated density distribution and in Fig. 6(d) the time evolution of the overlap $|\langle\psi(0)|\psi(t)\rangle|$ starting from the ground state in a disk-shaped box potential centered on a 512×512 grid. The disk diameter is chosen equal to half the grid size, and the simulation is run for $\tilde{g}N = 12\,800$. This simulation shows that the overlap between $\psi(\boldsymbol{r}, 0)$ and $\psi(\boldsymbol{r}, t)$ indeed recovers values close to 1 at times close to multiples of $2T/7$, as observed experimentally.

A closer inspection of Fig. 6(d) indicates that the time evolution of the overlap is in good approximation periodic with period $2T$, with a symmetry around $t = T$ as well as around $t = 2T$. If the evolution is effectively periodic with period $2T$, the symmetry around these points is expected. Indeed, the wave function is chosen real for $t = 0$, and will thus be real also at $2T$ (up to a global phase). Therefore, the evolution must be symmetric around those points thanks to time-reversal symmetry. On the other hand, this symmetry does not show up around the other local maxima $j2T/7$ ($j = 1, \ldots, 6$), indicating that one does not expect a full overlap with the initial state for those points.

In order to investigate further the revival around $2T$, we run a finite-size scaling analysis for the same grid sizes as for the triangles and for $a^2 = 1, 2, 4, 8, 16$ [Fig. 7(b)]. We find that the numerical results are compatible with a full recovery of the initial wave function at time $2T$, with a scalar product between the wave functions at times 0 and $2T$ attaining a maximum of 0.9986 for the largest grid size $N_s = 1024$ and $a^2 = 8$. In this case, the optimal value of a for a given N_s (marked with a dot in Fig. 7) increases with N_s; note that the optimal ratio $a/N_s \propto \xi/L$ decreases when N_s increases, which guarantees that the cloud remains in the Thomas-Fermi regime.

To conclude this section, we emphasize that the phenomenon described here is notably different from the existence of a breathing mode at frequency 2ω [14,15] that we mention in the Introduction and explore in Sec. II. Here, we observe a periodic motion of the whole cloud not just of the second moment $\langle r^2 \rangle$ of the position. We also note that the observed phenomenon is a genuine nonlinear effect, which cannot be captured by a linearization of the motion of the cloud around an equilibrium position. Indeed, the state of the gas at an intermediate time may dramatically differ from the state at initial time or after a full period both in terms of size and shape. A proper analysis of these breathers may require a multimode approach, with the observed phenomenon resulting from a mode synchronization effect via nonlinear couplings.

VI. SUMMARY AND OUTLOOK

In this paper, we investigate experimentally some important consequences of the dynamical symmetries of the two-dimensional Gross-Pitaevkii equation describing the evolution of a weakly interacting Bose gas in a harmonic potential. First, we show that the SO(2,1) symmetry leads to a periodic evolution of the potential energy and to scaling laws between the evolution of clouds with the same atom number and the same interaction parameter. Second, we show that in the quantum hydrodynamic regime, more symmetries allow one to describe the evolution of the gas by a single universal function irrespective of its size, atom number, trap frequency, and interaction parameter $\tilde{g}$. This universal evolution depends only on the initial shape and velocity field of the cloud. Third, we identify two geometrical boxlike potentials, equilateral triangle and disk, which lead to a periodic motion of the wave function when one starts with a gas uniformly filling these shapes and releases it in a harmonic potential of frequency ω. The periods of these breathers are π/ω and $4\pi/\omega$ for the triangles and the disks, respectively. This result is confirmed by a numerical simulation for a cloud initially in the Thomas-Fermi regime of the boxlike potential, giving an overlap between the initial state and the state after one period larger than 0.995 and 0.998 for the triangle and the disk, respectively.

The existence of these breathers raises several interesting questions. First, it is not immediate that their existence is a direct consequence of the dynamical symmetries of the system. If this is the case, such breathers could appear also for other systems exhibiting the SO(2,1) symmetry, like a three-dimensional unitary Fermi gas or a cloud of particles with a $1/r^2$ interaction potential. Remarkably, the latter case can be approached using classical (Newton) equations of motion; a preliminary numerical analysis with up to 10^5 particles indicates that an initial triangular (resp. disk) shape with uniform filling also leads to an approximate periodic evolution in a harmonic potential with same period $T/2$ (resp. $2T$) as the solution of the Gross-Pitaevskii equation. We also note that in the 1D case, the spectrum of the Hamiltonian of a gas of particles interacting with a repulsive $1/r^2$ potential is composed of evenly spaced energy levels, ensuring a periodic evolution of the system for any initial state [39,40].

The allowed shapes for such breathers is also an intriguing question. In our exploration (both experimental and numerical), we find this behavior only for triangles and disks, but one cannot exclude that complex geometrical figures can show a similar phenomenon. Another issue is related with thermal effects. For all studies reported here, we operate with a gas deeply in the degenerate regime, which is well approximated by the zero-temperature Gross-Pitaevskii formalism. A natural extension of our work is therefore to study to which extent the present findings will subsist in the presence of a significant nonsuperfluid component. For our experimental setup, this will require a significant increase in the vertical trapping frequency so that the vertical degree of freedom remains frozen for the thermal component of the gas.

Finally, we recall that the SO(2,1) symmetry is only an approximation for the description of a two-dimensional Bose gas. It is valid when the gas can be modeled by a classical field analysis, hence, for a small interaction parameter $\tilde{g} \ll 1$. For stronger interactions, one has to turn to a quantum treatment of the fluid. This breaks the scale invariance and the SO(2,1) symmetry that exist at the classical field level, providing an example of a "quantum anomaly" [19,41,42]. For example, the frequency of the breathing mode of a gas in a harmonic potential then differs from its classical value 2ω. It remains to be understood if a similar quantum anomaly shows up for the breathers described in this work.

ACKNOWLEDGMENTS

This work is supported by Domaine d'intérêt majeur (DIM) NanoK, ERC (Synergy UQUAM), QuantERA ERA-NET (NAQUAS project), and Grant No. ANR-18-CE30-0010. We thank Yvan Castin, Cheng Chin, Ignacio Cirac, Lei Feng, Jörg Schmiedmayer, and Steven Simon for stimulating discussions.

APPENDIX: SYMMETRY GROUPS OF THE SCHRÖDINGER AND 2D GROSS-PITAEVSKII EQUATIONS

For completeness, we summarize in this Appendix the main properties of the transformations that leave invariant the Schrödinger equation (i) for a free particle and (ii) for a particle confined in a harmonic potential. The ensemble of these transformations forms a group called the maximal kinematical invariance group, which is parametrized in the 2D case by eight real numbers. In what follows, we are interested only in the subgroup that is relevant for scale and conformal invariance. For example, in the case of a free particle, five parameters are related to space translations, changes of Galilean frame, and rotations, which do not play a role in our study. We are then left with three parameters corresponding to time translations, dilations, and special conformal transformations. These transformations also leave the 2D Gross-Pitaevskii equation invariant. In the following, we identify their generators and show that they obey the SO(2,1) commutation algebra. We follow closely the approach of Refs. [5,43], which was developed for the Schrödinger equation describing the motion of a single particle but also applies with little modifications to the case of the nonlinear Gross-Pitaevskii equation. In this Appendix, we set $\hbar = 1$ to simplify the notations.

1. Free particles

Although we are interested ultimately in the case where the particles evolve in a harmonic potential, we start by a brief summary of the free-particle case, for which the algebra is slightly simpler, while involving transformations of a similar type. In Ref. [5], it was shown that in addition to space translations, rotations, and Galilean transformations, the three following transformations leave invariant the free-particle Schrödinger equation:

(i) The translations in time

$$\boldsymbol{r} \to \boldsymbol{r}, \qquad t \to t + \beta, \tag{A1}$$

since the Hamiltonian has no explicit time dependence.

(ii) The dilations

$$\boldsymbol{r} \to \boldsymbol{r}/\lambda, \qquad t \to t/\lambda^2 \tag{A2}$$

already introduced in Eq. (1) of the main text.

(iii) The so-called "expansions"

$$\boldsymbol{r} \to \frac{\boldsymbol{r}}{\gamma t + 1}, \qquad \boldsymbol{t} \to \frac{t}{\gamma t + 1}, \tag{A3}$$

which correspond to a special conformal transformation for the time.

The combination of these transformations forms a three-parameter group with the most general transformation written as

$$\boldsymbol{r} \to g(\boldsymbol{r}, t) \equiv \frac{\boldsymbol{r}}{\gamma t + \delta}, \tag{A4}$$

$$t \to h(t) \equiv \frac{\alpha t + \beta}{\gamma t + \delta}, \tag{A5}$$

with the constraint $\alpha\delta - \beta\gamma = 1$. The dilation (A2) is obtained by setting $\beta = \gamma = 0$, $\delta = \lambda$, and $\alpha\delta = 1$.

Let us consider a function $\psi_1(\boldsymbol{r}, t)$ which is a solution of the Gross-Pitaevskii equation in free space:

$$\mathcal{P}_0[\psi_1; \boldsymbol{r}, t] = 0 \tag{A6}$$

with

$$\mathcal{P}_0[\psi; \boldsymbol{r}, t] \equiv i\frac{\partial \psi}{\partial t} + \frac{1}{2m}\boldsymbol{\nabla}_{\boldsymbol{r}}^2\psi - \frac{\tilde{g}N}{m}|\psi|^2\psi. \tag{A7}$$

Starting from $\psi_1(\boldsymbol{r}, t)$, we define the function $\psi_2(\boldsymbol{r}', t')$ as

$$\psi_2(\boldsymbol{r}', t') = f(\boldsymbol{r}, t)\psi_1(\boldsymbol{r}, t) \tag{A8}$$

with $\boldsymbol{r}'$, t' set as

$$\boldsymbol{r}' = g(\boldsymbol{r}, t), \qquad t' = h(t) \tag{A9}$$

and

$$f(\boldsymbol{r}, t) = (\gamma t + \delta)\exp\left(-i\frac{m\gamma r^2/2}{\gamma t + \delta}\right). \tag{A10}$$

With a tedious but straightforward calculation, one can check that $\psi_2(\boldsymbol{r}', t')$ is also a solution of the Gross-Pitaevskii equation

$$\mathcal{P}_0[\psi_2; \boldsymbol{r}', t'] = 0 \tag{A11}$$

for any value of the parameters $\alpha, \beta, \gamma, \delta$ with the constraint $\alpha\delta - \beta\gamma = 1$. The group of transformations (A4) and (A5) thus allows one to generate an infinite number of solutions of the Gross-Pitaevskii equation. We could pursue this analysis by determining the generators associated with the action of these transformations on the wave functions $\psi(\boldsymbol{r}, t)$, but we postpone it to the case of a harmonically confined system which is more relevant for our physical system. The two studies are anyway very similar, and the symmetry groups of the two systems have the same Lie algebra [5,43].

2. Particles in a harmonic trap

In the presence of an isotropic harmonic potential of frequency ω, the general transformations on position and time leaving invariant the Schrödinger equation are also defined by a set of four numbers $(\alpha, \beta, \gamma, \delta)$ with the constraint $\alpha\delta - \beta\gamma = 1$ [43]. Setting

$$\eta = \tan(\omega t), \qquad \eta' = \tan(\omega t'), \tag{A12}$$

the change in position is

$$\boldsymbol{r} \to \boldsymbol{r}' = g(\boldsymbol{r}, t) \equiv \frac{\boldsymbol{r}}{\lambda(t)} \tag{A13}$$

with

$$\lambda(t) = [[\alpha\sin(\omega t) + \beta\cos(\omega t)]^2 + [\gamma\sin(\omega t) + \delta\cos(\omega t)]^2]^{1/2}, \tag{A14}$$

while the transformation on time $t \to t' = h(t)$ reads

$$\eta' = \frac{\alpha\eta + \beta}{\gamma\eta + \delta}. \tag{A15}$$

Note that the time translations belong to this set of transformations, as expected for a time-independent problem. They are obtained by taking $\alpha = \delta = \cos(\omega t_0)$ and $\beta = -\gamma = \sin(\omega t_0)$.

We start with a solution ψ_1 of the Gross-Pitaevskii equation in the trap

$$\mathcal{P}_\omega[\psi_1; \boldsymbol{r}, t] = 0 \tag{A16}$$

with

$$\mathcal{P}_\omega[\psi; \boldsymbol{r}, t] = \mathcal{P}_0[\psi; \boldsymbol{r}, t] - \frac{1}{2}m\omega^2 r^2\psi. \tag{A17}$$

Using this group of transformations, we can generate another function $\psi_2(\boldsymbol{r}', t')$ satisfying

$$\mathcal{P}_\omega[\psi_2; \boldsymbol{r}', t'] = 0 \tag{A18}$$

following the definitions (A8) and (A9) with now

$$f(\boldsymbol{r}, t) = \lambda(t)\exp\left(-i\frac{m\dot{\lambda}r^2}{2\lambda}\right). \tag{A19}$$

The fact that ψ_2 is a solution of the Gross-Pitaevskii equation was proven for the noninteracting case in Ref. [43], and one can check that the contribution of the interaction term proportional to $|\psi|^2\psi$ cancels in the 2D case thanks to the scaling $f \propto \lambda$.

In the main text, we use a specific version of the transformation $(\boldsymbol{r}, t) \to (\boldsymbol{r}', t')$ that (i) maps the time $t = 0$ onto the time $t' = 0$, and (ii) is such that $\dot{\lambda}(0) = 0$ since we want to relate a real solution ψ_1 onto another real solution ψ_2 (ψ_1 and ψ_2 are both ground-state wave functions in a boxlike potential). These two conditions, in association with $\alpha\delta - \beta\gamma = 1$, impose $\beta = \gamma = 0$ and $\delta = 1/\alpha$, hence,

$$\lambda(t) = \left[\alpha^2 \sin^2(\omega t) + \frac{1}{\alpha^2}\cos^2(\omega t)\right]^{1/2} \tag{A20}$$

and

$$\tan(\omega t') = \alpha^2 \tan(\omega t). \tag{A21}$$

Finally, we note that the simple dilation transformation $\boldsymbol{r}' = \boldsymbol{r}/\sqrt{\zeta}$, $t' = t/\zeta$ allows one to relate a solution of the Gross-Pitaevskii equation $\psi_1(\boldsymbol{r}, t)$ in a trap with frequency ω_1 to a solution

$$\psi_2(\boldsymbol{r}', t') = \sqrt{\zeta}\psi_1(\boldsymbol{r}, t) \tag{A22}$$

in a trap with frequency $\omega_2 = \zeta\omega_1$:

$$\mathcal{P}_{\omega_1}[\psi_1; \boldsymbol{r}, t] = 0 \Rightarrow \mathcal{P}_{\omega_2}[\psi_2; \boldsymbol{r}', t'] = 0. \tag{A23}$$

We can thus combine this dilation with the transformation (A20) and (A21) in order to obtain the transformation that links two (initially real) solutions $\psi_1(\boldsymbol{r}, t)$ and $\psi_2(\boldsymbol{r}', t')$ of the Gross-Pitaevskii equation for a given $\tilde{g}N$ obtained in harmonic traps with frequencies $\omega_{1,2}$ and starting with homothetic initial conditions with characteristic lengths $L_{1,2}$. This transformation reads

$$\boldsymbol{r}' = \frac{\boldsymbol{r}}{\lambda(t)}, \qquad \tan(\omega_2 t') = \zeta\alpha^2 \tan(\omega_1 t) \tag{A24}$$

with

$$\lambda(t) = \left[\alpha^2\zeta^2 \sin^2(\omega_1 t) + \frac{1}{\alpha^2}\cos^2(\omega_1 t)\right]^{1/2} \tag{A25}$$

and $\alpha = L_2/L_1$, $\zeta = \omega_2/\omega_1$. This transformation corresponds to the scaling (10) used in the main text.

3. Generators and SO(2,1) symmetry

We now look for the infinitesimal generators of the transformation $\psi_1 \to \psi_2$ in the presence of a harmonic potential (Appendix Sec. II) and show that they fulfill the commutation algebra characteristic of the SO(2,1) group. We focus here on the transformation (A13)–(A15) which relates solutions of the Gross-Pitaevskii equation for the same nonlinear coefficient $\tilde{g}N$ and the same trap frequency ω.

We first note that the set of four numbers $(\alpha, \beta, \gamma, \delta)$ with the constraint $\alpha\delta - \beta\gamma = 1$ actually forms a set of three independent parameters for the free-particle case (Appendix Sec. I). To this set of numbers, we can associate a matrix

$$M = \begin{pmatrix} \alpha & \beta \\ \gamma & \delta \end{pmatrix} \tag{A26}$$

of the group $\mathrm{SL}(2, R)$. In order to simplify our discussion, we consider the following three subgroups of $\mathrm{SL}(2, R)$, each parametrized by a single parameter s_j, $j = 1, 2, 3$:

$$\begin{pmatrix} e^{s_1/2} & 0 \\ 0 & e^{-s_1/2} \end{pmatrix}, \quad \begin{pmatrix} \cosh(s_2/2) & \sinh(s_2/2) \\ \sinh(s_2/2) & \cosh(s_2/2) \end{pmatrix}, \tag{A27}$$

and

$$\begin{pmatrix} \cos(s_3/2) & -\sin(s_3/2) \\ \sin(s_3/2) & \cos(s_3/2) \end{pmatrix}. \tag{A28}$$

We obtain three independent generators by considering a small displacement from the unit matrix for each subgroup ($|s_j| \ll 1$). In all three cases, we write the passage from ψ_1 to ψ_2 as

$$\psi_2(\boldsymbol{r}, t) \approx [\hat{1} - is_j \hat{L}_j(t)]\psi_1(\boldsymbol{r}, t), \tag{A29}$$

where we introduce the time-dependent generator $\hat{L}_j(t)$. The goal is to determine explicitly these operators and their commutation relation in order to check that they satisfy the SO(2,1) algebra.

(a) Generator associated with s_1. We have in this case

$$M \approx \hat{1} + \frac{s_1}{2}\hat{\sigma}_z, \tag{A30}$$

where the $\hat{\sigma}_j$, $j = x, y, z$ are the Pauli matrices. We first get $\lambda(t) = 1 - (s_1/2)\cos(2\omega t)$ so that

$$f(\boldsymbol{r}, t) = 1 - \frac{s_1}{2}\cos(2\omega t) - is_1\frac{m\omega r^2}{2}\sin(2\omega t), \tag{A31}$$

and the infinitesimal changes in $\boldsymbol{r}$, t are

$$g(\boldsymbol{r}, t) \approx \boldsymbol{r}\left(1 + \frac{s_1}{2}\cos(2\omega t)\right), \quad h(t) = t + \frac{s_1}{2\omega}\sin(2\omega t). \tag{A32}$$

These expressions allow one to determine the passage from ψ_1 to ψ_2 as in Eq. (A29) with

$$\hat{L}_1(t) = -\frac{i}{2}\cos(2\omega t)(1 + \boldsymbol{r}\cdot\boldsymbol{\nabla}) + \frac{1}{2\omega}\sin(2\omega t)(m\omega^2 r^2 - i\partial_t). \tag{A33}$$

(b) Generator associated with s_2. We find

$$M \approx \hat{1} + \frac{s_2}{2}\hat{\sigma}_x. \tag{A34}$$

In this case, $\lambda(t) = 1 + (s_2/2)\sin(2\omega t)$, and

$$f(\boldsymbol{r},t)=1+\frac{s_2}{2}\sin(2\omega t)-is_2\frac{m\omega r^2}{2}\cos(2\omega t). \quad \text{(A35)}$$

It also provides the transformation of space and time coordinates:

$$g(\boldsymbol{r},t)\approx \boldsymbol{r}\left(1-\frac{s_2}{2}\sin(2\omega t)\right),$$
$$h(t)=t+\frac{s_2}{2\omega}\cos(2\omega t). \quad \text{(A36)}$$

This corresponds to a transformation similar to the one considered above in Eq. (A32) with the time translation $t\to t+\pi/(4\omega)$. The associated operator for the passage from ψ_1 to ψ_2 is thus

$$\hat{L}_2(t)=\frac{1}{2\omega}\cos(2\omega t)(m\omega^2 r^2-i\partial_t)+\frac{i}{2}\sin(2\omega t)(1+\boldsymbol{r}\cdot\boldsymbol{\nabla}). \quad \text{(A37)}$$

(c) Generator associated with s_3. Finally, we have for the third case,

$$M\approx\hat{1}-\frac{s_3}{2}i\hat{\sigma}_y. \quad \text{(A38)}$$

We simply have $\lambda(t)=1$, $f(\boldsymbol{r},t)=1$, and this case corresponds to the time translations mentioned above, for which we have

$$g(\boldsymbol{r},t)=\boldsymbol{r}, \qquad h(t)=t-s_3/2\omega. \quad \text{(A39)}$$

The operator $\hat{L}_3(t)$ is thus

$$\hat{L}_3(t)=\frac{i}{2\omega}\partial_t. \quad \text{(A40)}$$

From the expressions of the three generators $\hat{L}_j$, we easily find the commutations relations valid at any time

$$[\hat{L}_1,\hat{L}_2]=-i\hat{L}_3, \quad [\hat{L}_2,\hat{L}_3]=i\hat{L}_1, \quad [\hat{L}_3,\hat{L}_1]=i\hat{L}_2, \quad \text{(A41)}$$

which are characteristic of the Lorentz group SO(2,1). As explained in Ref. [15], this set of commutation relations allows one to construct, in particular, families of solutions with an undamped breathing motion.

[1] M. Bander and C. Itzykson, *Group Theory and the Hydrogen Atom (I)*, Rev. Mod. Phys. **38**, 330 (1966).

[2] R. Jackiw, *Introducing Scale Symmetry*, Phys. Today **25**, No. 1, 23 (1972).

[3] Y. Nakayama, *Scale Invariance vs Conformal Invariance*, Phys. Rep. **569**, 1 (2015).

[4] C. R. Hagen, *Scale and Conformal Transformations in Galilean-Covariant Field Theory*, Phys. Rev. D **5**, 377 (1972).

[5] U. Niederer, *The Maximal Kinematical Invariance Group of the Free Schrödinger Equation*, Helv. Phys. Acta **45**, 802 (1972).

[6] V. de Alfaro, S. Fubini, and G. Furlan, *Conformal Invariance in Quantum Mechanics*, Nuovo Cimento Soc. Ital. Fis. **34A**, 569 (1976).

[7] *The BCS-BEC Crossover and the Unitary Fermi Gas*, edited by W. Zwerger (Springer Science & Business Media, New York, 2011), Vol. 836.

[8] D. T. Son, *Vanishing Bulk Viscosities and Conformal Invariance of the Unitary Fermi Gas*, Phys. Rev. Lett. **98**, 020604 (2007).

[9] E. Elliott, J. A. Joseph, and J. E. Thomas, *Observation of Conformal Symmetry Breaking and Scale Invariance in Expanding Fermi Gases*, Phys. Rev. Lett. **112**, 040405 (2014).

[10] F. Werner and Y. Castin, *Unitary Gas in an Isotropic Harmonic Trap: Symmetry Properties and Applications*, Phys. Rev. A **74**, 053604 (2006).

[11] B. V. Svistunov, E. S. Babaev, and N. V. Prokof'ev, *Superfluid States of Matter* (CRC Press, Boca Raton, London, New York, 2015).

[12] C.-L. Hung, X. Zhang, N. Gemelke, and C. Chin, *Observation of Scale Invariance and Universality in Two-Dimensional Bose Gases*, Nature (London) **470**, 236 (2011).

[13] T. Yefsah, R. Desbuquois, L. Chomaz, K. J. Günter, and J. Dalibard, *Exploring the Thermodynamics of a Two-Dimensional Bose Gas*, Phys. Rev. Lett. **107**, 130401 (2011).

[14] Y. Kagan, E. L. Surkov, and G. V. Shlyapnikov, *Evolution of a Bose Gas under Variations of the Confining Potential*, Phys. Rev. A **54**, R1753 (1996).

[15] L. P. Pitaevskii and A. Rosch, *Breathing Mode and Hidden Symmetry of Trapped Atoms in Two Dimensions*, Phys. Rev. A **55**, R853 (1997).

[16] V. Gritsev, P. Barmettler, and E. Demler, *Scaling Approach to Quantum Non-Equilibrium Dynamics of Many-Body Systems*, New J. Phys. **12**, 113005 (2010).

[17] F. Chevy, V. Bretin, P. Rosenbusch, K. W. Madison, and J. Dalibard, *Transverse Breathing Mode of an Elongated Bose-Einstein Condensate*, Phys. Rev. Lett. **88**, 250402 (2002).

[18] E. Vogt, M. Feld, B. Fröhlich, D. Pertot, M. Koschorreck, and M. Köhl, *Scale Invariance and Viscosity of a Two-Dimensional Fermi Gas*, Phys. Rev. Lett. **108**, 070404 (2012).

[19] M. Olshanii, H. Perrin, and V. Lorent, *Example of a Quantum Anomaly in the Physics of Ultracold Gases*, Phys. Rev. Lett. **105**, 095302 (2010).

[20] T. Peppler, P. Dyke, M. Zamorano, I. Herrera, S. Hoinka, and C. J. Vale, *Quantum Anomaly and 2D-3D Crossover in Strongly Interacting Fermi Gases*, Phys. Rev. Lett. **121**, 120402 (2018).

[21] M. Holten, L. Bayha, A. C. Klein, P. A. Murthy, P. M. Preiss, and S. Jochim, *Anomalous Breaking of Scale*

Invariance in a Two-Dimensional Fermi Gas, Phys. Rev. Lett. **121**, 120401 (2018).

[22] T. Dauxois and M. Peyrard, *Physics of Solitons* (Cambridge University Press, Cambridge, England, 2006).

[23] C. Eigen, J. A. P. Glidden, R. Lopes, E. A. Cornell, R. P. Smith, and Z. Hadzibabic, *Universal Prethermal Dynamics of Bose Gases Quenched to Unitarity*, Nature (London) **563**, 221 (2018).

[24] S. Erne, R. Bücker, T. Gasenzer, J. Berges, and J. Schmiedmayer, *Universal Dynamics in an Isolated One-Dimensional Bose Gas Far from Equilibrium*, Nature (London) **563**, 225 (2018).

[25] M. Prüfer, P. Kunkel, H. Strobel, S. Lannig, D. Linnemann, C.-M. Schmied, J. Berges, T. Gasenzer, and M. K. Oberthaler, *Observation of Universal Dynamics in a Spinor Bose Gas Far from Equilibrium*, Nature (London) **563**, 217 (2018).

[26] J. L. Ville, T. Bienaimé, R. Saint-Jalm, L. Corman, M. Aidelsburger, L. Chomaz, K. Kleinlein, D. Perconte, S. Nascimbène, J. Dalibard, and J. Beugnon, *Loading and Compression of a Single Two-Dimensional Bose Gas in an Optical Accordion*, Phys. Rev. A **95**, 013632 (2017).

[27] M. Aidelsburger, J. L. Ville, R. Saint-Jalm, S. Nascimbène, J. Dalibard, and J. Beugnon, *Relaxation Dynamics in the Merging of N Independent Condensates*, Phys. Rev. Lett. **119**, 190403 (2017).

[28] One may question the validity of the Gross-Pitaevskii equation (GPE), hence, of scale invariance, after a long expansion time when the gas occupies a large area R^2. If we were interested in the ground state of a box of size $R \to \infty$ and a given $\tilde{g}N$, we would indeed expect deviations with respect to GPE because the relevant momenta $k \sim R^{-1}$ would tend to 0, and logarithmic corrections in k to the coupling constant would become significant [29]. Here, this issue is absent because the initial interaction energy is converted into kinetic energy at the beginning of the expansion. The relevant atomic momenta thus remain approximately $(2mE_{\rm int}/N\hbar^2)^{1/2}$ at all times, which validates the use of the GPE.

[29] D. S. Petrov, M. Holzmann, and G. V. Shlyapnikov, *Bose-Einstein Condensation in Quasi-2D Trapped Gases*, Phys. Rev. Lett. **84**, 2551 (2000).

[30] See Supplemental Material at http://link.aps.org/supplemental/10.1103/PhysRevX.9.021035 for details on the measurement of the vertical frequency and the experimental reconstruction of the scaling laws, for the measured density distributions starting from a cloud with a square shape, and for more results of numerical simulations starting from various geometrical shapes.

[31] L. Pitaevskii and S. Stringari, *Bose-Einstein Condensation and Superfluidity*, 2nd ed. (Oxford University Press, Oxford, 2016).

[32] I. Gotlibovych, T. F. Schmidutz, A. L. Gaunt, N. Navon, R. P. Smith, and Z. Hadzibabic, *Observing Properties of an Interacting Homogeneous Bose-Einstein Condensate: Heisenberg-Limited Momentum Spread, Interaction Energy, and Free-Expansion Dynamics*, Phys. Rev. A **89**, 061604(R) (2014).

[33] A. R. Bishop, J. A. Krumhansl, and S. E. Trullinger, *Solitons in Condensed Matter: A Paradigm*, Physica (Amsterdam) **1D**, 1 (1980).

[34] For the ground state of a harmonically confined 2D gas in the Thomas-Fermi limit, the mode frequencies are $\omega(2n^2 + 2nm + 2n + m)^{1/2}$ with n, m positive or null integers [35,36].

[35] S. Stringari, *Dynamics of Bose-Einstein Condensed Gases in Highly Deformed Traps*, Phys. Rev. A **58**, 2385 (1998).

[36] T.-L. Ho and M. Ma, *Quasi 1 and* 2*d Dilute Bose Gas in Magnetic Traps: Existence of Off-Diagonal Order and Anomalous Quantum Fluctuations*, J. Low Temp. Phys. **115**, 61 (1999).

[37] L.-C. Zhao, L. Ling, and Z.-Y. Yang, *Mechanism of Kuznetsov-Ma Breathers*, Phys. Rev. E **97**, 022218 (2018).

[38] Despite the fact that our parameters are well within the Thomas-Fermi regime, we perform the numerical analysis using the Gross-Pitaevskii equation (8) and not the quantum hydrodynamic equations (18) and (20). The reason is that the discontinuity of the density that appears in the latter case on the edge of the sample may lead to numerical singularities in the subsequent dynamics.

[39] F. Calogero, *Solution of the One-Dimensional N-Body Problems with Quadratic and/or Inversely Quadratic Pair Potentials*, J. Math. Phys. **12**, 419 (1971).

[40] B. Sutherland, *Exact Results for a Quantum Many-Body Problem in One Dimension. II*, Phys. Rev. A **5**, 1372 (1972).

[41] B. R. Holstein, *Anomalies for Pedestrians*, Am. J. Phys. **61**, 142 (1993).

[42] A. Cabo, J. L. Lucio, and H. Mercado, *On Scale Invariance and Anomalies in Quantum Mechanics*, Am. J. Phys. **66**, 240 (1998).

[43] U. Niederer, *The Maximal Kinematical Invariance Group of the Harmonic Oscillator*, Helv. Phys. Acta **46**, 191 (1973).

Tan's two-body contact across the superfluid transition of a planar Bose gas

Y.-Q. Zou, B. Bakkali-Hassani, C. Maury, É. Le Cerf, S. Nascimbene, J. Dalibard, and J. Beugnon
Laboratoire Kastler Brossel, Collège de France, CNRS,
ENS-PSL Research University, Sorbonne Université,
11 Place Marcelin Berthelot, 75005 Paris, France
(Dated: July 24, 2020)

Tan's contact is a quantity that unifies many different properties of a low-temperature gas with short-range interactions, from its momentum distribution to its spatial two-body correlation function. Here, we use a Ramsey interferometric method to realize experimentally the thermodynamic definition of the two-body contact, *i.e.* the change of the internal energy in a small modification of the scattering length. Our measurements are performed on a uniform two-dimensional Bose gas of ^{87}Rb atoms across the Berezinskii–Kosterlitz–Thouless superfluid transition. They connect well to the theoretical predictions in the limiting cases of a strongly degenerate fluid and of a normal gas. They also provide the variation of this key quantity in the critical region, where further theoretical efforts are needed to account for our findings.

The thermodynamic equilibrium of any homogeneous fluid is characterized by its equation of state. This equation gives the variations of a thermodynamic potential, *e.g.* the internal energy E, with respect to a set of thermodynamics variables such as the number of particles, temperature, size and interaction potential. All items in this list are mere real numbers, except for the interaction potential whose characterization may require a large number of independent variables, making the determination of a generic equation of state challenging.

A considerable simplification occurs for ultra-cold atomic fluids, when the average distance between particles d is much larger than the range of the potential between two atoms. Binary interactions can then be described by a single number, the s-wave scattering length a. Considering a as a thermodynamic variable, one can define its thermodynamic conjugate, the so-called Tan's contact [1–9]

$$C \equiv \frac{8\pi m a^2}{\hbar^2}\,\frac{\partial E}{\partial a}, \tag{1}$$

where the derivative is taken at constant atom number, volume and entropy, and m is the mass of an atom. For a pseudo-spin 1/2 Fermi gas with zero-range interactions, one can show that the conjugate pair (a, C) is sufficient to account for all possible regimes for the gas, including the strongly interacting case $a \gtrsim d$ [10, 11]. For a Bose gas, the situation is more complicated: formally, one needs to introduce also a parameter related to three-body interactions, and in practice this three-body contact can play a significant role in the strongly interacting regime [12–14].

Since the pioneering experimental works of [15, 16], the two-body contact has been used to relate numerous measurable quantities regarding interacting Fermi gases: tail of the momentum distribution, short distance behavior of the two-body correlation function, radio-frequency spectrum in a magnetic resonance experiment, etc. (see [17, 18] and refs. in). For the Bose gas case of interest here, experimental determinations of two- and three-body contacts are much more scarce, and concentrated so far on either the quasi-pure BEC regime [19, 20] or the thermal one [19, 21]. Here, we use a two-pulse Ramsey interferometric scheme to map out the variations of the two-body contact from the strongly degenerate, superfluid case to the non-degenerate, normal one.

We operate with a uniform, weakly-interacting two-dimensional (2D) Bose gas where the superfluid transition is of Berezinskii–Kosterlitz–Thouless (BKT) type [22, 23]. For our relatively low spatial density, effects related to the three-body contact are negligible and we focus on the two-body contact. It is well known that for the BKT transition, all thermodynamic functions are continuous at the critical point, except for the superfluid density [24]. Our measurements confirm that the two-body contact is indeed continuous at this point. We also show that the (approximate) scale invariance in 2D allows us to express it as a function of a single parameter, the phase-space density $\mathcal{D} = n\lambda^2$, where n is the 2D density, $\lambda = (2\pi\hbar^2/mk_{\rm B}T)^{1/2}$ the thermal wavelength and T the temperature. Our measurements around the critical point of the BKT transition provides an experimental milestone which shows the limits of the existing theoretical predictions in the critical region.

RESULTS

Accessing Tan's contact for a planar geometry. Our ultra-cold Bose gas is well described by the Hamiltonian $\hat{H}$, sum of the kinetic energy operator, the confining potential, and the interaction potential $\hat{H}_{\rm int} = a\hat{K}$ with

$$\hat{K} = \frac{2\pi\hbar^2}{m} \iint \hat{\psi}^\dagger(\boldsymbol{r})\,\hat{\psi}^\dagger(\boldsymbol{r}')\,\hat{\delta}(\boldsymbol{r}-\boldsymbol{r}')\,\hat{\psi}(\boldsymbol{r}')\,\hat{\psi}(\boldsymbol{r})\,\mathrm{d}^3r\,\mathrm{d}^3r'. \tag{2}$$

Here $\hat{\delta}(\boldsymbol{r})$ is the regularized Dirac function entering in the definition of the pseudo-potential [25] and the field operator $\hat{\psi}(\boldsymbol{r})$ annihilates a particle in $\boldsymbol{r}$. Using Hellmann–Feynman theorem, one can rewrite the contact defined in Eq. (1) as $C = 8\pi m a^2 \langle \hat{K} \rangle / \hbar^2$.

In our experiment, the gas is uniform in the horizontal xy plane, and it is confined with a harmonic potential of frequency ω_z along the vertical direction. We choose $\hbar\omega_z$ larger than both the interaction energy and the temperature, so that the gas is thermodynamically two-dimensional (2D). On the other hand, the extension of the gas $a_z = (\hbar/m\omega_z)^{1/2}$ along the direction z is still large compared to the scattering length a, so that the collisions keep their 3D character and Eq. (2) remains relevant [26]. Suppose first that the zero-range potential $\hat{\delta}(\boldsymbol{r}-\boldsymbol{r}')$ appearing in (2) does not need to be regularized. Then, after integration over z, C can be related to the in-plane two-body correlation function g_2:

$$\frac{C}{C_0} \stackrel{?}{=} g_2(0), \qquad C_0 \equiv 4(2\pi)^{3/2}\frac{a^2\bar{n}N}{a_z}, \tag{3}$$

where we introduced the average in normal order:

$$g_2(\boldsymbol{r}) = \frac{1}{\bar{n}^2}\langle : \hat{n}(\boldsymbol{r})\hat{n}(0) : \rangle, \tag{4}$$

with $\hat{n}(\boldsymbol{r})$ the operator associated with the 2D density, $\bar{n}$ its average value and N the atom number. For an ideal Bose gas, the value of $g_2(0)$ varies from 2 to 1 when one goes from the non-condensed regime to the fully condensed one [27], so that C_0 sets the scale of Tan's contact.

However, it is well known that $g_2(0)$ is generally an ill-defined quantity for an interacting fluid. For example in a Bose gas with zero-range interactions, one expects $g_2(r)$ to diverge as $1/r^2$ in 3D and $(\log r)^2$ in 2D when $r \to 0$ [12, 13]. On the other hand, when one properly regularizes the zero-range potential $\hat{\delta}$ in Eq. (2), Tan's contact is well-behaved and measurable. Here, we approach it by measuring the change in energy per atom $h\Delta\nu = \Delta E/N$ when the scattering length is changed by the small amount Δa. Replacing $\partial E/\partial a$ by $\Delta E/\Delta a$ in the definition (1), we obtain

$$\frac{C}{C_0} \approx \sqrt{2\pi}\,\frac{ma_z}{\hbar\bar{n}}\,\frac{\Delta\nu}{\Delta a}. \tag{5}$$

To measure the energy change $h\Delta\nu$ resulting for a small modification of the scattering length, we take advantage of a particular feature of the ^{87}Rb atom: All scattering lengths a_{ij}, with (i,j) any pair of states belonging to the ground-level manifold, take very similar values [28]. For example, Ref. [29] predicts $a_{11} = 100.9\,a_0$, $a_{22} = 94.9\,a_0$ and $a_{12} = 98.9\,a_0$, where the indices 1 and 2 refer to the two states $|1\rangle \equiv |F=1, m_z=0\rangle$ and $|2\rangle \equiv |F=2, m_z=0\rangle$ used in this work and a_0 is the Bohr radius. For an isolated atom, this pair of states forms the so-called clock transition at frequency $\nu_0 \simeq 6.8\,\mathrm{GHz}$, which is insensitive (at first order) to the ambiant magnetic field. Starting from a gas at equilibrium in $|1\rangle$, we use a Ramsey interferometric scheme to measure the microwave frequency required to transfer all atoms to the state $|2\rangle$. The displacement of this frequency with respect to ν_0 provides the shift $\Delta\nu$ due to the small modification of scattering length $\Delta a = a_{22} - a_{11}$.

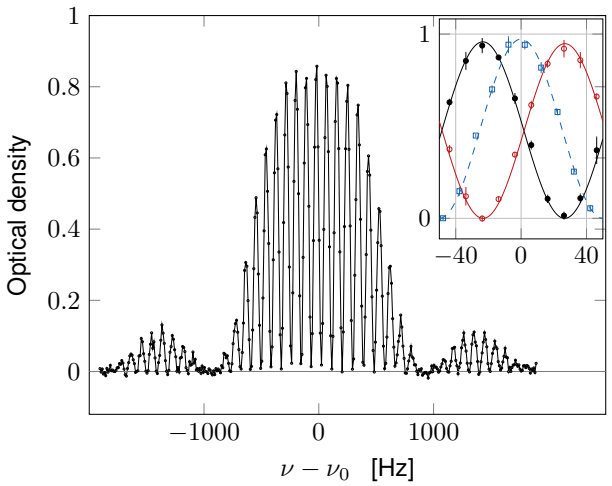

FIG. 1. Example of an interferometric Ramsey signal showing the optical density of the fraction of the gas in state $|2\rangle$ after the second Ramsey pulse, as a function of the microwave frequency ν. These data were recorded for $\bar{n} \approx 40$ atoms/µm^2 and $T \sim 22\,\mathrm{nK}$, $\tau_1 = 10\,\mathrm{ms}$. Here, τ_2 has been increased to 1 ms to limit the number of fringes for a better visibility. Inset. Filled black disks (resp. open red circles): central fringe for atoms in $|2\rangle$ (resp. $|1\rangle$) in the "standard" configuration $\tau_2 = 0.1\,\mathrm{ms}$. The density in $|1\rangle$ is obtained by applying a microwave π-pulse just before the absorption imaging phase. Blue squares: single-atom response measured during the ballistic expansion of the cloud by imaging atoms in $|2\rangle$. The lines in the inset are sinusoidal fits to the data. The vertical error bars of the inset correspond to the standard deviation of the 3 repetitions made for this measurement.

Ramsey spectroscopy on the clock transition. The Ramsey scheme consists in two identical microwave pulses, separated by a duration $\tau_1 = 10\,\mathrm{ms}$. Their duration $\tau_2 \sim 100\,\mu\mathrm{s}$ is adjusted to have $\pi/2$ pulses, *i.e.* each pulse brings an atom initially in $|1\rangle$ or $|2\rangle$ into a coherent superposition of these two states with equal weights. Just after the second Ramsey pulse, we measure the 2D spatial density $\bar{n}$ in state $|2\rangle$ in a disk-shaped region of radius 9 µm and using the absorption of a probe beam nearly resonant with the optical transition connecting $|2\rangle$ to the excited state $5P_{3/2}$, $F' = 3$. We infer from this measurement the fraction of atoms transferred into $|2\rangle$ by the Ramsey sequence, and we look for the microwave frequency ν_m that maximises this fraction.

An example of spectroscopic signal is shown in Fig. 1. In order to determine the "bare" transition frequency ν_0, we also perform a similar measurement on a cloud in ballistic expansion, for which the 3D spatial density has been divided by more than 100 and interactions play a negligible role. The uncertainty on the measured interaction-induced shift $\Delta\nu = \nu_m - \nu_0$ is on the order of 1 Hz. In principle, the precision of our measurements could be increased further by using a larger τ_1. In practice however, we have to restrict τ_1 to a value such that the spatial dy-

namics of the cloud, originating from the non-miscibility of the $1-2$ mixture ($a_{12}^2 > a_{11}a_{22}$), plays a negligible role [30]. Another limitation to τ_1 comes from atom losses, mostly due to 2-body inelastic processes involving atoms in $|2\rangle$. For $\tau_1 = 10\,\mathrm{ms}$, these losses affect less than 5% of the total population and can be safely neglected.

We see in Fig. 1 that there indeed exists a frequency ν_m for which nearly all atoms are transferred from $|1\rangle$ to $|2\rangle$, so that $E(N, a_{22}) - E(N, a_{11}) = N\,h(\nu_m - \nu_0)$ (see [31] for details). We note that for an interacting system, the existence of such a frequency is by no means to be taken for granted. Here, it is made possible by the fact that the inter-species scattering length a_{12} is close to a_{11} and a_{22}. We are thus close to the SU(2) symmetry point where all three scattering lengths coincide. The modeling of the Ramsey process detailed in [31] shows that this quasi-coincidence allows one to perform a Taylor expansion of the energy $E(N_1, N_2)$ (with $N_1 + N_2 = N$) of the mixed system between the two Ramsey pulses, and to expect a quasi-complete rephasing of the contributions of all possible couples (N_1, N_2) for the second Ramsey pulse. The present situation is thus quite different from the one exploited in [21] for example, where a_{11} and a_{12} were vanishingly small. It also differs from the generic situation prevailing in the spectroscopic measurements of Tan's contact in two-component Fermi gases, where a microwave pulse transfers the atoms to a third, non-interacting state [15].

Resonance shift $\Delta\nu$ and contact C. We show in Fig. 2 our measurements of the shift $\Delta\nu$ for densities ranging from 10 to 40 atoms/μm^2, and temperatures from 10 to 170 nK. Since $\hbar\omega_z/k_\mathrm{B} = 210\,\mathrm{nK}$, all data shown here are in the thermodynamic 2D regime $k_\mathrm{B}T < \hbar\omega_z$. More precisely, the population of the ground state of the motion along z, estimated from the ideal Bose gas model [32], is always $\gtrsim 90\,\%$. All shifts are negative as a consequence of $a_{22} < a_{11}$: the interaction energy of the gas in state $|2\rangle$ is slightly lower than in state $|1\rangle$. For a given density, the measured shift increases in absolute value with temperature. This is in line with the naive prediction of Eq. (3), since density fluctuations are expected to be an increasing function of T. Conversely for a given temperature, the shift is (in absolute value) an increasing function of density.

For the lowest temperatures investigated here, we reach the fully condensed regime in spite of the 2D character of the sample, as a result of finite size effects. In this case, the mean-field prediction for the shift reads $\Delta\nu = \bar{n}\,\hbar\,\Delta a/(\sqrt{2\pi}\,m a_z)$ [*i.e.* $C = C_0$ in Eq. (5)]. Our measurements confirm the linear variation of $\Delta\nu$ with $\bar{n}$, as shown in the inset of Fig. 2 summarizing the data for $T = 22\,\mathrm{nK}$. A linear fit to these data gives $\Delta a/a_0 = -5.7\,(1.0)$ where the error mostly originates from the uncertainty on the density calibration. In the following, we use this value of Δa for inferring the value of C/C_0 from the measured shift at any temperature, using Eq. (5). We note that this estimate for Δa is in good agreement with the prediction $\Delta a/a_0 = -6$ quoted in [29], as well as with our recent measurement [33] which is independent of the density calibration. The first corrections to the linear mean-field prediction were derived (in the 3D case) by Lee, Huang and Yang in [34]. For our densities, they have a relative contribution on the order of 5 % of the main signal ($\Delta\nu \lesssim 1\,\mathrm{Hz}$) [31], and their detection is borderline for our current precision.

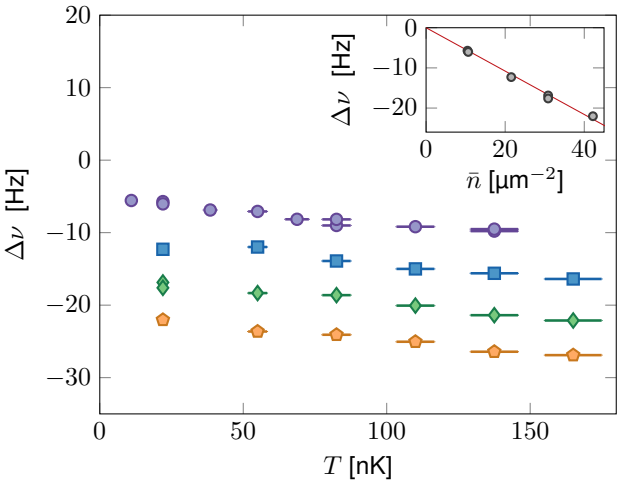

FIG. 2. Variations of the shift $\Delta\nu$ with temperature for various 2D spatial densities. Violet disks: $\bar{n} = 10.4\,(2)\,\mu\mathrm{m}^{-2}$, blue squares: $\bar{n} = 21.0\,(3)\,\mu\mathrm{m}^{-2}$, green diamonds: $\bar{n} = 31.5\,(3)\,\mu\mathrm{m}^{-2}$, orange pentagons: $\bar{n} = 42.0\,(1)\,\mu\mathrm{m}^{-2}$. The horizontal error bars represent the statistical uncertainty on the temperature calibration, except for the points at very low temperature (10-22 nK). These ultracold points are deeply in the Thomas-Fermi regime, where thermometry based on the known equation of state of the gas is not sensitive enough. The temperature is thus inferred from an extrapolation with evaporation barrier height of the higher temperature points. The error on the frequency measurement is below 1 Hz and is not shown in this graph. Inset: Variations of the shift $\Delta\nu$ with density at low temperature $T \sim 22\,\mathrm{nK}$, *i.e.* a strongly degenerate gas. The straight line is the mean-field prediction corresponding to $\Delta a = -5.7\,a_0$.

We summarize all our data in Fig. 3, where we show the normalized contact C/C_0 defined in Eq. (5) as a function of the phase-space density $\mathcal{D}$. All data points collapse on a single curve within the experimental error, which is a manifestation of the approximate scale invariance of the Bose gas, valid for a relatively weak interaction strength $\tilde{g} \lesssim 1$ [37, 38].

DISCUSSION

We now compare our results in Fig. 3 to three theoretical predictions. The first one is derived from the Bogoliubov approximation applied to a 2D quasi-condensate

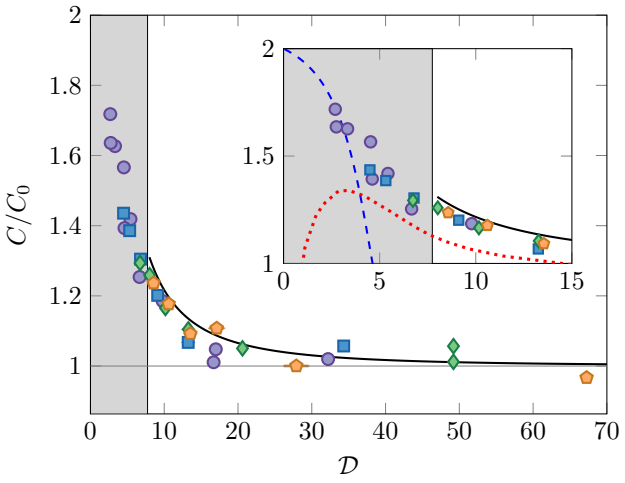

FIG. 3. Variations of the normalized Tan's contact C/C_0 with the phase-space density $\mathcal{D}$. The encoding of the experimental points is the same as in Fig. 2. The colored zone indicates the non-superfluid region, corresponding to $\mathcal{D} < \mathcal{D}_c \approx 7.7$. The continuous black line shows the prediction derived within Bogoliubov approximation. Inset: Zoom on the critical region. The dashed blue line is the prediction from [35], resulting from a virial expansion for the 2D Bose gas. The dotted red line shows the results of the classical field simulation of [36].

[39]. This prediction is expected to be valid only for $\mathcal{D}$ notably larger than the phase-space density at the critical point $\mathcal{D}_c$ (see methods), but it gives a fair account of our data over the whole superfluid region. Within this approximation, one can also calculate the two-body correlation function and write it as $g_2(r) = g_2^{T=0}(r) + g_2^{\text{thermal}}(r)$. One can then show the result [31]

$$\frac{C}{C_0} = 1 + g_2^{\text{thermal}}(0), \tag{6}$$

which provides a quantitative relation between the contact and the pair correlation function, in spite of the already mentioned singularity of $g_2^{T=0}(r)$ in $r = 0$.

For low phase-space densities, one can perform a systematic expansion of various thermodynamic functions in powers of the (properly renormalized) interaction strength [35], and obtain a prediction for C (dashed blue line in the inset of Fig. 3). By comparing the 0th, 1st and 2nd orders of this virial-type expansion, one can estimate that it is valid for $\mathcal{D} \lesssim 3$ for our parameters. When $\mathcal{D} \to 0$, the result of [35] gives $C/C_0 \to 2$, which is the expected result for an ideal, non-degenerate Bose gas. The prediction of [35] for $\mathcal{D} \sim 3$ compares favourably with our results in the weakly-degenerate case.

Finally we also show in Fig. 3 the results of the classical field simulation of [36] (red dotted line), which are in principle valid both below and above the critical point. Contrary to the quantum case, this classical analysis does not lead to any singularity for $\langle n^2(0)\rangle$, so that we can directly plot this quantity as it is provided in [36] in terms of the quasi-condensate density. For our interaction strength, we obtain a non-monotonic variation of C. This unexpected behavior, which does not match the experimental observations, probably signals that the present interaction strength $\tilde{g} = 0.16$ (see Methods) is too large for using these classical field predictions, as already suggested in [36].

Using the Ramsey interferometric scheme on a many-body system, we have measured the two-body contact of a 2D Bose gas over a wide range of phase-space densities. We could implement this scheme on our fluid thanks to the similarities of the three scattering lengths in play, a_{11}, a_{22}, a_{12}, corresponding to an approximate SU(2) symmetry for interactions. Our method can be generalized to the strongly interacting case $a_{ij} \gtrsim a_z$, as long as a Fano-Feshbach resonance allows one to stay close to the SU(2) point. One could then address simultaneously the LHY-type corrections at zero temperature [40, 41], the contribution of the three-body contact [13, 14], and the breaking of scale invariance expected at non-zero temperature. Finally we note that even for our moderate interaction strength, classical field simulations seem to fail to reproduce our results, although they could properly account for the measurement of the equation of state itself [37, 38]. The semi-classical treatment of Ref. [42] and quantum Monte Carlo approaches of Refs. [43, 44] should provide a reliable path to the modelling of this system. This would be particularly interesting in the vicinity of the BKT transition point where the usual approach based on the XY model [45], which neglects any density fluctuation, does not provide a relevant information on the behavior of Tan's contact.

METHODS

Preparation of the two-dimensional gas. The preparation and the characterization of our sample have been detailed in [46, 47] and we briefly outline the main properties of the clouds explored in this work. In the xy plane, the atoms are confined in a disk of radius 12 µm by a box-like potential, created by a laser beam properly shaped with a digital micromirror device. We use the intensity of this beam, which determines the height of the potential barrier around the disk, as a control parameter for the temperature. The confinement along the z direction is provided by a large-period optical lattice, with a single node occupied and $\omega_z/(2\pi) = 4.41\,(1)$ kHz. We set a magnetic field $B = 0.701\,(1)$ G along the vertical direction z, which defines the quantization axis. We use the expression $\mathcal{D}_c = \ln(380/\tilde{g})$ for the phase-space density at the critical point of the superfluid transition [48]. Here, $\tilde{g} = \sqrt{8\pi}\, a_{11}/a_z = 0.16$ is the dimensionless interaction strength in 2D, leading to $\mathcal{D}_c = 7.7$. We study Bose gases from the normal regime ($\mathcal{D} = 0.3\mathcal{D}_c$) to the

strongly degenerate, superfluid regime ($\mathcal{D} > 3\mathcal{D}_c$).

Acknowledgments. We thank Paul Julienne, Raphael Lopes, and Félix Werner for useful discussions. We acknowledge the contribution of Raphaël Saint-Jalm at the early stage of the project. This work was supported by ERC (Synergy Grant UQUAM), Quantera ERA-NET (NAQUAS project) and the ANR-18-CE30-0010 grant. LKB is a member of the SIRTEQ network of Région Ile-de-France.

Author contributions. Y.-Q.Z., B.B.-H. and C.M. performed the experiment and carried out the preliminary data analysis. Y.-Q.Z. performed the detailed data analysis. E.L.C. participated in the preparation of the experimental setup. S.N., J.D. and J.B. contributed to the development of the theoretical model. J.D. and J.B. wrote the manuscript with contributions from all authors.

Supplementary Material

Ramsey interferometry in a many-body system close the SU(2) symmetry point

In this section, we explain why the vicinity of the SU(2) symmetry point where all three scattering lengths are equal ($a_{11} = a_{12} = a_{22}$) allows one to reach a full transfer from $|1\rangle$ to $|2\rangle$ in the Ramsey sequence, in spite of the interactions between the particles. We first explore a two-particle model before turning to the general N-atom case.

The two-particle toy model

The analysis of a system with two particles only, which was pioneered by [49], is often used to gain insight in the N-body case, see e.g. [21, 50] in the context of microwave spectroscopy. Here we consider a pair of atoms each with two internal states $|1\rangle$ and $|2\rangle$ (Fig.4). The initial state of the two-particle system is

$$|11\rangle \otimes |\psi_0\rangle, \tag{7}$$

where $|\psi_0\rangle$ describes the external state of the pair and is symmetric by exchange of the two (bosonic) particles.

The two-body state just after the first $\pi/2$ pulse of the Ramsey sequence is

$$\left[\frac{1}{2}|A\rangle + \frac{1}{\sqrt{2}}|B\rangle + \frac{1}{2}|C\rangle\right] \otimes |\psi_0\rangle. \tag{8}$$

Here we have introduced the three states

$$|A\rangle = |11\rangle \qquad |B\rangle = \frac{1}{\sqrt{2}}\left(|12\rangle + |21\rangle\right) \qquad |C\rangle = |22\rangle \tag{9}$$

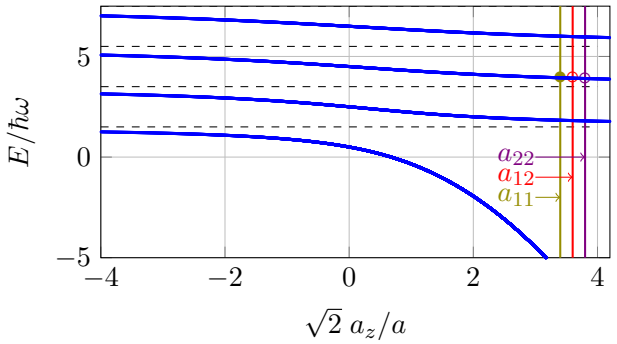

FIG. 4. Energy levels of the relative motion of zero angular momentum for a two-particle system in a 3D harmonic trap of frequency ω, as function of the scattering length. To model properly the experimental situation, the characteristic length $a_z = \sqrt{\hbar/m\omega}$ is chosen equal to the interparticle distance $d = \bar{n}^{-1/2}$ ($d \sim a_z \sim 160\,\mathrm{nm}$ for $\bar{n} = 40\,\mu\mathrm{m}^{-2}$, i.e. $\hbar\omega = \hbar^2\bar{n}/m$. Therefore the spacing $\sim 2\hbar\omega$ between adjacent levels is large compared to the interaction energy per particle, $\sim \hbar^2\bar{n}\tilde{g}/m$, since $\tilde{g} \ll 1$. The initial state $|\psi_0\rangle$ considered in the text is marked as $\bullet$ and the two other relevant states $|\phi_0\rangle$ and $|\chi_0\rangle$ are marked as $\circ$. All three scattering lengths a_{11}, a_{12}, a_{22} are close to each other (figure not to scale for actual Rb values).

which correspond to the triplet states, resulting from the coupling of the two internal states viewed as pseudo-spins 1/2.

The time evolution is described by three operators $\hat{U}_{ij}(t)$ and the state of the system reads at time t:

$$\frac{1}{2}|A\rangle \otimes \left(\hat{U}_{11}(t)|\psi_0\rangle\right) + \frac{1}{\sqrt{2}}|B\rangle \otimes \left(\hat{U}_{12}(t)|\psi_0\rangle\right) + \frac{1}{2}|C\rangle \otimes \left(\hat{U}_{22}(t)|\psi_0\rangle\right). \tag{10}$$

The action of the second $\pi/2$ pulse at time t reads:

$$|1\rangle \to \frac{1}{\sqrt{2}}\left(|1\rangle + \mathrm{e}^{\mathrm{i}\alpha}|2\rangle\right) \quad |2\rangle \to \frac{1}{\sqrt{2}}\left(|2\rangle - \mathrm{e}^{-\mathrm{i}\alpha}|1\rangle\right), \tag{11}$$

where $\alpha = 2\pi\nu t$ is the phase of the microwave at this time. After the second pulse, we find the fraction $f_2(t)$ transferred to internal state $|2\rangle$:

$$f_2(t,\alpha) = \frac{1}{2} + \frac{1}{4}\Re\left[\mathrm{e}^{\mathrm{i}\alpha}\left(\langle\hat{U}_{12}^\dagger\hat{U}_{11}\rangle + \langle\hat{U}_{22}^\dagger\hat{U}_{12}\rangle\right)\right], \tag{12}$$

where the averages are taken in state $|\psi_0\rangle$.

The contact is calculated as the derivative with respect to the scattering length of the energy of the system (here the pair of atoms) at constant entropy and in thermal equilibrium. Therefore we can suppose that $|\psi_0\rangle$ is an eigenstate of the two-particle system for the scattering length a_{11} and eventually perform a statistical average over $|\psi_0\rangle$ at the end of the analysis.

To calculate the various matrix elements $\langle \hat{U}_{ij}^\dagger \hat{U}_{kl} \rangle$ entering in the expression (12) of the Ramsey signal, we introduce the eigenbases of the two-particle system for the scattering lengths a_{12} and a_{22}, denoted respectively $\{|\phi_n\rangle\}$ and $\{|\chi_n\rangle\}$. For ^{87}Rb, the three scattering lengths a_{11}, a_{12}, a_{22} are close to each other (5% difference at most). This means that essentially one state contributes to the expansion of $|\psi_0\rangle$ on the basis $\{|\phi_n\rangle\}$ or $\{|\chi_n\rangle\}$:

$$|\psi_0\rangle \approx |\phi_0\rangle \approx |\chi_0\rangle. \tag{13}$$

This validates the assumption of constant entropy needed for the calculation of the contact: the populations of the eigenstates of the external motion of the two-particle system are quasi-unchanged by the Ramsey pulses (Fig.4).

With this assumption, we find

$$\langle \hat{U}_{12}^\dagger \hat{U}_{11} \rangle \approx \mathrm{e}^{\mathrm{i}(E_{12}-E_{11})t/\hbar}, \quad \langle \hat{U}_{22}^\dagger \hat{U}_{12} \rangle \approx \mathrm{e}^{\mathrm{i}(E_{22}-E_{12})t/\hbar} \tag{14}$$

where E_{ij} includes both the single atom energy $\pm h\nu_0/2$ and the interaction energy of the atom pair. The Ramsey signal now reads:

$$f_2(t) \approx \frac{1}{2} + \frac{1}{4}\cos\left[\alpha + (E_{12}-E_{11})t/\hbar\right] + \frac{1}{4}\cos\left[\alpha + (E_{22}-E_{12})t/\hbar\right]. \tag{15}$$

It is maximal for

$$2h\nu = E_{22} - E_{11} \tag{16}$$

as announced in the main text, and it reaches $f_2 = 1$ when a_{12} is equal to the arithmetic mean of a_{11} and a_{22}. These conclusions are unchanged when one subsequently performs a statistical average over $|\psi_0\rangle$.

Achieving a full transfer in the N-body Ramsey sequence

We consider a collection of N two-level atoms with internal states $|1\rangle, |2\rangle$, and we assume that the initial state for the Ramsey sequence corresponds to having all atoms in the internal state $|1\rangle$:

$$|\Psi_0\rangle = \frac{1}{\sqrt{N!}} \left(\hat{a}_1^\dagger\right)^N |0\rangle, \tag{17}$$

with a given external many-body state $|\psi_0\rangle$.

After the first $\pi/2$ pulse, the collective internal state is

$$|\Psi_1\rangle = \frac{1}{\sqrt{2^N N!}} \left(\hat{a}_1^\dagger + \hat{a}_2^\dagger\right)^N |0\rangle = \frac{1}{\sqrt{2^N N!}} \sum_{N_1=0}^{N} \binom{N}{N_1} \left(\hat{a}_1^\dagger\right)^{N_1} \left(\hat{a}_2^\dagger\right)^{N_2} |0\rangle. \tag{18}$$

We denote $E(N_1, N_2)$ the energy of the system with N_1 particles in $|1\rangle$ and $N_2 = N - N_1$ particles in $|2\rangle$. After the evolution for a duration t, the state becomes:

$$\frac{1}{\sqrt{2^N N!}} \sum_{N_1=0}^{N} \binom{N}{N_1} \mathrm{e}^{-\mathrm{i}E(N_1,N_2)t/\hbar} \left(\hat{a}_1^\dagger\right)^{N_1} \left(\hat{a}_2^\dagger\right)^{N_2} |0\rangle. \tag{19}$$

The second $\pi/2$ pulse at time t corresponds to

$$\hat{a}_1^\dagger \to \frac{1}{\sqrt{2}}\left(\hat{a}_1^\dagger + \mathrm{e}^{\mathrm{i}\alpha}\hat{a}_2^\dagger\right), \quad \hat{a}_2^\dagger \to \frac{1}{\sqrt{2}}\left(\hat{a}_2^\dagger - \mathrm{e}^{-\mathrm{i}\alpha}\hat{a}_1^\dagger\right), \tag{20}$$

where $\alpha = 2\pi\nu t$ is the phase of the microwave at time t.

In the binomial expansion (18), only the terms (N_1, N_2) that are close to $(N/2, N/2)$ contribute significantly. Therefore we perform a Taylor expansion of the energy of each term at first order in $q = (N_1 - N_2)/2$:

$$E\left(\frac{N}{2}+q, \frac{N}{2}-q\right) \approx E\left(\frac{N}{2}, \frac{N}{2}\right) + (\mu_1 - \mu_2)q \tag{21}$$

where

$$\mu_1 = \left(\frac{\partial E}{\partial N_1}\right)_{N_2}, \quad \mu_2 = \left(\frac{\partial E}{\partial N_2}\right)_{N_1}. \tag{22}$$

With this approximation, each term in the sum (19) has a phase that is proportional to $(N_1 - N_2)t$ and we expect a full transfer to level $|2\rangle$ after the second Ramsey pulse for :

$$h\nu = \mu_1 - \mu_2. \tag{23}$$

Validity of the expansion (21). In order to give a necessary condition on the parameters of the problem for (21) to hold, we consider the $T = 0$ case and use the expression for the mean-field energy:

$$E(N_1, N_2) = \frac{1}{2}(N_2 - N_1)h\nu_0 + \frac{\hbar^2}{2mL^2}\left(\tilde{g}_{11}N_1^2 + 2\tilde{g}_{12}N_1N_2 + \tilde{g}_{22}N_2^2\right), \tag{24}$$

where L^2 is the area of the box confining the gas. One then has the exact result:

$$E\left(\frac{N}{2}+q, \frac{N}{2}-q\right) = E\left(\frac{N}{2}, \frac{N}{2}\right) + \left[-h\nu_0 + \frac{\hbar^2}{2m}(\tilde{g}_{11} - \tilde{g}_{22})\bar{n}\right] q + \frac{\hbar^2}{2mL^2}(\tilde{g}_{11} + \tilde{g}_{22} - 2\tilde{g}_{12})q^2. \tag{25}$$

In practice, we operate the Ramsey scheme in the regime

$$\frac{\hbar t}{2m}|\tilde{g}_{11} - \tilde{g}_{22}|\bar{n} \sim 1 \tag{26}$$

to obtain a good precision on the determination of $\tilde{g}_{11} - \tilde{g}_{22}$. Using the fact that for the binomial distribution, $\langle q^2 \rangle = N/4$, we deduce that the contribution of

the last line of (25) [which was omitted in Eq. (21)] can be neglected if:

$$\frac{1}{4}\left|\tilde{g}_{11}+\tilde{g}_{22}-2\tilde{g}_{12}\right| \lesssim \left|\tilde{g}_{11}-\tilde{g}_{22}\right| \tag{27}$$

meaning that the interspecies scattering length a_{12} has to be close to the average of the intraspecies ones, a_{11} and a_{22}. This condition is well fulfilled for ^{87}Rb.

Using the approximate SU(2) symmetry

We have seen above that provided the inequality (27) is satisfied, one can achieve a full transfer from $|1\rangle$ to $|2\rangle$ in the Ramsey sequence operating in the regime (26), provided the microwave frequency is chosen such that

$$h\nu = \left(\frac{\partial E}{\partial N_1}\right)_{N_2} - \left(\frac{\partial E}{\partial N_2}\right)_{N_1}. \tag{28}$$

Here, the energy E is calculated for the parameters $N_1 = N_2 = N/2$ and the 3 scattering lengths a_{11}, a_{12} and a_{22}. Suppose now that all three scattering lengths are close to each other, so that we can expand:

$$E(N_1,N_2,a_{11},a_{12},a_{22}) \approx E(N_1,N_2,a,a,a) + (a_{12}-a_{11})\frac{\partial E}{\partial a_{12}} + (a_{22}-a_{11})\frac{\partial E}{\partial a_{22}} \tag{29}$$

where we have set $a \equiv a_{11}$. The SU(2) symmetry is exact at the point in parameter space where $a_{12} = a_{22} = a$.

We note that:

$$\frac{\partial^2 E}{\partial N_1\,\partial a_{12}}\left(\frac{N}{2},\frac{N}{2},a,a,a\right) = \frac{\partial^2 E}{\partial N_2\,\partial a_{12}}\left(\frac{N}{2},\frac{N}{2},a,a,a\right) \tag{30}$$

so that the term $\propto (a_{12}-a_{11})$ does not contribute to (28). This leads to

$$h\,\Delta\nu = (a_{22}-a_{11})\left[\frac{\partial^2 E}{\partial N_1\,\partial a_{22}} - \frac{\partial^2 E}{\partial N_2\,\partial a_{22}}\right]\left(\frac{N}{2},\frac{N}{2},a,a,a\right). \tag{31}$$

Now, the Hamiltonian of the binary system for a regularized zero-range potential is

$$\hat{H} = \hat{H}_0 + \sum_{i,j} a_{ij}\hat{K}_{ij} \tag{32}$$

where

$$\hat{K}_{ij} = \frac{2\pi\hbar^2}{m}\iint \hat{\psi}_i^\dagger(\boldsymbol{r})\,\hat{\psi}_j^\dagger(\boldsymbol{r}')\,\hat{\delta}(\boldsymbol{r}-\boldsymbol{r}')\,\hat{\psi}_j(\boldsymbol{r}')\,\hat{\psi}_i(\boldsymbol{r})\,\mathrm{d}^3r\,\mathrm{d}^3r'. \tag{33}$$

Hellmann–Feynman theorem thus leads to:

$$h\,\Delta\nu \approx (a_{22}-a_{11})\left[\frac{\partial\langle\hat{K}_{22}\rangle}{\partial N_1} - \frac{\partial\langle\hat{K}_{22}\rangle}{\partial N_2}\right]\left(\frac{N}{2},\frac{N}{2},a,a,a\right) \tag{34}$$

At the SU(2) point, we can connect the two-component system with the single component system with the same scattering length:

$$\langle\hat{K}_{22}\rangle = \frac{N_2^2}{(N_1+N_2)^2}\langle\hat{K}\rangle \tag{35}$$

We then find:

$$N\,h\,\Delta\nu \approx (a_{22}-a_{11})\,\langle\hat{K}\rangle, \tag{36}$$

which also reads, setting $\Delta a = a_{22}-a_{11}$:

$$C = \frac{16\pi^2 m a^2 N}{\hbar}\frac{\Delta\nu}{\Delta a}, \tag{37}$$

and which coincides with the expressions (3,5) of the main text.

Contact and two-body correlation within Bogoliubov approach

Bogoliubov operators and contact

We consider a 2D Bose gas confined in a square box $L\times L$ with periodic boundary conditions. We denote $\hat{a}_{\boldsymbol{k}}$ the operator that annihilates a particle with momentum $\hbar\boldsymbol{k}$. We assume that the temperature is low enough so that most of the particles accumulate in the ground state of the box $\boldsymbol{k}=0$. Since the confining box has a finite size, this does not violate Mermin-Wagner theorem, which holds for a gas in the thermodynamic limit. Note that instead of assuming a macroscopic population of $\boldsymbol{k}=0$, one may also use another version of the Bogoliubov approach in terms of phase and density fluctuations (see e.g. [39]). In that approach, which leads to the same results as the one used here, one assumes that the density fluctuations are small and that the phase fluctuations can be expanded as a Fourier series (no isolated vortex).

The Bogoliubov Hamiltonian is diagonalized by introducing the bosonic operators $\hat{b}_{\boldsymbol{k}} = u_k\hat{a}_{\boldsymbol{k}} - v_k\hat{a}^\dagger_{-\boldsymbol{k}}$ with

$$u_k, v_k = \pm\left[\frac{k^2+2\tilde{g}\bar{n}}{2k(k^2+4\tilde{g}\bar{n})^{1/2}} \pm \frac{1}{2}\right]^{1/2}, \tag{38}$$

and the energy of the Bogoliubov modes

$$\epsilon_k = \frac{\hbar^2 k}{2m}\left[k^2+4\tilde{g}\bar{n}\right]^{1/2}. \tag{39}$$

The Bogoliubov Hamiltonian reads:

$$\hat{H} = E_0 + \sum_{\boldsymbol{k}} \epsilon_k\,\hat{b}^\dagger_{\boldsymbol{k}}\hat{b}_{\boldsymbol{k}}. \tag{40}$$

In the case studied in the paper, where the thickness a_z of the gas is large compared to the scattering length, the

ground-state energy E_0 can be estimated by averaging the mean-field 3D result:

$$E_0^{(3\mathrm{D})} = \frac{2\pi\hbar^2 a}{m} n^{(3\mathrm{D})} N \tag{41}$$

over the Gaussian density profile $n^{(3\mathrm{D})}(z) = \bar{n}\, \mathrm{e}^{-z^2/a_z^2}/\sqrt{\pi a_z^2}$ along the z direction:

$$E_0 = \frac{\int E_0^{(3\mathrm{D})}(z)\; n(z)\; \mathrm{d}z}{\int n(z)\; \mathrm{d}z} = \frac{\hbar^2 \tilde{g}}{2m} \bar{n} N \tag{42}$$

The thermal averages are $\langle \hat{b}_{\boldsymbol{k}} \rangle = 0$ and $\langle \hat{b}^\dagger_{\boldsymbol{k}} \hat{b}_{\boldsymbol{k}'} \rangle = \delta_{\boldsymbol{k},\boldsymbol{k}'}\, \mathcal{N}_k$, where $\mathcal{N}_k$ is the Bose–Einstein distribution

$$\mathcal{N}_k = \left[\mathrm{e}^{\epsilon_k / k_\mathrm{B} T} - 1 \right]^{-1}. \tag{43}$$

The internal energy in thermal equilibrium thus reads:

$$E = E_0 + \sum_{\boldsymbol{k}} \epsilon_k \mathcal{N}_k. \tag{44}$$

The contact is by definition proportional to the derivative of this energy with respect to a at constant entropy, i.e. at constant populations $\mathcal{N}_k$ of the modes, which gives:

$$C = C^{T=0} + C^{\mathrm{thermal}} \tag{45}$$

with

$$C^{T=0} = \frac{8\pi m a^2}{\hbar^2} \frac{\partial E_0}{\partial a} = C_0 \tag{46}$$

and

$$\begin{aligned} C^{\mathrm{thermal}} &= \frac{8\pi m a^2}{\hbar^2} \left[\sum_{\boldsymbol{k}} \frac{\partial \epsilon_k}{\partial a} \mathcal{N}_k \right] \\ &= C_0\, \frac{2}{N} \sum_{\boldsymbol{k}} \frac{k}{\sqrt{k^2 + 4\tilde{g}\bar{n}}} \mathcal{N}_k. \end{aligned} \tag{47}$$

Density fluctuations

Average density. The average density of the gas is calculated from $\bar{n} = \langle \hat{n}(\boldsymbol{r}) \rangle$ with $\hat{n}(\boldsymbol{r}) = \hat{\psi}^\dagger(\boldsymbol{r}) \hat{\psi}(\boldsymbol{r})$, and it can be split into a $T = 0$ and a thermal component:

$$\bar{n}^{T=0} = \frac{N_0}{L^2} + \frac{1}{L^2} \sum_{\boldsymbol{k} \neq 0} v_k^2 \tag{48}$$

and

$$\bar{n}^{\mathrm{thermal}} = \frac{1}{L^2} \sum_{\boldsymbol{k} \neq 0} (u_k^2 + v_k^2)\, \mathcal{N}_k. \tag{49}$$

Density correlations. We start from the 4-field correlation function written in normal order $G_2(\boldsymbol{r}) = \langle \hat{\psi}^\dagger(0) \hat{\psi}^\dagger(\boldsymbol{r}) \hat{\psi}(\boldsymbol{r}) \hat{\psi}(0) \rangle$, which we expand up to first order in $n^{\mathrm{thermal}}/\bar{n}$:

$$\begin{aligned} G_2(\boldsymbol{r}) = \frac{N_0^2}{L^4} \;+\; \frac{N_0}{L^4} \times \\ \sum_{\boldsymbol{k} \neq 0} \mathrm{e}^{\mathrm{i}\boldsymbol{k}\cdot\boldsymbol{r}} \left(\langle \hat{a}_{-\boldsymbol{k}} \hat{a}_{\boldsymbol{k}} \rangle + \langle \hat{a}^\dagger_{-\boldsymbol{k}} \hat{a}^\dagger_{\boldsymbol{k}} \rangle + 2 \langle \hat{a}^\dagger_{\boldsymbol{k}} \hat{a}_{\boldsymbol{k}} \rangle \right) + 2 \langle \hat{a}^\dagger_{\boldsymbol{k}} \hat{a}_{\boldsymbol{k}} \rangle \end{aligned} \tag{50}$$

We can then calculate the g_2 function used in the main text:

$$g_2(\boldsymbol{r}) = \frac{G_2(\boldsymbol{r})}{\bar{n}^2} = g_2^{T=0}(\boldsymbol{r}) + g_2^{\mathrm{thermal}}(\boldsymbol{r}) \tag{51}$$

and we find by at first order in $(\bar{n} - \bar{n}_0)/\bar{n}$ [see e.g. [39]]:

$$g_2^{T=0}(\boldsymbol{r}) = 1 + \frac{2}{N} \sum_{\boldsymbol{k} \neq 0} \mathrm{e}^{\mathrm{i}\boldsymbol{k}\cdot\boldsymbol{r}} v_k (u_k + v_k) \tag{52}$$

and

$$g_2^{\mathrm{thermal}}(\boldsymbol{r}) = \frac{2}{N_0} \sum_{\boldsymbol{k} \neq 0} \mathrm{e}^{\mathrm{i}\boldsymbol{k}\cdot\boldsymbol{r}}\, (u_k + v_k)^2\; \mathcal{N}_k. \tag{53}$$

We notice that

$$(u_k + v_k)^2 = \frac{k}{\sqrt{k^2 + 4\tilde{g}\bar{n}}} \tag{54}$$

which shows the relation (6) of the main text:

$$\frac{C^{\mathrm{thermal}}}{C_0} = g_2^{\mathrm{thermal}}(0). \tag{55}$$

On the other hand, the integral giving $g_2^{T=0}$ in $\boldsymbol{r} = 0$ is UV divergent since $v_k \propto 1/k^2$ and $u_k + v_k \sim 1$ at infinity.

Lee-Huang-Yang (LHY) correction [34]

In 3D and at zero-temperature, the first beyond-mean-field correction to the contact is (see e.g. Eq.(2) in [19])

$$\frac{\delta C}{C} = \frac{5}{2} \times \frac{128}{15\sqrt{\pi}} \sqrt{n^{(3\mathrm{D})} a^3}. \tag{56}$$

In our setup, the average 3D density is $n^{(3\mathrm{D})} = \bar{n}/(a_z\sqrt{2\pi})$. For a 2D density $\bar{n} = 40\,\mathrm{atoms/\mu m^2}$ and $a_z = 160\,\mathrm{nm}$, this gives $\bar{n}^{(3\mathrm{D})} \approx 1.0 \times 10^{14}\,\mathrm{atoms/cm^3}$ and $\delta C/C \approx 4.7\,\%$. For this $\bar{n}$, the mean-field contribution to the contact corresponds to a shift $\Delta\nu = -22\,\mathrm{Hz}$ (Fig. 2 of the main text), and the LHY correction is $\approx 1\,\mathrm{Hz}$, within the uncertainty of our measurements. Note that a more precise theoretical estimate of the LHY correction for our planar geometry should start from the general expression of the ground-state energy of a 2D Bose gas [40, 41, 51] and the relation between the 2D scattering length and the 3D one [26].

Estimate for the contribution of the 3-body contact

Using the transition rates derived in [12], Fletcher et al. [21] have shown that the contribution of the 3-body contact to the many-body resonance shift is related to the shift due to the 2-body contact by:

$$\frac{\Delta\nu_3}{\Delta\nu_2} = 5.0\pi^2\, a\, \frac{C_3}{C_2}. \tag{57}$$

Now an estimate of C_3/C_2 for a dilute BEC is provided by [14]:

$$\frac{C_3}{C_2} \sim 0.02\, n^{(3D)} a^2 \tag{58}$$

so that the contribution of the 3-body contact is reduced by a factor $\sim n^{(3D)}a^3 \sim 10^{-5}$ with respect to the contribution of the 2-body contact. Even though the 2D nature of the thermodynamics of our gas may bring some significant corrections to this crude estimate, we can safely assume that effects related to the 3-body contact cannot be detected with our experimental protocol.

Virial expansion for a 2D Bose gas

In [35], H.c Ren gives the result of perturbative thermodynamics applied to a regularized contact potential in 2D. Strictly speaking, this is not a virial expansion, i.e. an expansion in powers of density or fugacity, since the author takes exactly into account all powers of $\bar{n}$ in the ideal gas case.

Starting from the 2D scattering length a_2, Ren introduces the dimensionless coupling

$$\alpha(T) = \frac{1}{\ln\left(\frac{\lambda^2}{2\pi a_2^2}\right) + \gamma} \tag{59}$$

where $\lambda(T)$ is the thermal wavelength and γ the Euler constant, which is related to $\tilde{g}$ by $\tilde{g} \approx 4\pi\alpha$. He then performs a systematic expansion of various thermodynamic functions in powers of α. Note that the T dependence of α explicitly breaks the scale invariance of the problem, as expected after regularization of the contact interaction in 2D. However for our experimental parameters, this T-dependence plays a negligible role.

The value of the free energy F reads at order 2 in α:

$$F(N, L^2, T, a_2) = F_0(N, L^2, T) \; + \alpha\, \frac{4\pi\hbar^2 N^2}{mL^2} - \; \alpha^2\, \frac{8\pi L^2\hbar^2}{m\lambda^4}\phi\left[1 - \mathrm{e}^{-N\lambda^2/L^2}\right], \tag{60}$$

where F_0 is the ideal Bose gas result and where the function $\phi(z)$ is defined by:

$$\phi(z) = B(z) + \frac{1}{2}D(z) \tag{61}$$

with

$$B(z) = \sum_{r,s,t=1}^{\infty} \frac{z^{r+s+t}}{\sqrt{rs(r+t)(s+t)}} \ln \frac{\sqrt{(r+t)(s+t)} + \sqrt{rs}}{\sqrt{(r+t)(s+t)} - \sqrt{rs}} \tag{62}$$

and

$$D(z) = \sum_{r,s=1}^{\infty} \frac{z^{r+s}}{rs} \ln \frac{2rs}{r+s}. \tag{63}$$

Tan's contact

$$C = \frac{8\pi m a^2}{\hbar^2} \left(\frac{\partial F}{\partial a}\right)_{N,L^2,T} \tag{64}$$

can then be calculated using (59) together with the link between the 2D (a_2) and 3D (a) scattering lengths and the size of the ground state along the z direction (a_z) [26, 52]

$$a_2 \approx 2.092\, a_z \exp\left(-\sqrt{\frac{\pi}{2}}\frac{a_z}{a}\right). \tag{65}$$

The result is plotted in Fig. 3 of the article.

[1] S. Tan, Annals of Physics **323**, 2971 (2008).
[2] G. Baym, C. Pethick, Z. Yu, and M. W. Zwierlein, Phys. Rev. Lett. **99**, 190407 (2007).
[3] M. Punk and W. Zwerger, Phys. Rev. Lett. **99**, 170404 (2007).
[4] E. Braaten and L. Platter, Phys. Rev. Lett. **100**, 205301 (2008).
[5] F. Werner, L. Tarruell, and Y. Castin, The European Physical Journal B **68**, 401 (2009).
[6] S. Zhang and A. J. Leggett, Phys. Rev. A **79**, 023601 (2009).
[7] R. Combescot, F. Alzetto, and X. Leyronas, Phys. Rev. A **79**, 053640 (2009).
[8] R. Haussmann, M. Punk, and W. Zwerger, Phys. Rev. A **80**, 063612 (2009).
[9] E. Braaten, in *BCS-BEC Crossover and the Unitary Fermi Gas*, edited by W. Zwerger (Springer, 2011).
[10] D. S. Petrov, Phys. Rev. A **67**, 010703 (2003).
[11] S. Endo and Y. Castin, Phys. Rev. A **92**, 053624 (2015).
[12] E. Braaten, D. Kang, and L. Platter, Phys. Rev. Lett. **106**, 153005 (2011).
[13] F. Werner and Y. Castin, Phys. Rev. A **86**, 053633 (2012).
[14] D. H. Smith, E. Braaten, D. Kang, and L. Platter, Phys. Rev. Lett. **112**, 110402 (2014).
[15] J. Stewart, J. Gaebler, T. Drake, and D. Jin, Phys. Rev. Lett. **104**, 235301 (2010).
[16] E. D. Kuhnle, H. Hu, X.-J. Liu, P. Dyke, M. Mark, P. D. Drummond, P. Hannaford, and C. J. Vale, Phys. Rev. Lett. **105**, 070402 (2010).
[17] C. Carcy, S. Hoinka, M. Lingham, P. Dyke, C. Kuhn, H. Hu, and C. Vale, Phys. Rev. Lett. **122**, 203401 (2019).
[18] B. Mukherjee, P. B. Patel, Z. Yan, R. J. Fletcher, J. Struck, and M. W. Zwierlein, Phys. Rev. Lett. **122**, 203402 (2019).

[19] R. Wild, P. Makotyn, J. Pino, E. Cornell, and D. Jin, Phys. Rev. Lett. **108**, 145305 (2012).
[20] R. Lopes, C. Eigen, A. Barker, K. G. H. Viebahn, M. Robert-de Saint-Vincent, N. Navon, Z. Hadzibabic, and R. P. Smith, Phys. Rev. Lett. **118**, 210401 (2017).
[21] R. J. Fletcher, R. Lopes, J. Man, N. Navon, R. P. Smith, M. W. Zwierlein, and Z. Hadzibabic, Science **355**, 377 (2017).
[22] V. L. Berezinskii, Soviet Physics JETP **34**, 610 (1971).
[23] J. M. Kosterlitz and D. J. Thouless, J. Phys. C: Solid State Physics **6**, 1181 (1973).
[24] J. M. Kosterlitz, Rev. Mod. Phys. **89**, 040501 (2017).
[25] K. Huang, *Statistical Mechanics* (Wiley, New York, 1987).
[26] D. S. Petrov and G. V. Shlyapnikov, Phys. Rev. A **64**, 012706 (2001).
[27] M. Naraschewski and R. J. Glauber, Phys. Rev. A **59**, 4595 (1999).
[28] E. G. M. van Kempen, S. J. J. M. F. Kokkelmans, D. J. Heinzen, and B. J. Verhaar, Phys. Rev. Lett. **88**, 093201 (2002).
[29] P. Altin, G. McDonald, D. Doering, J. Debs, T. Barter, J. Close, N. Robins, S. Haine, T. Hanna, and R. Anderson, New J. Phys. **13**, 065020 (2011).
[30] Note1, we also check that no detectable spin-changing collisions appear on this time scale: more than 99 % of the atoms stay in the clock state basis.
[31] for more details see Supplementary Material.
[32] L. Chomaz, L. Corman, T. Bienaimé, R. Desbuquois, C. Weitenberg, S. Nascimbene, J. Beugnon, and J. Dalibard, Nat. Commun. **6**, 6162 (2015).
[33] Y.-Q. Zou, B. Bakkali-Hassani, C. Maury, E. Le Cerf, S. Nascimbene, J. Dalibard, and J. Beugnon, arXiv:2007. (2020).
[34] T. D. Lee, K. Huang, and C. N. Yang, Phys. Rev. **106**, 1135 (1957).
[35] H.-c. Ren, Journal of statistical physics **114**, 481 (2004).
[36] N. V. Prokof'ev and B. V. Svistunov, Phys. Rev. A **66**, 043608 (2002).
[37] C.-L. Hung, X. Zhang, N. Gemelke, and C. Chin, Nature **470**, 236 (2011).
[38] T. Yefsah, R. Desbuquois, L. Chomaz, K. J. Günter, and J. Dalibard, Phys. Rev. Lett. **107**, 130401 (2011).
[39] C. Mora and Y. Castin, Phys. Rev. A **67**, 053615 (2003).
[40] C. Mora and Y. Castin, Phys. Rev. Lett. **102**, 180404 (2009).
[41] S. Fournais, M. Napiorkowski, R. Reuvers, and J. P. Solovej, Journal of Mathematical Physics **60**, 071903 (2019).
[42] L. Giorgetti, I. Carusotto, and Y. Castin, Phys. Rev. A **76**, 013613 (2007).
[43] M. Holzmann and W. Krauth, Phys. Rev. Lett. **100**, 190402 (2008).
[44] A. Rançon and N. Dupuis, Phys. Rev. A **85**, 063607 (2012).
[45] D. R. Nelson and J. M. Kosterlitz, Phys. Rev. Lett. **39**, 1201 (1977).
[46] J. L. Ville, T. Bienaimé, R. Saint-Jalm, L. Corman, M. Aidelsburger, L. Chomaz, K. Kleinlein, D. Perconte, S. Nascimbène, J. Dalibard, et al., Phys. Rev. A **95**, 013632 (2017).
[47] J. L. Ville, R. Saint-Jalm, E. Le Cerf, M. Aidelsburger, S. Nascimbène, J. Dalibard, and J. Beugnon, Phys. Rev. Lett. **121**, 145301 (2018).
[48] N. V. Prokof'ev, O. Ruebenacker, and B. V. Svistunov, Phys. Rev. Lett. **87**, 270402 (2001).
[49] T. Busch, B. G. Englert, K. Rzazewski, and M. Wilkens, Foundations of Physics **28**, 549 (1998).
[50] A. Sykes, J. Corson, J. D'Incao, A. Koller, C. Greene, A. Rey, K. Hazzard, and J. Bohn, Phys. Rev. A **89**, 021601 (2014).
[51] M. Schick, Phys. Rev. A **3**, 1067 (1971).
[52] L. Pricoupenko and M. Olshanii, Journal of Physics B: Atomic, Molecular and Optical Physics **40**, 2065 (2007).

Magnetic dipolar interaction between hyperfine clock states in a planar alkali Bose gas

Y.-Q. Zou, B. Bakkali-Hassani, C. Maury, É. Le Cerf, S. Nascimbene, J. Dalibard, and J. Beugnon*
Laboratoire Kastler Brossel, Collège de France, CNRS, ENS-PSL University, Sorbonne Université, 11 Place Marcelin Berthelot, 75005 Paris, France
(Dated: July 24, 2020)

In atomic systems, clock states feature a zero projection of the total angular momentum and thus a low sensitivity to magnetic fields. This makes them widely used for metrological applications like atomic fountains or gravimeters. Here, we show that a mixture of two such non-magnetic states still display magnetic dipole-dipole interactions. Using high resolution spectroscopy of a planar gas of ^{87}Rb atoms with a controlled in-plane shape, we explore the effective isotropic and extensive character of these interactions and demonstrate their tunability. Our measurements set strong constraints on the relative values of the s-wave scattering lengths a_{ij} involving the two clock states.

Quantum atomic gases constitute unique systems to investigate many-body physics thanks to the precision with which one can control their interactions [1, 2]. Usually, in the ultra-low temperature regime achieved with these gases, contact interactions described by the s-wave scattering length dominate. In the recent years, non-local interaction potentials have been added to the quantum gas toolbox. Long-range interactions can be mediated thanks to optical cavities inside which atoms are trapped [3]. Electric dipole-dipole interactions are routinely achieved via excitation of atoms in Rydberg electronic states [4]. Atomic species with large magnetic moments in the ground state, like Cr, Er or Dy, offer the possibility to explore the role of magnetic dipole-dipole interactions (MDDI) [5]. The latter case has led for instance to the observation of quantum droplets [6], roton modes [7], or spin dynamics in lattices with off-site interactions [8–10].

For alkali-metal atoms, which are the workhorse of many cold-atom experiments, the magnetic moment is limited to $\lesssim 1$ Bohr magneton (μ_B) and in most cases, MDDI have no sizeable effect on the gas properties [11]. However, some paths have been investigated to evidence their role also for these atomic species. A first route consists in specifically nulling the s-wave scattering length using a Feshbach resonance [12, 13], so that MDDI become dominant. A second possibility is to operate with a multi-component (or spinor) gas [14], using several states from the ground-level manifold of the atoms. One can then take advantage of a possible coincidence of the various scattering lengths in play. When it occurs, the spin-dependent contact interaction is much weaker than the spin-independent one, and MDDI can have a significant effect [15], e.g. on the generation of spin textures [16, 17] and on magnon spectra [18]. In all instances studied so far with these multi-component gases, each component possesses a non-zero magnetic moment and creates a magnetic field that influences its own dynamics, as well as the dynamics of the other component(s).

In this Letter, we present another, yet unexplored, context in which MDDI can influence significantly the physics of a two-component gas of alkali-metal atoms.

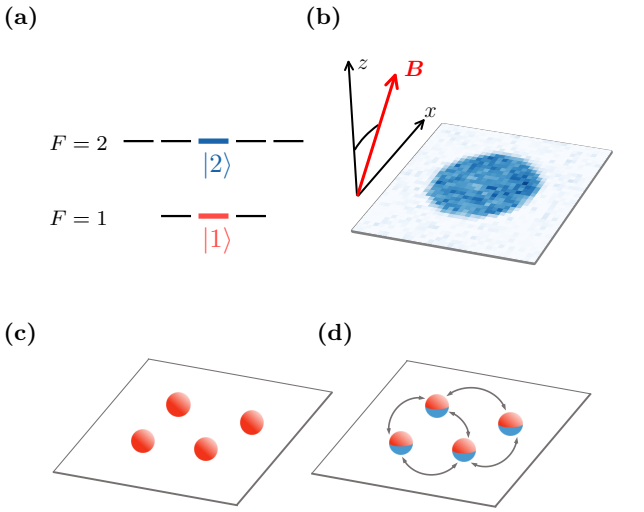

FIG. 1. (a) Level diagram of the hyperfine ground-level manifold showing the two states relevant to this work $|1\rangle \equiv |F = 1, m = 0\rangle$ and $|2\rangle \equiv |F = 2, m = 0\rangle$. (b) Image of the atomic cloud obtained through absorption imaging along the direction perpendicular to the atomic plane. Atoms are confined in the xy plane in a disk of radius 12 µm. The orientation of the magnetic field $\boldsymbol{B}$ is tuned in the xz plane. (c) Schematics of atoms prepared in the state $|1\rangle$, with no MDDI in this case. MDDI are also absent when all atoms are in $|2\rangle$. (d) Significant MDDI occur for atoms in a linear superposition of $|1\rangle$ and $|2\rangle$.

We operate with a superposition of the two hyperfine states of ^{87}Rb involved in the so-called hyperfine clock transition, $|1\rangle \equiv |F = 1, m_Z = 0\rangle$ and $|2\rangle \equiv |F = 2, m_Z = 0\rangle$, where the quantization axis Z is aligned with the uniform external magnetic field (Fig. 1a). For a single-component gas prepared in one of these two states, the average magnetization is zero by symmetry and MDDI have no effect. However, when atoms are simultaneously present in these two states, we show that magnetic interactions between them are non-zero, and that the corresponding MDDI can modify significantly the position of the clock transition frequency.

Our work constitutes a magnetic analog of the obser-

vation of electric dipole-dipole interactions (EDDI) between molecules in a Ramsey interferometric scheme [19]. There, in spite of the null value of the electric dipole moment of a molecule prepared in an energy eigenstate, it was shown that EDDI can be induced in a molecular gas by preparing a coherent superposition of two rotational states. Both in our work and in [19], the coupling between two partners results in a pure exchange interaction, with one partner switching from $|1\rangle$ to $|2\rangle$, and the other one from $|2\rangle$ to $|1\rangle$. This exchange Hamiltonian also appears for resonant EDDI between atoms prepared in different Rydberg states [20].

In spite of their different origin, the physical manifestations of MDDI in our setup are similar to the standard ones. Here, we study it for a 2D gas using high-resolution Ramsey spectroscopy (Fig. 1b) and we explicitly test two important features of DDI in this planar geometry: their effect does not depend on the in-plane shape of the cloud (isotropy), nor on its size (extensivity). More precisely, we recast the role of MDDI as a modification of the s-wave inter-species scattering length a_{12}, and show the continuous tuning of a_{12} by changing the orientation of the external magnetic field with respect to the atom plane. We obtain in this way an accurate information on the relative values of intra- and inter-species bare scattering lengths of the studied states.

We start with the restriction of the MDDI Hamiltonian to the clock state manifold [21], using the magnetic interaction between two electronic spins $\hat{\boldsymbol{s}}_A$ and $\hat{\boldsymbol{s}}_B$ with magnetic moments $\boldsymbol{m}_{A,B} = 2\mu_B \boldsymbol{s}_{A,B}$

$$\hat{V}_{\rm dd}(r,\boldsymbol{u}) = \frac{\mu_0\mu_B^2}{\pi r^3}[\hat{\boldsymbol{s}}_A\cdot\hat{\boldsymbol{s}}_B - 3(\hat{\boldsymbol{s}}_A\cdot\boldsymbol{u})(\hat{\boldsymbol{s}}_B\cdot\boldsymbol{u})], \quad (1)$$

where r is the distance between the two dipoles and $\boldsymbol{u}$ is the unit vector connecting them. The calculation detailed in [22] shows that MDDI do not modify the interactions between atoms in the same state $|1\rangle$ or $|2\rangle$, but induce a non-local, angle-dependent, exchange interaction (Figs. 1cd). The second-quantized Hamiltonian of the MDDI for the clock states is thus:

$$\hat{H}_{\rm dd}^{(1,2)} = \frac{\mu_0\mu_B^2}{4\pi}\iint {\rm d}^3r_A\,{\rm d}^3r_B \frac{1-3\cos^2\theta}{r^3}\,\hat{\Psi}_2^\dagger(\boldsymbol{r}_A)\,\hat{\Psi}_1^\dagger(\boldsymbol{r}_B)\,\hat{\Psi}_2(\boldsymbol{r}_B)\,\hat{\Psi}_1(\boldsymbol{r}_A), \quad (2)$$

where the $\hat{\Psi}_i(\boldsymbol{r}_\alpha)$ are the field operators annihilating a particle in state $|i\rangle$ at position $\boldsymbol{r}_\alpha$ and $r = |\boldsymbol{r}_A - \boldsymbol{r}_B|$.

We now investigate the spatial average value of $\hat{H}_{\rm dd}^{(1,2)}$. We note first that for a 3D isotropic gas, the angular integration gives $\langle\hat{H}_{\rm dd}^{(1,2)}\rangle_{\rm 3D} = 0$, as usual for MDDI [5]. We then consider a homogeneous quasi-2D Bose gas confined isotropically in the xy plane with area L^2. We assume that the gas has a Gaussian density profile along the third direction z, $n_{1,2}(z) = N_{1,2}e^{-z^2/\ell_z^2}/\sqrt{\pi}\ell_z L^2$, where $\ell_z = \sqrt{\hbar/m\omega_z}$ is the extension of the ground state of the harmonic confinement of frequency ω_z. One then finds [23–25]:

$$\langle\hat{H}_{\rm dd}^{(1,2)}\rangle_{\rm 2D} = \frac{\mu_0\mu_B^2 N_1 N_2}{3\sqrt{2\pi}\ell_z L^2}(3\cos^2\Theta - 1), \quad (3)$$

where Θ is the angle between the external magnetic field $\boldsymbol{B}$ and the direction perpendicular to the atomic plane. This energy is maximal and positive for $\boldsymbol{B}$ perpendicular to the atomic plane ($\Theta = 0$), and minimal and negative for $\boldsymbol{B}$ in the atomic plane ($\Theta = \pi/2$). Eq. (3) shows that the energy per atom in state $|1\rangle$ depends only on the spatial density N_2/L^2 of atoms in state $|2\rangle$, which proves the extensivity.

In 2D, the Fourier transform of the dipole-dipole Hamiltonian possesses a well-defined value at the origin $\boldsymbol{k} = 0$ [23]. Consequently, for a large enough sample (typically $L \gg \ell_z$), the average energy $\langle\hat{H}_{\rm dd}^{(1,2)}\rangle_{\rm 2D}$, evaluated by switching the integral (2) to Fourier space, is independent of the system shape. This contrasts with the 3D case, for which the MDDI energy changes sign when switching from an oblate to a prolate cloud [5, 26]. Considering the effective isotropy of the MDDI in this 2D configuration, it is convenient to describe their role as a change δa_{12} of the inter-species scattering length with respect to its bare value $a_{12}^{(0)}$. In 2D, interspecies contact interactions lead to $\langle\hat{H}_{\rm contact}^{(1,2)}\rangle_{\rm 2D} = \sqrt{8\pi}\,a_{12}\,\hbar^2 N_1 N_2/(m\ell_z L^2)$ and we deduce

$$\delta a_{12}(\Theta) = a_{\rm dd}\left(3\cos^2\Theta - 1\right), \quad (4)$$

where $a_{\rm dd} = \mu_0\mu_B^2 m/(12\pi\hbar^2)$.

We now tackle the experimental observation of this modification of the inter-species scattering length in a quasi-2D Bose gas. The experimental setup was described in [27, 28]. Basically, a cloud of ^{87}Rb atoms in state $|1\rangle$ is confined in a 2D box potential: A "hard-wall" potential provides a uniform in-plane confinement inside a 12 µm radius disk, unless otherwise stated. The vertical confinement can be approximated by a harmonic potential with frequency $\omega_z/2\pi = 4.4(1)$ kHz, corresponding to $\ell_z = 160$ nm. We operate in the weakly interacting regime characterized by the dimensionless coupling constant $\tilde{g} = \sqrt{8\pi}\,a_{11}/\ell_z = 0.16(1)$, where a_{11} is the s-wave scattering length for atoms in $|1\rangle$. The in-plane density of the cloud is $\bar{n} \approx 95/\mu{\rm m}^2$ and we operate at the lowest achievable temperature in our setup $T < 30$ nK. A ≈ 0.7 Gauss bias magnetic field $\boldsymbol{B}$ with tunable orientation is fixed during the experiment.

Spectroscopy is performed thanks to a Ramsey sequence similar to [29]. Atoms initially in $|1\rangle$ are coupled to state $|2\rangle$ with a microwave field tuned around the hyperfine splitting of 6.8 GHz. A first Ramsey pulse with a typical duration of a few tens of µs creates a superposition of the two clock states with a tunable weight. After an "interrogation time" $T_R = 10$ ms, a second identical Ramsey pulse is applied [30]. After this second pulse,

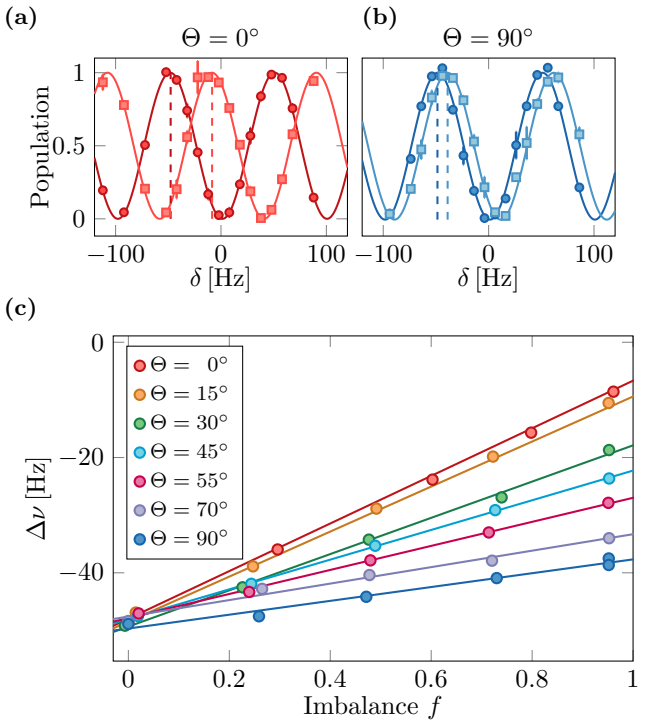

FIG. 2. (a-b) Normalized Ramsey oscillations measured for $\boldsymbol{B}$ perpendicular ($\Theta = 0°$) or parallel ($\Theta = 90°$) to the atomic plane. For both cases, we show the transferred population as a function of detuning δ to the single-atom resonance. In each case the resonance is marked by a vertical dashed line. The circles (resp. squares) correspond to a balanced (resp. unbalanced) mixture $f = 0$ (resp. $f \approx 0.95$). Vertical error bars represent the standard deviation from the 2 measurements realized for each points. (c) Variation of the frequency shift $\Delta\nu$ with the transferred fraction f. We restrict to positive imbalances, for which the population in $|2\rangle$ remains small enough to limit the role of two-body relaxation and spin-changing collisions. For each angle, the solid line is a linear fit to the data.

we perform absorption imaging to determine the population in $|2\rangle$. We measure the variation of this population as a function of the frequency of the microwave field, see Figs. 2ab. We fit a sinusoidal function to the data, so as to determine the resonance frequency of the atomic cloud. All frequency measurements $\Delta\nu$ are reported with respect to reference measurements of the single-atom response that we perform on a dilute cloud. The typical dispersion of the measurement of this single-atom response is about 1 Hz, and provides an estimate of our uncertainty on the frequency measurements. We checked that the measured resonance frequencies are independent of T_R in the range 5 to 20 ms. Shorter delays lead to a lower accuracy on the frequency measurement. For longer delays, we observe demixing dynamics [31] between the two components and a modification of the resonance frequency.

In the following, we restrict to the case of strongly degenerate clouds [32] described in the mean-field approximation. Consider first the case of a uniform 3D gas. The resonant frequency $\Delta\nu$ can be computed by evaluating the difference of mean-field shifts for the two components [29]:

$$\Delta\nu = \frac{\hbar}{M} n \left[a_{22} - a_{11} + (2a_{12} - a_{11} - a_{22}) f\right]. \quad (5)$$

Here the a_{ij} are the inter- and intra-species scattering lengths, $n = n_1 + n_2$ is the total 3D density of the cloud where each component i has a density n_i after the first Ramsey pulse and $f = (n_1 - n_2)/(n_1 + n_2)$ describes the population imbalance between the two states.

It is interesting to discuss briefly two limiting cases of Eq. (5). In the low transfer limit $f \approx 1$, the first Ramsey pulse produces only a few atoms in state $|2\rangle$, imbedded in a bath of state $|1\rangle$ atoms. Interactions within pairs of state $|2\rangle$ atoms then play a negligible role, so that the shift $\Delta\nu$ does not depend on a_{22}. It is proportional to $(a_{12} - a_{11})$, hence sensitive to MDDI. In the balanced case $f = 0$, the Ramsey sequence transforms a gas initially composed only of atoms in state $|1\rangle$ into a gas composed only of atoms in state $|2\rangle$. The energy balance between initial and final states then gives a contribution $\Delta\nu \propto (a_{22} - a_{11})$, which is insensitive to MDDI.

It is important to note that the validity of Eq. (5) for a many-body system is not straightforward and requires some care [33, 34]. We discuss in Ref. [35] the applicability of this approach to our experimental system, and show that it relies on the almost equality of the three relevant scattering lengths a_{ij} of the problem. Note also that in our geometry, even if the gas is uniform in plane, the density distribution along z is inhomogeneous and the spectroscopy measurement is thus sensitive to the integrated density $\bar{n}(x, y) = \int \mathrm{d}z\, n(x, y, z)$.

We now discuss the measurement of the frequency shift $\Delta\nu$ as a function of the imbalance f for different orientations of the magnetic field with respect to the atomic plane, see Fig. 2c. For each orientation, we confirm the linear behaviour expected from Eq. (5). The variation of the slope $\mathrm{d}\Delta\nu/\mathrm{d}f$ for different orientations reflects the expected modification of a_{12} with Θ of Eq. (4). More quantitatively, we fit a linear function to the data for each Θ. The ratio of the slope to the intercept of this line is $R(\Theta) = (a_{22} + a_{11} - 2a_{12}(\Theta))/(a_{22} - a_{11})$. Interestingly, this ratio is independent of the density calibration and is thus a robust observable.

The evolution of the measured ratio for different angles is shown in Fig. 3. For $\Theta = 0°$ and 90°, we also show the ratio measured for a density approximately twice smaller than the one of Fig. 2. These two points overlap well with the main curve, which confirms the insensitivity of R with respect to $\bar{n}$. We fit a sinusoidal variation $\Theta \mapsto \alpha + \beta\cos(2\Theta)$ to $R(\Theta)$ from which we extract $\alpha = 0.53(1)$

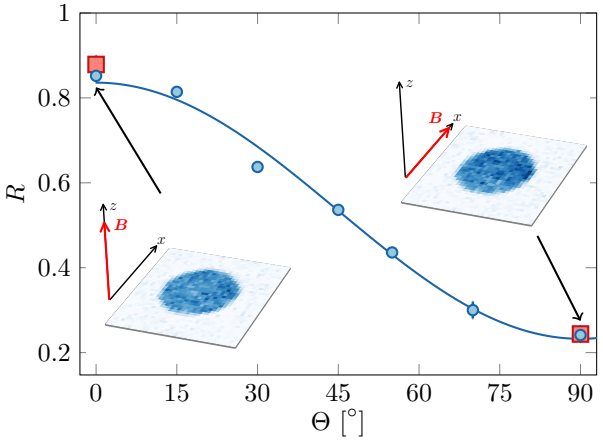

FIG. 3. Variation of the ratio $R(\Theta)$ determined from the data of Fig. 2c with the magnetic field orientation Θ. Blue circles (resp. red squares) correspond to the measurement at maximum density (resp. half density). The variation of this ratio is well fitted by a cosine variation compatible with the prediction for MDDI. The amplitude and offset of this variation allow one to determine accurately relative values of the scattering lengths. Vertical error bars represent the uncertainty obtained from the fitting procedure of the data in Fig.2. The uncertainty on the determination of the angles is limited by the geometrical arrangement of the coils generating the field $\boldsymbol{B}$, estimated here at the level of 1°.

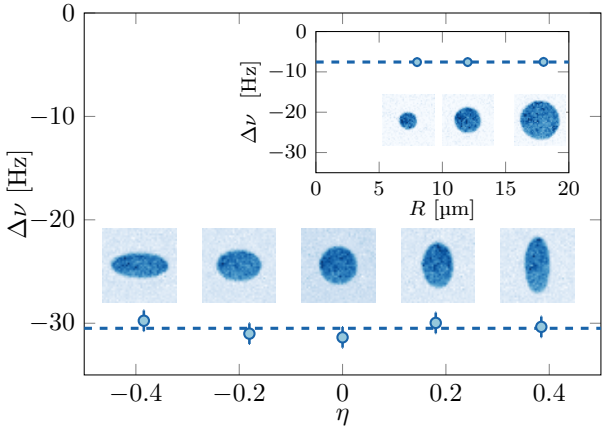

FIG. 4. Interaction shift $\Delta\nu$ as a function of the anisotropy parameter η. For a fixed density and an in-plane magnetic field, we vary the anisotropy of the elliptically-shaped 2D cloud. No dependence on the shape of the cloud is observed, in agreement with the expected isotropic character of MDDI in 2D when $R_{x,y} \gg \ell_z$. Vertical error bars represent the estimated 1 Hz accuracy on the determination of the single-atom resonance frequency. Inset: Interaction shift as a function of the size of the cloud, for $\boldsymbol{B}$ normal to the atom plane.

and $\beta = 0.30(1)$. We then determine $a_{22} - a_{11} = -3a_{\rm dd}/\beta$ and $a_{12}^{(0)} - a_{11} = a_{\rm dd}(3\alpha - 3 - \beta)/(2\beta)$. Using $a_{\rm dd} = 0.70\,a_0$, with a_0 the Bohr radius, we find $a_{22} - a_{11} = -7.0(2)\,a_0$ and $a_{12}^{(0)} - a_{11} = -2.0(1)\,a_0$. These results are in good agreement with the values predicted in [36], $a_{11} = 100.9\,a_0$, $a_{22} - a_{11} = -6.0\,a_0$ and $a_{12}^{(0)} - a_{11} = -2.0\,a_0$.

All experiments described so far have been realized with a fixed disk geometry. As stated above, the description of the contribution of MDDI as a modification of the inter-species scattering length relies on the effective isotropy of the interaction in our 2D system. We investigate this issue by measuring the frequency shift of the clock transition for an in-plane magnetic field orientation ($\Theta = 90°$), which breaks the rotational symmetry of the system. We operate with a fixed density ($\bar{n} \approx 80/\mu\text{m}^2$) and a varying elliptical shape. We choose a large imbalance $f \approx 0.95$ to have the highest sensitivity to possible modifications of a_{12}. We define an anisotropy parameter $\eta = (R_y - R_x)/(R_x + R_y)$ for the ratio of the lengths R_x and R_y of the two axes of the ellipse. We report in Fig. 4 the measured shifts as a function of η and confirm, within our experimental accuracy, this (counter-intuitive) independence of the MDDI energy with respect to the cloud shape. We have also investigated the influence of the size of the cloud on $\Delta\nu$ (inset of Fig. 4). Here we choose a disk-shaped cloud and a magnetic field perpendicular to the atomic plane. We observe no detectable change of $\Delta\nu$ when changing the disk radius from 8 to 18 μm , which confirms the absence of significant finite-size effects.

In conclusion, thanks to high resolution spectroscopy we revealed the non-negligible role of magnetic dipolar interactions between states with a zero average magnetic moment. We observed and explained the modification of the inter-species scattering length in a two-component cloud. Because of the smallness of MDDI in our case, we did not observe any modification of the global shape of the cloud. This contrasts with the case of single-component highly-magnetic dipolar gases where the shape of a trapped gas has been modified with a static [37–39] or time-averaged-field [11, 40]. Nevertheless, the effect observed here provides a novel control on the dynamics of two-component gases, for instance to tune their miscibility or to engineer spin textures. In addition, one can exploit the non-local character of MDDI by confining the atoms in a deep lattice at unit filling, where the exchange coupling evidenced here will implement the so-called quantum XX model [41] without requiring any tunneling between lattice sites. The extreme sensitivity of the clock transition and its protection from magnetic perturbations will then provide a novel, precise tool to detect the various phases of matter predicted within this model.

This work is supported by ERC (Synergy UQUAM), QuantERA ERA-NET (NAQUAS project) and the ANR-18-CE30-0010 grant. We thank F. Pereira dos Santos and P. Julienne for stimulating discussions. We acknowledge the contribution of R. Saint-Jalm at the early stage of the project.

* beugnon@lkb.ens.fr

[1] C. Chin, R. Grimm, P. Julienne, and E. Tiesinga, "Feshbach resonances in ultracold gases," Rev. Mod. Phys. **82**, 1225–1286 (2010).

[2] I. Bloch, J. Dalibard, and W. Zwerger, "Many-body physics with ultracold gases," Rev. Mod. Phys. **80**, 885–964 (2008).

[3] K. Baumann, C. Guerlin, F. Brennecke, and T. Esslinger, "Dicke quantum phase transition with a superfluid gas in an optical cavity," Nature **464**, 1301–1306 (2010).

[4] R. Löw, H. Weimer, J. Nipper, J.B. Balewski, B. Butscher, H.P. Büchler, and T. Pfau, "An experimental and theoretical guide to strongly interacting Rydberg gases," J. Phys. B: At., Mol. Opt. Phys. **45**, 113001 (2012).

[5] T. Lahaye, C. Menotti, L. Santos, M. Lewenstein, and T. Pfau, "The physics of dipolar bosonic quantum gases," Rep. Prog. Phys. **72**, 126401 (2009).

[6] I. Ferrier-Barbut, H. Kadau, M. Schmitt, M. Wenzel, and T. Pfau, "Observation of quantum droplets in a strongly dipolar Bose gas," Phys. Rev. Lett. **116**, 215301 (2016).

[7] L. Chomaz, R.M.W. van Bijnen, D. Petter, G. Faraoni, S. Baier, J.H. Becher, M.J. Mark, F. Waechtler, L. Santos, and F. Ferlaino, "Observation of roton mode population in a dipolar quantum gas," Nat. Phys. **14**, 442–446 (2018).

[8] A. de Paz, A. Sharma, A. Chotia, E. Maréchal, J.H. Huckans, P. Pedri, L. Santos, O. Gorceix, L. Vernac, and B. Laburthe-Tolra, "Nonequilibrium quantum magnetism in a dipolar lattice gas," Phys. Rev. Lett. **111**, 185305 (2013).

[9] S. Baier, M.J. Mark, D. Petter, K. Aikawa, L. Chomaz, Z. Cai, M. Baranov, P. Zoller, and F. Ferlaino, "Extended Bose-Hubbard models with ultracold magnetic atoms," Science **352**, 201–205 (2016).

[10] S. Lepoutre, J. Schachenmayer, L. Gabardos, B. Zhu, B. Naylor, E. Maréchal, O. Gorceix, A.M. Rey, L. Vernac, and B. Laburthe-Tolra, "Out-of-equilibrium quantum magnetism and thermalization in a spin-3 many-body dipolar lattice system," Nat. Commun. **10**, 1–9 (2019).

[11] S. Giovanazzi, A. Görlitz, and T. Pfau, "Tuning the dipolar interaction in quantum gases," Phys. Rev. Lett. **89**, 130401 (2002).

[12] M. Fattori, G. Roati, B. Deissler, C. D'Errico, M. Zaccanti, M. Jona-Lasinio, L. Santos, M. Inguscio, and G. Modugno, "Magnetic dipolar interaction in a Bose-Einstein condensate atomic interferometer," Phys. Rev. Lett. **101**, 190405 (2008).

[13] S.E. Pollack, D. Dries, M. Junker, Y. P. Chen, T.A. Corcovilos, and R.G. Hulet, "Extreme tunability of interactions in a ^{7}Li Bose-Einstein condensate," Phys. Rev. Lett. **102**, 090402 (2009).

[14] D.M. Stamper-Kurn and M. Ueda, "Spinor Bose gases: Symmetries, magnetism, and quantum dynamics," Rev. Mod. Phys. **85**, 1191–1244 (2013).

[15] S. Yi, L. You, and H. Pu, "Quantum phases of dipolar spinor condensates," Phys. Rev. Lett. **93**, 040403 (2004).

[16] M. Vengalattore, S.R. Leslie, J. Guzman, and D.M. Stamper-Kurn, "Spontaneously modulated spin textures in a dipolar spinor Bose-Einstein condensate," Phys. Rev. Lett. **100**, 170403 (2008).

[17] Y. Eto, H. Saito, and T. Hirano, "Observation of dipole-induced spin texture in an ^{87}Rb Bose-Einstein condensate," Phys. Rev. Lett. **112**, 185301 (2014).

[18] G.E. Marti, A. MacRae, R. Olf, S. Lourette, F. Fang, and D.M. Stamper-Kurn, "Coherent magnon optics in a ferromagnetic spinor Bose-Einstein condensate," Phys. Rev. Lett. **113**, 155302 (2014).

[19] B. Yan, S.A. Moses, B. Gadway, J.P. Covey, K.R.A. Hazzard, A.M. Rey, D.S. Jin, and J. Ye, "Observation of dipolar spin-exchange interactions with lattice-confined polar molecules," Nature **501**, 521–525 (2013).

[20] S. de Léséleuc, D. Barredo, V. Lienhard, A. Browaeys, and T. Lahaye, "Optical control of the resonant dipole-dipole interaction between Rydberg atoms," Phys. Rev. Lett. **119**, 053202 (2017).

[21] For all experiments reported here, the fraction of atoms in any other spin state remains below our detection sensitivity of 1%.

[22] "For details, see Supplemental Materials,".

[23] U.R. Fischer, "Stability of quasi-two-dimensional Bose-Einstein condensates with dominant dipole-dipole interactions," Phys. Rev. A **73**, 031602 (2006).

[24] A.K. Fedorov, I.L. Kurbakov, Y.E. Shchadilova, and Yu.E. Lozovik, "Two-dimensional Bose gas of tilted dipoles: Roton instability and condensate depletion," Phys. Rev. A **90**, 043616 (2014).

[25] C. Mishra and R. Nath, "Dipolar condensates with tilted dipoles in a pancake-shaped confinement," Phys. Rev. A **94**, 033633 (2016).

[26] S. Yi and L. You, "Trapped atomic condensates with anisotropic interactions," Phys. Rev. A **61**, 041604 (2000).

[27] J. L. Ville, T. Bienaimé, R. Saint-Jalm, L. Corman, M. Aidelsburger, L. Chomaz, K. Kleinlein, D. Perconte, S. Nascimbène, J. Dalibard, and J. Beugnon, "Loading and compression of a single two-dimensional Bose gas in an optical accordion," Phys. Rev. A **95**, 013632 (2017).

[28] R. Saint-Jalm, P. C. M. Castilho, É. Le Cerf, B. Bakkali-Hassani, J.-L. Ville, S. Nascimbene, J. Beugnon, and J. Dalibard, "Dynamical symmetry and breathers in a two-dimensional Bose gas," Phys. Rev. X **9**, 021035 (2019).

[29] D.M. Harber, H.J. Lewandowski, J.M. McGuirk, and E.A. Cornell, "Effect of cold collisions on spin coherence and resonance shifts in a magnetically trapped ultracold gas," Phys. Rev. A **66**, 053616 (2002).

[30] The imbalance f is tuned mostly by changing the pulse duration but for small pulses area it is more convenient to also decrease the Rabi frequency to avoid using very short microwave pulses.

[31] E. Timmermans, "Phase separation of Bose-Einstein condensates," Phys. Rev. Lett. **81**, 5718–5721 (1998).

[32] At non-zero temperature, quantum statistics of thermal bosons lead to multiply this shift by a factor which varies from 1 in the very degenerate regime to 2 for a thermal cloud.

[33] M.J. Martin, M. Bishof, M.D. Swallows, X. Zhang, C. Benko, J. von Stecher, A.V. Gorshkov, A.M. Rey, and J. Ye, "A quantum many-body spin system in an optical lattice clock," Science **341**, 632–636 (2013).

[34] R.J. Fletcher, R. Lopes, J. Man, N. Navon, R.P. Smith,

M.W. Zwierlein, and Z. Hadzibabic, "Two-and three-body contacts in the unitary Bose gas," Science **355**, 377–380 (2017).

[35] Y.-Q. Zou, B. Bakkali-Hassani, C. Maury, É. Le Cerf, S. Nascimbene, J. Dalibard, and J. Beugnon, "Tan's two-body contact across the superfluid transition of a planar Bose gas," arXiv:2007. (2020).

[36] P.A. Altin, G. McDonald, D. Döring, J.E. Debs, T.H. Barter, J.D. Close, N.P. Robins, S.A. Haine, T.M. Hanna, and R.P. Anderson, "Optically trapped atom interferometry using the clock transition of large ^{87}Rb Bose–Einstein condensates," New J. Phys. **13**, 065020 (2011).

[37] D.H. J. O'Dell, S. Giovanazzi, and C. Eberlein, "Exact hydrodynamics of a trapped dipolar Bose-Einstein condensate," Phys. Rev. Lett. **92**, 250401 (2004).

[38] J. Stuhler, A. Griesmaier, T. Koch, M. Fattori, T. Pfau, S. Giovanazzi, P. Pedri, and L. Santos, "Observation of dipole-dipole interaction in a degenerate quantum gas," Phys. Rev. Lett. **95**, 150406 (2005).

[39] T. Lahaye, T. Koch, B. Fröhlich, M. Fattori, J. Metz, A. Griesmaier, S. Giovanazzi, and T. Pfau, "Strong dipolar effects in a quantum ferrofluid," Nature **448**, 672–675 (2007).

[40] Y. Tang, W. Kao, K.Y. Li, and B.L. Lev, "Tuning the dipole-dipole interaction in a quantum gas with a rotating magnetic field," Phys. Rev. Lett. **120**, 230401 (2018).

[41] S. Sachdev, *Quantum Phase Transitions* (Cambridge University Press, 2006).

SUPPLEMENTAL MATERIAL

Restriction of the dipole-dipole interaction to the clock state manifold

In this section, we evaluate the action of the magnetic dipole-dipole interaction inside the two-level manifold relevant for the clock transition. First, using the general expression for the coupling between a spin 1/2 (here the outer electron) and a spin i (here the ^{87}Rb nucleus with $i = 3/2$), we obtain the decomposition of the clock states on the basis $|s_Z, i_Z\rangle$:

$$\begin{aligned}|1\rangle &\equiv |F=1, m_Z=0\rangle \\ &= \frac{1}{\sqrt{2}}\left(-|-\frac{1}{2};+\frac{1}{2}\rangle \;+\; |+\frac{1}{2};-\frac{1}{2}\rangle\right) \end{aligned} \tag{6}$$

and

$$\begin{aligned}|2\rangle &\equiv |F=2, m=0\rangle \\ &= \frac{1}{\sqrt{2}}\left(|-\frac{1}{2};+\frac{1}{2}\rangle \;+\; |+\frac{1}{2};-\frac{1}{2}\rangle\right). \end{aligned} \tag{7}$$

The magnetic interaction operator for two electronic spins $\hat{\boldsymbol{s}}_A$ and $\hat{\boldsymbol{s}}_B$ with magnetic moments $\boldsymbol{m}_{A,B} = 2\mu_B \boldsymbol{s}_{A,B}$ is given by

$$\hat{V}_{\rm dd}(r, \boldsymbol{u}) = \frac{\mu_0 \mu_B^2}{\pi r^3}[\hat{\boldsymbol{s}}_A \cdot \hat{\boldsymbol{s}}_B - 3(\hat{\boldsymbol{s}}_A \cdot \boldsymbol{u})(\hat{\boldsymbol{s}}_B \cdot \boldsymbol{u})], \tag{8}$$

where r is the distance between the two dipoles and $\boldsymbol{u}$ is the unit vector connecting them. We calculate the matrix elements of this operator in the basis $\{|11\rangle, |12\rangle, |21\rangle, |22\rangle\}$, restricting to elastic interactions which are the only relevant ones for the experimental time scale. This leaves us with four different matrix elements to compute: V_{1111}, V_{2222}, $V_{1212} = V_{2121}$ and $V_{1221} = V_{2112}$, where $V_{ijkl} = \langle kl|\hat{V}_{\rm dd}|ij\rangle$. The calculation in the basis (6,7) leads to

$$\hat{s}_Z|1\rangle = \frac{1}{2}|2\rangle, \qquad \hat{s}_Z|2\rangle = \frac{1}{2}|1\rangle \tag{9}$$

The operators $\hat{s}_X$ and $\hat{s}_Y$ couple states with different m_F values and the associated matrix elements V_{ijkl} inside the clock state manifold are zero. The magnetic interaction operator in Eq. (8) thus simplifies to

$$\hat{V}_{\rm dd}(r, \theta) = \frac{\mu_0 \mu_B^2}{\pi r^3}\,(1 - 3\cos^2\theta)\;\hat{s}_{Z,A}\,\hat{s}_{Z,B}. \tag{10}$$

We deduce that among the four matrix elements mentioned above, only

$$V_{1221} = V_{2112} = \frac{\mu_0 \mu_B^2}{4\pi r^3}\,(1 - 3\cos^2\theta) \tag{11}$$

is non-zero, where θ is the angle between $\boldsymbol{u}$ and the quantization axis. This shows that MDDI do not modify the interactions between atoms in the same state $|1\rangle$ or $|2\rangle$, but induce a non-local, angle-dependent, exchange interaction. The second-quantized Hamiltonian of the MDDI for the clock transition is thus:

$$\begin{aligned}\hat{H}_{\rm dd}^{(1,2)} = \frac{\mu_0 \mu_B^2}{4\pi} \iint {\rm d}^3 r_A\, {\rm d}^3 r_B\; \frac{1 - 3\cos^2\theta}{|\boldsymbol{r}_A - \boldsymbol{r}_B|^3} \\ \times\; \hat{\Psi}_2^\dagger(\boldsymbol{r}_A)\,\hat{\Psi}_1^\dagger(\boldsymbol{r}_B)\,\hat{\Psi}_2(\boldsymbol{r}_B)\,\hat{\Psi}_1(\boldsymbol{r}_A), \end{aligned} \tag{12}$$

where the $\hat{\Psi}_i(\boldsymbol{r}_\alpha)$ are the field operators annihilating a particle in state $|i\rangle$ at position $\boldsymbol{r}_\alpha$.

Calculation of δa_{12}

We consider a gas with a density distribution $n(x, y, z) = \rho(x, y)e^{-z^2/\ell_z^2}/(\ell_z\sqrt{\pi})$ subject to a magnetic field $\boldsymbol{B} = B(\cos\Theta\,\boldsymbol{u}_z + \sin\Theta\,\boldsymbol{u}_x)$ which defines the quantization axis Z for the spin states. We compute the mean-field energy associated to magnetic dipole-dipole interactions following Ref. [23]. In Fourier space, we express the mean-field energy as

$$\langle H_{dd}\rangle = \frac{1}{2}\frac{1}{(2\pi)^3}\int {\rm d}^3 k\; \tilde{n}(\boldsymbol{k})\; \tilde{V}_{dd}(\boldsymbol{k})\; \tilde{n}(-\boldsymbol{k}) \tag{13}$$

where $\tilde{V}_{dd}(\boldsymbol{k}) = 3\mu_0\mu_B^2[\cos^2\alpha - 1/3]$ is the Fourier transform of the dipole-dipole interaction with α the angle of the wavevector $\boldsymbol{k}$ with respect to $\boldsymbol{B}$. The Fourier transform of the density distribution is given by $\tilde{n}(\boldsymbol{k}) = e^{k_z^2\ell_z^2/4}\tilde{\rho}(k_x, k_y)$. Introducing $k = |\boldsymbol{k}|$, we have $\cos(\alpha) = (k_z\cos\Theta + k_x\sin\Theta)/k$ and we get

$$\langle H_{dd}\rangle = \frac{\mu_0\mu_B^2}{3\sqrt{2\pi}\ell_z}\left\{\frac{1}{(2\pi)^2}\int {\rm d}^2 k\;\tilde{\rho}(k_x, k_y)\;\tilde{\rho}(-k_x, -k_y)\left[(3\cos^2\Theta - 1) + \left(\frac{k_x^2}{k_\perp^2}\sin^2\Theta - \cos^2\Theta\right)\mathcal{F}(k_\perp\ell_z)\right]\right\}, \tag{14}$$

where we have introduced $k_\perp = \sqrt{k_x^2 + k_y^2}$ and $\mathcal{F}(k_\perp\ell_z) = 3\sqrt{\pi/2}k_\perp\ell_z e^{k_\perp^2\ell_z^2/2}\,{\rm erfc}(k_\perp\ell_z^2/\sqrt{2})$. For a

uniform system, $\rho(k_x, k_y) = \delta(k_x)\delta(k_y)$ and we recover Eq.(3). Consider now the case of spins aligned along the x axis corresponding to $\Theta = \pi/2$, as in Fig. 4 of the main text. For a cloud shape with typical length scales larger than ℓ_z, the influence of the shape of the cloud via the integration over k_x and k_y scales with $\mathcal{F}(k_\perp \ell_z) \sim k_\perp \ell_z$, which is a small parameter in the 2D case considered here. Thus, the mean-field shift is expected to be independent of the in-plane geometry of the cloud.

Bibliography

BIBLIOGRAPHY

[1] Pyotr Kapitza. "Viscosity of liquid helium below the λ-point". In: *Nature* 141.3558 (1938), pp. 74–74 (cited on page xi).

[2] John F Allen and AD Misener. "Flow of liquid helium II". In: *Nature* 141.3558 (1938), pp. 75–75 (cited on page xi).

[3] Mike H Anderson, Jason R Ensher, Michael R Matthews, Carl E Wieman, and Eric A Cornell. "Observation of Bose-Einstein condensation in a dilute atomic vapor". In: *science* 269.5221 (1995), pp. 198–201 (cited on page xi).

[4] Cl C Bradley, CA Sackett, JJ Tollett, and Randall G Hulet. "Evidence of Bose-Einstein condensation in an atomic gas with attractive interactions". In: *Physical review letters* 75.9 (1995), p. 1687 (cited on page xi).

[5] Kendall B Davis, M-O Mewes, Michael R Andrews, Nicolaas J van Druten, Dallin S Durfee, DM Kurn, and Wolfgang Ketterle. "Bose-Einstein condensation in a gas of sodium atoms". In: *Physical review letters* 75.22 (1995), p. 3969 (cited on page xi).

[6] Immanuel Bloch, Jean Dalibard, and Wilhelm Zwerger. "Many-body physics with ultracold gases". In: *Reviews of modern physics* 80.3 (2008), p. 885 (cited on pages xi, xii).

[7] MR Andrews, CG Townsend, H-J Miesner, DS Durfee, DM Kurn, and W Ketterle. "Observation of interference between two Bose condensates". In: *Science* 275.5300 (1997), pp. 637–641 (cited on page xi).

[8] Immanuel Bloch, Theodor W Hänsch, and Tilman Esslinger. "Measurement of the spatial coherence of a trapped Bose gas at the phase transition". In: *Nature* 403.6766 (2000), pp. 166–170 (cited on page xi).

[9] KW Madison, F Chevy, W Wohlleben, and Jl Dalibard. "Vortex formation in a stirred Bose-Einstein condensate". In: *Physical review letters* 84.5 (2000), p. 806 (cited on pages xi, 120).

[10] JR Abo-Shaeer, C Raman, JM Vogels, and Wolfgang Ketterle. "Observation of vortex lattices in Bose-Einstein condensates". In: *Science* 292.5516 (2001), pp. 476–479 (cited on pages xi, 120).

[11] Ph Courteille, RS Freeland, DJ Heinzen, FA Van Abeelen, and BJ Verhaar. "Observation of a Feshbach resonance in cold atom scattering". In: *Physical Review Letters* 81.1 (1998), p. 69 (cited on page xi).

[12] S Inouye, MR Andrews, J Stenger, H-J Miesner, DM Stamper-Kurn, and W Ketterle. "Observation of Feshbach resonances in a Bose–Einstein condensate". In: *Nature* 392.6672 (1998), pp. 151–154 (cited on page xi).

[13] Simon L Cornish, Neil R Claussen, Jacob L Roberts, Eric A Cornell, and Carl E Wieman. "Stable ^{85}Rb Bose-Einstein condensates with widely tunable interactions". In: *Physical Review Letters* 85.9 (2000), p. 1795 (cited on page xi).

[14] Zoran Hadzibabic, Peter Krüger, Marc Cheneau, Baptiste Battelier, and Jean Dalibard. "Berezinskii–Kosterlitz–Thouless crossover in a trapped atomic gas". In: *Nature* 441.7097 (2006), pp. 1118–1121 (cited on pages xi, xii).

[15] Toshiya Kinoshita, Trevor Wenger, and David S Weiss. "Observation of a one-dimensional Tonks-Girardeau gas". In: *Science* 305.5687 (2004), pp. 1125–1128 (cited on page xi).

[16] Belén Paredes, Artur Widera, Valentin Murg, Olaf Mandel, Simon Fölling, Ignacio Cirac, Gora V Shlyapnikov, Theodor W Hänsch, and Immanuel Bloch. "Tonks–Girardeau gas of ultracold atoms in an optical lattice". In: *Nature* 429.6989 (2004), pp. 277–281 (cited on page xi).

[17] Axel Griesmaier, Jörg Werner, Sven Hensler, Jürgen Stuhler, and Tilman Pfau. "Bose-Einstein condensation of chromium". In: *Physical Review Letters* 94.16 (2005), p. 160401 (cited on page xi).

[18] Mingwu Lu, Nathaniel Q Burdick, Seo Ho Youn, and Benjamin L Lev. "Strongly dipolar Bose-Einstein condensate of dysprosium". In: *Physical review letters* 107.19 (2011), p. 190401 (cited on page xi).

[19] Thierry Lahaye, Tobias Koch, Bernd Fröhlich, Marco Fattori, Jonas Metz, Axel Griesmaier, Stefano Giovanazzi, and Tilman Pfau. "Strong dipolar effects in a quantum ferrofluid". In: *Nature* 448.7154 (2007), pp. 672–675 (cited on page xi).

[20] T Kovachy, P Asenbaum, C Overstreet, CA Donnelly, SM Dickerson, A Sugarbaker, JM Hogan, and MA Kasevich. "Quantum superposition at the half-metre scale". In: *Nature* 528.7583 (2015), pp. 530–533 (cited on page xi).

[21] Sara L Campbell, RB Hutson, GE Marti, A Goban, N Darkwah Oppong, RL McNally, L Sonderhouse, JM Robinson, W Zhang, BJ Bloom, et al. "A Fermi-degenerate three-dimensional optical lattice clock". In: *Science* 358.6359 (2017), pp. 90–94 (cited on page xi).

[22] Shimon Kolkowitz, Igor Pikovski, Nicholas Langellier, Mikhail D Lukin, Ronald L Walsworth, and Jun Ye. "Gravitational wave detection with optical lattice atomic clocks". In: *Physical Review D* 94.12 (2016), p. 124043 (cited on page xi).

[23] RM Godun, PBR Nisbet-Jones, JM Jones, SA King, LAM Johnson, HS Margolis, K Szymaniec, SN Lea, K Bongs, and P Gill. "Frequency ratio of two optical clock transitions in $^{171}Yb^{+}$ 171 and constraints on the time variation of fundamental constants". In: *Physical review letters* 113.21 (2014), p. 210801 (cited on page xi).

[24] Liang Hu, Enlong Wang, Leonardo Salvi, Jonathan N Tinsley, Guglielmo M Tino, and Nicola Poli. "Sr atom interferometry with the optical clock transition as a gravimeter and a gravity gradiometer". In: *Classical and Quantum Gravity* 37.1 (2019), p. 014001 (cited on page xi).

[25] Immanuel Bloch, Jean Dalibard, and Sylvain Nascimbene. "Quantum simulations with ultracold quantum gases". In: *Nature Physics* 8.4 (2012), pp. 267–276 (cited on page xii).

[26] Markus Greiner, Olaf Mandel, Tilman Esslinger, Theodor W Hänsch, and Immanuel Bloch. "Quantum phase transition from a superfluid to a Mott insulator in a gas of ultracold atoms". In: *nature* 415.6867 (2002), pp. 39–44 (cited on page xii).

[27] Michael Köhl, Henning Moritz, Thilo Stöferle, Kenneth Günter, and Tilman Esslinger. "Fermionic atoms in a three dimensional optical lattice: Observing Fermi surfaces, dynamics, and interactions". In: *Physical review letters* 94.8 (2005), p. 080403 (cited on page xii).

[28] Zoran Hadzibabic and Jean Dalibard. "Two-dimensional Bose fluids: An atomic physics perspective". In: *arXiv preprint arXiv:0912.1490* (2009) (cited on pages xii, 6, 18).

[29] VL Berezinsky. "Destruction of long-range order in one-dimensional and two-dimensional systems possessing a continuous symmetry group. II. Quantum systems." In: *Zh. Eksp. Teor. Fiz.* 61 (1972), p. 610 (cited on pages xii, 7).

[30] John Michael Kosterlitz and David James Thouless. "Ordering, metastability and phase transitions in two-dimensional systems". In: *Journal of Physics C: Solid State Physics* 6.7 (1973), p. 1181 (cited on pages xii, 7).

[31] Georgios Roumpos, Michael Lohse, Wolfgang H Nitsche, Jonathan Keeling, Marzena Hanna Szymańska, Peter B Littlewood, Andreas Löffler, Sven Höfling, Lukas Worschech, Alfred Forchel, et al. "Power-law decay of the spatial correlation function in exciton-polariton condensates". In: *Proceedings of the National Academy of Sciences* 109.17 (2012), pp. 6467–6472 (cited on pages xii, 18).

[32] Wolfgang H Nitsche, Na Young Kim, Georgios Roumpos, Christian Schneider, Martin Kamp, Sven Höfling, Alfred Forchel, and Yoshihisa Yamamoto. "Algebraic order and the Berezinskii-Kosterlitz-Thouless transition in an exciton-polariton gas". In: *Physical Review B* 90.20 (2014), p. 205430 (cited on pages xii, 18).

[33] Davide Caputo, Dario Ballarini, Galbadrakh Dagvadorj, Carlos Sánchez Muñoz, Milena De Giorgi, Lorenzo Dominici, Kenneth West, Loren N Pfeiffer, Giuseppe Gigli, Fabrice P Laussy, et al. "Topological order and thermal equilibrium in polariton condensates". In: *Nature materials* 17.2 (2018), pp. 145–151 (cited on pages xii, 18).

[34] Suzanne Dang, Marta Zamorano, Stephan Suffit, Kenneth West, Kirk Baldwin, Loren Pfeiffer, Markus Holzmann, and François Dubin. "Observation of Algebraic Time Order for Two-Dimensional Dipolar Excitons". In: *arXiv preprint arXiv:2001.01309* (2020) (cited on pages xii, 18).

[35] Pierre Cladé, Changhyun Ryu, Anand Ramanathan, Kristian Helmerson, and William D Phillips. "Observation of a 2D Bose gas: from thermal to quasicondensate to superfluid". In: *Physical review letters* 102.17 (2009), p. 170401 (cited on pages xii, 18).

[36] Zoran Hadzibabic, Peter Krüger, Marc Cheneau, Baptiste Battelier, and Jean Dalibard. "Berezinskii–Kosterlitz–Thouless crossover in a trapped atomic gas". In: *Nature* 441.7097 (2006), pp. 1118–1121 (cited on pages xii, 18).

[37] PA Murthy, I Boettcher, L Bayha, M Holzmann, D Kedar, M Neidig, MG Ries, AN Wenz, G Zürn, and S Jochim. "Observation of the Berezinskii-Kosterlitz-Thouless phase transition in an ultracold Fermi gas". In: *Physical review letters* 115.1 (2015), p. 010401 (cited on pages xii, 18).

[38] Rémi Desbuquois, Tarik Yefsah, Lauriane Chomaz, Christof Weitenberg, Laura Corman, Sylvain Nascimbène, and Jean Dalibard. "Determination of scale-invariant equations of state without fitting parameters: Application to the two-dimensional Bose gas across the Berezinskii-Kosterlitz-Thouless transition". In: *Physical review letters* 113.2 (2014), p. 020404 (cited on pages xii, 9).

[39] Tarik Yefsah, Rémi Desbuquois, Lauriane Chomaz, Kenneth J Günter, and Jean Dalibard. "Exploring the thermodynamics of a two-dimensional Bose gas". In: *Physical review letters* 107.13 (2011), p. 130401 (cited on pages xii, 9).

[40] Nikolay Prokof'ev and Boris Svistunov. "Two-dimensional weakly interacting Bose gas in the fluctuation region". In: *Physical Review A* 66.4 (2002), p. 043608 (cited on pages xii, 12, 13, 35).

[41] Chen-Lung Hung, Xibo Zhang, Nathan Gemelke, and Cheng Chin. "Observation of scale invariance and universality in two-dimensional Bose gases". In: *Nature* 470.7333 (2011), pp. 236–239 (cited on page xii).

[42] LP Pitaevskii and A Rosch. "Breathing modes and hidden symmetry of trapped atoms in two dimensions". In: *Physical Review A* 55.2 (1997), R853 (cited on pages xii, 10).

[43] Raphaël Saint-Jalm, Patricia CM Castilho, Édouard Le Cerf, Brice Bakkali-Hassani, J-L Ville, Sylvain Nascimbene, Jérôme Beugnon, and Jean Dalibard. "Dynamical symmetry and breathers in a two-dimensional Bose gas". In: *Physical Review X* 9.2 (2019), p. 021035 (cited on pages xii, 10, 36, 37).

[44] Biswaroop Mukherjee, Zhenjie Yan, Parth B Patel, Zoran Hadzibabic, Tarik Yefsah, Julian Struck, and Martin W Zwierlein. "Homogeneous atomic Fermi gases". In: *Physical review letters* 118.12 (2017), p. 123401 (cited on pages xii, 41).

[45] Alexander L Gaunt, Tobias F Schmidutz, Igor Gotlibovych, Robert P Smith, and Zoran Hadzibabic. "Bose-Einstein condensation of atoms in a uniform potential". In: *Physical review letters* 110.20 (2013), p. 200406 (cited on pages xii, 41).

[46] JL Ville, Tom Bienaimé, R Saint Jalm, Laura Corman, Monika Aidelsburger, Lauriane Chomaz, Katharina Kleinlein, D Perconte, Sylvain Nascimbène, Jean Dalibard, et al. "Loading and compression of a single two-dimensional Bose gas in an optical accordion". In: *Physical Review A* 95.1 (2017), p. 013632 (cited on pages xii, 29).

[47] CJ Myatt, EA Burt, RW Ghrist, Eric A Cornell, and CE Wieman. "Production of two overlapping Bose-Einstein condensates by sympathetic cooling". In: *Physical Review Letters* 78.4 (1997), p. 586 (cited on pages xiii, 68).

[48] J Stenger, S Inouye, DM Stamper-Kurn, H-J Miesner, AP Chikkatur, and W Ketterle. "Spin domains in ground-state Bose-Einstein condensates". In: *Nature* 396.6709 (1998), pp. 345–348 (cited on pages xiii, 68).

[49] H-J Miesner, DM Stamper-Kurn, Jörn Stenger, Shin Inouye, AP Chikkatur, and Wolfgang Ketterle. "Observation of metastable states in spinor Bose-Einstein condensates". In: *Physical Review Letters* 82.11 (1999), p. 2228 (cited on pages xiii, 68).

[50] F Schreck, Lev Khaykovich, KL Corwin, G Ferrari, Thomas Bourdel, Julien Cubizolles, and Christophe Salomon. "Quasipure Bose-Einstein condensate immersed in a Fermi sea". In: *Physical Review Letters* 87.8 (2001), p. 080403 (cited on page xiii).

[51] Andrew G Truscott, Kevin E Strecker, William I McAlexander, Guthrie B Partridge, and Randall G Hulet. "Observation of Fermi pressure in a gas of trapped atoms". In: *Science* 291.5513 (2001), pp. 2570–2572 (cited on page xiii).

[52] SB Papp, JM Pino, and CE Wieman. "Tunable miscibility in a dual-species Bose-Einstein condensate". In: *Physical review letters* 101.4 (2008), p. 040402 (cited on pages xiii, 68).

[53] Satoshi Tojo, Yoshihisa Taguchi, Yuta Masuyama, Taro Hayashi, Hiroki Saito, and Takuya Hirano. "Controlling phase separation of binary Bose-Einstein condensates via mixed-spin-channel Feshbach resonance". In: *Physical Review A* 82.3 (2010), p. 033609 (cited on pages xiii, 68).

[54] Stewart D Jenkins and TA Brian Kennedy. "Dynamic stability of dressed condensate mixtures". In: *Physical Review A* 68.5 (2003), p. 053607 (cited on pages xiii, 68).

[55] E Nicklas, H Strobel, T Zibold, C Gross, BA Malomed, PG Kevrekidis, and MK Oberthaler. "Rabi flopping induces spatial demixing dynamics". In: *Physical review letters* 107.19 (2011), p. 193001 (cited on pages xiii, 68).

[56] E Nicklas, W Muessel, H Strobel, PG Kevrekidis, and MK Oberthaler. "Nonlinear dressed states at the miscibility-immiscibility threshold". In: *Physical Review A* 92.5 (2015), p. 053614 (cited on pages xiii, 68).

[57] Eike Nicklas, Markus Karl, Moritz Höfer, Aisling Johnson, Wolfgang Muessel, Helmut Strobel, Jiří Tomkovič, Thomas Gasenzer, and Markus K Oberthaler. "Observation of scaling in the dynamics of a strongly quenched quantum gas". In: *Physical review letters* 115.24 (2015), p. 245301 (cited on page xiii).

[58] S De, DL Campbell, RM Price, A Putra, Brandon M Anderson, and IB Spielman. "Quenched binary Bose-Einstein condensates: Spin-domain formation and coarsening". In: *Physical Review A* 89.3 (2014), p. 033631 (cited on pages xiii, 68, 69).

[59] KM Mertes, JW Merrill, R Carretero-González, DJ Frantzeskakis, PG Kevrekidis, and DS Hall. "Nonequilibrium dynamics and superfluid ring excitations in binary Bose-Einstein condensates". In: *Physical review letters* 99.19 (2007), p. 190402 (cited on pages xiii, 68).

[60] Cheng-An Chen and Chen-Lung Hung. "Observation of Townes solitons in two-dimensional Bose gases". In: *arXiv preprint arXiv:1907.12550* (2019) (cited on pages xiii, 68).

[61] Eddy Timmermans. "Phase separation of Bose-Einstein condensates". In: *Physical review letters* 81.26 (1998), p. 5718 (cited on pages xiii, 66, 73, 74, 78, 80, 82–85, 92, 95, 99, 101, 103, 105, 106, 110–112, 119).

[62] Yujiro Eto, Masaya Kunimi, Hidekatsu Tokita, Hiroki Saito, and Takuya Hirano. "Suppression of relative flow by multiple domains in two-component Bose-Einstein condensates". In: *Physical Review A* 92.1 (2015), p. 013611 (cited on pages xiii, 69).

[63] DM Stamper-Kurn, H-J Miesner, AP Chikkatur, S Inouye, J Stenger, and W Ketterle. "Quantum tunneling across spin domains in a Bose-Einstein condensate". In: *Physical review letters* 83.4 (1999), p. 661 (cited on pages xiii, 69).

[64] Yujiro Eto, Masahiro Takahashi, Masaya Kunimi, Hiroki Saito, and Takuya Hirano. "Nonequilibrium dynamics induced by miscible–immiscible transition in binary Bose–Einstein condensates". In: *New Journal of Physics* 18.7 (2016), p. 073029 (cited on pages xiii, 69).

[65] Scott Beattie, Stuart Moulder, Richard J Fletcher, and Zoran Hadzibabic. "Persistent currents in spinor condensates". In: *Physical review letters* 110.2 (2013), p. 025301 (cited on pages xiii, 69).

[66] MA Hoefer, JJ Chang, C Hamner, and P Engels. "Dark-dark solitons and modulational instability in miscible two-component Bose-Einstein condensates". In: *Physical Review A* 84.4 (2011), p. 041605 (cited on pages xiii, 69).

[67] CR Cabrera, L Tanzi, J Sanz, B Naylor, P Thomas, P Cheiney, and L Tarruell. "Quantum liquid droplets in a mixture of Bose-Einstein condensates". In: *Science* 359.6373 (2018), pp. 301–304 (cited on pages xiii, 69).

[68] G Semeghini, G Ferioli, L Masi, C Mazzinghi, L Wolswijk, F Minardi, M Modugno, G Modugno, M Inguscio, and M Fattori. "Self-bound quantum droplets of atomic mixtures in free space". In: *Physical review letters* 120.23 (2018), p. 235301 (cited on pages xiii, 69).

[69] Hiromitsu Takeuchi, Naoya Suzuki, Kenichi Kasamatsu, Hiroki Saito, and Makoto Tsubota. "Quantum Kelvin-Helmholtz instability in phase-separated two-component Bose-Einstein condensates". In: *Physical Review B* 81.9 (2010), p. 094517 (cited on pages xiii, 69).

[70] Naoya Suzuki, Hiromitsu Takeuchi, Kenichi Kasamatsu, Makoto Tsubota, and Hiroki Saito. "Crossover between Kelvin-Helmholtz and counter-superflow instabilities in two-component Bose-Einstein condensates". In: *Physical Review A* 82.6 (2010), p. 063604 (cited on pages xiii, 69).

[71] Tsuyoshi Kadokura, Tomohiko Aioi, Kazuki Sasaki, Tetsuo Kishimoto, and Hiroki Saito. "Rayleigh-Taylor instability in a two-component Bose-Einstein condensate with rotational symmetry". In: *Physical Review A* 85.1 (2012), p. 013602 (cited on pages xiii, 69).

[72] N David Mermin and Herbert Wagner. "Absence of ferromagnetism or antiferromagnetism in one-or two-dimensional isotropic Heisenberg models". In: *Physical Review Letters* 17.22 (1966), p. 1133 (cited on page 4).

[73] Pierre C Hohenberg. "Existence of long-range order in one and two dimensions". In: *Physical Review* 158.2 (1967), p. 383 (cited on page 4).

[74] RE Peierls. "Bemerkungen über umwandlungstemperaturen". In: *Helv. Phys. Acta* 7.2 (1934), p. 81 (cited on page 4).

[75] Rudolf Peierls. "Quelques propriétés typiques des corps solides". In: *Annales de l'institut Henri Poincaré*. Vol. 5. 3. 1935, pp. 177–222 (cited on page 4).

[76] Jean-Loup Ville. "Quantum gases in box potentials: sound and light in bosonic Flatland". PhD thesis. PSL Research University, 2018 (cited on pages 6, 27, 30, 38).

[77] JL Ville, R Saint-Jalm, É Le Cerf, M Aidelsburger, S Nascimbène, J Dalibard, and J Beugnon. "Sound propagation in a uniform superfluid two-dimensional Bose gas". In: *Physical review letters* 121.14 (2018), p. 145301 (cited on pages 6, 7, 36).

[78] DJ Bishop and JD Reppy. "Study of the superfluid transition in two-dimensional He 4 films". In: *Physical Review Letters* 40.26 (1978), p. 1727 (cited on pages 8, 9).

[79] Nikolay Prokof'ev, Oliver Ruebenacker, and Boris Svistunov. "Critical point of a weakly interacting two-dimensional Bose gas". In: *Physical review letters* 87.27 (2001), p. 270402 (cited on page 8).

[80] Jean Dalibard. "Fluides quantiques de basse dimension et transition de Kosterlitz-Thouless". Notes de cours du Collège de France. 2017 (cited on pages 9, 17).

[81] Raphaël Saint Jalm. "Exploring two-dimensional physics with Bose gases in box potentials: phase ordering and dynamical symmetry". PhD thesis. Université Paris Sciences et Lettres, 2019 (cited on pages 11, 18, 20, 27, 33, 37).

[82] Daniel S Fisher and PC Hohenberg. "Dilute Bose gas in two dimensions". In: *Physical Review B* 37.10 (1988), p. 4936 (cited on page 12).

[83] Claude Cohen-Tannoudji and Cécile Robilliard. "Wave functions, relative phase and interference for atomic Bose–Einstein condensates". In: *Comptes Rendus de l'Académie des Sciences-Series IV-Physics* 2.3 (2001), pp. 445–477 (cited on page 16).

[84] M Naraschewski and RJ Glauber. "Spatial coherence and density correlations of trapped Bose gases". In: *Physical Review A* 59.6 (1999), p. 4595 (cited on pages 20, 21).

[85] Yiquan Zou, Brice Bakkali-Hassani, Chloé Maury, Édouard Le Cerf, Sylvain Nascimbène, Jean Dalibard, and Jérôme Beugnon. "Tan's two-body contact across the superfluid transition of a planar Bose gas". In: *arXiv preprint arXiv:2007.12385* (2020) (cited on pages 22, 120, 121).

[86] Yiquan Zou, Brice Bakkali-Hassani, Chloé Maury, Édouard Le Cerf, Sylvain Nascimbène, Jean Dalibard, and Jérôme Beugnon. "Magnetic dipolar interaction between hyperfine clock states in a planar alkali Bose gas". In: *arXiv preprint arXiv:2007.12389* (2020) (cited on pages 22, 103, 120).

[87] R Hanbury Brown and Richard Q Twiss. "A test of a new type of stellar interferometer on Sirius". In: *Nature* 178.4541 (1956), pp. 1046–1048 (cited on page 22).

[88] Masami Yasuda and Fujio Shimizu. "Observation of two-atom correlation of an ultracold neon atomic beam". In: *Physical review letters* 77.15 (1996), p. 3090 (cited on pages 22, 23).

[89] Simon Fölling, Fabrice Gerbier, Artur Widera, Olaf Mandel, Tatjana Gericke, and Immanuel Bloch. "Spatial quantum noise interferometry in expanding ultracold atom clouds". In: *Nature* 434.7032 (2005), pp. 481–484 (cited on pages 22, 23).

[90] T Rom, Th Best, D Van Oosten, U Schneider, S Fölling, B Paredes, and I Bloch. "Free fermion antibunching in a degenerate atomic Fermi gas released from an optical lattice". In: *Nature* 444.7120 (2006), pp. 733–736 (cited on pages 22, 23).

[91] Martijn Schellekens, Rodolphe Hoppeler, Aurélien Perrin, J Viana Gomes, Denis Boiron, Alain Aspect, and Christoph I Westbrook. "Hanbury Brown Twiss effect for ultracold quantum gases". In: *Science* 310.5748 (2005), pp. 648–651 (cited on page 22).

[92] Tom Jeltes, John M McNamara, Wim Hogervorst, Wim Vassen, Valentina Krachmalnicoff, Martijn Schellekens, Aurélien Perrin, Hong Chang, Denis Boiron, Alain Aspect, et al. "Comparison of the Hanbury Brown–Twiss effect for bosons and fermions". In: *Nature* 445.7126 (2007), pp. 402–405 (cited on page 22).

[93] Jerome Esteve, J-B Trebbia, Thorsten Schumm, Alain Aspect, Christoph I Westbrook, and Isabelle Bouchoule. "Observations of density fluctuations in an elongated Bose gas: Ideal gas and quasicondensate regimes". In: *Physical review letters* 96.13 (2006), p. 130403 (cited on page 23).

[94] Thibaut Jacqmin, Julien Armijo, Tarik Berrada, Karen V Kheruntsyan, and Isabelle Bouchoule. "Sub-Poissonian fluctuations in a 1D Bose gas: from the quantum quasicondensate to the strongly interacting regime". In: *Physical review letters* 106.23 (2011), p. 230405 (cited on pages 23, 24).

[95] DM Harber, HJ Lewandowski, JM McGuirk, and Eric A Cornell. "Effect of cold collisions on spin coherence and resonance shifts in a magnetically trapped ultracold gas". In: *Physical Review A* 66.5 (2002), p. 053616 (cited on pages 24, 120).

[96] Laura Corman. "The two-dimensional Bose Gas in box potentials". PhD thesis. 2016 (cited on pages 27, 51).

[97] Katharina Kleinlein. *Setting up a new experiment for investigating artificial magnetism of two-dimensional Bose gases*. 2014 (cited on page 27).

[98] TP Meyrath, F Schreck, JL Hanssen, C-S Chuu, and MG Raizen. "A high frequency optical trap for atoms using Hermite-Gaussian beams". In: *Optics express* 13.8 (2005), pp. 2843–2851 (cited on page 29).

[99] TC Li, H Kelkar, D Medellin, and MG Raizen. "Real-time control of the periodicity of a standing wave: an optical accordion". In: *Optics express* 16.8 (2008), pp. 5465–5470 (cited on page 29).

[100] S Al-Assam, RA Williams, and CJ Foot. "Ultracold atoms in an optical lattice with dynamically variable periodicity". In: *Physical Review A* 82.2 (2010), p. 021604 (cited on page 29).

[101] Martin Miranda, A Nakamoto, Y Okuyama, A Noguchi, M Ueda, and M Kozuma. "All-optical transport and compression of ytterbium atoms into the surface of a solid immersion lens". In: *Physical Review A* 86.6 (2012), p. 063615 (cited on page 29).

[102] Klaus Hueck, Niclas Luick, Lennart Sobirey, Jonas Siegl, Thomas Lompe, and Henning Moritz. "Two-dimensional homogeneous Fermi gases". In: *Physical review letters* 120.6 (2018), p. 060402 (cited on page 35).

[103] Laura Corman, Jean-Loup Ville, Raphaël Saint-Jalm, Monika Aidelsburger, Tom Bienaimé, Sylvain Nascimbène, Jean Dalibard, and Jérôme Beugnon. "Transmission of near-resonant light through a dense slab of cold atoms". In: *Physical Review A* 96.5 (2017), p. 053629 (cited on page 36).

[104] Raphaël Saint-Jalm, Monika Aidelsburger, JL Ville, Laura Corman, Zoran Hadzibabic, Dominique Delande, Sylvain Nascimbene, Nicolas Cherroret, Jean Dalibard, and Jérôme Beugnon. "Resonant-light diffusion in a disordered atomic layer". In: *Physical Review A* 97.6 (2018), p. 061801 (cited on page 36).

[105] Tin-Lun Ho and Qi Zhou. "Obtaining the phase diagram and thermodynamic quantities of bulk systems from the densities of trapped gases". In: *Nature Physics* 6.2 (2010), pp. 131–134 (cited on page 41).

[106] Robert P Smith, Naaman Tammuz, Robert LD Campbell, Markus Holzmann, and Zoran Hadzibabic. "Condensed fraction of an atomic Bose gas induced by critical correlations". In: *Physical review letters* 107.19 (2011), p. 190403 (cited on page 41).

[107] Sergey Turtaev, Ivo T Leite, Kevin J Mitchell, Miles J Padgett, David B Phillips, and Tomáš Čižmár. "Comparison of nematic liquid-crystal and DMD based spatial light modulation in complex photonics". In: *Optics express* 25.24 (2017), pp. 29874–29884 (cited on page 41).

[108] Florence Nogrette, Henning Labuhn, Sylvain Ravets, Daniel Barredo, Lucas Béguin, Aline Vernier, Thierry Lahaye, and Antoine Browaeys. "Single-atom trapping in holographic 2D arrays of microtraps with arbitrary geometries". In: *Physical Review X* 4.2 (2014), p. 021034 (cited on page 41).

[109] Philip Zupancic, Philipp M Preiss, Ruichao Ma, Alexander Lukin, M Eric Tai, Matthew Rispoli, Rajibul Islam, and Markus Greiner. "Ultra-precise holographic beam shaping for microscopic quantum control". In: *Optics express* 24.13 (2016), pp. 13881–13893 (cited on page 41).

[110] Daniel Barredo, Vincent Lienhard, Sylvain De Leseleuc, Thierry Lahaye, and Antoine Browaeys. "Synthetic three-dimensional atomic structures assembled atom by atom". In: *Nature* 561.7721 (2018), pp. 79–82 (cited on page 41).

[111] G Gauthier, I Lenton, N McKay Parry, M Baker, MJ Davis, H Rubinsztein-Dunlop, and TW Neely. "Configurable microscopic optical potentials for Bose-Einstein condensates using a digital-micromirror device". In: *arXiv preprint arXiv:1605.04928* (2016) (cited on page 41).

[112] Jinyang Liang, Rudolph N Kohn Jr, Michael F Becker, and Daniel J Heinzen. "1.5% root-mean-square flat-intensity laser beam formed using a binary-amplitude spatial light modulator". In: *Applied optics* 48.10 (2009), pp. 1955–1962 (cited on page 41).

[113] Jinyang Liang, Rudolph N Kohn Jr, Michael F Becker, and Daniel J Heinzen. "High-precision laser beam shaping using a binary-amplitude spatial light modulator". In: *Applied optics* 49.8 (2010), pp. 1323–1330 (cited on page 41).

[114] Christophe Dorrer and Jonathan D Zuegel. "Design and analysis of binary beam shapers using error diffusion". In: *JOSA B* 24.6 (2007), pp. 1268–1275 (cited on page 41).

[115] Mohammadamin Tajik, Bernhard Rauer, Thomas Schweigler, Federica Cataldini, João Sabino, Frederik S Møller, Si-Cong Ji, Igor E Mazets, and Jörg Schmiedmayer. "Designing arbitrary one-dimensional potentials on an atom chip". In: *Optics Express* 27.23 (2019), pp. 33474–33487 (cited on page 41).

[116] C Dorrer and J Qiao. "Direct binary search for improved coherent beam shaping and optical differentiation wavefront sensing". In: *Applied optics* 57.29 (2018), pp. 8557–8565 (cited on pages 42, 44).

[117] Avinash Kumar, Romain Dubessy, Thomas Badr, Camilla De Rossi, Mathieu de Goër de Herve, Laurent Longchambon, and Hélène Perrin. "Producing superfluid circulation states using phase imprinting". In: *Physical Review A* 97.4 (2018), p. 043615 (cited on page 42).

[118] Ludovic Keiser, Hadrien Bense, Pierre Colinet, J Bico, and Etienne Reyssat. "Marangoni bursting: evaporation-induced emulsification of binary mixtures on a liquid layer". In: *Physical review letters* 118.7 (2017), p. 074504 (cited on pages 61, 62).

[119] Ludovic Keiser, Hadrien Bense, Cyril Sturtz, Pierre Colinet, Benoît Roman, José Bico, and Étienne Reyssat. "Fragmentation de Marangoni: les gouttes qui s'éclatent". In: *Reflets de la physique* 59 (2018), pp. 32–35 (cited on page 61).

[120] Pierre-Gilles De Gennes and Françoise Brochard-Wyart. *Gouttes, bulles, perles et ondes*. Belin, 2015 (cited on pages 62, 63).

[121] Yvan Castin. "Bose-Einstein condensates in atomic gases: simple theoretical results". In: *Coherent atomic matter waves*. Springer, 2001, pp. 1–136 (cited on page 64).

[122] Kean Loon Lee, Nils B Jørgensen, I-Kang Liu, Lars Wacker, Jan J Arlt, and Nick P Proukakis. "Phase separation and dynamics of two-component Bose-Einstein condensates". In: *Physical Review A* 94.1 (2016), p. 013602 (cited on page 65).

[123] Miki Ota, Stefano Giorgini, and Sandro Stringari. "Magnetic phase transition in a mixture of two interacting superfluid Bose gases at finite temperature". In: *Physical review letters* 123.7 (2019), p. 075301 (cited on page 65).

[124] DS Hall, MR Matthews, JR Ensher, CE Wieman, and Eric A Cornell. "Dynamics of component separation in a binary mixture of Bose-Einstein condensates". In: *Physical Review Letters* 81.8 (1998), p. 1539 (cited on page 68).

[125] Igor Ferrier-Barbut, Marion Delehaye, Sebastien Laurent, Andrew T Grier, Matthieu Pierce, Benno S Rem, Frédéric Chevy, and Christophe Salomon. "A mixture of Bose and Fermi superfluids". In: *Science* 345.6200 (2014), pp. 1035–1038 (cited on page 68).

[126] LE Sadler, JM Higbie, SR Leslie, M Vengalattore, and DM Stamper-Kurn. "Spontaneous symmetry breaking in a quenched ferromagnetic spinor Bose–Einstein condensate". In: *Nature* 443.7109 (2006), pp. 312–315 (cited on page 68).

[127] Joon Hyun Kim, Deokhwa Hong, and Yong-il Shin. "Observation of Two Sound Modes in a Binary Superfluid Gas". In: *arXiv preprint arXiv:1907.10289* (2019) (cited on page 69).

[128] PA Altin, Gordon McDonald, Daniel Doering, JE Debs, TH Barter, JD Close, NP Robins, SA Haine, TM Hanna, and RP Anderson. "Optically trapped atom interferometry using the clock transition of large ^{87}Rb Bose–Einstein condensates". In: *New Journal of Physics* 13.6 (2011), p. 065020 (cited on page 69).

[129] AM Kaufman, RP Anderson, Thomas M Hanna, Eite Tiesinga, Paul S Julienne, and DS Hall. "Radio-frequency dressing of multiple Feshbach resonances". In: *Physical Review A* 80.5 (2009), p. 050701 (cited on page 69).

[130] C Hamner, Yongping Zhang, JJ Chang, Chuanwei Zhang, and P Engels. "Phase winding a two-component Bose-Einstein condensate in an elongated trap: Experimental observation of moving magnetic orders and dark-bright solitons". In: *Physical review letters* 111.26 (2013), p. 264101 (cited on page 69).

[131] PA Altin, Gordon McDonald, Daniel Doering, JE Debs, TH Barter, JD Close, NP Robins, SA Haine, TM Hanna, and RP Anderson. "Optically trapped atom interferometry using the clock transition of large ^{87}Rb Bose–Einstein condensates". In: *New Journal of Physics* 13.6 (2011), p. 065020 (cited on pages 74, 99–103, 110).

[132] X Antoine and R Duboscq. *GPELab, a Matlab toolbox for computing stationary solutions and dynamics of Gross-Pitaevskii equations*. 2014 (cited on page 75).

[133] Weizhu Bao, Dieter Jaksch, and Peter A Markowich. "Numerical solution of the Gross–Pitaevskii equation for Bose–Einstein condensation". In: *Journal of Computational Physics* 187.1 (2003), pp. 318–342 (cited on page 75).